FOSSIL ENERGY

DOE/BC/14994-20
(OSTI ID: 750288)

MODIFICATION OF CHEMICAL AND PHYSICAL FACTORS IN STEAMFLOOD TO INCREASE HEAVY OIL RECOVERY

Final Report
December 1999

By
Y.C. Yortsos
C. Du
I.N. Tsimpanogiannis
S. Poulou
N. Kanellopoulos
A.K. Stubos
B. Xu
D. Salin
H. Kharabaf
B. Sundaryanto
L. Zhan

Work Performed Under Contract No. DE-FG22-96BC14994/SUB

University of Southern California
Los Angeles, California

National Petroleum Technology Office
U. S. DEPARTMENT OF ENERGY
Tulsa, Oklahoma

DISCLAIMER

This report was prepared as an account of work sponsored by an agency of the United States Government. Neither the United States Government nor any agency thereof, nor any of their employees, makes any warranty, expressed or implied, or assumes any legal liability or responsibility for the accuracy, completeness, or usefulness of any information, apparatus, product, or process disclosed, or represents that its use would not infringe privately owned rights. Reference herein to any specific commercial product, process, or service by trade name, trademark, manufacturer, or otherwise does not necessarily constitute or imply its endorsement, recommendation, or favoring by the United States Government or any agency thereof. The views and opinions of authors expressed herein do not necessarily state or reflect those of the United States Government.

This report has been reproduced directly from the best available copy.

DOE/BC/14994-20
Distribution Category UC-122

Modification of Chemical and Physical Factors in Steamflood to Increase Heavy Oil Recovery

By
Y.C. Yortsos
C. Du
I.N. Tsimpanogiannis
S. Poulou
N. Kanellopoulos
A.K. Stubos
B. Xu
D. Salin
H. Kharabaf
B. Sundaryanto
L. Zhan

January 2000

Work Performed Under Contract No. DE-FG22-96BC14994/SUB

Prepared for
U.S. Department of Energy
Assistant Secretary for Fossil Energy

Thomas B. Reid, Project Manager
National Petroleum Technology Office
P.O. Box 3628
Tulsa, OK 74101

University of Southern California
Petroleum Engineering Program
Department of Chemical Engineering
Los Angeles, CA 90089-1211

Table of Contents

Abstract v

Acknowledgements vii

Introduction 1

Publications 3

1. Displacement Regimes in Fully-Developed Steam Injection (*Y.C. Yortsos*) 7

2. A Numerical Study of the Critical Gas Saturation in a Porous Medium (*C. Du and Y.C. Yortsos*) 23

3. A Scaling Theory of Drying in Porous Media (*I.N. Tsimpanogiannis and .C. Yortsos*) (*with the collaboration of S. Poulou, N. Kanellopoulos and A.K. Stubos*) 49

4. Phase Diagram of Fully Developed Drainage: A Study of the Validity of the Buckley-Leverett Equation (*Y.C. Yortsos and B. Xu*) (*and with the collaboration of D. Salin*) 81

5. Invasion Percolation with Memory (*H. Kharabaf and Y.C. Yortsos*) 103

6. Optimization of Fluid Front Dynamics in Porous Media Using Rate Control: Equal Mobility Fluids (*B. Sundaryanto and Y.C. Yortsos*) 141

7. Identification of the Permeability Field of a Porous Medium from the Injection of a Passive Tracer (*L. Zhan and Y.C. Yortsos*) 177

ABSTRACT

The objectives of this contract were to continue previous work and to carry out new fundamental studies in the following areas of interest to thermal recovery: displacement and flow properties of fluids involving phase change in porous media; the effect of reservoir heterogeneity at various scales; flow properties of non-Newtonian fluids; and the optimization of recovery processes. The specific projects are motivated by and address the need to improve heavy oil recovery from typical reservoirs as well as less conventional fractured reservoirs producing from vertical or horizontal wells.

This report covers work performed in the various physicochemical factors for the improvement of oil recovery efficiency. In this context the following general areas were studied: (i) The understanding of vapor-liquid flows in porous media, including processes in steam injection; (ii) The effect of reservoir heterogeneity in a variety of forms, from pore scale to macroscopic scale; (iii) The flow properties of additives for the improvement of recovery efficiency, particularly foams and other non-Newtonian fluids; and (iv) The development of optimization methods to maximize various measures of oil recovery.

ACKNOWLEDGEMENTS

The research reported in this volume was supported by the U.S. Department of Energy under contract DE-FG22-96BC14994/SUB, subcontracted from Stanford University. We would like to express our gratitude to Tom Reid, our DOE Project Manager, for his steady support and commitment. Many thanks are also due to Professor Bill Brigham and Dr. Louis Castanier of SUPRI for their continuing interest and support.

INTRODUCTION

Thermal methods, and particularly steam injection, are recognized as most promising for the efficient recovery of heavy oil. Despite significant progress, however, important technical issues remain open. Specifically, still inadequate is our knowledge of the complex interaction between porous media and the various fluids of thermal recovery (steam, water, heavy oil, gases, and chemicals). While, the interplay of heat transfer and fluid flow with pore- and macro-scale heterogeneity is largely unexplored.

The objectives of this contract were to continue previous work and to carry out new fundamental studies in the following areas of interest to thermal recovery: the displacement patterns and flow properties of fluids involving phase change, such as condensation-evaporation, and the onset of gas flow in solution gas drive in porous media; the effect of reservoir heterogeneity; the flow properties and patterns of various non-Newtonian fluids, particularly those involving yield stress, such as foams and Bingham plastics; and the development of methods to optimize recovery processes. The specific projects are motivated by and address the need to improve recovery from typical reservoirs as well as less conventional fractured reservoirs producing from vertical or horizontal wells.

The studies completed under this contract involve various research tools, including analysis, computations and experiments. We have extensively used pore networks for pore-level modeling and flow visualization using micromodels. Simulation at the pore-scale and the reservoir scale were also understaken. The work has been detailed in a variety of technical publications, conference papers, topical reports and Ph.D Dissertations. Lists of the various publications and theses for which full or partial support was provided by this contract are separately described below.

Due to lack of space, in this report we selectively present representative publications of the work conducted in the following areas: (i) The delineation of the patterns at the pore-network scale in steam injection; (ii) The development of the critical gas saturation in solution gas-drive processes, in relation to foamy oils; (iii) The study of drying patterns during the evaporation of a liquid in a mtarix block, in the ocntext of oil recovery by gas injection; (iv) The phase diagram of fully-developed drainage that accounts for reservoir heterogeneity; (v) The development of a theoretical tool for the description of the displacement patterns in fluids with yield stress, which is the building block for the study of foams and Bingham plastics; (vi) The development of optimization methods to maximize various measures of oil recovery; and (vii) A direct method to identify the permeability heterogeneity of laboratory samples. These contributions are in various stages of publication, as can be also seen from the list attached below.

This contract has supported partly or fully the PhD study of the following students: Pouya Amili, Changan Du, Chunsan Jia, Persefoni Kechagia, Hooshang Kharabaf, Maryam Shariati, Bagus Sudaryanto, Ioannis Tsimpanogiannis and Lang Zhan. In addition, it has partly supported the post-doctoral work of Baomin Xu, May 1995-May 1998, and Catherine Laroche, January 1999-December 1999.

A list of the publications resulting from the research supported is shown below.

1. Yortsos, Y.C., *Probing Pore Structures by Sorption Isotherms and Mercury Porosimetry*, chapter 3 in *Experimental Methods in Porous Media*, P.-Z. Wong, editor, Academic Press, pg. 69-117 (1999).

2. Du, C., and Yortsos, Y.C., *A Numerical Study of the Critical Gas Saturation in a Porous Medium*, Transport in Porous Media **35**, 205-225 (1999).

3. Tsimpanogiannis, I.N., Yortsos, Y.C., Poulou, S., Kanellopoulos, N., and Stubos, A.K., *A Scaling Theory of Drying in Porous Media*, Phys. Rev. E **59**, 4353- 4365 (1999).

4. Xu, B., Kamath, J., Yortsos, Y.C., and Lee, S.H., *Use of Pore-Network Models to Simulate Laboratory Corefloods in a Heterogeneous Carbonate Sample*, SPEJ, 179-187 (1999).

5. Loggia, D., Rakotomalala, N., Salin, D. and Yortsos, Y.C., *The Effect of Mobility Gradients on Viscous Instabilities in Miscible Flows in Porous Media*, Phys. Fluids **11**, 740-742 (1999).

6. Yortsos, Y.C., *The Permeability Variogram from Pressure Transients of Multiple Wells*, special GSA (Geological Society of America) book, "Theory, Modeling and Field Investigation in Hydrogeology: A Special Volume in Honor of Shlomo P. Neuman's 60th Birthday", in press (1999).

7. Lajeunesse, E., Martin J., Rakotomalala, N., Salin, D., and Yortsos, Y.C., *Miscible Displacement in a Hele-Shaw Cell at High Rates*, J. Fluid Mech., in press (1999).

8. Tsimpanogiannis, I.N., Yortsos, Y.C., and Stubos, A.K., *A Note on the Evaporation of a Stagnant Liquid*, Ind. Eng. Chem. Res., to appear (1999).

9. Zhang, Y., Shariati, M. and Yortsos, Y.C., *The Spreading of Immiscible Fluids in Porous Media Under the Influence of Gravity*, Transport in Porous Media, to appear (1999).

10. Sudaryanto, B., and Yortsos, Y.C., *Optimization of Fluid Front Dynamics in Porous Media Using Rate Control: I. Equal Mobility Fluids*, Phys. Fluids, submitted (1999).

11. Zhan, L., and Yortsos, Y.C., *Identification of the Permeability Field of a Porous Media from the Injection of a Passive Tracer*, Phys. Rev. E, submitted (1999).

12. Yortsos, Y.C., Choi, Y., Yang, Z.M., and Shah, P.C., *Analysis and Interpretation of the Water-Oil Ratio in Waterfloods*, SPEJ, to appear (1999).

13. Yortsos, Y.C., *Immiscible Displacement in Fractured Rocks: Upscaling Issues*, Special AGU publication to honor Paul Witherspoon, submitted (1999).

14. Zhan, L., and Yortsos, Y.C., *Identification of the Permeability Heterogeneity of Porous Media from the Displacement of a Passive Tracer*, proceedings of the 10th European Symposium on Improved Oil Recovery, Brighton, UK (August 18-20, 1999).

15. Poulou, S., Stubos, A.K., and Yortsos, Y.C., *A Pore-Network Numerical Model for the Recovery of Oil by Evaporation and Diffusion from Fractured Reservoirs*, proceedings of the 2nd Greek Scientific Conference in Chemical Engineering, University of Thesaloniki, Thesaloniki, Greece (May 26-29, 1999).

16. Yortsos, Y.C., *Displacement Regimes in Fully-Developed Steam Injection*, paper SPE 54117, proceedings of the 1999 SPE International Thermal Operations and Heavy Oil Symposium, Bakersfield, CA (March 17-19, 1999).

17. Amili, P. and Yortsos, Y.C., *Stability of Heat Pipes in Vapor-Dominated Systems*, Proc. 24th Annual Workshop Geothermal Reservoir Engineering, Stanford, CA (Jan. 25-27, 1999).

18. Yortsos, Y.C., Xu, B., and Salin, D., *Phase Diagram of Fully Developed Drainage: A Study of the Validity of the Buckley-Leverett Equation*, SPEJ, submitted (1998).

19. Yang, Z., and Yortsos, Y.C., *Effect of No-Flow Boundaries on Viscous Fingering in Porous Media of Large Aspect Ratio*, SPEJ **3**, 285-292 (1998).

20. Kharabaf, H., and Yortsos, Y.C., *A Pore-Network Model for Foam Formation and Propagation in Porous Media*, SPEJ **13**, 42-53 (1998).

21. Xu, B., Yortsos, Y.C., and Salin, D., *Invasion Percolation with Viscous Forces*, Phys. Rev. E **57**, 739-751 (1998).

22. Loggia, D., Salin, D. and Yortsos, Y.C., *A Note on the Effect of Dispersion on the Stability of Non-monotonic Mobility Profiles in Porous Media*, Phys. Fluids **10**, 747-749 (1998).

23. Shah, C., Kharabaf, H., and Yortsos, Y.C., *Immiscible Displacements Involving Power-Law Fluids in Porous Media*, Proceedings, Seventh UNITAR International Conference on Heavy Crude and Tar Sands, Beijing, China (Oct. 27-30, 1998).

24. Sudaryanto, B. and Yortsos, Y.C., *Optimal Control of Displacement Processes in Porous Media*, paper presented at the 6th European Conference on the Mathematics of Oil Recovery, Peebles, Scotland (Sept. 8-11, 1998).

25. Yortsos, Y.C., Tsimpanogiannis, I., Poulou, S., Stubos, A.S. and Kanellopoulos, N.K., *Scaling of Diffusion-Driven Displacement Patterns in Porous Media*, Proceedings, Computational Methods in Water Resources XII, **1**, 461-468 (1998).

26. Satik, C. and Yortsos, Y.C., *Pore-Network Studies of Steam Injection in Porous Media*, SPEJ, accepted (1997).

27. Kharabaf, H., and Yortsos, Y.C., *Invasion Percolation with Memory*, Phys. Rev. E **55**, 7177-7191 (1997).

28. Yang, Z., and Yortsos, Y.C., *Asymptotic Solutions of Miscible Displacements in Geometries of Large Aspect Ratio*, Phys. Fluids **9**, 286-298 (1997).

29. Y.C. Yortsos, *Discussion of Pressure and Volume Evolution During Gas Phase Formation in Solution Gas Drive Processes*, SPEJ **2**, 223-226 (1997).

30. Yortsos, Y.C., and Al-Afaleg, N., *The Permeability Variogram from Pressure Transients of Multiple Wells: I. Theory and 1-D Application*, SPEJ, **2** 328-337 (1997).

31. Yortsos, Y.C., Xu, B. and Salin, D., *Phase Diagram of Fully Developed Drainage*, Phys. Rev. Lett., **79**, 4581-4584 (1997).

32. Haghighi, M., and Yortsos, Y.C., *Visualization of Steam Injection in Fractured Systems Using Micromodels*, paper SPE 37520 presented at the International Symposium on Thermal Operations and Heavy Oil, Bakesrfield, CA (Feb. 10-12, 1997).

33. Yang, Z.M., and Yortsos, Y.C., *Asymptotic Regimes in Miscible Displacements in Random Porous Media*, paper SPE 35456 presented at the SPE/DOE Symposium for Improved Oil Recovery, Tulsa, OK (Apr. 21-24, 1996).

1. DISPLACEMENT REGIMES IN FULLY-DEVELOPED STEAM INJECTION

Y.C. Yortsos

ABSTRACT

We present an analysis of the displacement properties during the dynamic invasion of steam in a porous medium. Two fully developed regimes are identified, similar to the Stabilized Displacement (SD) and the Capillary-Viscous Fingering (CVF) regimes of the isothermal drainage problem (Yortsos et al., 1997). Phase change and heat transfer affect the scaling of the various properties of these regimes. Near the advancing steam front, phase change and heat transfer bring about a qualitative change in the flow permeabilities, although not in the displacement pattern, which remains of the Invasion Percolation type, if injection rates are sufficiently small. The relative permeabilities in this region are larger than those for the isothermal displacement problem. A condition is developed to delineate the regions of validity of these two regimes.

INTRODUCTION

Understanding the mechanisms of flow and the displacement properties in a steam zone is a subject of continuous interest to processes in thermal oil recovery (Prats, 1982), boiling in porous media (Ramesh and Torrance, 1993) and geothermal applications (Schubert and Straus, 1979). In thermal recovery processes, injected or in-situ generated steam displaces initial liquids in-place, such as water and oil, and liquid water generated by steam condensation. Although these displacements involve immiscible fluids, possible effects of phase change, associated with steam condensation, and of heat and mass transfer, have raised the question whether or not the aspects of conventional, isothermal, immiscible displacement are also applicable to steam injection. A significant issue is whether in a steam displacement process the flow patterns will depend on phase change and heat transfer parameters. Given that patterns dictate the various phase configurations, resolving this issue will elucidate the relative permeabilities of steam and water phases, which are important quantities for thermal recovery modeling and need to be determined (Sanchez and Schechter, 1987).

In this paper, we consider the simpler problem of the displacement of an initial subcooled liquid water by injected steam in a porous medium. Neglecting for a moment, the possibility of an oscillatory advance of the steam front, due to rapid condensation and evaporation events (Kong et al., 1992, see also Kneafsey and Pruess, 1999), the displacement process involved is primary drainage, a non-wetting vapor phase displacing a wetting liquid phase. In the absence of phase change, this process has been well understood (see works by Lenormand et al., 1988, Lenormand, 1989, Xu et al., 1998). Recently, we have shown that fully-developed drainage takes the form of one of two different patterns, either a stabilized displacement (SD) or a capillary-viscous fingering (CVF) pattern, depending on the values of the capillary number, $Ca = \frac{q\mu_{nw}}{\gamma}$, and the viscosity ratio, $M = \frac{\mu_{nw}}{\mu_w}$ (Yortsos et al., 1997, 1998, Xu et al., 1998) (see Fig. 1). Here, q is the injection velocity, μ stands for viscosity, γ is the interfacial tension between the two fluids and subscripts nw and w stand for non-wetting and wetting fluids, respectively. The flow properties can be obtained from a knowledge of

the displacement pattern. For example, in the SD case, the advancing front is followed by a viscous-stabilized compact pattern (Fig. 1), where relative permeability and capillary pressure functions could in principle be inferred from percolation concepts (Heiba et al., 1982, Wilkinson, 1984). In CVF, the displacement pattern is diffuse, dominated by viscous fingers, the scaling and properties of which are still not clearly understood, however.

When the injected fluid is subject to phase change, such as steam condensation, the pattern structure will be affected also by heat transfer to the initial subcooled liquids and to the surrounding impermeable rock strata, and may possibly be time-dependent (Satik and Yortsos, 1995). In the case of steam displacement of oil, the process will be additionally complicated by three-phase flow issues, as well as by mass transfer, if the oil contains volatile components. Thus, the determination of the displacement patterns in these processes is substantially more complicated. However, little is known, at present, about this problem.

Closely related is the problem of determining relative permeabilities. In modeling relative permeabilities in steam injection, two different approaches have been taken. In one, practiced mostly in the geothermal literature, the relative permeabilities of steam and water are assumed to be straight lines, the application being mostly to countercurrent water-steam flows. In another approach, taken mostly in the thermal recovery literature, the relative permeabilities are assumed to be identical to those for conventional, isothermal, immiscible displacements. The application here is mostly to steady-state, adiabatic concurrent flow. Sanchez and Schechter (1987) measured steam-water relative permeabilities during steady-state, concurrent and isothermal flow of steam and water and found that they are identical to those for a non-condensible gas-water system. Using percolation theory, Parlar and Yortsos (1987) reached the same conclusions, under the hypothesis of isothermal conditions and lack of heat losses.

However, the assumption of constant temperature, or of negligible heat transfer, and thus of negligible phase change, is not uniformly valid in a steam zone, and certainly not near the steam front region, or where heat losses to the surrounding formations are expected to be significant. In such regions, the flow patterns and distribution will be different from those for the isothermal case. A first attempt to analyze this issue was taken by Satik and Yortsos (1995) who provided a numerical study of steam injection using 2-D pore-network models. They modeled the invasion of steam in a liquid-occupied porous meidum under non-isothermal conditions (see also the related analysis of boiling, Satik and Yortsos, 1996). Their results showed the existence of different patterns and flow distributions, depending on the injection variables and also of the time elapsed.

The objective of this paper is to complement the work of Satik and Yortsos (1995) by providing a theoretical analysis of the steam invasion problem at the pore-network level. In particular, we want to address the issue of how to generalize the results for isothermal drainage, reached by Yortsos et al. (1997) and Xu et al. (1998), and therefore how to model relative permeabilities, in steam injection under non-isothermal conditions. The paper is organized as follows: First, we address the questions of whether or not an Invasion Percolation (IP) pattern, at sufficiently small injection rates, can be sustained under non-isothermal and phase-change conditions, and if so what are the expected flow conductances. Then, we describe features of two fully-developed displacement patterns, analogous to the SD and the CVF patterns for isothermal displacement of Yortsos et al. (1997) (Fig. 1). Finally, we present a phase diagram for these two patterns in the capillary umber-mobility ratio dia-

gram. As in the isothermal case, the delineation of these two regimes essentially constitutes a stability analysis of steam injection at the pore-network level.

ANALYSIS

We consider the injection of a condensible vapor phase, such as steam, in a porous medium, to displace its liquid, initially at subcooled conditions. At least during the initial stages of the displacement, in all cases, or near the leading edge of the front throughout the process, in the case of SD, capillary forces are dominant. It is known that in this case, under isothermal displacement conditions, and in the absence of phase change, the pattern is Invasion Percolation (IP). According to IP rules, this pattern forms one-site-at-a-time by the penetration of the pore throat with the smallest capillary threshold among all pore throats available to the front. A typical IP pattern is shown in Fig. 2. We remark that Satik and Yortsos (1995) showed in their simulations that IP patterns are possible for steam injection at sufficiently low rates. Using percolation theory, Xu et al. (1998) determined the extent of the region near the front, where capillary forces dominate, as a function of the capillary number and the viscosity ratio, by requiring that the pressure drops in the displacing and displaced phases across this region is sufficiently small for IP to apply. When phase change is involved, however, it is not clear, first that an IP pattern can be sustained, even at sufficiently small injection rates, and second that the flow distributions will be the same with those in the isothermal problem. These two issues are successively addressed in the following sections.

Invasion percolation with phase change

In conventional immiscible displacement under IP conditions, the invasion of one pore at a time is the combined result of a constant injection rate and the incompressibility of the two phases. Then, the mass balances at a front meniscus I read (Fig. 3)

$$u_{iI} = u_{dI} = v_I \tag{1}$$

where u_I denotes normal velocity, v_I is the normal velocity of the meniscus, and subscripts i, d and I stand for the invading (non-wetting) phase, the defending (wetting) phase and the meniscus, respectively. At IP conditions, only one meniscus, that with the smallest capillary threshold, advances at a given time step (for example, meniscus A in Fig. 3). For all other mensici, where capillary thresholds are large (for example meniscus I in Fig. 3), the mass balances (1) read

$$u_{iI} = u_{dI} = v_I = 0 \tag{2}$$

Flow conductances and relative permeabilities of displacing and displaced phases can be determined by applying a constant pressure drop across two opposite boundaries of the known IP pattern, imposing no-flow conditions across any menisci not on the two boundaries and calculating the resulting flow rates. The small values of the relative permeability of the invading phase, under these conditions, reflect the tortuosity of the IP pattern.

In problems with phase change, mass and energy balances are different, however. Now, for an arbitrary interface at the front I, steam, water and interface velocities are related according to

$$\rho_s(u_{sI} - v_I) = \rho_w(u_{wI} - v_I) \tag{3}$$

and

$$\rho_s L_v(u_{sI} - v_I) = -\lambda \frac{\partial T}{\partial n}|_I \tag{4}$$

where ρ stands for density, L_v is the latent heat of vaporization, λ is thermal conductivity, T denotes temperature, n is the unit normal to the interface directed towards the liquid phase and subscripts s and w stand for steam and condensed water, respectively. In contrast to the isothermal problem, if capillarity prevents a pore throat from being invaded, steam may still arrive and condense at that meniscus to supply the heat transfer rate required by the temperature field donwstream. Thus, in contrast to isothermal displacements, incoming steam and outgoing condensed water fluxes across a stationary meniscus are not necessarily zero, but they are related to the temperature field, according to (3)-(4), which for $v_I = 0$ read as follows

$$u_{sI} = -\frac{\lambda}{\rho_s L_v}\frac{\partial T}{\partial n}|_I \quad \text{and} \quad u_{wI} = -\frac{\lambda}{\rho_w L_v}\frac{\partial T}{\partial n}|_I \tag{5}$$

Conversely, the penetration of a new pore will require not only that the capillary threshold be exceeded, but also that the temperature of that pore is sufficiently close to the steam temperature, so that heat transfer requirements can be met during the next time step. The distribution of the steam and water flow fields, in response to heat transfer requirements, will be drastically different and will make steam injection a problem qualitatively different from isothermal displacement.

Nonetheless, in the absence of inertia effects (see below) and at sufficiently small rates (see also below), the main forces on a meniscus will still be due to capillarity, thus the sequence of penetration events would still be dictated by the capillary thresholds of the throats neighboring the front. Hence, we expect that IP rules would still be applicable at the leading edge of the front, as in conventional displacements. Indeed, such patterns were obtained in the pore-network simulations of Satik and Yortsos (1995), as discussed above. However, penetration of a pore at the next time step may not occur or even not be possible, depending on the temperature field of the region to be invaded, as discussed above. Although not affecting IP patterns, at low rates, the phase change and heat transfer requirements will affect the flow fields of invading and defending phases, hence their flow conductivities. Thus, the relative permeabilities will not be identical to the conventional, at least near the leading edge of the displacement. In addition, steam condensation at various places at the front could make the rate of advance of the front significantly smaller than that based on the volumetric rate of steam injection (to which it would otherwise coincide under conditions of isothermal displacement) by a factor which can be as large as the density ratio ρ_w/ρ_s. These issues are further discussed below.

We conclude that at least during the initial stages of the displacement, or near the front throughout the process, in the case of SD, the pattern is still Invasion Percolation (IP), as

in the isothermal problem. As in the isothermal displacement problem, we further expect fully-developed steam injection to be described by one of two different regimes: a SD, where a fractal front of dimensionless extent (in pore length units) σ exists, and where the pattern is IP, followed by a viscous-stabilized compact pattern; and a CVF regime, where the pattern is controlled by viscous forces. Intermediate, time-dependent patterns may also develop, as shown in Satik and Yortsos (1995). In the next section we describe some of the expected properties of these regimes.

Properties of fully-developed regimes

To determine the extent of the steam front in SD, we follow the same approach as in Xu et al. (1998) and seek the variation of the capillary pressure, P_c, across this region. For this we need an estimate of the corresponding changes in the pressure of the non-wetting (steam) and the wetting (liquid) phases. In this region, the steam occupies a fractal pattern, the conductance of which, in the isothermal case, scales non-linearly with its extent. However, the flow distributions of steam and displaced water in this region are not necessarily the same as in the isothermal problem, as pointed out above, due to the fact that steam will condense at various places, in order to satisfy heat transfer requirements according to (5) (and also heat transfer to surrounding rock strata).

This coupling with the temperature field makes the problem of determining flow fields, and relative permeabilities, quite complex, and possibly time-dependent. As pointed out above, the flow conductances can be obtained by solving for the pressure field in the percolation cluster, across which a pressure drop is imposed. However, now the boundary conditions at the various interfaces of the cluster will be constant-flux (rather than zero-flux) conditions, as specified by the temperature field (equation (5)). The end result would be that the tortuosity of the fractal IP pattern will have a different (and smaller) effect on the conductances of steam and water phases, which now will also depend on the temperature field in the liquid phase (and the surroundings).

A detailed analysis of this problem will not be presented here. Instead, we will proceed by making the plausible *conjecture* that the pressure drop-flow rate relationship for steam will be similar to the isothermal case as in Xu et al. (1998), but with a smaller conductance exponent α, to reflect the smaller resistance to flow due to condensation. This presumed power law dependence must be verified by additional study, however. Under this assumption, we will have

$$\Delta P_s \sim \frac{u_s \mu_s}{r_m} \sigma^{\frac{\alpha+\nu(D-1)}{\nu}} \tag{6}$$

where r_m is a typical pore size, u_s is the steam velocity in this region, ν is the correlation length exponent of percolation and D is the percolation mass exponent (Stauffer and Aharony, 1992). Implicit in (6) is the assumption that $\alpha < \zeta$, where ζ is the conductance exponent of percolation. An immediate implication of (6) is that the relative permeabilities at the leading edge of the front will be larger than in the isothermal case in this region, not because the pattern is different from IP, which it is not, but because the flow conductance has a different scaling with length under non-isothermal and phase-change conditions. Thus,

we expect that the conventional scaling of the non-wetting relative permeability near the percolation threshold, namely

$$k_{rnw} \sim S_{nw}^{\frac{t\nu}{\beta}} \tag{7}$$

where t and β denote the conductivity and percolation probability exponents of percolation, respectively, would be replaced by the different expression

$$k_{rs} \sim S_s^{\frac{(\alpha+\nu(d-2))\nu}{\beta}} \tag{8}$$

where d denotes dimensionality. Because of the above inequality and the relation $t = \zeta + \nu(d-2)$, equation (8) shows that the steam relative permeability near the front is larger than in the conventional immiscible displacement, for the same saturation, reflecting effects of condensation. Although the precise dependence remains to be determined, this tendency is qualitatively in the same direction with the linear model of steam relative permeabilities, refered to above.

Likewise, the flow field, hence the pressure drop, of the liquid will be affected by the condensing steam. As in the isothermal case, the pressure drop of the liquid would be a linear function of the front extent σ (but with a different, condensation-dependent, prefactor), hence

$$\Delta P_w \sim \frac{u_w \mu_w}{r_m} \sigma \tag{9}$$

Now, near the front, the prevailing non-isothermal conditions will cause most of the steam to condense. In this limiting case, therefore, the overall velocity of the water will be mostly due to condensed steam, thus we expect further

$$u_w \sim \frac{\rho_s u_s}{\rho_w} \tag{10}$$

based on which (9) becomes

$$\Delta P_w \sim \frac{\rho_s u_s \mu_w}{\rho_w r_m} \sigma \tag{11}$$

Combining (6) and (11) gives the variation of the capillary pressure across the front in this limit

$$\Delta P_c \sim \frac{u_s \mu_s}{r_m} \sigma \left(b\sigma^{\frac{\alpha+\nu(D-1)}{\nu}} - M_e \sigma \right) \tag{12}$$

where b is a dimensionless constant and M_e is the ratio of the kinematic viscosities ($M_e = \frac{\rho_s}{\rho_w} M$). By proceeding as in Xu et al. (1998) we can determine the spatial extent of the front σ. Under the above conditions one can derive the equation

$$\left(b\sigma^{\frac{\alpha+\nu(D-1)}{\nu}} - M_e \sigma \right) \sim \frac{2\Sigma}{Ca_{Fs}} \sigma^{-\frac{1}{\nu}} \tag{13}$$

where Σ is a measure of the standard deviation of the pore-size distribution, and the capillary number was based on the average steam velocity at the front.

Comparing (13) with the expression in Xu et al. (1998) for isothermal displacement we note two differences: First, the exponent α is smaller than its isothermal counterpart ζ reflecting the influence of heat transfer (it reduces to the latter under isothermal conditions). Second, the effective viscosity ratio is being replaced by the ratio in kinematic viscosities, reflecting the condensation of steam in the front region. The fact that in problems involving phase change the ratio of kinematic viscosities is the effective viscosity ratio was noted before in macroscopic analyses of steam injection (Miller, 1975, Prats, 1982).

Given the similarity between expression (13) and that for isothermal displacement, we can follow directly the analysis of Xu et al. (1998) to determine the properties of σ, etc. For example, at small values of the capillary number, we can show the following scaling

$$\sigma \sim \left(\frac{Ca_{Fs}}{2\Sigma}\right)^{-\frac{\nu}{1+\alpha+\nu(D-1)}} \tag{14}$$

The smaller value of α above shows that condensation will result in a more sensitive dependence of the front region extent on the capillary number. Other properties follow in a straightforward manner.

The upstream region of a SD will have similar properties with those of the isothermal case. For example, away from the steam front, the steam zone will be a region practically under isothermal conditions, thus the two displacements will have little differences. As a result, we expect that the relative permeabilities in that region should not be much different from their isothermal counterparts. On the other hand, near the steam front, or at places neighboring impermeable rock strata, steam condensation due to heat losses may also occur. This will affect the flow distributions, hence the relative permeabilities to steam and water. We expect that these will tend to approach the linear model, although the specific dependence needs to be more carefully determined.

The other regime expected for fully-developed steam injection will have features similar to the CVF regime of isothermal displacement (Xu et al., 1998) with two notable exceptions. First, and in contrast to isothermal displacement, heat transfer will tend to stabilize the displacement pattern by reducing finger growth and by increasing finger thickness. For example, the macroscopic stability analysis of Miller (1975), the results of which can be extrapolated here, shows that heat conduction is stabilizing steam front fingers. Second, the reduction in the effective mobility of the two fluids, due to condensation, will also affect the properties in this regime. For example, if we follow the approach of Xu et al. (1998), and in the absence of heat conduction, the finger width is predicted to have the scaling

$$\sigma \sim \left(\frac{CaM_e}{2\Sigma}\right)^{-\frac{\nu}{\nu+1}} \tag{15}$$

which indicates a thickness larger by a factor of about $1000^{\frac{\nu}{\nu+1}} \approx 30$ from conventional viscous fingers under otherwise similar conditions. This limiting result, based on negligible heat conduction but accounting for steam condensation, demonstrates the well known stabilizing influence of condensing flows.

We must note that a possibly important effect in this regime of higher rates could be the effect of inertia and the possible large oscillations of menisci. Indeed, at sufficiently large velocities, inertia effects will dominate over capillary and viscous forces and will lead

to new patterns. An analysis of this problem remains to be done. Also, the oscillation of menisci during steam front advance also can be a non-trivial process. Such oscillations may accompany the penetration of a pore throat. For instance, if, due to fluctuations in heat transfer, steam must condense locally, the corresponding meniscus will retract accordingly. The corresponding loss in steam volume must be replaced by an equal volume of liquid, which due to the large density differences, however, comprises a manyfold larger amount of mass. The required mass flow rate can only be provided by the backwards flow of liquid water, which can be accomplished if there is a local pressure lowering. The resulting liquid flows may be inertia-dominated and exert non-trivial effects. On the other hand, the lowering of the saturation temperature, which will result from the lower pressure, will lead to a reduction in the heat loss rate and will act to stabilize the advance of the meniscus. At present, these effects are not well understood.

Phase diagram

Consider, now, the problem of describing the boundary between the two developed regimes of stabilized displacement (SD) and CVF. We will follow Yortsos et al. (1997) and focus on the initial phase of the displacement, where the pattern is of the IP type, of a linear extent $\chi(t) \leq \chi_\epsilon$, where χ_ϵ is to be determined. The pattern will first depart from percolation, where capillary forces are dominant, at $\chi(t) = \chi_\epsilon$, at which point the transition towards a fully developed displacement starts. According to Yortsos et al. (1997), the latter will either become of the SD type (with a compact region following an IP front) or of the CVF type, depending on whether at χ_ϵ, the percolation probability p decreases or increases in the direction of displacement, respectively (and in which case the problem is Invasion Percolation in a Stabilized or a Destabilized Gradient, respectively).

The analysis follows the steps for the SD case presented above. First, we must determine the capillary pressure variation across χ, where percolation concepts apply, and which in absolute values reads as follows

$$|\Delta P_c| \sim \frac{u_s \mu_s}{r_m} \left| c\chi^{\frac{1+\alpha+\nu(D-1)}{\nu}} - M_e \chi \right| \tag{16}$$

where c is another dimensionless constant. In the above we have used the exponent α (yet to be determined) to reflect the influence of heat transfer and phase change on flow conductivities, and assumed that condensation at the front modifies the viscosity ratio to M_e. These two features correspond to the limit when phase change effects are strong. To define χ_ϵ we follow Lenormand (1989), as described in Yortsos et al. (1997). After several manipulations one obtains the following equation for determining χ_ϵ

$$\frac{Ca}{\Sigma} \chi_\epsilon^{\frac{\nu+1}{\nu}} \left| c\chi_\epsilon^{\frac{\alpha+\nu(D-2)}{\nu}} - M_e \right| \sim \epsilon \tag{17}$$

which is qualitatively the same as in Yortsos et al. (1997). Based on (17) these authors further showed that the type of the displacement patterns to be obtained depends on the relative magnitudes of Ca and M_e, as follows:

If $M_e < M^*$ (where M^* is approximately equal to 1), the displacement is unconditionally stabilized and will be of the SD type. In the opposite case ($M_e > M^*$), the displacement will still be stabilized (SD), provided that

$$\frac{Ca}{\Sigma} M_e^{\frac{1+\alpha+\nu(D-1)}{\alpha+\nu(D-2)}} \leq O(\epsilon) \tag{18}$$

Otherwise, a CVF regime will emerge.

The regions of validity of the two regimes according to the above criteria are shown in the log-log plot of Fig. 4. The two regimes are separated by a curve which at large Ca is asymptotically the vertical line $M_e = M^*$, while at Ca is given by the straight line (in $\log Ca$-$\log M_e$ coordinates) defined by condition (18). This straight line has a negative slope equal to $\frac{1+\alpha+\nu(D-1)}{\alpha+\nu(D-2)}$. We note that as α increases, the slope of the curve increases, indicating that the region of validity of the SD diminishes. This reflects the increased flow conductance of the vapor phase as α decreases. Now, in many realistic situations, the value of the effective mobility ratio (equal here to the ratio of the kinematic viscosities), is sufficiently small for the SD regime to be valid under all injection conditions. In such cases, the relative permeabilities in the steam zone would be given by their isothermal counterparts, except near the front, where they would be larger as a result of the phase change.

CONCLUSIONS

In this paper we presented an analysis of the displacement properties during the dynamic invasion of steam in a porous medium. Near the advancing front, phase change and heat transfer bring about a qualitative change in the flow conductances, although not in the displacement pattern, which remains of the Invasion Percolation type, if injection rates are sufficiently small. The relative permeabilities in this region are larger than those for the isothermal displacement problem. Two fully developed regimes were identified, similar to the SD and the CVF regimes of the isothermal drainage problem. Phase change and heat transfer affect the scaling of the various properties of these two regimes. A condition was also developed to delineate the regions of validity of these two regimes. Additional work is required to further understand quantitatively the various properties, however. Not included, but potentially important, effects of inertia, also need further study.

NOMENCLATURE

b: prefactor of the power-law, dimensionless
c: prefactor of the power-law, dimensionless
Ca: capillary number, dimensionless
d: Euclidean dimension exponent, dimensionless
D: mass dimension exponent, dimensionless
k: relative permeability, dimensionless
L_v: latent heat, $[\mathrm{L}^2\mathrm{T}^{-2}]$

M: viscosity ratio, dimensionless
M_e: ratio of kinematic viscosities, dimensionless
n: normal vector, [L]
P: pressure, [$ML^{-1}T^{-2}$]
q: injection velocity, [LT^{-1}]
r: pore size, [L]
S: saturation, dimensionless
t: conductivity exponent, dimensionless
T: temperature, [K]
u: flow velocity, [LT^{-1}]
v: interface velocity, [LT^{-1}]

α: modified conductance exponent, dimensionless
β: percolation exponent, dimensionless
γ: interfacial tension, [MT^{-2}]
ζ: conductance exponent, dimensionless
λ: thermal conductivity, [$MLT^{-3}K^{-1}$]
μ: viscosity, [$ML^{-1}T^{-1}$]
ν: correlation length exponent, dimensionless
ρ: density, [ML^{-3}]
σ: front width, dimensionless
Σ: standard deviation of the pore size distribution, dimensionless
χ: distance, dimensionless

Subscripts

d: defending
F: front
i: invading
I: pertaining to interface I
m: mean
nw: non-wetting
r: relative
s: steam
w: wetting
ϵ: limiting

REFERENCES

1. A.A. Heiba, M. Sahimi, L.E. Scriven and H.T. Davis, SPE 11015 (1982).

2. T. Kneafsey and K. Pruess, *Water Res. Res.*, in press (1999).

3. X. Kong, M. Haghighi and Y.C. Yortsos, *Fuel* **71**, 1465 (1992).

4. R. Lenormand, E. Touboul and C. Zarcone, *J. Fluid Mech.* **189**, 165 (1988).

5. R. Lenormand, *Proc. Roy. Soc. Lond.* **A423**, 159 (1989).

6. C.A. Miller, *AICHEJ* **21**, 474 (1975).

7. M. Parlar and Y.C. Yortsos, SPE 16969 (1987).

8. M. Prats, *Thermal Recovery*, SPE Monograph, Dallas, TX (1982).

9. P.S. Ramesh and K.E. Torrance, *J. Fluid Mech.* **257** (1993).

10. J.M. Sanchez and R.S. Schechter, SPE 16967 (1987).

11. C. Satik and Y.C. Yortsos, SPE 30751 (1995).

12. C. Satik and Y.C. Yortsos, *J. Heat Transf.* **118**, 455 (1996).

13. G. Schubert and J. Straus, *J. Geophys. Res.* **84**, 1621 (1979).

14. D. Stauffer and A. Aharony, *Introduction to Percolation Theory*, Francis-Taylor (1992).

15. D. Wilkinson, *Phys. Rev. A* **30**, 520 (1984).

16. B. Xu, Y.C. Yortsos and D. Salin, *Phys. Rev. E* **57**, 739 (1998).

17. Y.C. Yortsos, B. Xu and D. Salin, *Phys. Rev. Lett.* **79**, 4581 (1997).

18. Y.C. Yortsos, B. Xu and D. Salin, SPE 49318 (1998).

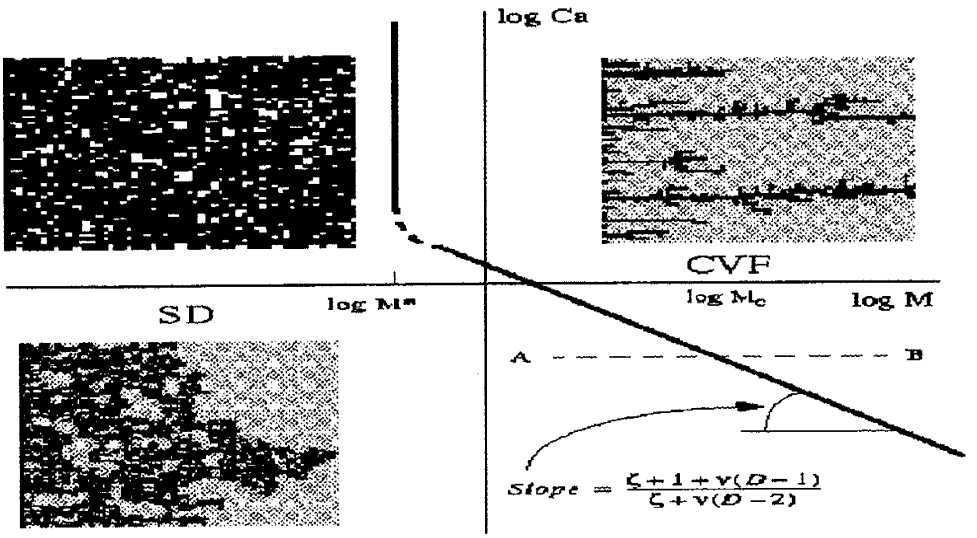

Figure 1: Phase diagram of fully-developed isothermal drainage (from Yortsos et al., 1997).

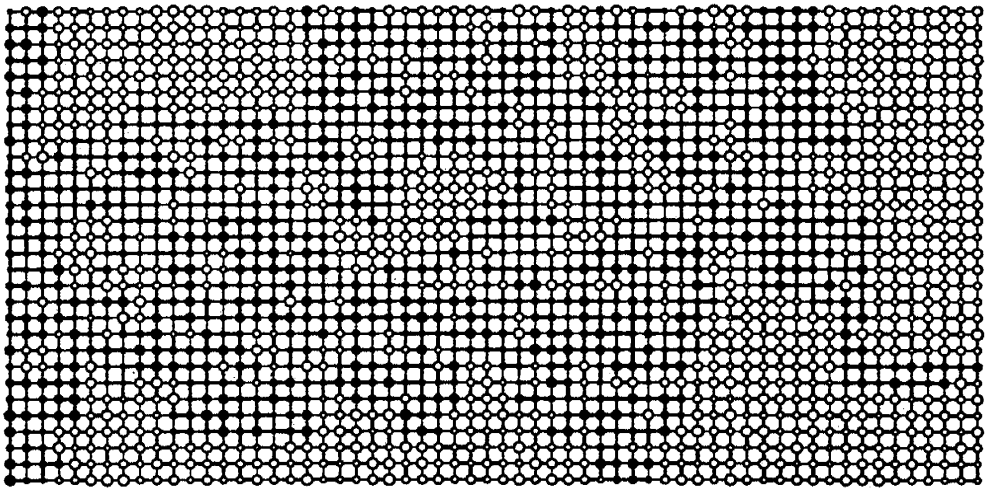

Figure 2: Invasion percolation pattern.

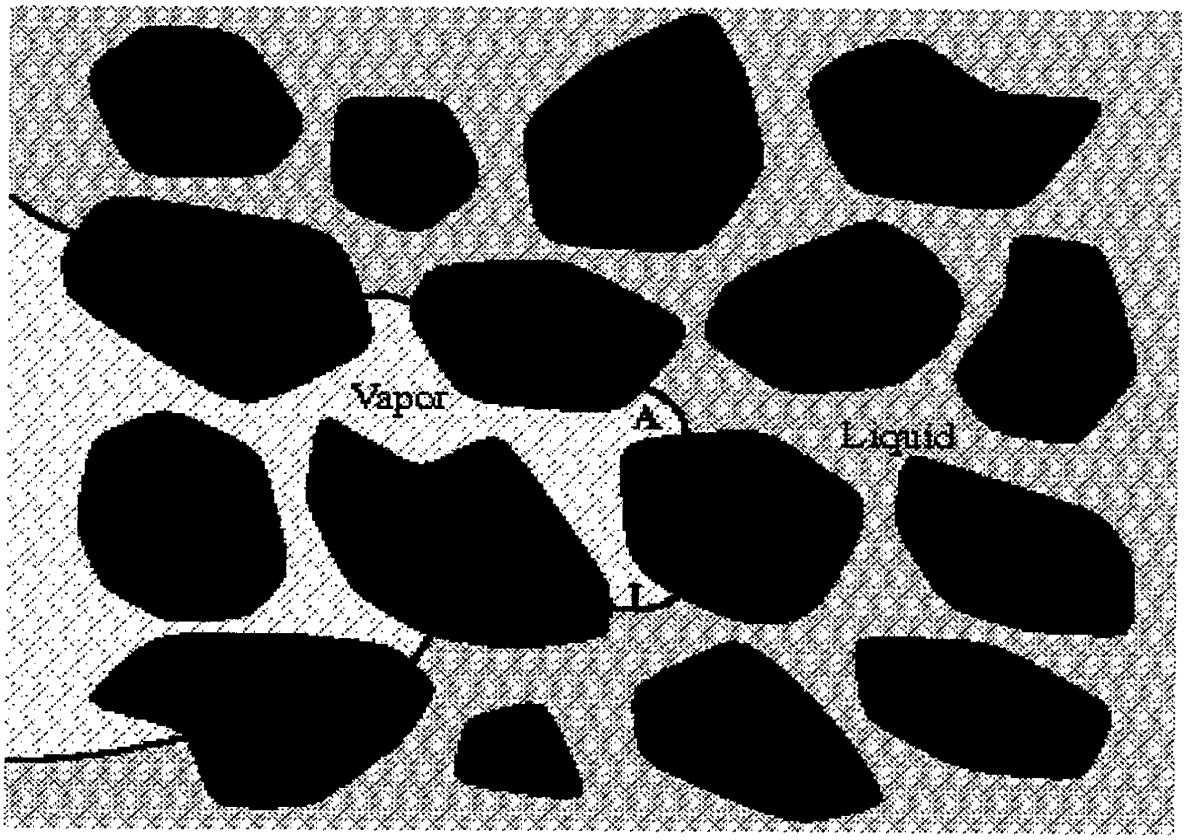

Figure 3: Schematic of a vapor-liquid interface in a porous medium.

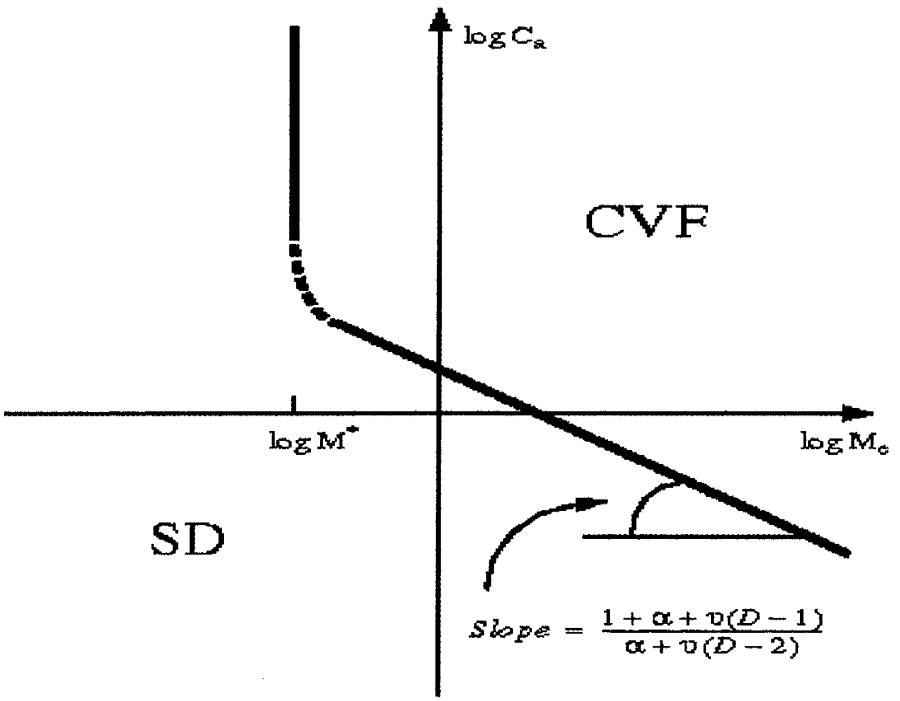

Figure 4: Phase diagram of fully developed steam injection. SD denotes stabilized displacement, CVF denotes displacement controlled by viscous forces and heat transfer. The possibility of an inertia-controlled regime at high values of the injection rate (high capillary numbers) cannot be excluded.

2. A NUMERICAL STUDY OF THE CRITICAL GAS SATURATION IN A POROUS MEDIUM

C. Du and Y.C. Yortsos

ABSTRACT

We use pore-network simulations to study the dependence of the critical gas saturation in solution-gas drive processes on the geometric parameters of the porous medium. We show that for a variety of growth regimes (including global and local percolation, instantaneous and sequential nucleation, and mass-transfer driven processes), the critical gas saturation, S_{gc}, follows a power-law scaling with the final nucleation fraction (fraction of sites activated), f_q. For 3-D processes, this relation reads $S_{gc} \sim f_q^{0.16}$, indicating a sensitive dependence of S_{gc} to f_q at very small values of f_q.

INTRODUCTION

The critical gas saturation, S_{gc}, in a solution gas-drive process in a porous medium denotes the gas saturation at which the onset of bulk gas flow occurs. In the typical application, gas is liberated from the liquid solution containing light components by pressure decline (Hunt et al, 1956, Handy, 1958). Other processes, for example boiling, involve the application of a heat flux. Knowledge of the magnitude of S_{gc} and of the factors that control it, is important to various oil recovery processes. Below the critical gas saturation, mostly liquid flows, the gas being constrained by capillarity in relatively small clusters of pores ("bubbles"). As the critical saturation is reached, however, a gas sample-spanning cluster forms and bulk flow of gas commences. Subsequent to this, gas is preferentially produced, due to its low mobility, with detrimental effects on liquid production rates.

Understanding the factors that determine S_{gc} has been sought in many past studies (e.g. see Dumore, 1970, Danesh et al., 1987). A recent summary can be found in Li and Yortsos (1995a). Early studies (e.g. Kennedy and Olson, 1952, Wieland and Kennedy, 1957) focused on the application of homogeneous nucleation theory to predict rates of generation of gas bubbles. More recently, the emphasis shifted on understanding the process by combining nucleation and the subsequent bubble growth in the porespace. In particular, the specific form of the nucleation mechanism, whether homogeneous or heterogeneous, has been sidestepped as an issue (Yousfi et al., 1991), and the prevailing view is that the most critical factor is what controls the appearance of a macroscopic bubble, which will eventually occupy a pore body. In other related applications, this factor has been recognized by various authors to be the capillary roughness of the pore walls (Crum, 1982, Atchley and Prosperetti, 1989).

Yortsos and Parlar (1989) represented capillary roughness in terms of a hydrophobic cavity, the size of which was distributed (and assumed, ad hoc, to be correlated to the pore size). Yousfi et al. (1991) pointed out the importance of the capillary roughness, although they did not proceed with a specific model. In this paper, we follow the same line of reasoning and define nucleation as the process that leads to the appearance of a macroscopic bubble, and more precisely as that at which the capillary resistance of the cavity in the pore wall is exceeded for the adjacent pore body to be occupied by a gas bubble. As an illustration,

consider a cavity (or other geometric expression of pore wall roughness) at the pore wall that contains a stable gas bubble (either pre-existing or nucleated by some nucleation mechanism) (Figure 1). The bubble will remain trapped by capillarity in the wall (hence "macroscopic" nucleation will not occur) as long as the following constraint between the local pressures applies

$$P_V - P_L \leq \frac{2\gamma}{r_w} \tag{1}$$

where r_w is the mean radius of curvature of the cavity mouth, γ is the gas-liquid interfacial tension, P_V is the pressure in the gas bubble and P_L is the liquid pressure at the interface. The gas pressure is related to the molecular composition of the liquid solution. By assuming simple thermodynamic equilibria, such as Henry's law, we may further write

$$P_V = KC \tag{2}$$

where K is an equilibrium constant and C is the concentration of the light component ("gas") in the liquid. It is then apparent that a reduction in the liquid pressure, or an increase in the gas concentration (supersaturation) could lead to the growth (and possible detachment from the wall) of the gas bubble and the filling of its adjacent pore body (Figure 1). In this context, therefore, the site will be activated (nucleation will occur) when the capillary threshold of the cavity, $\frac{2\gamma}{r_w}$, is exceeded for the first time.

The growth of the gas phase at the pore and pore-network scales, following nucleation, was studied in detail by Li and Yortsos (1995a, 1995b) and Satik and Yortsos (1996) in the two contexts of solution gas-drive and boiling, respectively (see also Satik et al., 1995, for a related study). Effective continuum models, which ignore, however, the pore structure, have also been used (e.g. Mulu and Longeron, 1989, Kashchiev and Firoozabadi, 1993, Firoozabadi and Kashchiev, 1996). Li and Yortsos (1995b) combined pore-network visualization experiments and pore-network simulation to develop insight on the growth of multiple bubbles evolving from a variety of nucleation centers. These authors identified the following growth regimes:

1. A global percolation regime, in which gas-liquid interfaces in *any* gas-occupied pore advance one-at-a-time by invading perimeter pore throats in order of increasing capillary resistance (or, equivalently, of decreasing radius). This regime, first proposed by Yortsos and Parlar (1989) in their study using a Bethe lattice representation of the porous medium, is based on the assumption that growth is sufficiently slow so that concentration profiles are quasi-static. Li and Yortsos (1995a) derived a condition for the validity of this regime and showed that it applies at low pressure decline rates and low permeability media. Experiments by Kamath and Boyer (1993) showed the relevance of this regime in solution gas-drive in tight porous media, in qualitative agreement with Li and Yortsos (1995a).

2. A local percolation regime, in which gas-liquid interfaces belonging to the *same* cluster advance one-at-a-time, following the above-mentioned order of increasing capillary resistance. Because of competition for solute mass and possible mass transfer effects (diffusion, screening, etc.), in this case, however, interfaces in other clusters may not grow, even though they may neighbor perimeter throats with smaller capillary resistance. Mass transfer was simulated by various methods, including a rule-based DLA (Diffusion-Limited-Aggregation) approach, as well as using full numerical simulation at the pore-network scale.

The findings of Li and Yortsos (1995a) showed that S_{gc} depends mainly on the nucleation fraction (namely the fraction of sites nucleated up to the time the critical gas saturation was reached) and to a lesser extent on the manner of nucleation. We must emphasize, again, that in this paper nucleation refers to the process leading to the appearance of a macroscopic, pore-filling bubble. When nucleation is "instantaneous", which occurs when all nucleation sites are activated at once, the critical gas saturation was found to be independent of the pressure decline rate. This is not the case for "sequential" nucleation, however, where sites are activated progressively, and where the critical saturation was shown to increase with the pressure decline rate (see also Du and Yortsos, 1997). Instantaneous nucleation was proposed by Firoozabadi and Kashchiev (1996) as a predominant mechanism in porous media. The results of Li and Yortsos (1995a) suggest that depending on the particular conditions, S_{gc} can be considerably high, in general agreement with measured critical gas saturations in real cores (Kortekaas and Poelgeest, 1989). On the other hand, infinitesimally small values have also been reported (Firoobazadi et al., 1989).

In this paper we explore the dependence of the critical gas saturation on the nucleation fraction and the geometrical parameters that control it, by carrying out Monte Carlo simulations in pore networks. We consider global and local percolation regimes, as defined above, so that the movement of interfaces is only constrained by capillarity. Instantaneous and gradual nucleation mechanisms are both studied. The general objective of the study is to obtain a relation between S_{gc} and the nucleation fraction, and to also probe its dependence on the geometric characteristics of the porous medium. For this purpose, we introduce a cavity size distribution, $\alpha_c(r)$, the relation of which to the pore-throat size distribution, $\alpha_b(r)$, dictates the nucleation and occupancy sequence. Specific objectives are to test numerically two theoretical hypotheses: one proposed by Yortsos and Parlar (1989), which states that the onset of critical gas saturation coincides with the percolation threshold of percolation processes originating from multiple nucleation centers, and another by Li and Yortsos (1995a), who proposed a scaling relation of S_{gc} to size and nucleation fraction. We must point out that in this paper, the effect of the pressure decline rate is not explicitly considered. The implicit assumption is that presure decline rates are sufficiently small for capillarity in pore throats to control the menisci movement locally. At large pressure decline rates, snap-off of gas bubbles, bubble division in pore throats and ganglia motion and coalescence will occur (see Bora et al., 1997, for a recent visualization). Such processes are not considered here.

SIMULATIONS

We proceed by assuming a pore-network representation of the porous medium, with distributed pore throats (bonds) and pore bodies (sites). In addition, we assume that nucleation sites, in the form of cavities or other shapes of pore-wall roughness, characterized by a mean radius of curvature, are distributed in the network, one each at every pore body (actually such cavities represent the largest nucleation cavity in a given pore). This distribution is random and in general unrelated to the pore throat or pore body size distributions. In our terminology, a nucleation site is activated when its capillary resistance, as given by equation (1) is first exceeded (Figure 1). The evolving gas bubble is assumed to occupy the host pore body, which thus forms the origin for the subsequent growth of a gas cluster. Multiple clusters can grow from multiple nucleation sites. A typical figure from Li and Yortsos

(1995a) illustrating the evolving cluster patterns is shown in Figure 2. In our simulations, 2-D square and 3-D cubic lattices of size L^E, where E (equal to 2 or 3) is the (Euclidean) dimension of the lattice, were used. Here L is the dimensionless size of the lattice, expressed as a number of pore lengths. In all processes, pore throat and cavity sizes were assigned randomly, namely no spatial correlations were considered. First, we simulated the growth of clusters assuming conditions of global percolation.

a. Global Percolation

In this regime, the growth of clusters follows the order of increasing capillary resistance of pore throats in the perimeter of all clusters. The process is similar to invasion percolation (IP) (see Feder, 1988), with the important difference that here growth occurs from multiple clusters (and not from a single cluster, as in standard IP), while nucleation sites may become activated sequentially in the process. Two cases were considered, an "instantaneous" nucleation, in which all sites to be activated were activated simultaneously at the onset of the process, and a "sequential" nucleation, in which sites were activated gradually during the process.

Instantaneous Nucleation

In this case, the size distribution of cavities is irrelevant (or equivalently, the distribution of sites contains a very narrow, delta function-like, region). Also, in the absence of pressure decline rate effects, the actual time of activation is not relevant. The process is parametrized by the nucleation fraction, f_q, defined as

$$f_q = \frac{N}{L^E} \tag{3}$$

where N denotes the number of sites activated. In the simulation, this was accomplished by randomly occupying with gas a fraction f_q of pore bodies. Subsequent to the onset of nucleation, the gas clusters grow following the above-mentioned percolation rules, in which the size of the throat neighboring a gas-liquid interface is the controlling parameter.

Sequential Nucleation

When the sites are not activated all at once, the specific size distributions of pore throats and cavities become important. The simulation proceeds by first activating the largest nucleation site in the lattice. During the process, either a gas cluster grows or another nucleation site is activated. This is determined by whether or not there exists among the perimeter throats of the cluster a pore throat with size larger than the (currently) available largest nucleation site. If there exists, growth occurs without activation of that site. Otherwise, the nucleation site is activated and the new gas cluster becomes part of the growth process. It is apparent that the particular form of the size distributions and the degree of overlap are key parameters to this process.

Typical simulations were carried out using Rayleigh or uniformly distributed sizes (Figure 3). The Rayleigh distributions for throats and cavities have the form

$$\alpha_i(r) = \frac{\pi r}{2r_i^2}\exp\left(-\frac{\pi r^2}{4r_i^2}\right) \quad ; \quad i = b, w \tag{4}$$

Here, the important parameter is the ratio β, of mean sizes

$$\beta \equiv \frac{r_w}{r_b} \tag{5}$$

We must note that in the simulations of sequential nucleation, the nucleation fraction f_q denotes the final value of the fraction of sites nucleated when the critical gas saturation is reached (namely, when a sample-spanning cluster forms). Contrary to the previous problem, however, this value is not fixed a priori, but varies for different processes. In the typical simulations reported here, the variation of f_q is accomplished by considering fixed size distributions (for example of the Rayleigh type) and by varying the ratio of mean sizes, β.

b. Local Percolation

Simulations were also performed by considering mass transfer effects and the competition between clusters. In this case, individual clusters grow by following local percolation rules (namely in each cluster the throat to be penetrated next is the largest), however, different clusters grow at the different rates dictated by the rate of mass transfer to them. Thus, the order by which pore throats in different clusters are invaded is not only affected by capillarity but also by the rates of mass transfer to individual clusters. At conditions of quasistatic diffusion, mass transfer can be simulated by a random walk (which is obtained using the well-known DLA algorithm, Feder, 1988). Then, the process of cluster growth would be a combination of percolation and DLA rules. The rate of growth of a given cluster is taken to be proportional to the number of walkers that reach that cluster, which is also another expression of the mass flow rate reaching the cluster. This rate will be affected from the competition from other clusters, which here is simulated by the frequency of collisions between the walker and the various clusters. However, each cluster grows locally by invading the throat with the smallest capillary resistance (largest radius), thus following local percolation rules. Two different random walk methods were used: one in which the walkers originate from the perimeter of the lattice, which essentially corresponds to a fixed supersaturation applied to the perimeter, and another in which the walkers originate from random points within the lattice (a modified DLA algorithm). The latter can be shown to mimic processes at constant rates of decline of the supersaturation, namely at constant pressure decline rates. The pattern of Figure 3 is obtained using such an algorithm. Because it is actually more relevant to a physical process, we will only report results using the modified DLA algorithm. Note though, that in all these problems, only instantaneous nucleation was considered, as sequential activation requires knowledge of both pressure and concentration fields, which these rule-based algorithms cannot supply. More details can be found in Li and Yortsos (1995a).

RESULTS AND DISCUSSION

As previously mentioned, the simulations at global percolation were analysed to check two hypotheses. The hypothesis of Yortsos and Parlar (1989) states that the onset of critical gas saturation corresponds to the standard condition of percolation, namely that at that point the percolation probability p is equal to the lattice percolation threshold, p_c. The definition of percolation probability is

$$p \equiv \int_{r_d}^{\infty} \alpha_b(r) dr \tag{6}$$

where r_d is the minimum size of gas-occupied throats at any stage of the process. The hypothesis states that at S_{gc}, we shall have

$$\int_{r_{d,c}}^{\infty} \alpha_b(r) dr = p_c \tag{7}$$

In 3-D cubic lattices, the accepted value of p_c for bond percolation is approximately 0.25 (Stauffer, 1985). Table 1 presents multiple realization results for the average value of p at the onset of the critical gas saturation in 3-D cubic lattices for the case of instantaneous nucleation and for different nucleation fractions. Also shown is the standard deviation obtained. The results show that as the nucleation fraction increases, the average value of p approaches the expected p_c value for 3-D bond percolation, with a standard deviation that diminishes as the nucleation fraction (and the lattice size) increase. As is typical of these spatially uncorrelated problems, the standard deviation approaches asymptotically zero at sufficiently large values of the lattice size. When only a few nucleation centers are involved, the percolation threshold is approached from above (as pertains to an IP process). However, in the case of multiple nucleation centers, the threshold is approached from below (as in the case of Ordinary Percolation (OP)). Similar conclusions were reached from 2-D simulations (Table 2, where the expected percolation threshold p_c is 0.5) as well as for the case of 3-D percolation with sequential nucleation (Table 3). The latter case was performed by varying the ratio β, as discussed above. The fact that the particular order of nucleation sequence does not affect the percolation threshold supports the validity of the hypothesis under rather general conditions. We conclude that the results in Tables 1-3 support this premise of Yortsos and Parlar (1989). This is of importance for the subsequent development of a relationship between S_{gc} and f_q.

The second hypothesis tested in the simulations involves the variation of the critical gas saturation with f_q, which was conjectured by Li and Yortsos (1995a) to have the following relationship

$$S_{gc}(L; f_q) = (\text{const}) L^{D-E} + (\text{const}) f_q^{1-\frac{D}{E}} \tag{8}$$

where D is the mass fractal dimension of the percolation cluster (equal to 1.89 for 2-D OP, to 1.82 for 2-D IP with trapping, and to 2.53 for 3-D OP or IP, with or without trapping), and the prefactors are numerical constants. The arguments leading to this equation are as follows: In the limit of very small f_q, for instance with one nucleation site only, the critical gas saturation corresponds to the volume fraction of the percolation cluster only, hence it must satisfy the same scaling as the latter, namely

$$S_{gc}(L;0) \sim L^{D-E} \tag{9}$$

(for example, see Feder, 1988). Incidentally, we may point out that (9) also provides the scaling with sample size of the "critical gas saturation" in external drives. Note that in this limit, the value approaches zero as the lattice size increases (although the rate of approach is algebraic and rather slow, e.g. $S_{gc} \sim L^{-0.11}$ in 2-D). However, when the nucleation fraction increases, the main contribution to S_{gc} arises from finite clusters growing around the nucleation sites and not from the percolation cluster. On the average, these clusters have a linear size proportional to the average spacing between nucleation centers, l_q, where $l_q \sim f_q^{-\frac{1}{E}}$, as can be readily shown. Each of them contributes a total of l_q^D pores occupied by gas, thus the overall contribution to S_{gc} would be

$$S_{gc}(\infty; f_q) \sim f_q^{1-\frac{D}{E}} \tag{10}$$

Note that in this limit, there is a very sensitive dependence of S_{gc} on f_q at small f_q, in view of the small exponents in 2-D and 3-D. (For example, equation (10) reads $S_{gc} \sim f_q^{0.05}$ and $S_{gc} \sim f_q^{0.16}$, in 2-D and 3-D, respectively). The implication is that most of the variation of S_{gc} will occur in a range of very small values of f_q. Li and Yortsos (1995a) proposed equation (8) as a linear superposition of the two expressions (9) and (10).

Results from the simulations with instantaneous nucleation are shown in Figure 4. We used 100, 50 and 10 different realizations for the three different sizes 20×20×20, 30×30×30 and 40×40×40, respectively. The largest nucleation fraction used is approximately 0.24, corresponding to a quite large value of S_{gc}. To test the theoretical prediction (8) the results were plotted vs. the variable $f_q^{1-\frac{D}{E}}$. We observe that the resulting curves have two qualitatively different regimes: An almost flat regime, at low f_q, where the critical gas saturation is insensitive to $f_q^{1-\frac{D}{E}}$ and only depends (weakly) on the lattice size. And another regime at larger f_q, where a straight line behavior is well obeyed. For a given nucleation fraction, S_{gc} is shown to slightly increase as the size increases. Figure 5 shows the standard deviation of S_{gc}. Its relatively small value and its decreasing trend as the lattice size increases, indicate the deterministic nature of the results obtained.

Results from simulations with sequential nucleation are shown in Figure 6. Rayleigh distributions were used for throats and cavities. Even though nucleation occurs sequentially, the overall behavior is very similar, if not identical, to that for instantaneous nucleation. Flat and straight line regimes are clearly distinguished and a cross-over region can be identified with properties similar to the previous. Figure 7 shows simulation results for sequential nucleation but with a uniform distribution of throats and cavity sizes in a 20×20×20 lattice. Also in this case, the results are very similar to the previous (Figures 4, 6).

The behavior shown in Figures 4-7 supports the validity of the two limits (9) and (10), but not of the composite curve (8) proposed by Li and Yortsos (1995a). Instead, it appears that S_{gc} can be modeled by a cross-over function, $g_E(x)$, where

$$S_{gc} \sim L^{D-E} g_E(f_q L^E) \tag{11}$$

and the function g_E depends on the dimensionality and has the scaling behavior

$$g_E(x) \sim \text{const} \quad \text{as} \quad x \ll 1 \quad ; \quad g_E(x) \sim x^{1-\frac{D}{E}} \quad \text{as} \quad x \gg 1 \tag{12}$$

We tested this relation by plotting the numerical results obtained in a $S_{gc}L^{E-D}$ vs. f_qL^E plot (Figures 8a and 8b for 2-D and 3-D, respectively). A variety of results for instantaneous or sequential nucleations and for different lattice sizes are plotted. It is shown that conjecture (12) for the scaling function $g_E(x)$ is well satisfied. The data from the various simulations collapse into a single scaling curve with the properties indicated in (12). In particular the asymptotic approach to a straight line with the predicted slope is apparent (particularly in 2-D, where much larger sizes can be used in the computations).

Equation (11) suggests that there is a cross-over nucleation fraction, f_q^*, scaling as

$$f_q^* \sim L^{-E} \tag{13}$$

which delineates the two regimes. From the definition of the nucleation fraction, this further implies that cross-over occurs after a *finite* number of nucleation centers have been activated. Figure 4 shows that this occurs approximately at a number of about 12 centers, for the particular simulations, with the flat regime reached when only one or two nucleation centers are activated. Equation (13) shows that in the limit of very large lattice sizes, the cross-over point f_q^* vanishes, hence in this limit, the critical gas saturation would approach the relation

$$S_{gc}(\infty; f_q) = f_q^{1-\frac{D}{E}} \tag{14}$$

which is the same as equation (10) but with the prefactor equal to 1. Figures 4-7 and the limiting equation (14) suggest that the dependence of S_{gc} on the nucleation fraction f_q is independent (except for some finite-size effects) of the nucleation sequence or the size distributions, and only depends on the final fraction of sites activated (nucleated) when the critical gas saturation is reached. Equation (14) is the main result of this paper.

The independence of the limiting results to the particular size distributions used can be proved readily by considering the case of instantaneous nucleation. The keys to the proof utilize the concept of percolation probability p defined in (7). In their study using Bethe lattices, Yortsos and Parlar (1989) showed that the saturation curves originating from different activation centers depend only on p and the initial fraction of activated centers. In our terminology, their results read as

$$S_g = X(p; f_q) \tag{15}$$

where X is an accessibility function that depends on the lattice and the dimensionality, but not on the throat size distribution. This result was also verified for regular lattices by Du (1996) using numerical simulations. Since the onset of critical gas saturation corresponds to the particular limit $p = p_c$, it follows that for a fixed lattice geometry, $S_{gc} = X(p_c; f_q)$ only depends on f_q and it is independent of the size distribution used. Here, it was assumed that all sites are of equal volumes and that there exists no site-bond correlation. Violation of this assumption would certainly affect the universality claimed.

A similar argument can be used to show the independence of (14) from the particular nucleation sequence. At the onset of S_{gc}, the smallest throat radius penetrated is $r_{d,c}$, given

by equation (7). Consider, now, two different nucleation sequences, with the same overall fraction f_q activated at S_{gc}. We have

$$f_q = \int_{r_{d,c}}^{\infty} \alpha_c(r) dr \tag{16}$$

which derives from the fact that all cavity sizes larger than $r_{d,c}$ must be activated before S_{gc} is reached. As long as these are randomly distributed, their contribution to S_{gc} will on average be the same, since each cluster emanating from any such nucleation center will consist of penetrated throats of radius larger than $r_{d,c}$. The sequence of nucleation may affect the degree of overlap of various clusters. However, the overall result will on average be independent of it.

Equation (14) represents an important result. Its utility in a practical application, however, requires knowledge of the cavity and throat size distributions. Indeed, equation (7) indirectly defines $r_{d,c}$, which upon substitution in (16) determines f_q, which is used in turn to evaluate S_{gc} in (14). It is not difficult to see that different distributions would yield different f_q, thus different S_{gc}. Yortsos and Parlar (1989) took the *ad hoc* model that the size of each cavity is proportional to its host pore throat, from which they obtained the variation of S_{gc} in terms of the parameter β for a Bethe lattice. In this paper, we will use the previous Rayleigh distributions to relate the critical gas saturation to β as follows. Solving for $r_{d,c}$ in (7) we find

$$r_{d,c} = r_b \left(-\frac{4 \ln p_c}{\pi} \right)^{\frac{1}{2}} \tag{17}$$

from which the nucleation fraction at S_{gc} is obtained

$$f_q = p_c^{\beta - 2} \tag{18}$$

thus,

$$S_{gc} = p_c^{(1-\frac{D}{E})\beta^{-2}} \quad (= 0.25^{0.16\beta^{-2}} \quad \text{for } 3-\text{D cubic lattices}) \tag{19}$$

Of course, different expressions than (19) will be otained if we use different size distributions (for example, uniform, etc.). Equation (19) shows that S_{gc} increases as the coordination number of the lattice, Z, decreases which should be expected given the importance of the lattice connectivity (and where we note that for 3-D, $p_c \approx \frac{1.5}{Z}$), and as the ratio β between the characteristic cavity and pore sizes increases (which leads to an increasing f_q). Equation (refnew) is plotted in Figure 9 which shows the variation of S_{gc} vs. β for a 3-D cubic lattice. It is noted that the critical gas saturation depends sensitively on β at small values of the latter.

The above results were obtained assuming a global percolation regime. When this assumption is not valid, the competition for solute and mass transfer in the system will affect the rates of growth of individual clusters. We simulated such processes using two rule-based DLA algorithms, which mimic quasi-static diffusion (Li and Yortsos, 1995a). The difference between the two algorithms is that the first (percolation-DLA) corresponds to a problem of fixed far-field supersaturation, while the second (percolation-modified DLA) corresponds to

a problem of constant pressure decline rate in the far-field. Details of the resulting patterns are discussed in Li and Yortsos (1995a). Only the instantaneous nucleation problem was simulated.

Results from different realizations in a $30\times30\times30$ lattice are shown in Figure 10 for the percolation-modified DLA case (see also Figure 3 for a typical pattern evolution in this case). The results on the mean value can be fitted using the same equations as for the global percolation case and indicate good agreement with equation (11). The percolation-modified DLA regime shows an excellent fit, which leads us to believe that the behavior at large lattice sizes would become identical to (14). The results for the percolation-DLA regime also indicate a straight line in the region of low f_q. However, this line does not pass from the point (1,1) and it is unclear whether the behavior at large L for the percolation-DLA regime would collapse to equation (14). Given that this regime actually represents the rather unrealistic case of a constant supersaturation, we will not discuss it further.

The fact that incorporation of cluster competition and mass transfer does not significantly affect the S_{gc}-f_q relationship is, at first glance, surprising. A possible explanation, at least for the modified-DLA case, which corresponds to the constant pressure decline rate, is the following: At very small nucleation fractions, the growth is not affected by mass transfer (for example, consider the trivial limit of only one nucleation center). At larger fractions, the spacing between growing clusters is small, the availability of solute is about the same to all clusters, and on average the process behaves as in the global percolation case. It is unclear whether or not the same behavior will be also shown when sequential nucleation is allowed. For example, in a constant pressure decline rate process, we expect that as the pressure decline rate increases, there is a higher probability for the activation of new nucleation sites during the evolution of the process, hence we expect a larger nucleation fraction at S_{gc} (and possibly a larger S_{gc}) as the pressure decline rate increases. For the problem to show the same behavior as above, namely for S_{gc} to be independent of the particular nucleation sequence, requires that when a new nucleation center is activated, there is sufficient mass flux to support the growth of the cluster from that center, which will ensue due to the likely strong local supersaturation. At least at early stages of such growth, this condition will be enforced, as capillary thresholds of pore throats are more likely to be exceeded (hence the cluster to grow) when the local concentration C is smaller (compare with equations (1)-(2)), which is also a condition for larger diffusive fluxes to the cluster. It is likely, therefore, that the sequential nucleation case will result in a similar dependence as (14). Here, however, the nucleation fraction f_q would also depend in a non-trivial manner on the pressure decline rate, and not only on the geometrical characteristics of the pore and cavity sizes. This important effect is considered in a separate study (Du and Yortsos, 1997).

The above results are valid for spatially uncorrelated pore throats. Spatial correlations will affect the development of the gas phase clusters, much like in a drainage process, although the two additional aspects of growth from multiple sites and mass transfer of the present problem will also be influenced. Spatial correlations can act in a two-fold manner: To modify the percolation threshold, typically towards lower values, as the extent of the correlation increases, and to make the process stochastic, if for example the spatial correlation is of the self-affine type (e.g. fBm fields, see Du et al., 1996). Since it is directly related to the percolation threshold (compare with equations (7) and (16)), the critical gas saturation will also be affected by the degree of correlation. In particular, it will become realization-

dependent for the case of large correlation lengths. A similar effect would be exerted if the local microstructure is anisotropic, which is the case in many natural rocks. In such cases, the present results must be interpreted with care.

A wide range of experimental values for S_{gc} has been reported (from less than 1% to as high as 30%). This range is well within the present theory, given the appropriate parameter values (see for example Figure 9). Unfortunately, it is difficult to have a priori knoweldge of the precise nucleation characteristics of the porous medium (for example, of the nucleation cavity size distribution), thus a direct comparison of the theory with experiments is not possible at present. The theory does predict, however, that even rather small values in the nucleation fraction can give non-negligible critical gas saturations. It also calls attention to the fact that finite-size effects associated with the sample, where measurements are made, can be important and need to be removed, e.g. by using a scaling relation of the type shown in (11).

CONCLUSIONS

In this paper, we reported on a study of the sensitivity of the critical gas saturation on the nucleation characteristics of the porous medium in a solution gas-drive process. It was found that the onset of the critical gas saturation coincides with the condition that the percolation probability p equals the percolation threshold of the lattice, p_c, which confirms the original hypothesis of Yortsos and Parlar (1989). The dependence of the critical gas saturation on the final nucleation fraction (namely the fraction of activated sites) was studied and was found to obey for a sufficiently large system the power-law scaling $S_{gc} = f_q^{1-\frac{D}{E}}$, where D is the fractal dimension of the percolation cluster. This dependence was established regardless of the particular nucleation sequence (instantaneous or sequential) or the particular regime of bubble growth (global or local percolation, with or without dominant mas transfer characteristics). It was assumed, however, that the growth pattern of each cluster is controlled locally by capillarity, hence percolation theory results apply. This assumption is expected to lose validity at large pressure decline rates (for instance for the very sharp decline rates of Bora et al., 1997). The result found indicates that the critical gas saturation is very sensitive to small values of the nucleation fraction, but is less sensitive to the latter at larger values. The dependence on the nucleation fraction makes the critical gas saturation in internal drives qualitatively different from its value in external drives, where the formation of gas connectivity is associated with invasion percolation and depends only on the sample size, e.g. as described in (9).

NOMENCLATURE

C = Concentration of solute (dissolved gas)
D = Fractal dimension
E = Euclidean dimension
f_q = Nucleation fraction
K = Solubility constant

l	=	Length
L	=	Pore network linear size
N	=	Number of activated sites
p	=	Percolation probability
P	=	Pressure
r	=	Pore or cavity size
S_{gc}	=	Critical gas saturation
α	=	Probability density function
β	=	Ratio of characteristic cavity and throat sizes
γ	=	Interfacial tension

Subscripts

b	=	Pore throat
c	=	Critical
L	=	Liquid
V	=	Vapor
w	=	Cavity

REFERENCES

1. Atchley, A. A. and Prosperetti, A.: "The Crevice Model of Bubble Nucleation", *J. Acoust. Soc. Am.* **86**, 1065-1084 (1989).

2. Bora, R., Maini, B.B. and Chakma, A.: "Flow Visualization Studies of Solution Gas-Drive Process in Heavy-Oil Reservoirs Using a Glass Micromodel", SPE 37519 presented at the 1997 SPE International Thermal Operations and Heavy Oil Symposium, Bakersfield, CA (Feb. 10-12, 1997).

3. Crum, L.A.: "Nucleation and Stabilization of Microbubbles in Liquids", *Appl. Sci. Res.* **38**, 101-115 (1982).

4. Danesh, A., Peden, J.M., Krinis, D. and Henderson, G.D.: "Pore Level Visual Investigation of Oil Recovery by Solution Gas Drive and Gas Injection", SPE 16956, presented at the 1987 SPE Fall Meeting, Dallas, TX (Sep. 27-30, 1987).

5. Dumoré, J.M.: "Development of Gas Saturation During Solution Gas Drive in an Oil Layer below a Gas Cap", *SPEJ*, 211-218 (1970).

6. Du, C., *Ph.D. Thesis*, University of Southern California (1996).

7. Du, C., Satik, C., and Yortsos, Y.C.: "Percolation in a Fractional Brownian Motion Lattice", *AIChEJ*, **42**, 2392-2395 (1996).

8. Du, C., and Yortsos, Y.C., in preparation (1997).

9. Feder, J., *Fractals*, Chapter 7, Plenum Press, New York (1988).

10. Firoobazadi, A., and Kaschiev, D.: "Pressure and Volume Evolution During Gas Phase Formation in Solution Gas Drive Process", *SPEJ* **1**, 219-228 (1996).

11. Firoozabadi, A., Ottesen, B. and Mikklesen, M.: "Measurement and Modeling of Supersaturation and Critical Gas Saturation: Part 1, Measurements", SPE 19694 presented at the 1989 SPE Fall Meeting, San Antonio, TX (Oct. 8-11, 1989).

12. Handy, L.L.: "A Laboratory Study of Oil Recovery by Solution Gas Drive", *AIME Trans.* **213**, 310-315 (1958).

13. Hunt, E.B. Jr., and Berry, V.J. Jr.: "Evolution of Gas from Liquids Flowing through Porous Media", *AIChE J* **2**, 560-567 (1956).

14. Kamath, J. and Boyer, R. E.: "Critical Gas Saturation and Supersaturation in Low Permeability Rocks", SPE 26663 presented at the 193 SPE Fall Meeting, Houston, TX (Oct 3-6, 1993).

15. Kashchiev, D. and Firoozabadi, A.: "Kinetics of the Initial Stage of Isothermal Gas Phase Formation", *J. Chem. Phys.* **98**, 1 (1993).

16. Kennedy, H.T. and Olson, C.R.: "Bubble Formation in Supersaturated Hydrocarbon Mixtures", *AIME Trans.*, **195**, 271-278 (1952).

17. Kortekaas, T.F.M. and Poelgeest, F.V.: "Liberation of Solution Gas During Pressure Depletion of Virgin and Watered-Out Reservoirs", SPE 19693 presented at the 1989 SPE Fall Meeting, San Antonio, TX (Oct. 8-11, 1989).

18. Li, X. and Yortsos, Y.C., "Theory of Multiple Bubble Growth in Porous Media by Solute Diffusion", *Chem. Eng. Sci.* **50**, 1247-1271 (1995a).

19. Li, X. and Yortsos, Y.C.: "Visualization and Simulation of Bubble Growth in Pore Networks", *AIChEJ* **41**, 214-222 (1995b).

20. Moulu, J. C. and Longeron, D.: "Solution-Gas Drive: Experiments and Simulation", paper presented at the fifth European Symposium on Improved Oil Recovery, Budapest, Hungary (April 1989).

21. Satik, C. and Yortsos, Y.C., "A Pore-Network Study of Bubble Growth in Porous Media Driven by Heat Transfer", *J. Heat Transf.* **118**, 455-462 (1996).

22. Satik, C., Li, X. and Yortsos, Y. C., "Scaling of Single-Bubble Growth in a Porous Medium" *Phys. Rev. E* **51**, 3286-3295 (1995).

23. Stauffer, D., *Introduction to Percolation Theory*, Taylor and Francis, Inc. (1985).

24. Wieland, D.R. and Kennedy, H.T.: "Measurement of Bubble Frequency in cores", *AIME Trans.* **210**, 123-125 (1957).

25. Yortsos, Y. C. and Parlar, M.: "Phase Change in Binary Systems in Porous Media: Application to Solution Gas Drive", SPE 19697 presented at the 1989 SPE Fall Meeting, San Antonio, TX (Oct. 8-9, 1989).

26. Yousfi, El., Zarcone, C., Bories, S. and Lenormand, R.: "Mechanisms of Solution Gas Liberation during Pressure Depletion in Porous Media", *C. R. Acad. Sci. Paris*, t. **313**, Serie II, 1093-1098 (1991).

Size	Number of realizations	Nucleation fraction(number)	Mean p_c	Std of p_c
20x20x20	100	$1.250\times10^{-4}(1)$	0.3122	0.0705
		$2.500\times10^{-4}(2)$	0.2775	0.0323
		$1.250\times10^{-2}(100)$	0.2434	0.0109
		$1.875\times10^{-2}(150)$	0.2431	0.0113
		$2.500\times10^{-1}(2000)$	0.2431	0.0113
30x30x30	50	$3.704\times10^{-5}(1)$	0.2924	0.0406
		$7.407\times10^{-5}(2)$	0.2737	0.0264
		$3.704\times10^{-3}(100)$	0.2496	0.0058
		$5.556\times10^{-3}(150)$	0.2495	0.0058
		$1.852\times10^{-2}(500)$	0.2495	0.0058

Table 1: The mean value of the percolation probability at the onset of the critical gas saturation and its standard deviation for 3-D cubic lattices and instantaneous nucleation with various nucleation fractions. Two different lattice sizes and multiple realizations were performed.

Size	Number of realizations	Nucleation fraction(number)	Mean p_c	Std of p_c
100x100	100	$1.000\times10^{-4}(1)$	0.5151	0.0341
		$1.000\times10^{-3}(10)$	0.4953	0.0100
		$1.000\times10^{-2}(100)$	0.4950	0.0099
	20	$5.000\times10^{-2}(500)$	0.4973	0.0091
		1.000(10000)	0.4973	0.0091
200x200	50	$2.500\times10^{-5}(1)$	0.5087	0.0231
		$1.000\times10^{-3}(40)$	0.4967	0.0077
		$5.000\times10^{-3}(200)$	0.4967	0.0077
	20	0.500(20000)	0.4949	0.0071

Table 2: The mean value of the percolation probability at the onset of the critical gas saturation and its standard deviation for 2-D square lattices and instantaneous nucleation with various nucleation fractions. Two different lattice sizes and multiple realizations were performed.

Size	Number of realizations	Nucleation fraction(number)	Mean p_c	Std of p_c
20x20x20	100	$1.263\times10^{-4}(1.01)$	0.3104	0.0662
		$3.125\times10^{-4}(2.50)$	0.2669	0.0174
		$1.539\times10^{-2}(123.12)$	0.2432	0.0112
		$2.397\times10^{-2}(191.74)$	0.2431	0.0113
		$7.592\times10^{-2}(607.39)$	0.2431	0.0113
30x30x30	20	$4.259\times10^{-5}(1.15)$	0.2783	0.0279
		$1.870\times10^{-4}(5.05)$	0.2581	0.0072
		$3.737\times10^{-3}(100.90)$	0.2499	0.0047
		$7.640\times10^{-2}(2062.90)$	0.2499	0.0047
40x40x40	20	$1.875\times10^{-5}(1.20)$	0.2675	0.0190
		$7.422\times10^{-5}(4.75)$	0.2543	0.0076
		$2.003\times10^{-3}(128.20)$	0.2490	0.0042
		$1.571\times10^{-2}(1005.20)$	0.2490	0.0042

Table 3: The mean value of the percolation probability at the onset of the critical gas saturation and its standard deviation for 3-D cubic lattices and sequential nucleation with various nucleation fractions. Three different lattice sizes and multiple realizations were performed.

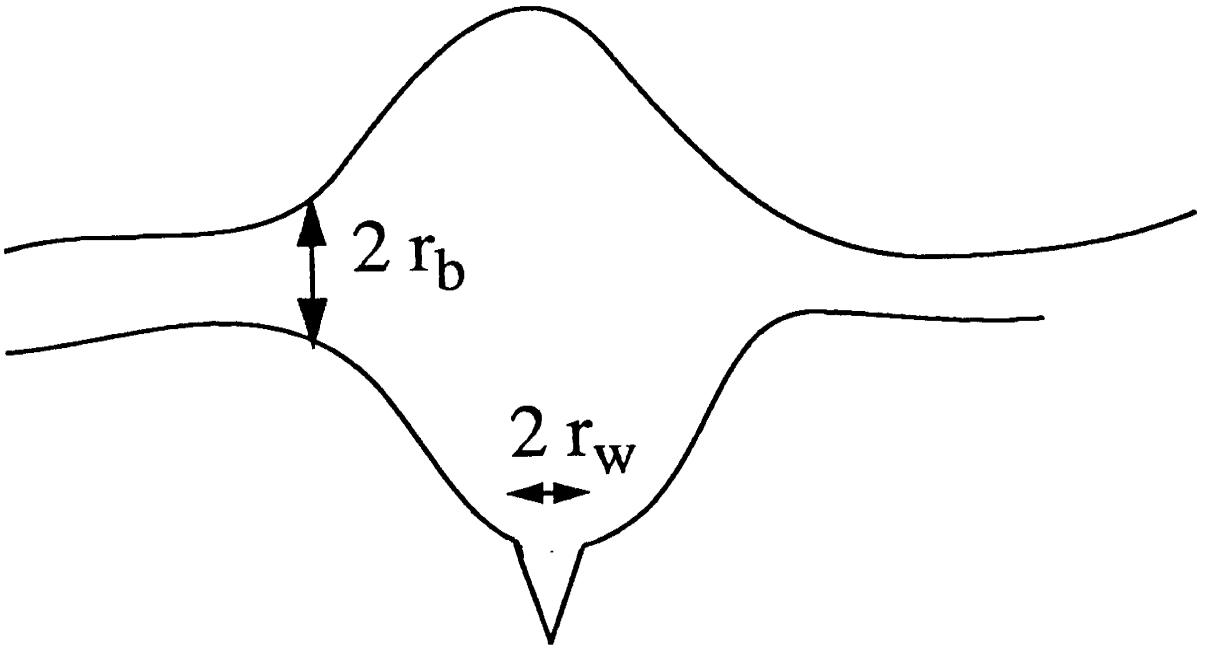

Figure 1: Schematic of a nucleation site in a host pore body.

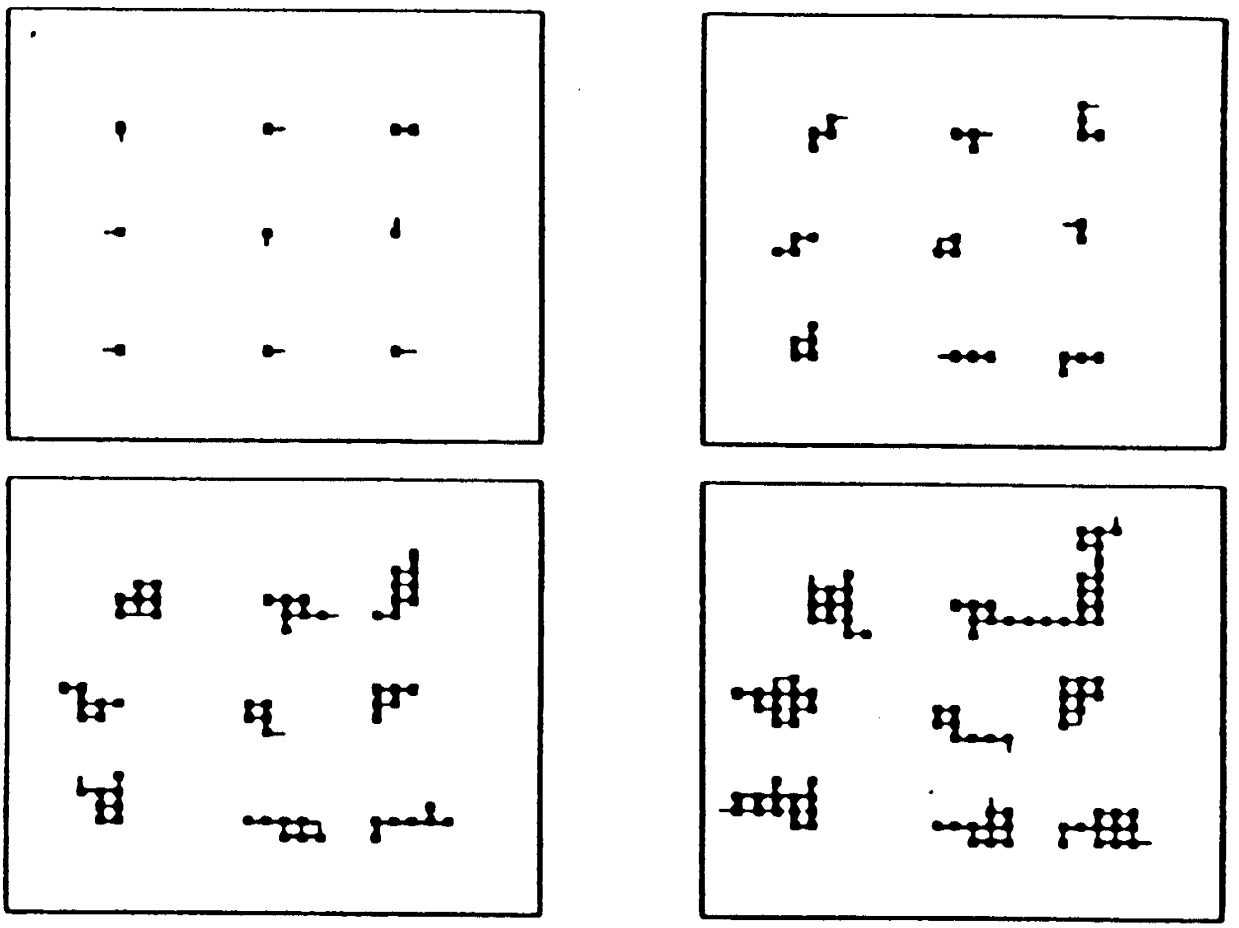

Figure 2: Evolution of bubble growth patterns as a function of time (from Li and Yortsos, 1995a). The pattern follows percolation-modified DLA rules.

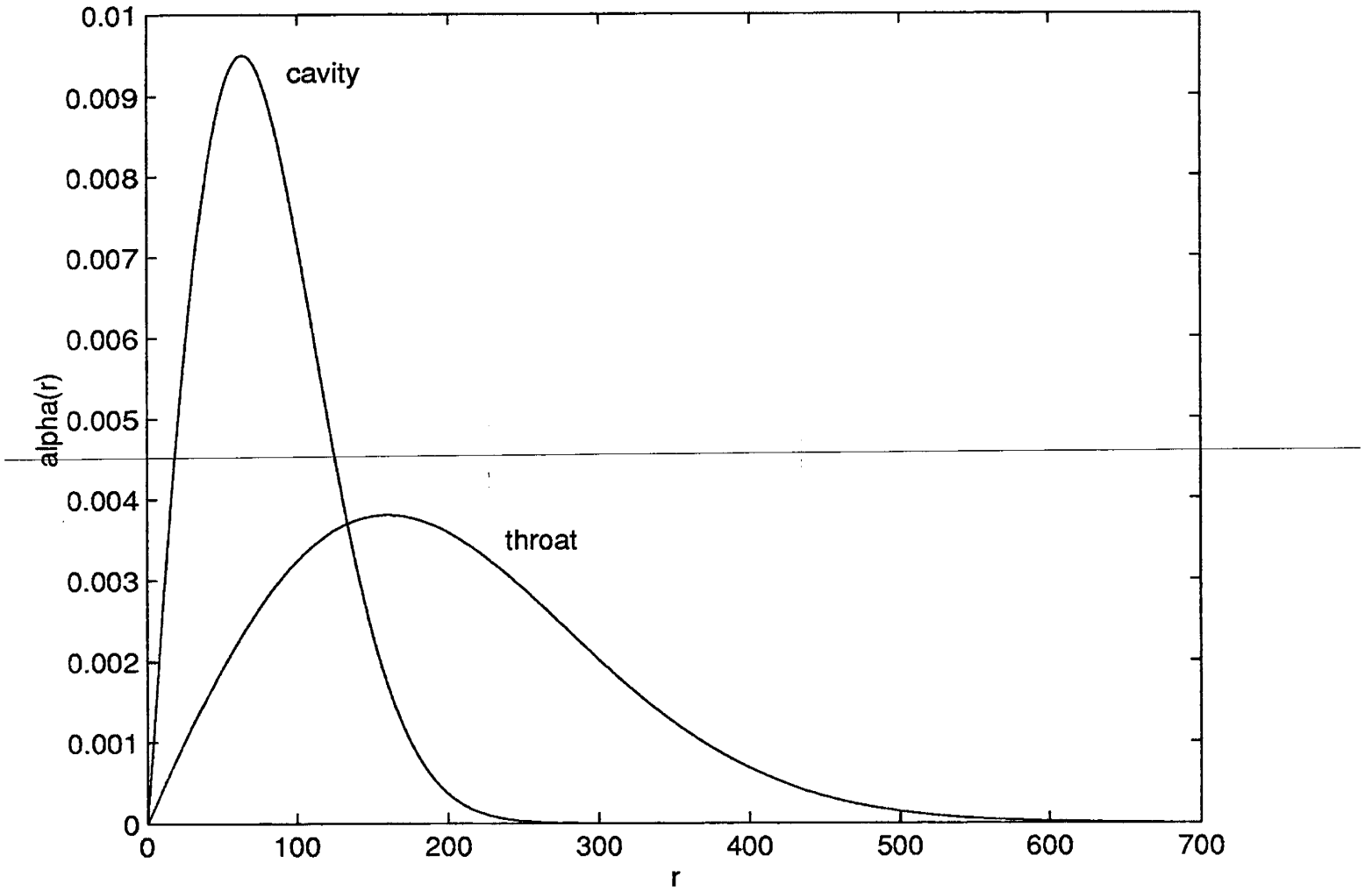

Figure 3: Characteristic Rayleigh cavity and pore throat size distributions. The sizes are dimensionless.

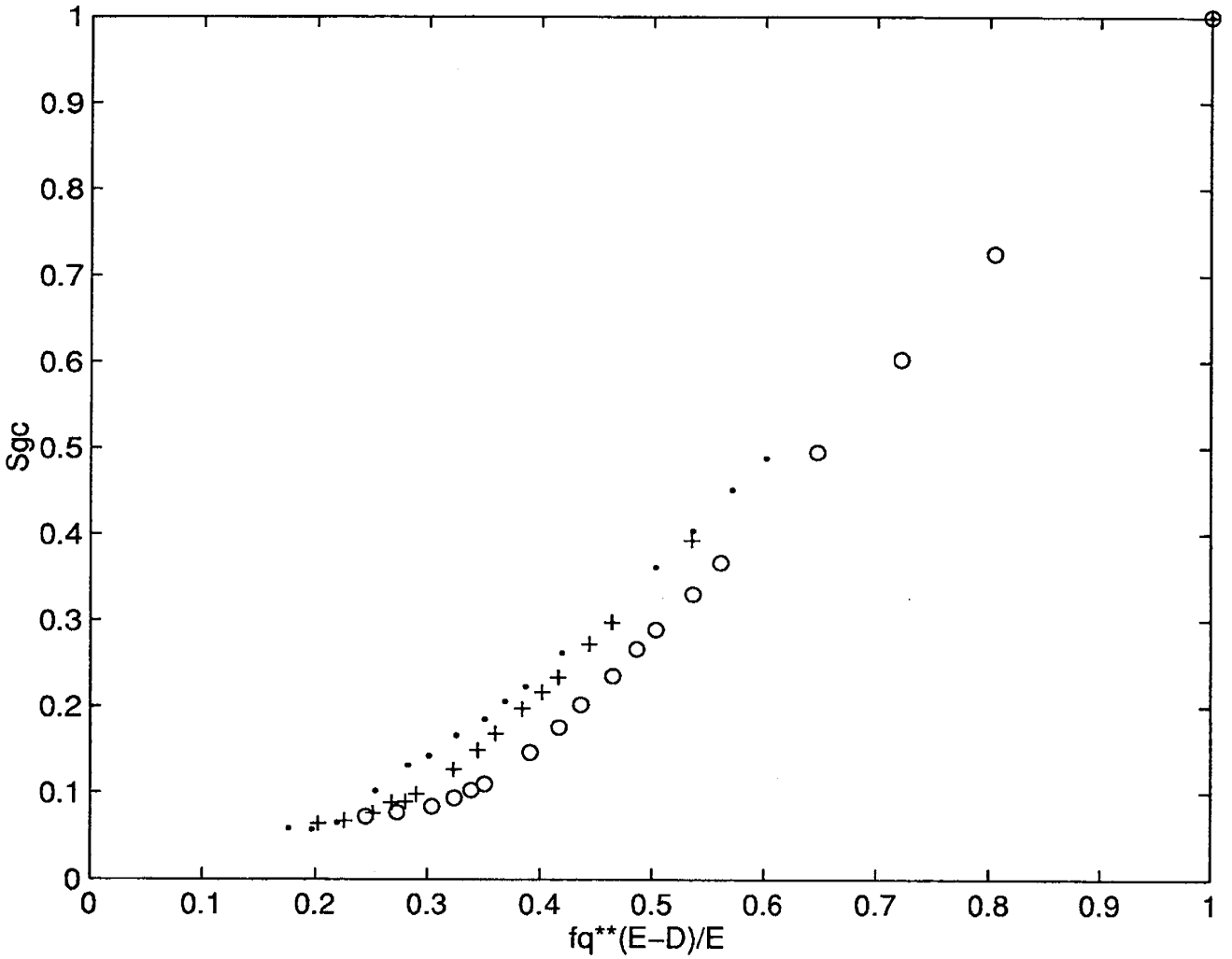

Figure 4: The mean value of the critical gas saturation as a function of the nucleation fraction for the case of instantaneous nucleation and a Rayleigh distribution of throats and cavity sizes. Circles, crosses and dots refer to sizes $20\times20\times20$, $30\times30\times30$ and $40\times40\times40$, respectively.

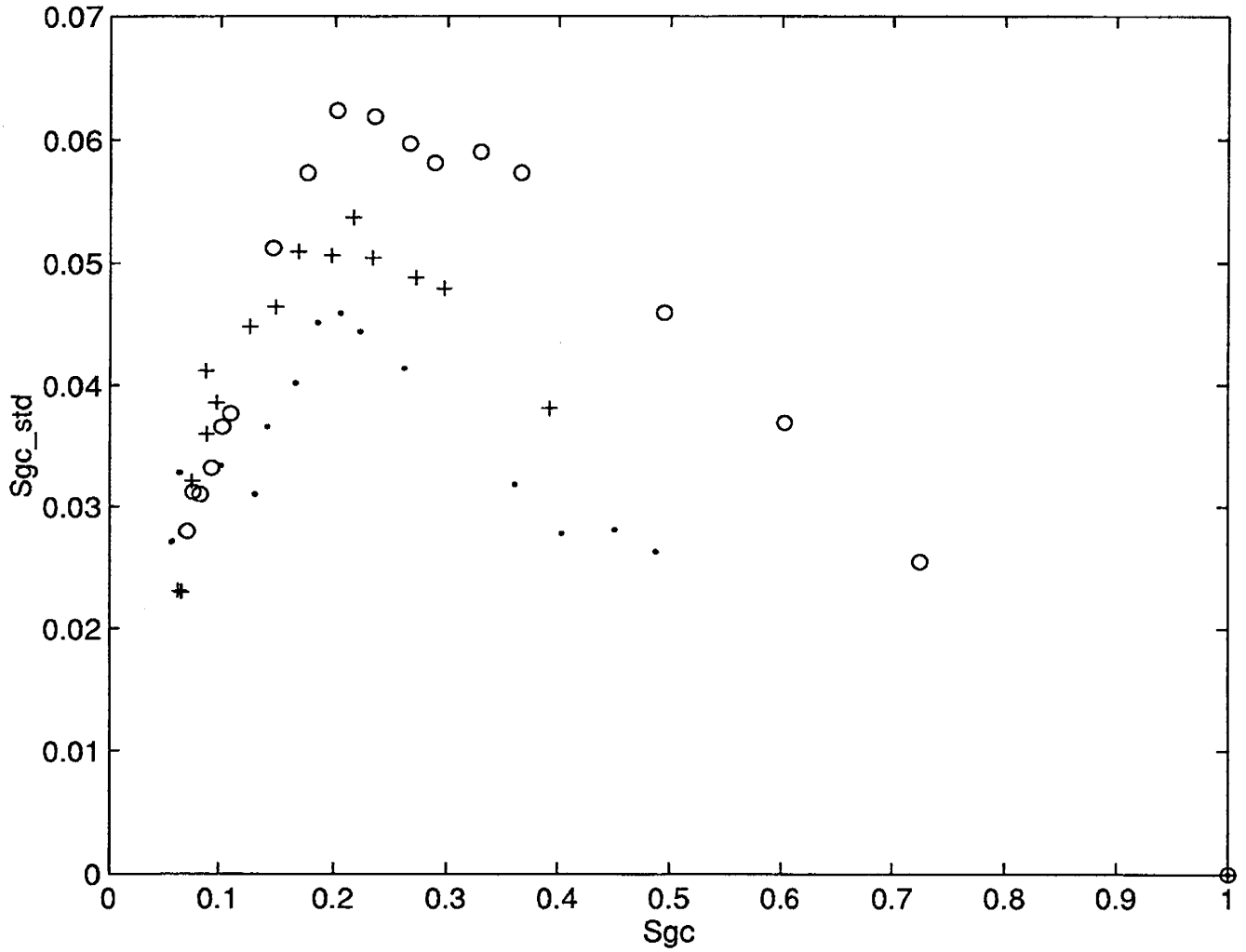

Figure 5: The standard deviation of the critical gas saturation as a function of the critical gas saturation for the case of instantaneous nucleation. Circles, crosses and dots refer to sizes $20\times20\times20$, $30\times30\times30$ and $40\times40\times40$, respectively.

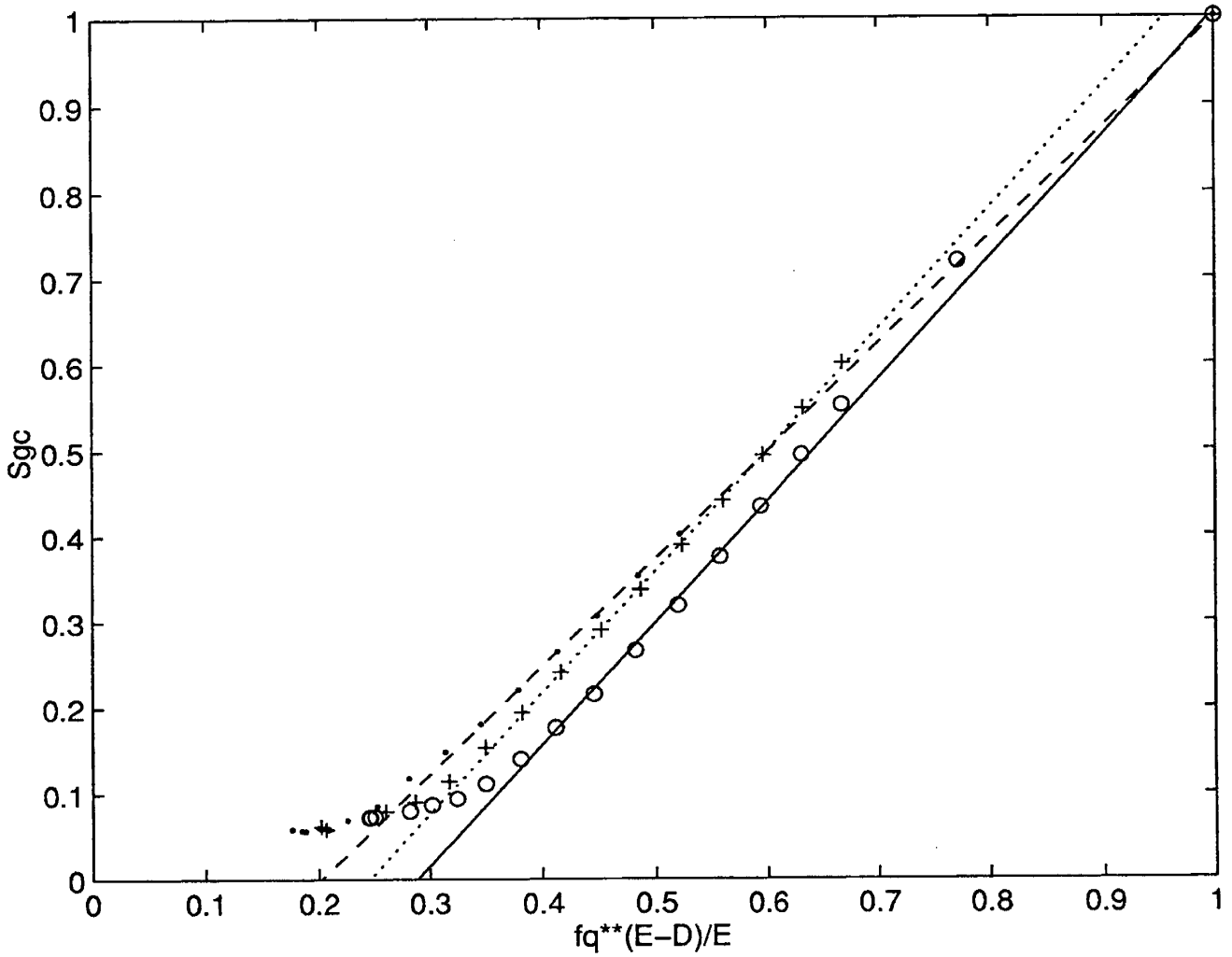

Figure 6: The mean value of the critical gas saturation as a function of the nucleation fraction for the case of sequential nucleation and a Rayleigh distribution of throats and cavity sizes. Circles, crosses and dots refer to sizes $20\times20\times20$, $30\times30\times30$ and $40\times40\times40$, respectively.

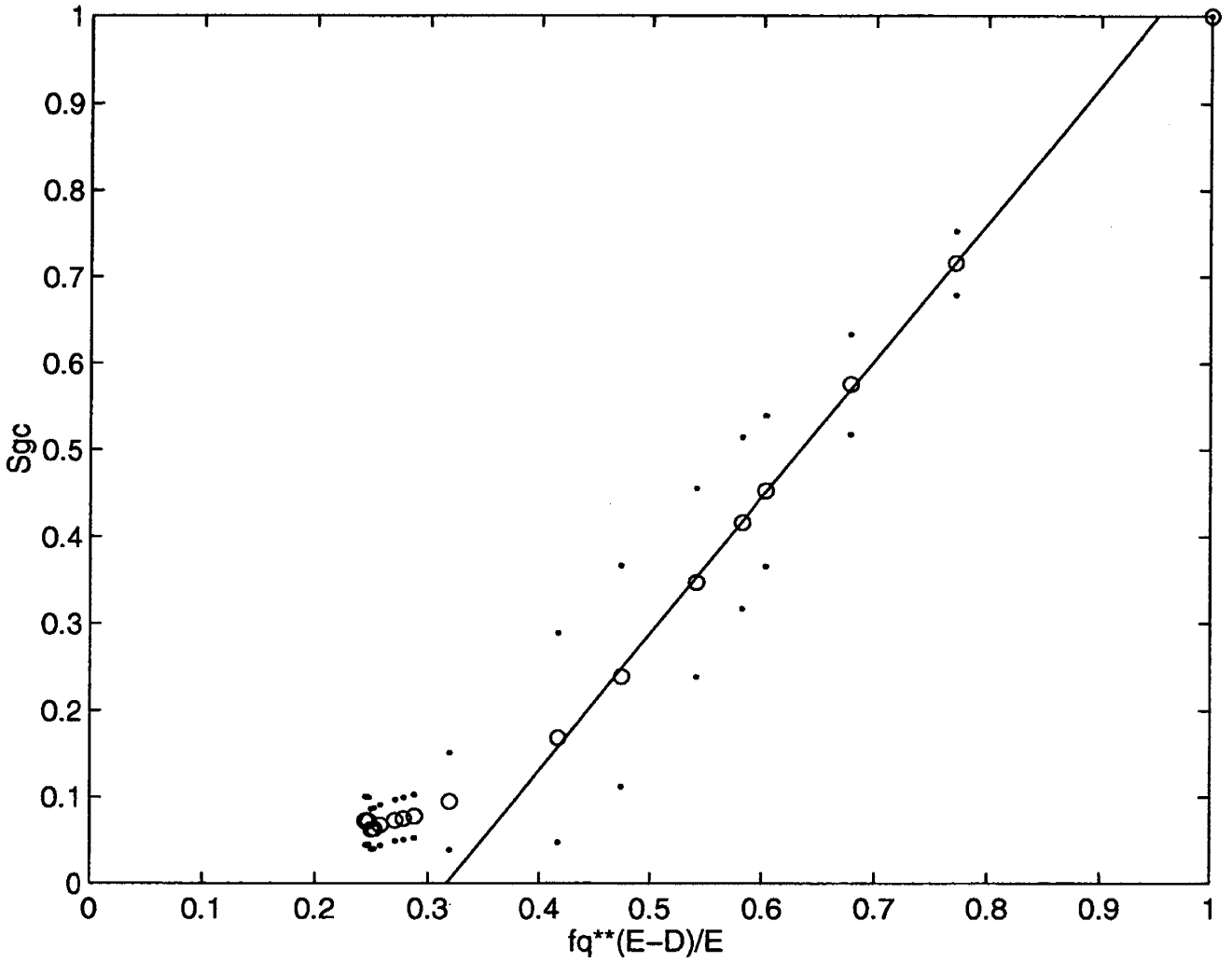

Figure 7: The critical gas saturation as a function of the nucleation fraction for the case of sequential nucleation and a uniform distribution of throats and cavity sizes. Circles denote mean values, dots denote the standard deviation. The simulations were done in a $20 \times 20 \times 20$ lattice.

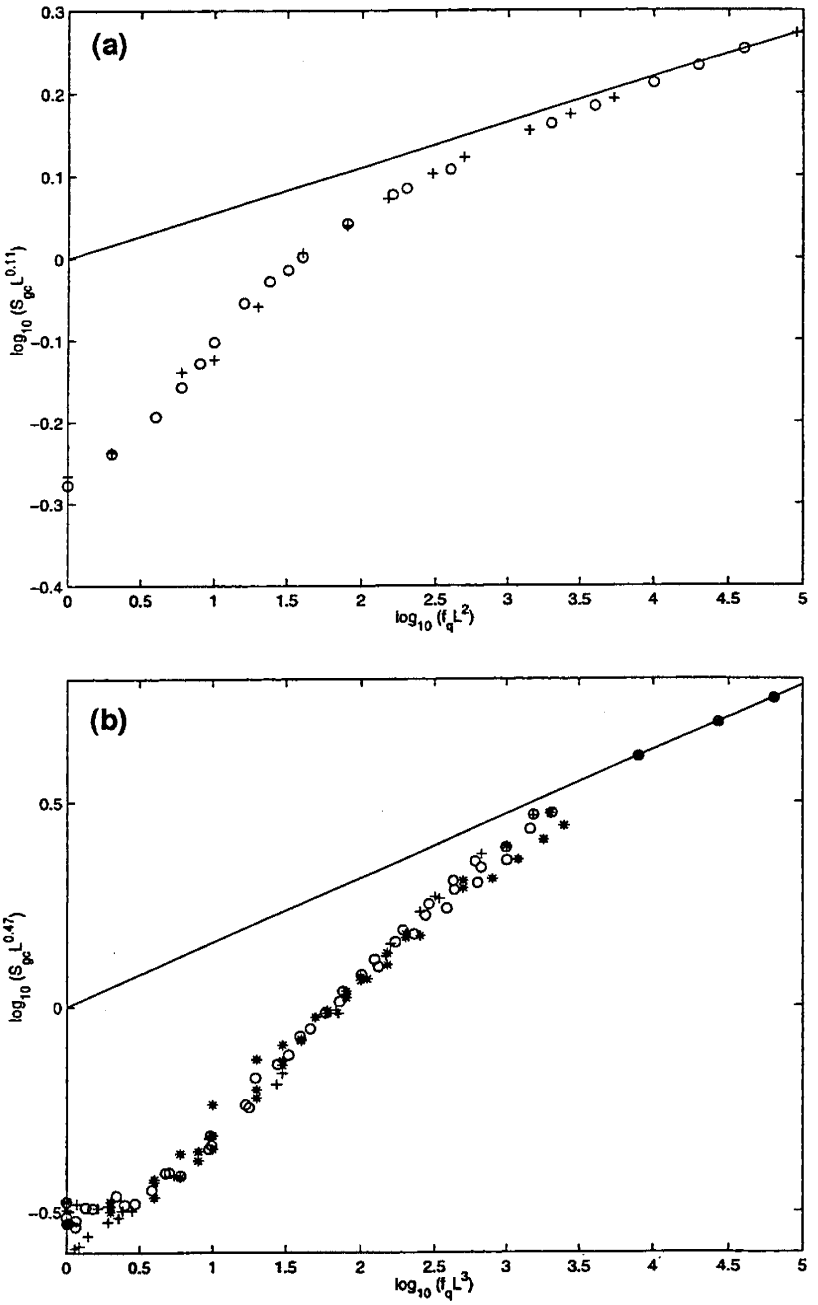

Figure 8: Plot of $S_{gc}L^{E-D}$ vs. f_qL^E for 2-D (a) and 3-D (b) simulations, respectively. The solid line is the theoretical straight line asymptote with slope 0.055 and 0.1566 in the respective dimensions. Results for different lattice sizes, and instantaneous and sequential nucleation are shown. In (a) circles and crosses refer to sizes 200×200 and 300×300 respectively at instantaneous nucleation. In (b) stars refer to instantaneous nucleation, circles refer to sequential nucleation and crosses refer to sequential nucleation and a uniform distribution for $\alpha_c(r)$ and $\alpha_b(r)$.

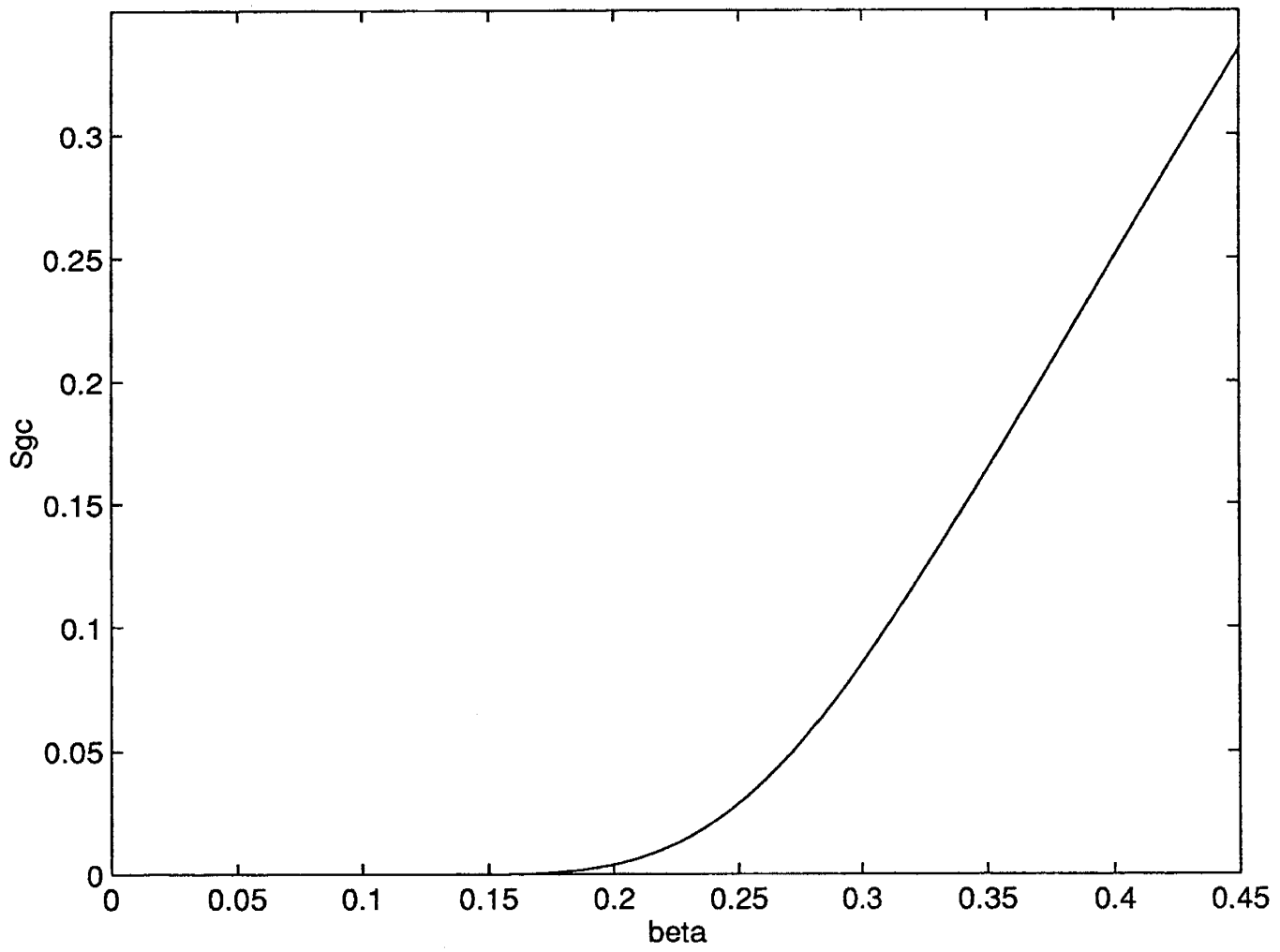

Figure 9: The variation of the critical gas saturation as a function of the geometric parameter β, which is the ratio of the characteristic cavity to throat sizes.

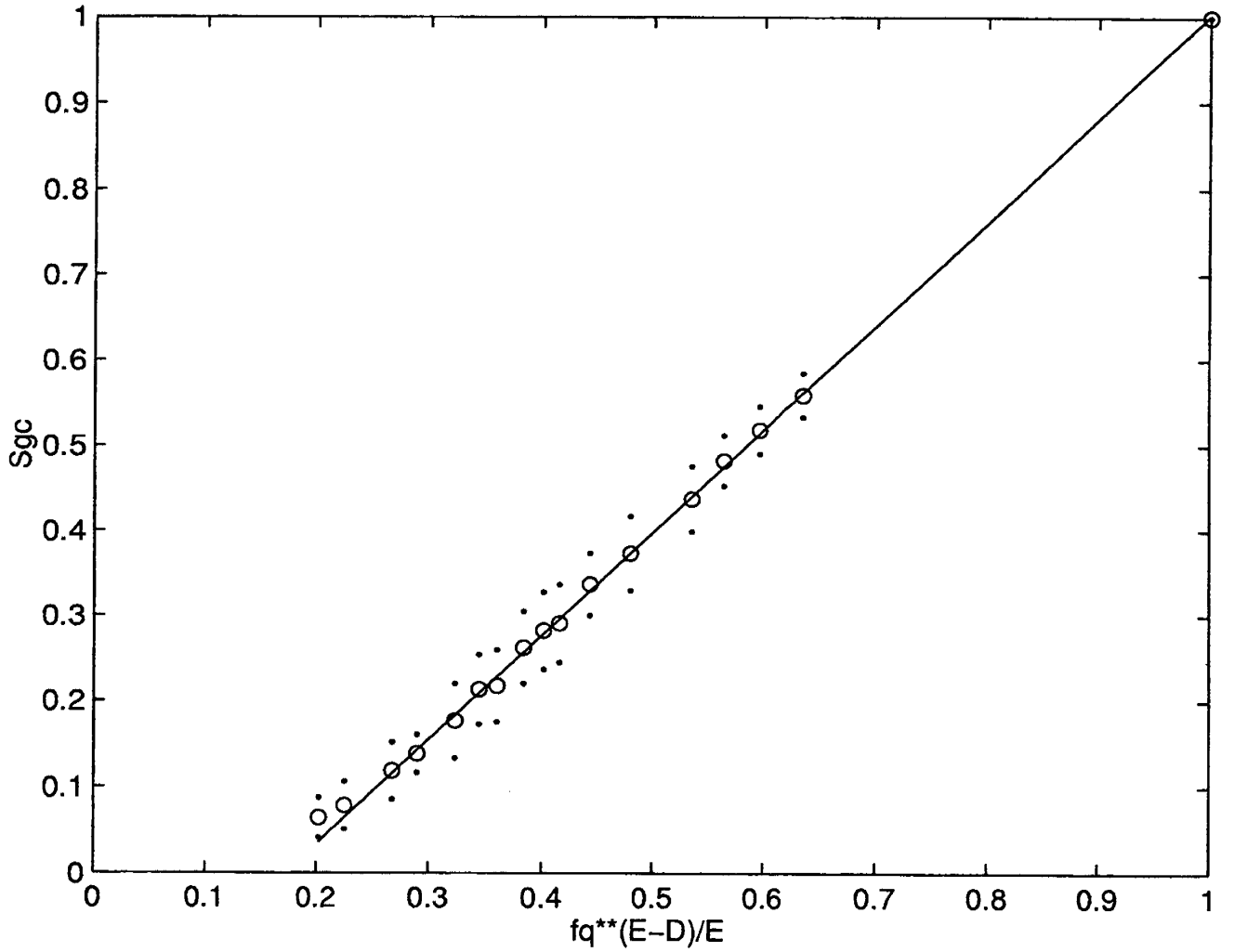

Figure 10: The critical gas saturation as a function of the nucleation fraction for the case of a Percolation- Modified DLA process at instantaneous nucleation in a 30×30×30 lattice. Circles denote mean values, dots denote the standard deviation.

3. A SCALING THEORY OF DRYING IN POROUS MEDIA

I.N. Tsimpanogiannis and Y.C. Yortsos
(with the collaboration of S. Poulou, N. Kanellopoulos and A.K. Stubos)

ABSTRACT

Concepts of immiscible displacements in porous media driven by mass transfer are utilized to model drying of porous media. Visualization experiments of drying in 2-D glass micromodels are conducted to identify pore-scale mechanisms. Then, a pore network approach is used to analyze the advancing drying front. It is shown that in a porous medium, capillarity induces a flow which effectively limits the extent of the front, which would otherwise be of the percolation type, to a finite width. In conjuction with the predictions of a macroscale stable front, obtained from a linear stability analysis, the process is shown to be equivalent to Invasion Percolation in a Stabilizing Gradient (IPSG). A power-law scaling relation of the front width with a diffusion-based capillary number is also obtained. This capillary number reflects the fact that drying is controlled by diffusion in contrast to external drainage. The scaling exponent predicted is compatible with the experimental results of Shaw [1]. A framework for a continuum description of the upstream drying regimes is also developed.

INTRODUCTION

The drying of porous media is a problem of significant scientific and applied interest. Chen and Pei [2] note that drying is one of the most energy consuming processes in industry. Applications include the drying of granular materials such as soils, rocks, minerals, building materials and ceramic powders; drying processes in the wood (Simpson [3, 4]), paper and textile industry; coating technology; and the drying of foodstuff (Fortes and Okos [5]) and pharmaceutical products. In a different context, in-situ drying of porous media is involved in recent methods for the remediation of contaminated soils by soil vapor extraction or soil venting (Ho and Udell [6]), as well as in the recovery of volitile hydrocarbons from underground oil reservoirs by gas injection (Le Romancer et al. [7], Le Gallo et al. [8]).

The development of a general mathematical framework to model drying of porous media has been a rather challenging research topic for several decades (Waananen et al. [9]). Although a plethora of methods have been presented, and while industrial designers are faced with the demand to design complicated processes regarding "real" problems, there are still many unresolved questions, even for "simpler" problems (Prat [10]). Traditionally, the description of drying in porous media is based on phenomenological approaches that consider the medium as a structureless continuum. In these, partial differential equations are postulated that relate the evolution in spacetime of volume-averaged quantities, such as moisture content and temperature. Phenomenological and empirical parameters are then used to relate fluxes to gradients, often drawn from an analogy with non-equilibrium thermodynamics (for example, see Luikov [11]). However, in these approaches, the pore microstructure and the underlying phenomena, which are key to the quantitative understanding of the process, are essentially ignored.

On a fundamental level, drying is a phase chage of a (usually) one-component liquid into a (usually) two-component gas, and involves at various stages the motion (receding) of

individual gas-liquid menisci (see schematic of Figure 1). The menisci reside in the porespace of the porous medium and are subject to the interfacial forces between liquid, gas and solid surfaces. Due to the disorder in the porespace geometry, however, their distribution is also disordered in general. The physical processes involve evaporation of the volatile liquid in the gas phase, driven by concentration gradients, countercurrent diffusion in the gas, possible liquid flow through connected films, and the accompanying receding of menisci. All these interactions are influenced by the porous medium microstructure to a significant degree.

In general, four different spatial regimes can be distinguished during a drying process (Figure 2): A far-field regime consisting of the initial liquid phase; a regime where the liquid phase is macroscopically connected and where both gas and liquid phases are "macroscopically continuous"; a third regime in which the liquid phase has been disconnected in individual clusters of variable sizes (blobs) as a result of drying; and a fourth regime consisting of the liquid phase in the form of pendular rings or films covering the solid surface, the thickness of which is progressively reduced, towards a "totally dry" regime. In the last three regimes the gas phase is macroscopically continuous. Shaw [1] has also postulated that liquid films may provide hydraulic connectivity to the liquid phase in all three regimes. It is apparent that an appropriate account of the various pore-scale events in all these regimes is fundamental to the accurate representation of any macroscopic description (Whitaker [12]).

Pore-network approaches for describing drying of porous media were recently proposed by Nowicki et al. [13] and in a series of papers by Prat and coworkers (Prat [14, 15], Laurindo and Prat [16, 17]). In a related context, Pot et al. [18] used lattice-gas cellular automata to simulate evaporation phenomena in 2-D porous media. Nowicki et al. [13] developed a rather comprehensive pore-network simulation of the process, and accounted for both capillary and viscous forces. However, the authors did not dwelve on the particular patterns that develop or on their effect on the drying rates. Prat [14, 15] and Laurindo and Prat [16, 17] studied pattern formation during drying assuming capillary forces only and ignoring viscous forces. The importance of film flows was also discussed [17]. Based on the assumption of percolation patterns and under isothermal conditions, they proceeded to compute evaporation and drying rates by solving a quasi-static diffusion equation in the gas phase. However, earlier drying experiments in glass-bead packs by Shaw [1] suggested that viscous forces are not negligible, and in fact are needed to explain the formation of a front width (separating continuous liquid from gas) of a finite size. This, Shaw [1] attempted to scale using scaling expressions obtained from external drainage (see below). Despite the limitation on viscous forces, however, Prat's studies are important in that they represent the first attempt to theoretically characterize drying patterns and their rate of change in porous media.

As in other processes involving two-phase, immiscible flows in porous media, the following two aspects of drying patterns need to be understood: (i) Their geometrical structure, which dictates transport and capacitance; and (ii) their rates of change. This is the main motivation of this paper. We consider the application of a pore-network approach, as in Nowicki et al.[13], Prat [14, 15], and Laurindo and Prat [16], but with specific objectives to understand the structure of drying patterns, particularly in the frontal region. From such an analysis, the derivation of effective macroscopic models can then be obtained. Drying, involving gas-liquid interfaces, can benefit from advances in the analogous problem of external drainage, which is reviewed below. What is novel in drying, however, is the additional effect of mass

transfer in the gas phase, which actually drives the process. This needs to be analysed in some detail.

The paper is organized as follows: First, we give a brief review of recent findings in isothermal drainage processes, which have a direct bearing on drying. Then, experiments in 2-D micromodel geometries are presented to visualize mechanisms during drying and to help in the development of the theory. Based on the experimental observations, a theoretical approach is subsequently developed, which combines arguments borrowed from isothermal drainage and from the related bubble growth problem, where mass transfer is a key process. We use scaling arguments to show that drying is actually a process of Invasion Percolation in a Stabilizing Gradient (IPSG) (see below for a definition), from which we can infer the scaling of the front width as a function of the drying parameters. To demonstrate the transition from a percolation-only pattern, which was studied by Prat, to a stabilizing gradient and an IPSG, a linear stability analysis of the front in the appropriate geometries must be performed. This analysis will precede the main theoretical developments. We close by providing a framework for a macroscopic description based on transverse averages, and by commenting on the modeling of the other regimes.

We show that the scaling so obtained is compatible with Shaw's [1] experimental results. Thus, although near the leading edge of the front, the displacement pattern will be of the percolation type (assumed by Prat and co-workers to be valid for the entire pattern), as the width of the front increases, viscous forces become increasingly important, leading to a displacement described by IPSG. Our analysis also sheds light to a process of liquid flow, termed "capillary pumping" by Le Romancer et al. [7], in their modeling of oil recovery from fractured reservoirs by gas injection. We show that this effect is actually the consequence of accounting for both capillary and viscous terms in the process. As in previous pore-scale studies in drying (Nowicki et al. [13], Prat [15]), our analysis is restricted to isothermal problems. We also neglect convection in the gas phase, which is expected to be progressively of secondary importance, and gravity. The effect of the latter can be directly incorporated. However, effects of heat transfer and convection need a separate analysis, which will be attempted in a future study.

PRELIMINARIES

Drying involves gas-liquid interfaces and mass transfer and should be subject to an analysis similar to external drainage and to bubble growth in porous media. Because of the expected similarities, we briefly review in this section recent advances in these two areas.

Consider, first, drainage, namely the displacement of a wetting phase by a non-wetting phase in a porous medium in the absence of phase change. In drainage, menisci reside in pores or at the entrance of pore-throats with a curvature corresponding to the local capillary pressure, defined as the difference between the non-wetting (gas) and wetting (liquid) phase pressures,

$$P_c \equiv P_{nw} - P_w = 2\gamma\mathcal{H} \tag{1}$$

Here, γ is the interfacial tension between the fluids, $\mathcal{H}$ is the mean curvature of the meniscus and a zero contact angle was assumed. In the absence of buyoancy and/or viscous forces, the

capillary pressure, thus the mean curvature, are spatially uniform. A meniscus will penetrate a pore throat, adjacent to which it resides, when the capillary pressure first exceeds the capillary entry pressure for that pore throat (roughly equal to $2\gamma/r$, where r is the pore throat size). In drainage at constant rate, the sequence of pore penetration can be modeled by Invasion Percolation (IP), where at each time step only one pore throat is invaded, that with the least capillary resistance (or, equivalently, the largest radius) among all throats at the perimeter of the interface. During this step, all other menisci remain stationary or fluctuate slightly. This type of displacement gives rise to a self-similar fractal pattern in the displacing phase, which eventually approaches that of the percolation cluster. The properties of the latter have been discussed in detail in various publications [19, 20]. Because of the self-similarity involved, however, defining a mean-front position is not operationally useful.

However, if gravity and/or viscous forces are also important, a percolation pattern will not develop over the entire region of displacement. When only gravity forces are important, the capillary pressure will vary with the elevation h of the interface, since $P_c = g_x \Delta\rho h$, where g_x is the component of gravity in the direction of displacement and $\Delta\rho = \rho_w - \rho_{nw}$. Then, the displacement acquires the features of a different pattern, namely Invasion Percolation in a Gradient (IPG) [21, 22, 23, 24, 25, 26]. In this case, the competition between gravity and capillary forces is expressed through the Bond number

$$B = \frac{g_x \Delta\rho k}{\gamma} \tag{2}$$

where k is the permeability of the porous medium (which is roughly proportional to the square of a mean pore size $k \sim r_m^2$, Katz and Thompson, [27]). Now, one needs to further distinguish two cases:

(i) If $B > 0$, for example, in the downwards displacement of a heavier by a lighter fluid, the two phases are separated by a front of finite width, σ_G, which scales with the Bond number as [21, 22]

$$\sigma_G \sim B^{-\frac{\nu}{\nu+1}} \tag{3}$$

where ν is the correlation length exponent of percolation. For a non-zero B, the front width is finite. Then, the front is not self-similar, but rather self-affine [29] (Fig. 3a). Within the front, the pattern has the fractal characteristics of the percolation cluster. However, upstream of the front, the pattern is compact. Thus, a mean front position can be usefully defined. In essence, this reflects the transition of the displacement from an IP to a piston-like pattern. The latter is the pattern that develops when only gravity (and not capillarity) acts (and which would be piston-like in this case). We shall refer to this as Invasion Percolation in a Stabilizing Gradient (IPSG). Hulin et al. [23] experimentally demonstrated the application of IPG in a drainage problem stabilized by gravity.

(ii) On the other hand, if $B < 0$, for example, in the downwards displacement of a lighter by a heavier fluid, the displacement is Invasion Percolation in a Destabilizing Gradient (IPDG). This pattern has the different features of capillary fingering (Fig. 3b), in which the displacement occurs by invading fingers of a mean width still given by (3), the local characteristics of which are still controlled by percolation. This regime has been discussed in detail in Frette et al. [30] and Meakin et al. [31].

The effect of viscous forces is more complex. At larger scales, where viscous effects predominate, two limiting patterns are expected, Piston-like Displacement (PD) and Viscous Fingering (VF), depending on whether the ratio $M = \frac{\mu_w}{\mu_{nw}}$, between the viscosities of the two fluids, is smaller or greater than 1, respectively. Essentially, this reflects the Saffman-Taylor instability [32]. At smaller scales, however, where capillary forces are important, the problem becomes similar to IPSG (case of small M) or IPDG (case of large M) (Yortsos et al., [33], Xu et al, [34]). In the first case, in particular, fully-developed drainage involves an advancing front of a finite width, σ_V, as in the case of stabilizing gravity, followed by a more compact pattern. The front width can be shown to scale with the front capillary number, $Ca_F = \frac{v\mu_{nw}}{\gamma}$, as [28, 34]

$$\sigma_V \sim \left(\frac{Ca_F}{\Sigma}\right)^{-\frac{\nu}{1+\zeta+\nu(D-1)}} \tag{4}$$

where v is the front velocity, μ denotes viscosity, Σ is the dimensionless variance of the pore-size distribution, ζ is the conductance exponent of percolation and D is the fractal dimension of the percolation cluster. Values for the various percolation exponents can be found in classical texts on percolation, for example in Stauffer and Aharony [35]. The properties of these patterns and the conditions delineating the various regimes were recently discussed in detail in Yortsos et al. [33] and Xu et al. [34].

Although subject to similar considerations, drying also involves the additional effect of mass transfer in the gas phase, which actually drives the process. A certain analogy can be drawn between drying and the problem of bubble growth in porous media, recently investigated by Li and Yortsos [36, 37], and Satik and Yortsos [38], where the driving force for phase change and the ensuing growth of the gas phase is diffusion of mass or heat in the liquid (for the case of solution gas or boiling, respectively). When a bubble (more properly a gas "cluster") grows in a porous medium, its pattern at small bubble sizes will be of the percolation type. However, at larger sizes capillary forces are less significant, and the displacement pattern is controlled by diffusion and viscous (and gravity) effects (Satik et al. [41]). Diffusion in the liquid is known to destabilize such a liquid-to-gas phase change, leading to a Mullins-Sekerka instability (see [39, 40] for the particular application), thus the pattern gradually becomes of the viscous fingering type. The boundaries in the parameter space that delineate patterns in bubble growth were described in Satik et al. [41] by using scaling arguments and pore-network simulations. The same authors also proposed kinetic expressions to describe the rates of growth of bubble growth patterns. Key to their description was the modeling of the diffusion process and its coupling with viscous and capillary phenomena. Such an approach could also be fruitfully used in the context of drying.

It could be noted that because it is essentially a process of gas displacing liquid, one might naively anticipate drying to involve IPDG patterns of the viscous fingering type, in analogy with external drainage in which the displacing fluid is less viscous, or with the bubble growth problem at large sizes. However, this is misleading: drying is not driven by external injection, but by *internal* diffusion in the gas phase. This differs from external drainage, but also from bubble growth, where diffusion occurs in the liquid phase. These processes conspire to give patterns that are characterized by the stabilizing IPSG process, as will be shown below.

EXPERIMENTAL

To visualize the mechanisms involved in drying in porous media we conducted experiments in transparent etched-glass micromodels. These micromodels consist of two glass plates fused together, on one of which a specific square pore network pattern is etched. Micromodles have been valuable in providing an understanding of the qualitative features of various displacement processes in porous media (see Buckley [42] for a review). In the context of phase change, a most recent application involves the bubble growth experiments reported in Li and Yortsos [36] and the drying experiments by Laurindo and Prat [16]. In our application, the typical micromodel has size 25 cm $\times$ 10 cm, while the etched pores are channels with an estimated depth of 100 μm. The pore body/throat thickness is spatially distributed, following a specified Rayleigh distribution, with an average pore throat radius of 450 μm and an average pore body radius of 900 μm. These dimensions are specified before etching the glass plate. Due to imperfections in the glass and the lack of precise control in etching and fusion, however, the final dimensions are somewhat different. Also, although originally rectangular, the channels can become "eye-shaped" after fusion, as pointed out by Chatzis et al. [46] and Vizica and Payatakes [44]. The final shape depends on the time of fusion among other parameters. Details of the manufacturing procedure can be found in Chatzis [43]. One entry port and one exit port on opposite sides of the micromodel serve to inject and recover the fluids. The experimental apparatus, shown in Figure 4, consists of the micromodel, of two reservoirs for the supply of the liquid and gas phases (denoted in the Figure as "oil" and "gas"), of a syringe pump, a camera for visualization, a video tape recorder and a data processing system. Typical liquids used were n-pentane, n-hexane and distilled water. The gas phase in the experiments was air.

The experiments consist of first saturating the micromodel with the liquid phase and subsequently displacing it with the gas at relatively high injection rates until the liquid phase is macroscopically disconnected from the two ports. At that time the gas injection rate was decreased to low rates and the drying process commences. This arrangement is actually different on the macroscopic scale than Shaw's [1], where only one side is open to flow, there is no primary drainage or external liquid displacement, and the only mechanism for the movement of menisci is due to mass transfer. However, the basic drying mechanisms at the microscale are the same in both experiments. In fact, the theoretical model to be developed below will pertain to Shaw's configuration. The main difference is in mass transfer, which in our experiments can also occur by forced convection due to the particular configuration (see also Jia et al. [45], for a related application). In most of the experiments, however, the injection rate was kept quite low (of the order of 0.052 ml/min) resulting into small Peclet numbers and a predominantly diffusive mass transfer mechanism.

Figure 5 shows two snapshots of the interfacial pattern at different times during drying. The evaporation of the liquid and the resulting receding of the interface at various places are apparent. We note the existence of many clusters of different sizes, containing macroscopically disconnected liquid. The clusters are disordered and reflect the difference in the capillary characteristics of different pores. The interface is generally "rough", although it is difficult to ascertain self-affinity or self-similarity. Important findings from the visualization experiments included the following:

(i) Typically, the penetration of gas into the liquid and the receding of the meniscus occured in the form of sudden jumps, one-at-a-time, which were separated by finite time intervals. These jumps are similar to "rheon" events in external drainage and reflect the fact that for a pore to be invaded, a capillary pressure threshold must be exceeded, following which displacement and filling of the adjacent pore body will occur rapidly. During that time, interfaces pinned by capillarity in other pores are adjusted as a result of liquid incompressibility (see also below). Rheon events will predominate when the displacement is controlled by capillarity, as was the case in many of these experiments. When, however, drying rates are fast, as was the case with the experiments involving n-pentane, or at higher gas injection rates, the displacement was also found to occur at the same time in more than one pores, although several interfaces remained pinned during the same time.

(ii) Even though the plan views in Figure 5 indicate gas-only and liquid-only occupied regions, a careful monitoring of the changes in the liquid-gas interface revealed that liquid films existed at the surfaces of pores invaded by gas. Figure 6 is a close-up of the gas-liquid interface, and shows the trace of wetting films left behind during the invasion of a pore by gas. The existence of films was also indirectly deduced from observing the emptying of some pores occupied by liquid, which would be topologically impossible in the absence of connected films. Wetting films in corners and crevices following drainage of a wetting liquid have been documented in various drainage studies (e.g. see Lenormand et al. [47]). In his experiments, Shaw [1] inferred that connected liquid films help in the transport of liquid towards the open edge of the cell where it can evaporate. Prat [14, 15] and Laurindo and Prat [16, 17] also reported the existense of thin liquid films.

The above mechanisms of drying process will be incorporated in the pore-network theory to be developed subsequently. Before we proceed, however, it is necessary to understand large-scale effects of diffusion and mass transfer. These can be studied in the absence of capillarity and pore microstructure.

FRONT STABILITY IN THE ABSENCE OF CAPILLARITY

It was pointed out in a previous section that while small-scale features of a displacement process are set by capillarity, larger-scale characteristics are set by transport (such as viscous flow or diffusion). This is certainly the case both in external drainage (Xu et al. [34]) and in bubble growth (Satik et al. [41]). The percolation pattern will ultimately (at large capillary numbers, see also below) evolve into a pattern dictated by the large scale. To understand this pattern, and thus to infer whether the process will be of the IPSG or the IPDG type, the stability of drying in an effective porous medium in the absence of capillarity must be analuzed.

Consider a planar drying front advancing in an isotropic and homogeneous effective medium, with a geometry that mimics the experiments by Shaw [1], as shown in Figure 7. The liquid phase consists of a vaporizing single component, while the gas phase is a mixture of two components at constant pressure. A sharp interface seperates gas from liquid, thus for the purposes of this section we ignore effects of microstructure or film flows. Isothermal conditions are assumed. The top boundary is open to gas flow, has zero molar concentration of the vaporized liquid and a constant gas pressure. The bottom boundary is

impermeable to liquid, thus all changes in liquid content are due to drying. We will examine the stability of the front to transverse perturbations in the absence of capillarity. For the purposes of this section, which is to reveal macroscopic features, the analysis will be based on a continuum description. We consider quasi-static diffusion in the gas phase and assume that the profiles (which are generally time-dependent) are "frozen" when the perturbation is imposed. Quasi-static diffusion is expected to be valid when the ratio of the equilibrium concentration of the volatile component in the gas phase to its molar density in the liquid phase is small, which is the case at low partial pressures (see Appendix). The more general problem involving unsteady-state diffusion and convection will be described in a separate study (see also Appendix). Assuming a frozen state during perturbations is a standard approach for the stability of time-varying base-states (see, for example, Tan and Homsy [48]).

Let the front that separates liquid- from gas-occupied regions be denoted by the following equation in the notation of Figure 7

$$\mathcal{F}(z,y,t) \equiv z - F(y,t) = 0 \tag{5}$$

and recall the definitions

$$\mathbf{n} = \frac{\nabla \mathcal{F}}{|\nabla \mathcal{F}|} \tag{6}$$

and

$$v_n = -\frac{\mathcal{F}_t}{|\nabla \mathcal{F}|} \tag{7}$$

for the outer normal (pointing towards the liquid) and the normal velocity at the front, respectively. The governing equations in the liquid-occupied region involve Darcy's law for the flow of the liquid phase

$$\mathbf{u}_l = -\frac{k}{\mu_l} \nabla P_l \tag{8}$$

from which, and with the use of the continuity equation, we obtain a Laplace equation for the liquid pressure

$$\nabla^2 P_l = 0 \tag{9}$$

This equation is subject to the following boundary conditions

$$P_l = P_v \quad \text{at} \quad z = F(y,t) \tag{10}$$

where P_v is the gas pressure, assumed constant, due to the small gas viscosity, and

$$\frac{\partial P_l}{\partial z} = 0 \quad \text{at} \quad z = L \tag{11}$$

where L denotes the longitudinal extent.

For negligibe convection and transient effects the condensible component A satisfies the quasi-static diffusion equation (see Appendix),

$$\nabla^2 c_A = 0 \tag{12}$$

where c_A is the concentration of the condensible species (see also Prat [14, 15]). The corresponding boundary conditions are

$$c_A = 0 \quad \text{at} \quad z = 0 \tag{13}$$

and

$$c_A = c_e \equiv x_{Ae} c \quad \text{at} \quad z = F(y,t) \tag{14}$$

at the inlet and the front, respectively. Here, we defined the equilibrium mole fraction, $x_{Ae} = \frac{P_{vA}}{P_v}$, where P_{vA} is the partial pressure of A, and the total gas concentration, c, which because of the assumed constant pressure, can also be taken as a constant ($c = \frac{P_v}{RT}$ for an ideal gas, where R is the ideal gas constant and T is absolute temperature).

Concentration and pressure fields are coupled at the interface by mass balances. For the vaporizing liquid we have

$$-\mathcal{D}_{AB} \frac{\partial c_A}{\partial n} = \frac{\rho_l}{M_A}(u_{ln} - v_n) \quad \text{at} \quad z = F(y,t) \tag{15}$$

where $\mathcal{D}_{AB}$ is the diffusion coefficient, ρ_l is the mass density of the liquid, M_A is the molecular weight and n denotes the normal to the interface. The interface is a material surface, thus,

$$v_n = u_{gn} \tag{16}$$

The assumption made here is that the liquid consists of a single volatile component and that convection effects are secondary.

Consider, now, the base state in the absence of perturbations (denoted by superscript bar). Then, the front is located at $z = f(t)$ and we readily find the base state

$$\bar{c} = \frac{z c_e}{f(t)} \quad \text{for} \quad 0 < z < f(t) \tag{17}$$

$$\bar{P}_l = P_v \quad \text{for} \quad f(t) < z < L \tag{18}$$

and

$$\bar{v}_n = \bar{v}_z \equiv \dot{f} = \frac{c_e M_A \mathcal{D}_{AB}}{\rho_l f} \tag{19}$$

The latter can be integrated to yield the front location (assuming $f(0) = 0$)

$$f = \sqrt{\frac{2 c_e M_A \mathcal{D}_{AB}}{\rho_l} t} \tag{20}$$

This expression also results in the quasi-static limit from the more general analysis presented in the Appendix.

For the stability analysis we assume a "frozen" state at $t = t_0$, take normal modes, varying as $\exp(i\alpha y + \omega(t - t_0))$, namely

$$c = \bar{c} + \epsilon\sigma(z,t)\exp(i\alpha y + \omega t) \tag{21}$$

$$P_l = P_v + \epsilon\Pi(z,t)\exp(i\alpha y + \omega t) \tag{22}$$

and

$$F(y,t) = f(t) + \epsilon\exp(i\alpha y + \omega t) \tag{23}$$

and inquire about the sign of the rate of growth, ω, of disturbances of wavenumber α. In the above notation, ϵ has dimensions of length. Substituting (21) to (12) and the boundary condition (13) gives

$$\sigma = 2A\sinh(\alpha z) \tag{24}$$

The constant A is evaluated by using boundary condition (14) and the base state solution evaluated at the front location. After some calculations we arrive at the result

$$\sigma = -\frac{c_{Ae}\sinh(\alpha z)}{f\sinh(\alpha f)} \tag{25}$$

Working likewise with the pressure field wee find that Π satisfies a Laplace equation, the solution of which subject to the no-flux and constant pressure conditions at the two boundaries, respectively, is identically zero, $\Pi = 0$. Thus, at this level of approximation, the liquid phase is stagnant, as intuitively expected. However, consideration of capillarity at the microscale (and the interfacial curvature it implies) leads to viscous flow in the liquid phase, as will be shown below. This flow will set the main features of the drying pattern at the microscale.

A final substitution of the above into the coupling equation at the front, leads to the following expression for the rate of growth of disturbances

$$\omega = -\frac{\mathcal{D}_{AB}M_A c x_{Ae}\alpha}{\rho_l f\tanh(\alpha f)} < 0 \tag{26}$$

It is apparent that the rate of growth ω is negative, which implies that this displacement is unconditionally stable. The physical intrepretation of the stability result is straightforward: If a protuberance of the front into the gas region forms, gas-phase diffusion rates will be higher at the tip compared to the base, due to the compression of iso-concentration curves at the tip (Figure 7). In the absence of liquid flow, this will result in a locally larger velocity at the tip, hence in the smoothing of the protuberance, and in stability. Thus, even though it is effectively a process of a less viscous fluid displacing a more viscous fluid in a porous medium (where in external drainage one would expect a viscous fingering instability), the fact that the process is driven internally by diffusion in the gas phase renders the frontal displacement a stable process. In a sense, this is analogous to the melting of a solid, in which the receding interface is also linearly stable (Langer [39]). On the other hand, this is in contrast with the problem of bubble growth in porous media refered to above, where the process is also internally driven by diffusion, although in the liquid phase, and where in

the absence of capillarity, the problem is linearly unstable (Li and Yortsos [40]). The phase change analogy with that problem is solidification in a supersaturated solution.

The important implication of the previous analysis is that in the absence of capillary forces the drying pattern in the porous medium will be piston-like (PD). Because of the relatively low drying rates in applications, however, capillarity will be important over sufficiently small scales (compare with Figure 5) and must be considered, as shown below. Before we proceed, we note that a qualitatively similar result to (26) is also expected in the more general problem, where net gas phase convection is considered. This analysis, which also includes spherical geometries, will be considered in a separate study.

FRONT DESCRIPTION USING A PORE-NETWORK ANALYSIS

Consider, now, a description of the frontal region during drying by accounting for the effect of the pore structure (Figures 5-6). Locally, the interface is described by an equation similar to (5), across which boundary conditions (15) and (16) apply. However, here menisci in the porespace must conform to the curvature of the pore in which they reside. Thus, across the meniscus, liquid and vapor pressures are related through the capillary pressure

$$P_l = P_v - \frac{2\gamma}{r} \tag{27}$$

where, assuming locally spherical shapes, the mean pore curvature is r. A convection-diffusion equation describes mass transfer in the vapor phase, while the fluid flow in both phases is described locally by Stokes' law. In the following, we will focus on the structure of the front. For this, capillarity must be considered. We will show, first, that the latter induces a viscous flow, the magnitude of which dictates the extent of the front and its pattern. Then, the scaling of the front width and the basic properties of the pattern are discussed.

(1) Capillarity-Induced Flow (Capillary Pumping)

Because of the capillary forces in the constriction of pore throats, a meniscus will not penetrate a pore throat, for example throat i of radius $r_{p,i}$ in Figure 6, until the capillary pressure across the meniscus exceeds for the first time the capillary barrier of that throat, $\frac{2\gamma}{r_{p,i}}$. Until this happens, the normal velocity of this meniscus will be negligible, therefore, the meniscus will remain *pinned*. During this period of time, however, diffusion proceeds over the entire gas-liquid interface, which requires that menisci will be receding in other pores of size greater than $r_{p,i}$ (for example pore j in Figure 6) or along corners containing non-displaced liquid. Thus, at any time during the process, the drying front will reside in pores of two different types: (i) Completely Empty (CE) (Figure 8a), in which menisci are stationary at the pore throats; and (ii) Partly Empty (PE) (Figure 8b), in which menisci are receding. Partly empty pores are either pore bodies, or pores containing liquid left behind in cornerns, crevices or films and which might be connected hydraulically to the bulk liquid. The rate of meniscus displacement due to evaporation is determined from the solution of the overall problem. When the capillary pressure barrier across a throat adjacent to a CE pore is exceeeded, the corresponding pore is invaded and becomes a PE pore.

Consider, now, equation (15) applied to the meniscus on the CE pore throat i. Since evaporation continues occuring, regardless of whether the meniscus is stationary or moving, the normal liquid velocity u_{ln} in (15) must be negative. This implies a liquid flow in the direction from receding to stationary menisci (for example, from the PE pore containing capillary j to the CE pore containing capillary i). It follows that capillary forces in a drying process will induce a flow, the magnitude of which depends on the drying rates. This is to be contrasted to the prediction of a stagnant liquid obtained from the linearized stability analysis above, where capillarity was neglected. This flow is due to the variation of pore throat curvatures and it is capillary-driven (from "large" to "small" capillaries). In the particular application involving gas injection to recover oil from fractured rocks, a simplified process of the same type was termed *capillary pumping* by Le Romancer et al. [7].

(2) Drying Patterns

The capillarity-induced flow will impart a corresponding viscous pressure gradient, hence

$$P_{l,j} > P_{l,i} \tag{28}$$

Then, under the further assumption of a constant pressure in the gas,

$$P_{c,i} > P_{c,j} \tag{29}$$

namely, as drying continues, the capillary pressure will be positive and may also increase with time in locations where the meniscus is stationary and pinned (CE pores of type i). An analogous statement was also made by Shaw [1], although in his analysis it was attributed to countercurrent gas-liquid flow. It is possible, therefore, that after sufficient time has elapsed, the capillary barrier at such a pore throat i will be exceeded for the first time and the meniscus at that location will also start receding. This mechanism restricts the development of the front, which cannot be extended too much, or become very tortuous, but will be limited instead to a finite width. To estimate its extent, we need to analyze the pattern developed.

Assume for a moment that the drying pattern of the front is of the IP type, as assumed for example by Prat [14, 15]. Then, *all but one* of the pore bodies containing the front would be of the CE type, the only PE pore being that invaded from a pore throat with the least capillary barrier, among all throats currently containing front menisci. As shown above, however, there would be liquid flow from the PE pore to a CE pore, which may ultimately cause one or more pore throats to be invaded, even though their capillary barrier is not the smallest among the perimeter throats, as originally assumed. Under such conditions, therefore, the evolution of the IP pattern would be disrupted.

The analysis is facilitated if we make the following assumptions:

1. The pressure drop across two adjacent pore bodies (e.g sites k and m in Figure 6) can be approximated by a Poiseuille-type law

$$Q_{k\to m} = \frac{G_{km}}{\mu_l}(P_{l,k} - P_{l,m}) \tag{30}$$

where $Q_{k\to m}$ is the flow rate across the two sites and the conductance G_{km} depends only on the geometry. This is a standard assumption in modeling displacements in porous media (e.g. see [13, 36, 37, 49, 50]).

2. The pressure in the gas phase is spatially uniform. Given the small value of the gas viscosity compared to that of the liquid, this assumption is expected to be valid even at relatively large drying rates.

3. The transport in the gas phase is by quasi-static diffusion only. Under certain conditions that favor large drying rates (for example, elevated temperatures), convection in the gas phase can be important. To infer its effect, however, the momentum balance in the gas phase needs to be considered. An extensive account of the more general problem using pore-network simulation will be considered in a separate study.

As inferred from the linearized stability analysis above, in the absence of capillarity, the front would be piston-like, with some local roughness. Capillarity will keep interfaces, otherwise favored to grow by diffusion, pinned in place, until their capillary pressure barrier is exceeded. The characteristic length over which percolation rules apply and the pattern is of the IP type is estimated below.

Consider drying in a pore-network of lateral extent L. We will denote the dimensionless mean position of the front by $X_f(t)$ and its width by $\sigma_{ft}(t)$, or by $\sigma_f(t)$, where after sufficiently large time $\sigma_{ft}(t)$ $(or\ \ \sigma_f(t)) \ll X_f(t)$. Here, lengths have been dimensionalized using the pore length l, subscript ft indicates front tail in 3-D and subscript f indicates front in 2-D geometries (e.g. see Gouyet et al. [24], for the difference in the two geometries). Contrary to the case of a 2-D square lattice, to be discussed below, here both phases can be continuous simultaneously.

If we were to neglect any viscous pressure drop in the liquid phase, the capillary pressure, hence the percolation probability p, on the front would be spatially constant (the percolation probability being equal to the percolation threshold, $p = p_c$, where, for 3-D cubic lattices, $p_c = 0.25$ and for 2-D square lattices, $p_c = 0.5$). Due to the capillary pumping mechanism described earlier, however, the capillary pressure, hence the percolation probability, will vary spatially. For a constant gas pressure, the characteristic variation $|\Delta P_c|$ across the front is related to that of the liquid pressure, namely

$$|\Delta P_c| = |\Delta P_l| \tag{31}$$

Because the flow of the liquid in a pore-network can be described by Poiseuille's law, and the displaced phase is continuous, then,

$$|\Delta P_l| \sim \frac{u_D \mu_l \sigma_{ft} l}{k} \tag{32}$$

where we introduced the characteristic velocity u_D and the permeability k (which scales approximately as l^2). The characteristic velocity u_D is due to diffusion, and to a first approximation,

$$u_D \sim \frac{\mathcal{D}_{AB} M_A c}{\rho_l} \left|\frac{\partial x_A}{\partial n}\right| \sim \frac{\mathcal{D}_{AB} M_A c x_{Ae}}{\rho_l l X_f} \tag{33}$$

where we estimated concentration gradients in the gas phase by their base-state values. Substitution into (31) gives the following result for the variation of P_c in the front region

$$|\Delta P_c| \sim \frac{\mathcal{D}_{AB} M_A c x_{Ae} \mu_l}{\rho_l l^2} \frac{\sigma_{ft}}{X_f} \tag{34}$$

Equations (32)-(34) are order of magnitude estimates. Determining the exact pressure and concentration fields requires the solution of flow and transport problems in a disordered pore network, which are coupled at the front according to (15), with $v_n = 0$ for all CE pores and with $u_n = \frac{\sum_f u_n}{N_f}$, for the single PE pore, where the sum is over all N_f CE pores at the front. The development of such a simulator is currently in progress [51]. Nonetheless, order of magnitude estimates are useful for obtaining scaling relations.

Consider, now, the variation of the percolation probability in the front region, which will be affected by the variation of P_c. The two are related as follows

$$|\Delta P_c| \sim \frac{2\gamma\Sigma}{r_m} |\Delta p| \tag{35}$$

where Σ is the dimensionless variance of the pore size distribution, $\alpha(r)$, and r_m is a characteristic pore size. In the derivation of (35) we made use of the results $P_c = \frac{2\gamma}{r}$ and $p = \int_r^\infty \alpha(r) dr$. Use of (35) in (34) and substituting $r_m \sim l$ gives the following expression for the variation of p

$$|\Delta p| \sim \frac{Ca_D}{2\Sigma} \frac{\sigma_{ft}}{X_f} \tag{36}$$

where we introduced a diffusion-based capillary number $Ca_D = \frac{\mathcal{D}_{AB} M_A \mu_l c x_{Ae}}{\gamma l \rho_l}$. This capillary number includes the supersaturation $C_e = c x_{Ae}$, which drives the drying process, leading to the characteristic velocity $\frac{\mathcal{D}_{AB}}{l} \sim \frac{\mathcal{D}_{AB}}{\sqrt{k}}$. A similar diffusion-based capillary number was used in the related phase change problem involving bubble growth by Li and Yortsos [36, 37], and Satik and Yortsos [41]. This reflects the fact that drying is internally driven and differentiates the process from external injection.

The final step for determining σ_{ft} makes use of a self-consistency argument, similar to IPG. As the process in the frontal region is in the percolation regime, then p must follow the percolation scaling [24]

$$|p - p_c| \sim \sigma_{ft}^{-\frac{1}{\nu}} \tag{37}$$

Substitution of (37) in (36) gives the final scaling result

$$\sigma_{ft} \sim \left(\frac{2\Sigma X_f}{Ca_D} \right)^{\frac{\nu}{1+\nu}} \tag{38}$$

This equation sets the length scale at the front over which the IP pattern is valid. By definition, this length scale coincides with the front-tail width. The scaling is identical to that in IPSG, provided that the Bond number is identified as $B = \frac{Ca_D}{2\Sigma X_f}$. According to (38), the front width increases as the capillary number decreases, as the front position increases (namely as the drying rates slow down), or as the disorder in the medium increases. Thus, wider fronts are expected for higher values in the interfacial tension, smaller liquid viscosities

and larger drying times. Given that the velocity of the front, v_f, is inversely proportional to its mean position (recall the base-state scaling $X_f \sim \sqrt{t}$), we further rewrite (38) as

$$\sigma_{ft} \sim \left(\frac{2\Sigma}{v_f Ca_D}\right)^{\frac{\nu}{1+\nu}} \tag{39}$$

This expression will be used below for a comparison with the experimental data. Finally, it is worth noting that the exponent found is identical to Lenormand's [49] for the delineation of the percolation limit in the drainage of a viscous fluid, even though the two problems are actually quite different.

We summarize this section as follows: During drying the frontal region consists of a front of a finite width, σ_{ft}. Within the front, the displacement has the fractal properties of an IP interface. Upstream of the front, however, the displacement is compact. Therefore, the process can be approximated as IPSG. Xu et al. [34] show how various properties of the front during displacement processes can be approximated by simple versions of IPSG. The scaling of the width of the front is given by (38), thus the front width is predicted to increase with increasing distance from the boundary. As in other problems, where growth is controlled internally, namely by diffusion within one of the two phases, the appropriate capillary number is based on the diffusive strength and the supersaturation applied. Typical values obtained fall within the range of external drainage in porous media.

COMPARISON WITH EXPERIMENTS

To check the validity of the theory we used the experimental results of Shaw [1]. These experiments were conducted in a Hele-Shaw cell of thickness 15-20 μm, packed with glass beads of size 0.5 μm. We estimate that the cell consisted of 30-40 bead layers, thus pertaining effectively to a 3-D geometry. The experimental configuration is similar to that studied theoretically above, with one side of the model open to purge the drying liquid, while all other sides were impermeable to flow. For these experimental conditions we estimated that Ca_D is of the order of 10^{-8}. Figure 9 reprinted from Shaw [1] shows in logarithmic coordinates the scaling of the front width with the front velocity. The least-squares fit to the data gives a straight line with slope -0.48 $\pm$ 0.1. Compared to the theoretical equation (39), which also predicts a straight line with slope -0.47 for 3-D and -0.57 for 2-D, the agreement is, at first glance, quite good. However, a more careful comparison shows that this cannot be considered conclusive. Given that the front width in Shaw's experiments is several times larger than the spacing of the cell, it is likely that the pattern development is quenched along the third dimension, and that the experiment is effectively in a 2-D geometry. Under such conditions, the agreement is not as strong. Furthermore the 3-D scaling was developed for the front tail width, σ_{ft}, where the pattern is fractal, which may not be the same quantity experimentally measured. Thus, even under the assumption of a 3-D pattern, theoretical predictions and experimental results may actually pertain to two different quantities (different definitions of front width). For these reasons, although compatible with the experiments, the theory presented cannot be conclusively confirmed from these experiments.

Shaw [1] used Wilkinson's [28] theory for external drainage to interpret the experimental results. As discussed in a previous section, this power law has the dependence shown in (4)

with an exponent that equals -0.38 or -0.25 in 2-D or 3-D, respectively. We believe, however, that the immiscible, external drainage theory is actually not relevant to the present problem, which as explained above is driven by diffusion in the gas phase, and where the corresponding viscous pressure drop is in the displaced wetting phase. By contrast, scaling (4) reflects the stabilizing effect of viscous forces occuring in the *displacing* phase (which here is the relatively non-viscous gas phase, thus leading to an apparent contradiction) (see also Xu et al. [34]). The inadequacy of equation (4) was recognized by Shaw [1] who subsequently proposed a different power law similar to (39), without, however, elaborating on the mass transfer aspects of the problem.

IMPLICATIONS FOR A MACROSCOPIC DESCRIPTION

The previous section described the structure of the frontal region, which because of its percolation and fractal characteristics requires a local analysis. In the upstream regimes, however, a macroscopic description is possible. The elements of this description are discussed below.

Consider, first, the pattern upstream of the front. The discussion will be restricted to 3-D geometries, where flow in this regime is bicontinuous. Immediately adjacent to the front, there exists a bi-continuous region upstream of the leading edge, where the pattern is locally IP, except that now the process is above the percolation threshold, as an increasing number of smaller-size throats have been invaded. Assuming sufficiently small slope in the liquid saturation profile, volume-averaged quantities can be defined, hence we can postulate a continuous description in this region. The analogous problem for drainage processes was studied in Xu et al. [34]. Using transverse averages, the mass balance on the liquid reads as

$$\rho_l \left[\phi \frac{\partial S_l}{\partial t} + \frac{\partial q_{l,z}}{\partial z} \right] = -\mathcal{R} \tag{40}$$

where the liquid flow rate, $q_{l,z}$, is expressed using a generalized Darcy's law

$$q_{l,z} = -\frac{k k_{r,l}(S_l)}{\mu_l} \frac{\partial P_l}{\partial z} \tag{41}$$

involving the relative permeability function $k_{r,l}(S_l)$. The liquid pressure is related to the capillary pressure function, $P_c(S_l)$, via

$$P_l = P_v - P_c(S_l) \tag{42}$$

The two functions $k_{r,l}(S_l)$ and $P_c(S_l)$ correspond to primary drainage, and they can be computed in a straightforward fashion using IP. The rate of evaporation, $\mathcal{R} \equiv \frac{\mathcal{D}_{AB} M_{Ac}}{V} \int_{\mathcal{A}_{lg}} \frac{\partial x_A}{\partial n} dA$, expresses the net mass transfer from the liquid to the gas phase, occuring over the gas-liquid interfacial area $\mathcal{A}_{lg}$, where V is volume and $\mathbf{n}$ is the unit normal to the interface pointing towards the liquid. In the dilute-limit approximation considered here, this process is linear with respect to the concentrations, thus we may further take

$$\mathcal{R} = \frac{\mathcal{D}_{AB} M_{Ac}}{l^2} (x_{Ae} - x_{Ag}) G(S_l) \tag{43}$$

where x_{Ag} is the transverse average of the mole fraction in the gas phase. Because the pattern of all interfaces is still dictated by IP (although here it is above the percolation threshold), the effective gas-liquid area and the dimensionless scaling function $G(S_l)$ can be computed by solving a quasistatic diffusion problem around a percolation cluster. The results of this study will be reported elsewhere. We expect, however, that G has a non-monotonic dependence, vanishing both near the front (where $S_l \to 1$) and far upstream of the front (where S_l approaches zero).

The system of equation (40)-(43) is completed with a mass balance for the volatile component in the gas phase. In the dilute limit, the overall mass balance reads

$$\phi \frac{\partial S_g}{\partial t} + \frac{\partial q_{g,z}}{\partial z} = 0 \tag{44}$$

while the mass balance for the volatile component becomes

$$\phi S_g \frac{\partial x_{Ag}}{\partial t} + q_{g,z} \frac{\partial x_{Ag}}{\partial z} = \frac{\partial}{\partial z} \left(\mathcal{D}(S_l) \frac{\partial x_{Ag}}{\partial z} \right) + \frac{\mathcal{R}}{c} \tag{45}$$

where the diffusion coefficient $\mathcal{D}(S_l)$ is to be computed from a percolation study. The system of equations (40)-(45) can be solved to determine the saturation profiles in the regime of bicontinuous phases.

The regime far upstream of the front consists of disconnected ganglia of the liquid phase. Reasoning as in the scaling analysis for the front, we can conclude that their characteristic size has the same scaling as given for the front, namely equation (38), where now X_f denotes the average location of these stationary ganglia. The description of this problem can still be obtained with the above equations (40)-(45), except that the liquid velocity must now be set to zero. These problems are currently under study.

CONCLUSIONS

In this paper we used concepts of immiscible displacements in porous media driven by mass transfer to model certain aspects of drying of porous media. Visualization experiments of drying in 2-D glass micromodels were conducted to identify mechanisms concerning the motion of gas-liquid interfaces at the pore-scale. Then, a pore network approach was introduced, utilizing arguments from isothermal drainage, particularly Invasion Percolation in a Stabilizing Gradient (IPSG), and from the related bubble growth problem.

A specific objective of this work was the analysis of the frontal region separating the initial liquid from the upstream two-phase region. A linear stability analysis in an effective porous medium, in the absence of capillarity or microstructure, showed that planar drying fronts are stable due to diffusion in the gas phase. For a porous medium with a microstructure, however, capillarity induces a viscous flow, termed in other contexts as "capillary pumping". The developing pressure gradients effectively limit the extent of the front, which would otherwise be of the percolation type, to a finite width. In conjuction with the prediction of a macroscale stable front, capillarity, diffusion and viscous effects result in a process similar to Invasion Percolation in a Stabilizing Gradient (IPSG). A power-law scaling relation of the front width with a diffusion-based capillary number was then developed. This capillary number reflects the fact that the process is internally driven due to diffusion, as in bubble

growth problems but in contrast to external drainage. The scaling exponent predicted was found to be consistent with the experiments of Shaw [1], although a conclusive proof was not obtained. A continuum description was also developed for the regimes upstream of the front, the detailed analysis of which will be reported in a separate study.

ACKNOWLEDGMENTS

The research of SP, AKS and NK was partially funded by the JOULE Programme of the European Commission (Contract JOF3-CT95-0008). We would also like to acknowledge the help of N. Konstantinou and G. Petrou of NCRS "Demokritos" in the micromodel tests.

References

[1] T.M. Shaw, *Phys. Rev. Lett.*, **59,** 1671-1674 (1987).

[2] P. Chen, and D.C.T. Pei, *Int. J. Heat Mass Transfer*, **32,** 297-310 (1989).

[3] W.T. Simpson,*Drying Technology,* **2,** 235-264 (1983).

[4] W.T. Simpson, *Drying Technology,* **3,** 353-368 (1984).

[5] M. Fortes, and M.R. Okos, In *Advances in Drying,* **1,** 119-154, (Hemisphere Publishing, New York, 1980).

[6] C.K. Ho, and K.S. Udell, *Int. J. Heat Mass Transfer*, **38,** 339-350 (1995).

[7] J.F Le Romancer, D. Defives, F. Kalaydjian, and G. Fernades, Paper presented at the IEA Collaborative Project on Enhanced Oil Recovery Workshop and Symposium, Bergen, Norway, 28-31 August (1994).

[8] Y. Le Gallo, J.F. Le Romancer, B. Bourbiaux, and G. Fernandes, SPE 38924, SPE Meeting, San Antonio (Oct. 5-8, 1997).

[9] K.M. Waananen, J.B. Litchfield, and M.R. Okos, *Drying Technology*, **11,** 1-40 (1993).

[10] M. Prat, *Drying Technology*, **9,** 1181-1208 (1991).

[11] A.V. Luikov, A.V., *Heat and Mass Transfer in Capillary Porous Bodies,* (Pergamon Press, London, 1966).

[12] S. Whitaker, In *Advances in Heat Transfer,* **13,** 119-203, (Academic Press, New York, 1977).

[13] S.C. Nowicki, H.T. Davis, and L.E. Scriven, *Drying Technology*, **10,** 925-946 (1992).

[14] M. Prat, M., *Int. J. Multiphase Flow*, **19,** 691-704 (1993).

[15] M. Prat, *Int. J. Multiphase Flow*, **21,** 875-892 (1995).

[16] J.M. Laurindo, and M. Prat, *Chem. Eng. Sci.*, **51,** 5171-5185 (1996).

[17] J.M. Laurindo, and M. Prat, *Chem. Eng. Sci.*, **53,** 2257-2269 (1998).

[18] V. Pot, C. Appert, A. Melayah, D.H. Rothman, and S. Zaleski, *J. Phys. II (France)*, **6,** 1517-1534 (1996).

[19] D. Wilkinson, and J.F. Willemsen *J Phys. A,* **16,** 3365-3376 (1983).

[20] J. Feder, *Fractals,* (Plenum, New York, 1988).

[21] D. Wilkinson, *Phys. Rev. A,* **30,** 520-531 (1984).

[22] B. Sapoval, M. Rosso, and J.F. Gouyet, *J. Physique Lett.,* **46,** L149-L156 (1985).

[23] J.P. Hulin, E. Clement, C. Baudet, J.F. Gouyet, and M. Rosso, *Phys. Rev. Lett.,* **61,** 333-336 (1988).

[24] J.F. Gouyet, M. Rosso, and B. Sapoval, *Phys. Rev. B,* **37,** 1832-1838 (1988).

[25] A. Birovljev, L. Furuberg, J. Feder, T. Jossang, K.J. Maloy, and A. Aharony, *Phys. Rev. Lett.,* **67,** 584-587 (1991).

[26] M. Chaouche, N. Rakotomalala, D. Salin, B. Xu, and Y.C. Yortsos, *Phys. Rev. E,* **49,** 4133-4139 (1994).

[27] A.J. Katz, and A.H. Thompson, *Phys. Rev. B,* **34,** 8179-8181 (1986).

[28] D. Wilkinson, *Phys. Rev. A,* **34,** 1380-1391 (1986).

[29] A.L. Barabasi, and H.F. Stanley, *Fractal Concepts in Surface Growth,* (Cambridge University Press, Cambridge, 1995).

[30] V. Frette, J. Feder, T. Jossang, and P. Meakin, *Phys. Rev. Lett.,* **68,** 3164-3167 (1992).

[31] P. Meakin, J. Feder, V. Frette, and T. Jossang, *Phys. Rev. A,* **46,** 3357-3368 (1992).

[32] P.G. Saffman, and G.I. Taylor, *Proc. Roy. Soc. Lond. A,* **245,** 312-329 (1958).

[33] Y.C. Yortsos, B. Xu, and D. Salin, *Phys. Rev. Lett.,* **79,** 4581-4584 (1997).

[34] B. Xu, Y.C. Yortsos, and D. Salin, *Phys. Rev. E, Phys. Rev. E,* **57,** 739-751 (1998).

[35] D. Stauffer, and A. Aharony, *Introduction to Percolation Theory,* (Taylor and Francis, London, 1992).

[36] X. Li, and Y.C. Yortsos, *AIChE J.*, **41,** 214-222 (1995a).

[37] X. Li, and Y.C. Yortsos, *Chem. Eng. Sci.*, **50,** 1247-1271 (1995b).

[38] C. Satik, and Y.C. Yortsos, *A.S.M.E. Journal of Heat Transfer*, **118,** 155-462 (1995).

[39] J.S. Langer, *Rev. Mod. Phys.*, **52,** 1-28 (1980).

[40] X. Li, and Y.C. Yortsos, *Phys. Fluids*, **6,** 1663-1676 (1994).

[41] C. Satik, X. Li, and Y.C. Yortsos, *Phys. Rev. E*, **51,** 3286-3295 (1995).

[42] J.S. Buckley, *Interfacial Phenomena in Petroleum Recovery,* N.R. Morrow, ed., (Marcel Dekker Inc., New York, 1990).

[43] I. Chatzis, N.R. Morrow, and H.T. Lim, *SPE Journal,* 311-326 (1983).

[44] O. Vizica, and A. Payatakes, *PhysicoChemical Hydrodynamics,* **11,** 187-204 (1989).

[45] C. Jia, K. Shing, and Y.C. Yortsos, *J. Cont. Hydr.*, to appear (1998).

[46] I. Chatzis, PRRC Report No 80-12, New Mexico Institute of Technology (1982).

[47] R. Lenormand, C. Zarcone, and A. Sarr, *J. Fluid Mech.,* **135,** 337-353 (1983).

[48] C.T. Tan, and G.M. Homsy, *Phys. Fluids,* **29,** 3549-3556 (1986).

[49] R. Lenormand, R., *Proc. R. Soc. Lond. A*, **423,** 159-168 (1989).

[50] M. Blunt, and P. King, *Transport in Porous Media*, **6,** 407-443 (1991).

[51] S. Poulou, A.K. Stubos and Y.C. Yortsos, in preparation (1998).

[52] R.B. Bird, W.E. Stewart, and E.L. Lightfoot, *Transport Phenomena,* (Wiley, New York, 1960).

[53] E.L. Cussler, *Diffusion: Mass Transfer in Fluid Systems,* (Cambridge University Press, Cambridge, 1984).

APPENDIX

In this Appendix we consider the base-state for the more general problem that includes unsteady-state diffusion and convection. The condensible component A satisfies the mass balance

$$\frac{\partial c_A}{\partial t} + \nabla \cdot \mathbf{N}_A = 0 \tag{A-1}$$

where $\mathbf{N}_A$ is its molar flux, expressed for a binary mixture as

$$\mathbf{N}_A = -c\mathcal{D}_{AB}\nabla x_A + x_A(\mathbf{N}_A + \mathbf{N}_B) \tag{A-2}$$

Here, c_A is the molar concentration, x_A is the molar fraction of A ($c_A = cx_A$), and $\mathbf{N}_B$ is the molar flux of the non-condensible species. The latter is also conserved

$$\frac{\partial c_B}{\partial t} + \nabla \cdot \mathbf{N}_B = 0 \tag{A-3}$$

The corresponding boundary conditions read

$$x_A = 0 \quad \text{at} \quad z = 0 \tag{A-4}$$

and

$$x_A \equiv x_{Ae} = \frac{P_{vA}(T)}{P_v} \quad \text{at} \quad z = F(y,t) \tag{A-5}$$

at the inlet and the front, respectively. The equilibrium vapor pressure P_{vA} is a function of temperature, among other factors.

For a porous medium, the mass-averaged velocity in the gas phase, $\mathbf{u}_v = \frac{M_A \mathbf{N}_A + M_B \mathbf{N}_B}{\rho_A + \rho_B}$, satisfies Darcy's law

$$\mathbf{u}_v = -\frac{k}{\mu_v} \nabla P_v \tag{A-6}$$

where M denotes molecular weight. Because of the small gas viscosity, however, the gas pressure can be assumed constant, which for isothermal conditions also implies a constant molar concentration c. Note also, that from (A-6) and the definition of the mass-averaged velocity we have the general relation

$$\nabla \times \mathbf{u}_v = \mathbf{0} \tag{A-7}$$

This can be used in the more general case where 2-D concentration and pressure fields must be evaluated. Concentration and pressure fields are coupled at the interface by mass balances. For the vaporizing liquid,

$$j_{An} \equiv M_A N_{An} - \rho_{Ae} v_n = \rho_l (u_{ln} - v_n) \quad \text{at} \quad z = F(y,t) \tag{A-8}$$

while for the non-condensible component B

$$j_{Bn} \equiv M_B N_{Bn} - \rho_{Be} v_n = 0 \quad \text{at} \quad z = F(y,t) \tag{A-9}$$

where $\mathbf{j}$ is the mass flux, v_n is the velocity of the receding interface, ρ_l is the mass density of the liquid and ρ_{Ae} and ρ_{Be} denote mass density of species A or B in the gas phase at equilibrium, thus $\rho_{Ae} = x_{Ae} c M_A$.

Consider, now, the base state in the absence of perturbations (denoted by superscript bar). Then, all fluxes are along the z direction only, the front is located at $z = f(t)$ and the base state is described as follows. The base-state liquid pressure corresponds to a stagnant liquid

$$\bar{P}_l = P_v \quad \text{for} \quad f(t) < z < L \tag{A-10}$$

the base-state fluxes are

$$\bar{N}_{Az} \approx -\frac{\rho_l}{M_A} v_z \quad \text{and} \quad \bar{N}_{Bz} = \frac{\rho_{Be}}{M_B} v_z \tag{A-11}$$

where we implied $\rho_{Ae} \ll \rho_l$, while the mole fraction is given from

$$\bar{N}_{Az} = -c\mathcal{D}_{AB}\frac{d\bar{x}_A}{dz} + \bar{x}_A(\bar{N}_{Az} + \bar{N}_{Bz}) \tag{A-12}$$

To solve the unsteady-state problem we take the *ansatz* that the front position is proportional to the square root of time,

$$f(t) = 2\lambda\sqrt{\mathcal{D}_{AB}t} \tag{A-13}$$

where λ is a dimensionless parameter to be determined. Noting that for constant c, the total molar flux is constant

$$N_{Az} + N_{Bz} = \rho_l \dot{f}\left[\frac{\rho_{Be}}{\rho_l M_B} - \frac{1}{M_A}\right] \tag{A-14}$$

the mass balance for species A, equation (A-1) reads

$$c\frac{\partial x_A}{\partial t} + \rho_l \dot{f}\left[\frac{\rho_{Be}}{\rho_l M_B} - \frac{1}{M_A}\right]\frac{\partial x_A}{\partial z} = c\mathcal{D}_{AB}\frac{\partial^2 x_A}{\partial z^2} \tag{A-15}$$

where we made use of (A-11), dot denotes derivative with respect to time and we evaluated v_z at $z = f(t)$. We will seek the solution of this problem using the similarity variable $\eta = \frac{z}{2\sqrt{\mathcal{D}_{AB}t}}$. Then, equation (A-15) becomes

$$x'' + 2x'(\eta - \phi) = 0 \tag{A-16}$$

where primes denote derivative with respect to η and we defined

$$\phi = \lambda\frac{\rho_l}{c}\left[\frac{\rho_{Be}}{\rho_l M_B} - \frac{1}{M_A}\right] \tag{A-17}$$

This equation is to be solved subject to the boundary conditions

$$x_A = x_{Ae} \quad \text{at} \quad \eta = \lambda \tag{A-18}$$

and

$$x_A = 0 \quad \text{at} \quad \eta = 0 \tag{A-19}$$

Note that because the integration interval here is $0 < z < f(t)$ and $f(0) = 0$, there is no need to satisfy an initial condition, in contrast to the problems considered by Bird et al. [52] and Cussler [53]. The latter authors solved a similar problem, except that they made the assumptions of a fixed interface [52] or of a vanishing flux for species B [53].

The solution of (A-16)-(A-19) is

$$x_A = x_{Ae}\frac{\mathrm{erf}(\eta - \phi) + \mathrm{erf}\phi}{\mathrm{erf}(\lambda - \phi) + \mathrm{erf}\phi} \tag{A-20}$$

The unknown parameter λ is obtained by substitution of this solution in the first equation of (A-11). After some manipulations, we find that λ solves the transcendental equation

$$\lambda\left[1+x_{Ae}\left(\frac{M_A}{M_B}\frac{\rho_{Be}}{\rho_l}-1\right)\right]=\frac{cx_{Ae}M_A\exp(-(\lambda-\phi)^2)}{\sqrt{\pi}\rho_l(\mathrm{erf}(\lambda-\phi)+\mathrm{erf}\phi)} \tag{A-21}$$

In (A-21), it must be recalled that ϕ is proportional to λ (see equation (A-17). Equation (A-21) shows that the front grows proportionally to the square root of time, as expected. Of interest is the dilute limit $|x_{Ae}\left(\frac{M_A}{M_B}\frac{\rho_{Be}}{\rho_l}-1\right)|\ll 1$, considered in the main text, in which case $\lambda \ll 1$ and (A-21) gives

$$\lambda^2=\frac{x_{Ae}cM_A}{2\rho_l} \tag{A-22}$$

which when inserted in (A-13) gives

$$f=\sqrt{\frac{2c\mathcal{D}_{AB}M_Ax_{Ae}}{\rho_l}t} \tag{A-23}$$

which is the equation in the text. In this limit, the convective term vanishes and the concentration field is quasistatic (namely it satisfies a Laplace equation, the base-state profile for the mole fraction being linear).

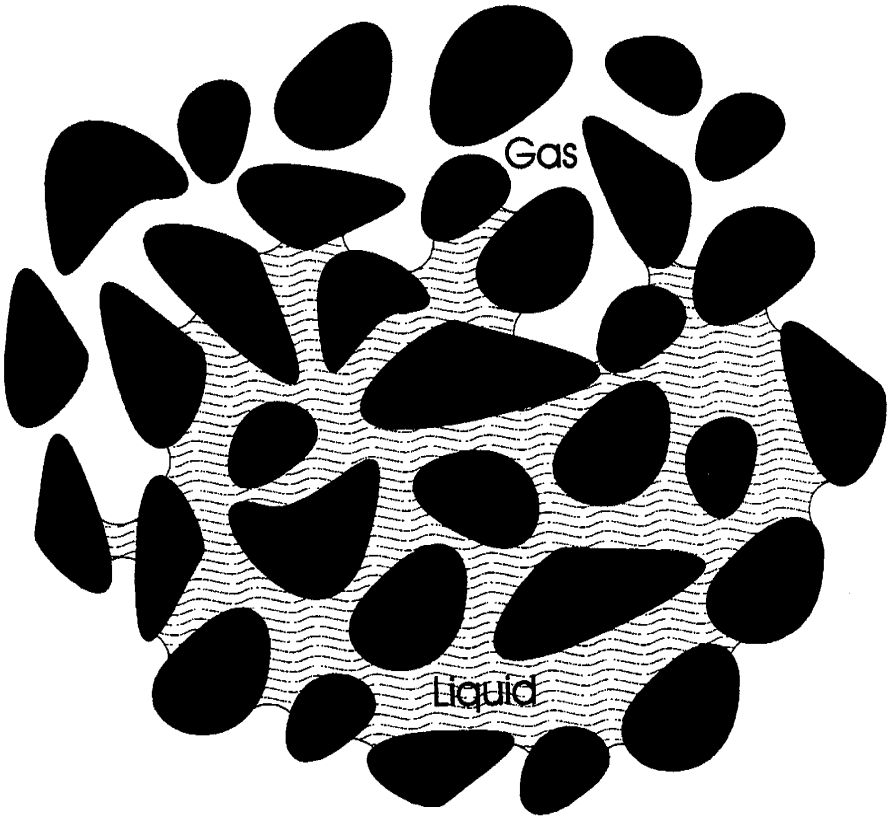

Figure 1: Schematic of liquid-gas interfaces during drying in porous media.

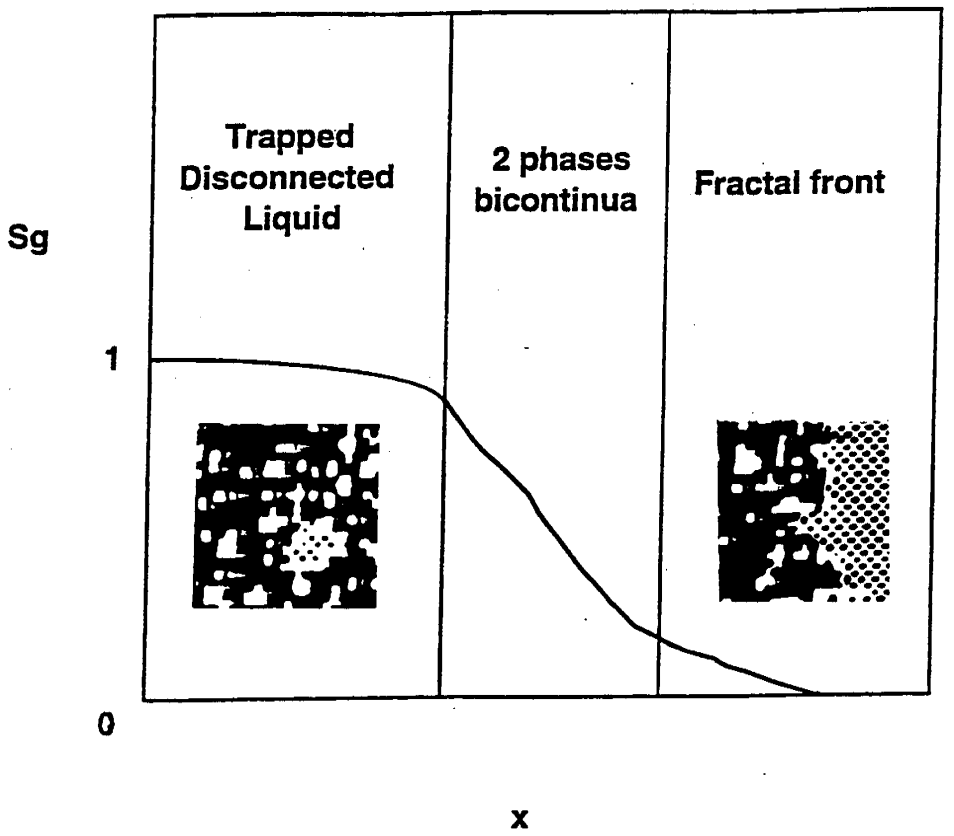

Figure 2: Schematic description of drying regimes in porous media, obtained from 2-D pore network simulations. Dots and white areas denote liquid-occupied regions, dark shaded areas denote gas-occupied regions. (Due the 2-D topological limitations a schematic of the 2-Phase biconntinua regime is not feasible).

(a)

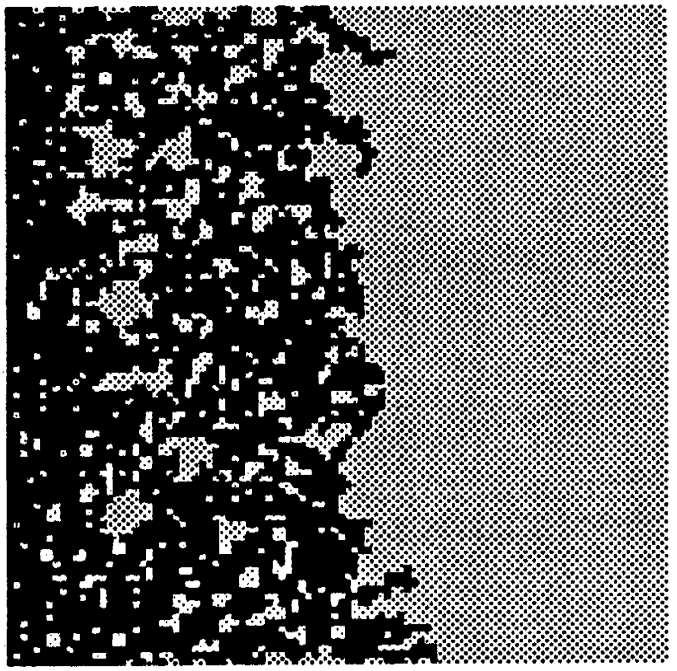

(b)

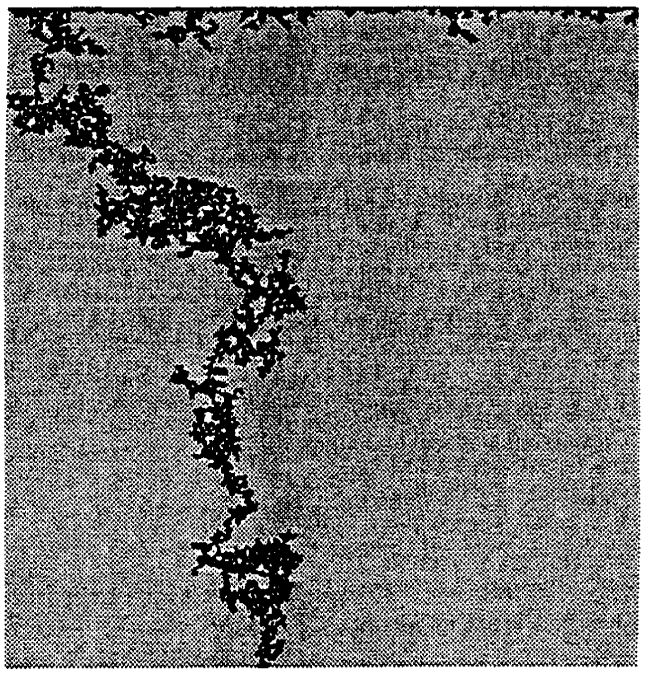

Figure 3: a. Self-affine front during extairnal drainage indicating an Invasion Percolation in a Stabilizing Gradient (IPSG) process. b. Single finger in extairnal drainage indicating an Invasion Percolation in a Destabilizing Gradient (IPDG) process.

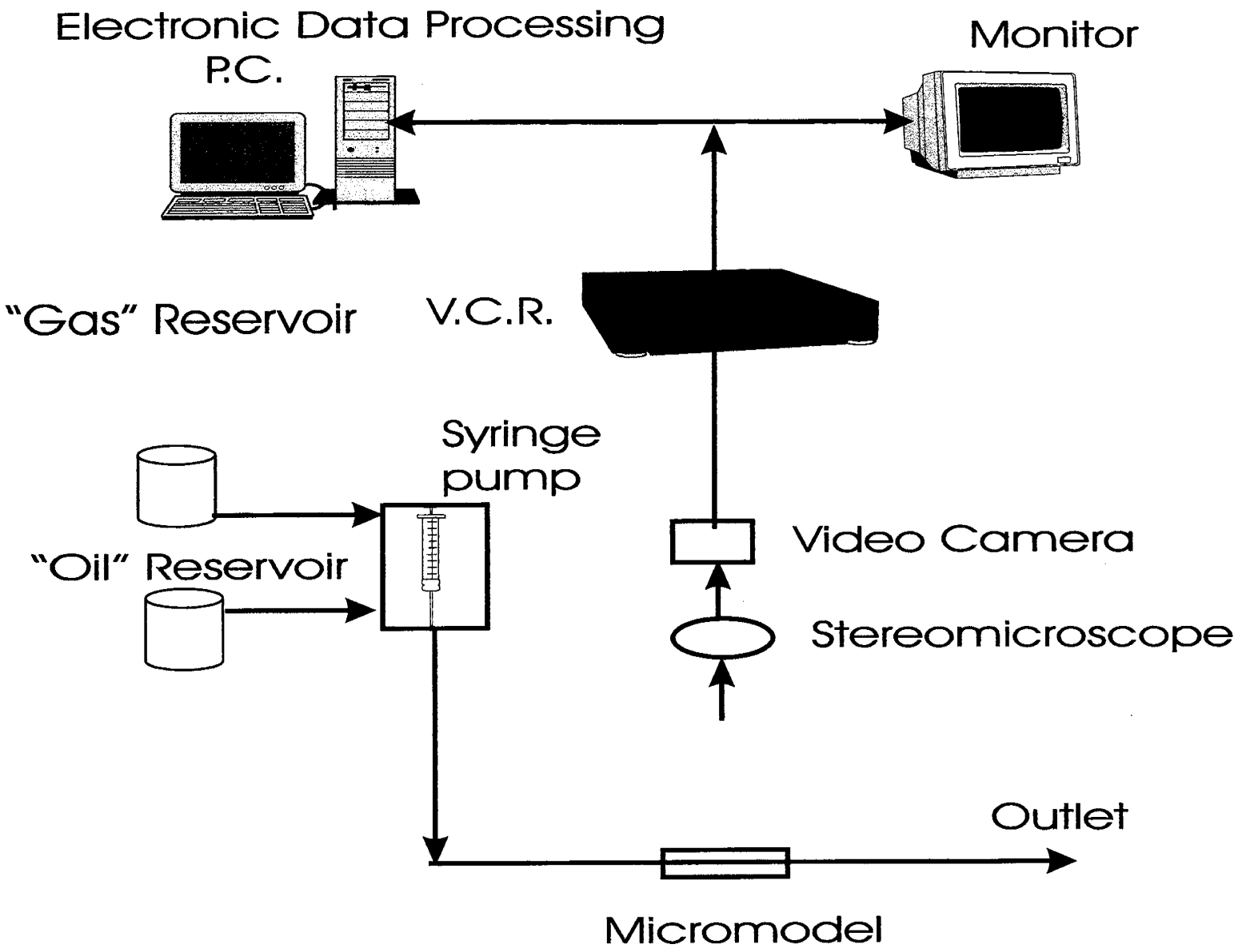

Figure 4: Schematic of the experimental apparatus.

(a)

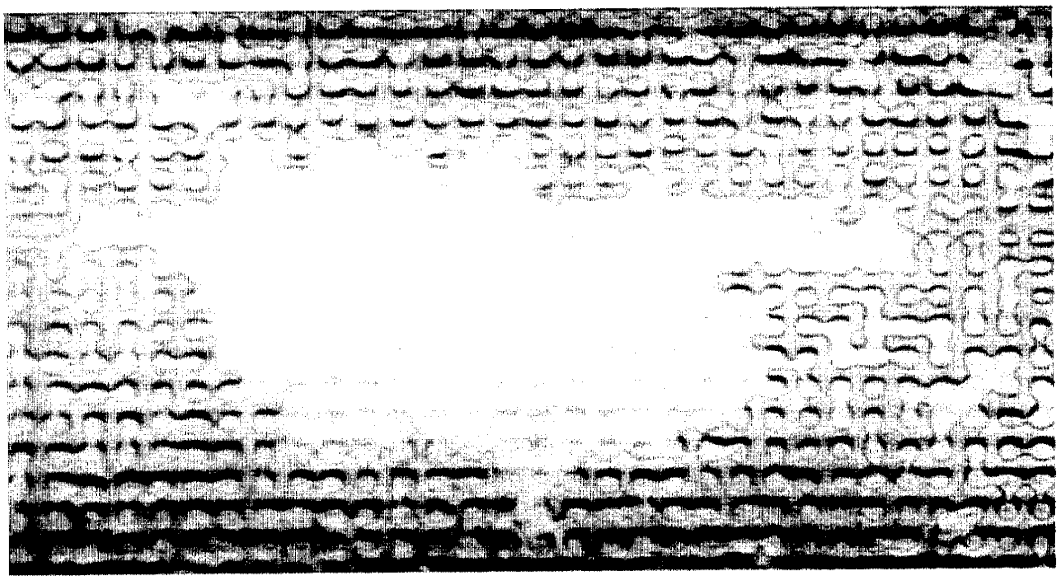

(b)

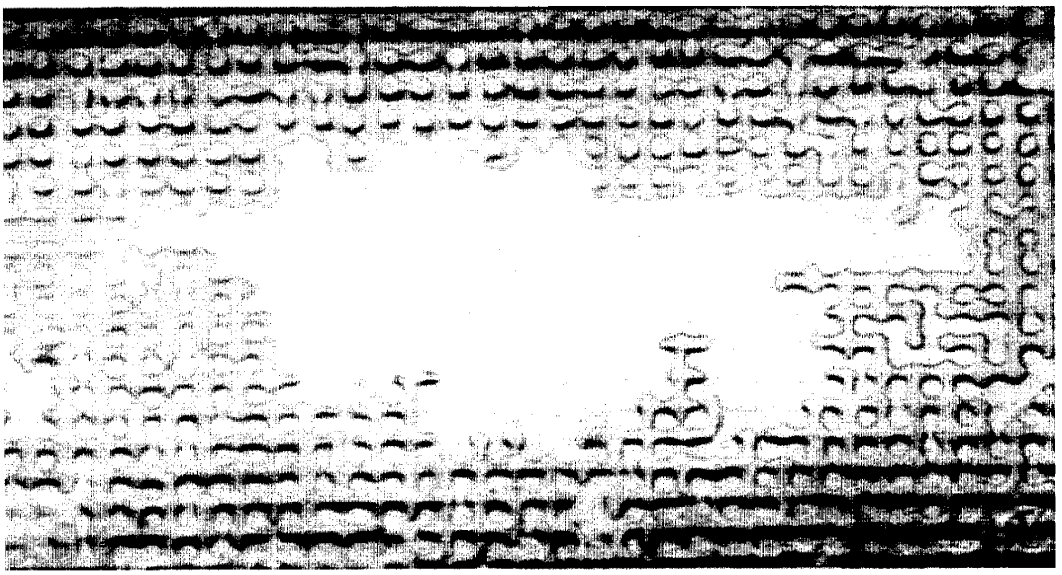

Figure 5: Two different snapshots (5a and 5b) of the interfacial patterns at two different times from the micromodel experiments. (system: air/n-hexane).

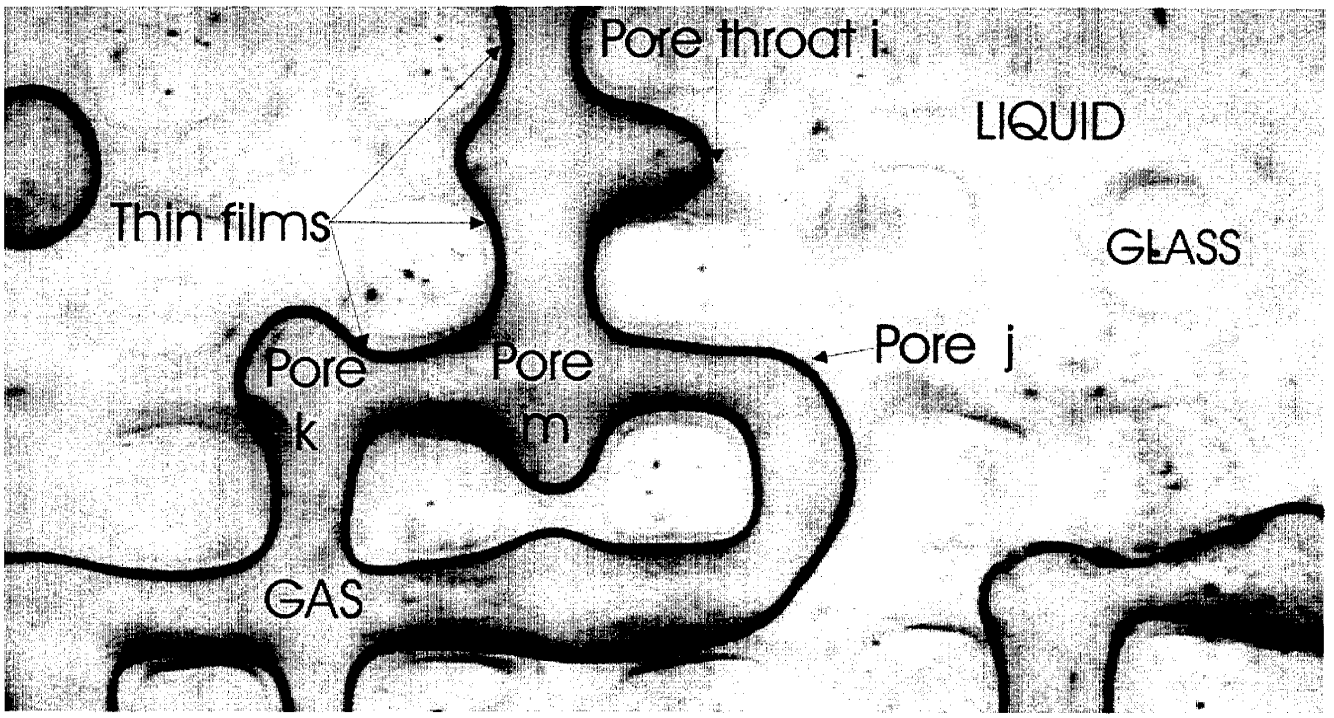

Figure 6: Close-up of the gas-liquid interface during drying in the micromodel experiments.

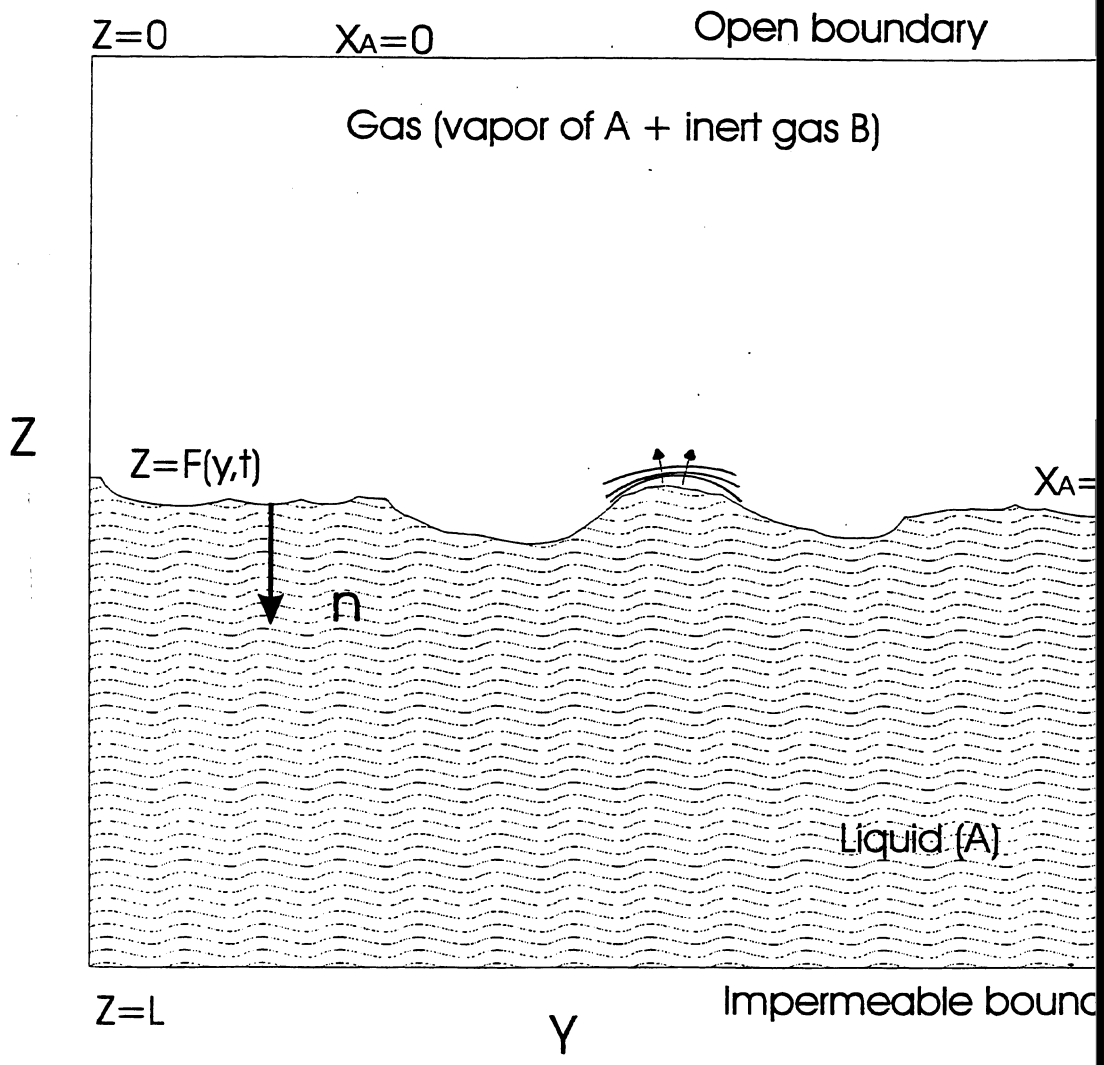

Figure 7: A schematic of the planar drying front geometries for the stability analy in an effective porous medium. Near the indicated protuberance, concentration the gas phase are compressed leading to enhanced mass transfer, hence to sta the protuberance.

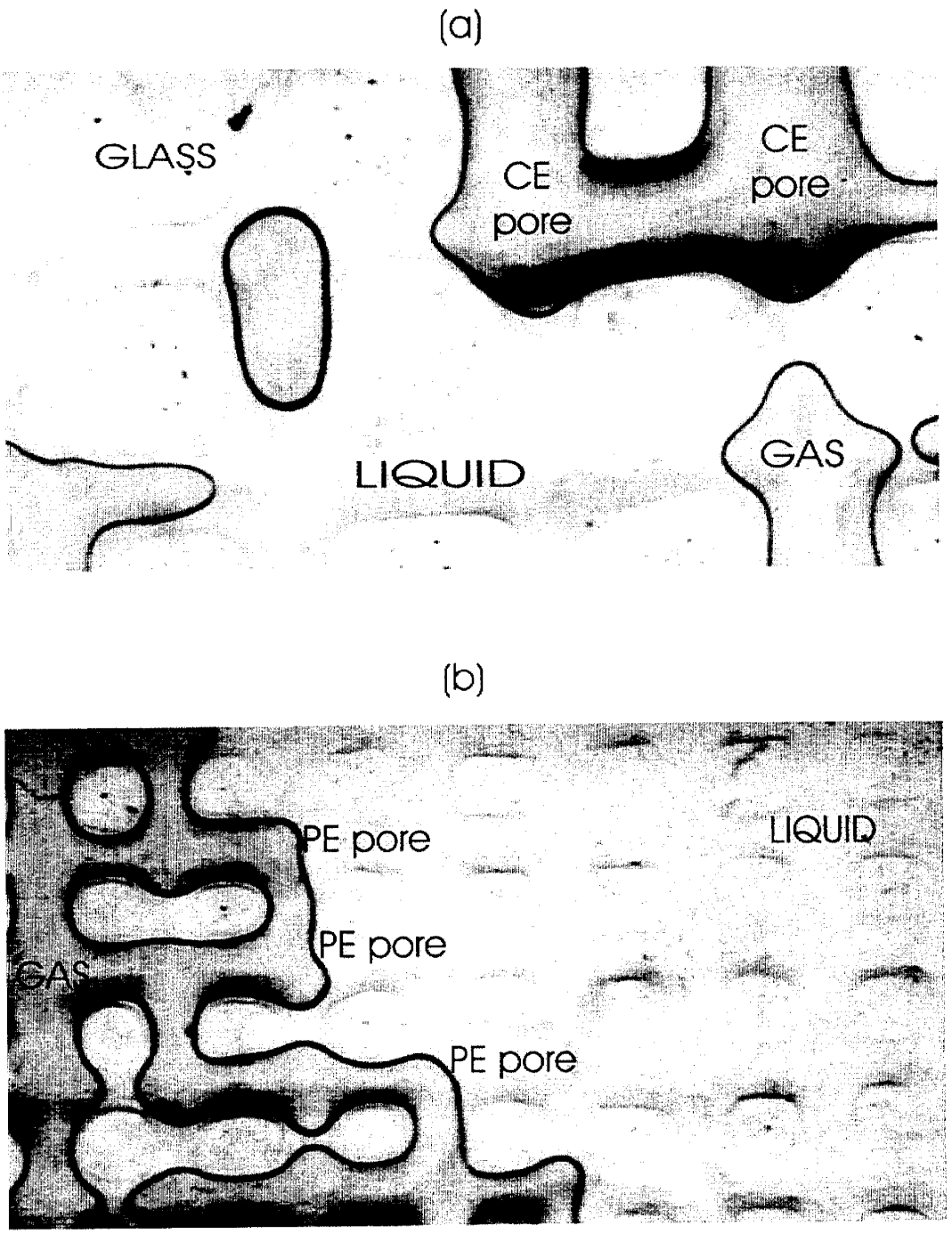

Figure 8: Experimental visualization of two different types of pores during drying: a) Completly Empty (CE) pores, b) Partly Empty (PE) pores.

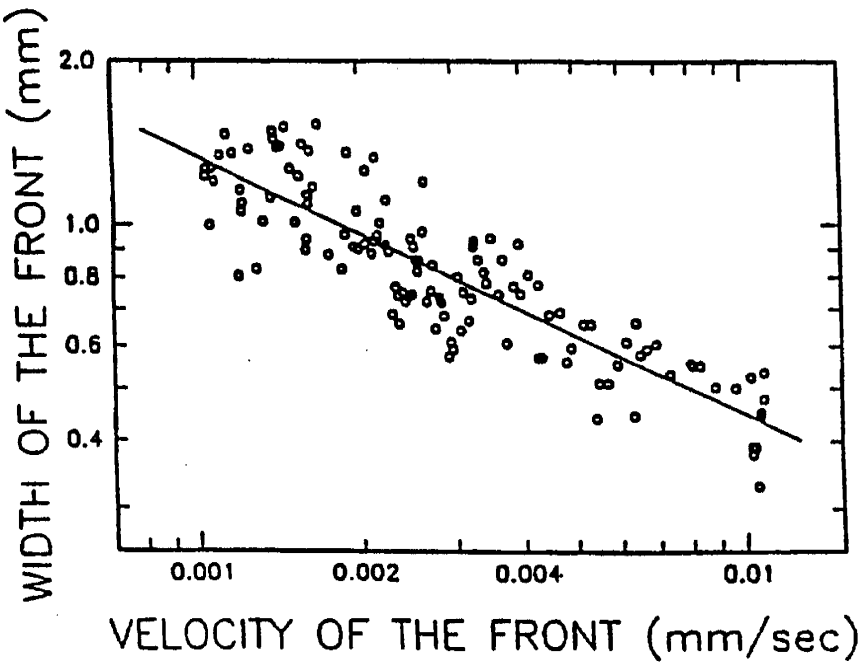

Figure 9: Variation of the width of the drying front with its average velocity. A least-squares fit to the data gives an exponent of -0.48 $\pm$ 0.1.

4. PHASE DIAGRAM OF FULLY DEVELOPED DRAINAGE: A STUDY OF THE VALIDITY OF THE BUCKLEY-LEVERETT EQUATION

Y.C. Yortsos and B. Xu
(and with the collaboration of D. Salin)

ABSTRACT

Despite the significant progress made in recent years, a fundamental understanding of immiscible displacements at the macroscale is lacking. In this paper we use a version of percolation theory, based on Invasion Percolation in a Gradient, to connect drainage processes at the pore-network scale with the displacement at the macroscale. When the mobility ratio M is sufficiently small, the displacement is stabilized and can be described by Invasion Percolation in a Stabilizing Gradient. In the opposite case, the displacement has common features with Invasion Percolation in a Destabilizing Gradient. A phase diagram of fully developed drainage is then developed. The transition between stabilized displacement and fingering is controlled by the change of the sign of the gradient of the percolation probability, and the transition boundary is described by a scaling law involving the capillary number and the viscosity ratio. The theory is subsequently extended to correlated pore networks and a phase diagram involving the correlation length λ is constructed. As the regimes of stabilized displacement are also those for which conventional theories (such as the Buckley-Leverett equation) apply, the phase diagram helps to delineate their validity.

INTRODUCTION

The mathematical description of immiscible displacements in porous media is based on a classical methodology developed several decades ago (for example, see Collins, 1961). This is founded on two postulates: that capillary equilibrium betwen the fluids exists to relate their pressure difference to saturation-dependent capillary pressure functions, and that saturation-dependent relative permeabilities can be defined, which allow extending Darcy's law to multiphase flow (e.g. see Dullien, 1992). The resulting non-linear differential equations have been the subject of extensive discussion and analysis. For one-dimensional flows, in particular, this formulation reduces to the celebrated Buckley-Leverett equation in petroleum engineering, or to the Richards equation in hydrology, respectively. These two equations have been the fundamental building blocks for many developments in the respective fields (e.g. see Bear, 1972, Marle, 1981, Lake, 1989).

A rigorous derivation of this formalism has been attempted by essentially two approaches: Volume-averaging or homogenization, which in principle incorporate pore-scale processes (Whitaker, 1986, Auriault et al., 1989), and pore-network models, where single-pore variation is neglected in favor of a variation at the pore-network scale (see Dullien, 1992). However, neither of these approaches have been shown to be capable, so far, to rigorously lead to the conventional, and widely used, formalism. Homogenization can be usefully applied when the various length scales of the problem are separated. In the context of immiscible displacement, this means that saturation profiles must be sufficiently smooth, a requirement that is equivalent to capillary equilibrium over a sufficiently large length scale. This imposes

a restriction on the magnitude of the capillary number, expressing the relative ratio of viscous to capillary forces. Moreover, the distribution of phases under these conditions must be obtained by methods other than homogenization (for example, one based on Invasion Percolation, see below).

Pore-network models represent a useful alternative to homogenization. However, their main success, so far, has been in providing the distribution of immiscible phases over the pore-network in the absence of viscous forces, namely under conditions of capillary control (e.g. Heiba et al., 1982). In this case, the problem reduces to a generic statistical physics problem, that of percolation. From detailed studies of the various models of Ordinary Percolation (OP) and, particularly, Invasion Percolation (IP), the effect of various parameters, such as the pore size distribution, the network topology, the correlation structure, etc., on flow properties, such as the conductivity (or relative permeability) of a phase, can be obtained (for example, see Heiba et al., 1982, Wilkinson, 1984 and 1986, among other studies). In the presence of viscous forces, where saturation profiles are no longer stationary and involve gradients, simple percolation models are not applicable. A number of pore network models that simulate displacements involving both viscous and capillary forces, have been developed (Lenormand et al., 1988, Blunt and King, 1991, Chaouche et al., 1993). In fact, there are increasing efforts to use pore-network models for the *ab initio* description of immisicible displacements in real porous media, at least at the laboratory scale (see, for example, recent works by Xu et al., 1997, and Oren et al., 1997). However, a connection of these results to the conventional formalism has yet to be established.

We note in passing that similar considerations also apply to the process of scaling up from the macroscopic (differential) scale to a larger (for example, the megascopic or the coarse-grid) scale. Homogenization again presupposes a condition of relatively flat saturation profiles, which can only be attained under conditions of capillary equilibrium. To describe the distribution of phases under such conditions, large-scale versions of percolation theory can be developed, paralleling pore-network models, in which the numerical lattice is mapped into an equivalent pore-network (see Yortsos et al., 1993). Based on this approach, large-scale properties, such as relative permeabilities can be obtained in terms of the permeability distribution. When viscous forces cannot be neglected, however, (and this is increasingly more likely as the scales of interest increase) this approach does not strictly apply. The question of the validity of the traditional description must then be addressed.

The objective of this paper is to describe a methodology for delineating the conditions under which the conventional approach is valid. The methodology is based on a discrete, pore-network decsription and relies on a key premise: that for the conventional continuum model involving differential equations (namely, the Buckley-Leverett model) to be valid, the displacement at the pore-network scale must not be viscous fingering. In our approach, therefore, the distinguishing characteristic of the validity of the conventional model is not that viscous forces are not significant, but rather that they do not lead to viscous fingering at the small scale. Thus, the constraint to be obtained involves not only the capillary number, but the viscosity ratio as well. In some sense, our approach is a form of stability analysis of immiscible displacement at the pore-network scale. Indeed, our results will be compared with conventional stability analyses. The key to the present approach is the recognition that viscous forces lead to a gradient in capillary pressure, which will in turn impart a gradient in the percolation probability, to be defined shortly below. The conventional approach will be

valid, as long as this gradient is negative, in which case it leads to a stabilized displacement at the pore-network scale, as explained in more detail below.

Delineating the conditions for the validity of the Buckley-Leverett model is essentially equivalent to developing a phase diagram of the process in a parameter space involving the capillary number, the mobility ratio and the correlation length. Because it pertains to a fully-developed displacement, however, this phase diagram is different from Lenormand's (1989), who focused on the classification of displacements in square $L \times L$ networks. Lenormand identified three different regimes (see Figure 1), namely Invasion Percolation (IP), Piston-Like Displacement (PL) and Viscous Fingering (VF), which were separated by boundaries that depend on the size L of the network. As the displacement proceeds (namely as L increases), the process is likely to fall in-between these regimes. Our approach, on the other hand, pertains to fully-developed displacement, the boundaries between the regimes to be obtained not involving a length scale, other than the correlation length (in the case of correlated heterogeneity). In some sense, the phase diagram to be obtained characterizes the full transition between IP and PL and IP and VF, respectively, in Lenormand's diagram, as depicted in the arrows $A \rightarrow B$ and $C \rightarrow D$ in Figure 1.

This study will be restricted to primary drainage processes. Extension to imibibition should be possible, following a similar method, but will not be attempted here due to the qualitatively different mechanisms that are possible in the latter (Lenormand, 1990, Blunt, 1997). We will describe the phase diagram in the presence of capillary, viscous and gravity forces for the two cases of uncorrelated and correlated heterogeneity, respectively. This paper, therefore, complements related work in the area published in Yortsos et al. (1997) and Xu et al. (1998), where the elements of this approach were first presented.

The paper is organized as follows: Because of its close relation to the process of Invasion Percolation in a Gradient (IPG), aspects of the latter will be first reviewed briefly. Subsequently, we will present the basic aspects of our approach for an uncorrelated pore network. This part parallels the report of Yortsos et al. (1997). Capillary, viscous and gravity forces will be considered. The effect of gravity is new and is discussed in a separate section. We must note, though, that we will not consider in this study the possibility of gravity override or gravity underrun, and we will restrict the analysis to gravity acting in the direction of displacement only. The case of gravity override requires a more extensive analysis and will be presented elsewhere. The last section presents displacements in a field with correlated heterogeneity, which also constitutes the main contribution of this paper.

BRIEF REVIEW OF IPG

Invasion Percolation in a Gradient (IPG) is IP in a field where the percolation probability p has a spatial gradient (e.g. Gouyet et al., 1988), typically due to a hydrostatic or permeability field, namely

$$\frac{dp}{dx} \sim -B \tag{1}$$

where x is dimensionless distance and B is the Bond number. The latter is related to hydrostatic or permeability gradients through expressions of the type $B = \Delta\rho g_x r_m^2/\gamma$ (Hulin et al., 1988), where $\Delta\rho$ is the density difference, g_x is the acceleration of gravity in the

direction of displacement, r_m is the mean pore size and γ is the interfacial tension, or $B = -d\sqrt{k}/dx$ (Chaouche et al., 1994), where k is the permeability, in the respective cases. If $B > 0$, then p decreases in the direction of displacement, and the latter involves an IP frontal region of finite extent, σ, scaling as (Wilkinson, 1984, Gouyet et al., 1988)

$$\sigma \sim B^{-\frac{\nu}{\nu+1}} \tag{2}$$

The fractal front is followed by a compact region, the transversely-averaged properties of which were elucidated in Gouyet et al. (1988). We will denote this process as Invasion Percolation in a Stabilizing Gradient (IPSG). In the opposite case ($B < 0$, p increasing in the direction of displacement), the process is destabilizing and proceeds in the form of capillary fingers, the scaling of the average thickness of which with $|B|$ also satisfies (2), namely

$$\sigma \sim |B|^{-\frac{\nu}{\nu+1}} \tag{3}$$

(see Frette et al., 1992, Meakin et al., 1992). We will denote this process as IPDG. It has been used to infer the properties of gas migrating upwards in a liquid-filled porous medium.

Consider now drainage in a random porous medium. In the absence of viscous forces, the displacement pattern will be IP, where the front advances by penetrating the largest size throat available, and the capillary pressure $P_c = P_{nw} - P_w$, is spatially uniform (Chandler et al., 1982). In the presence of viscous forces, however, a gradient (negative or positive) will develop in P_c. In view of the relations

$$P_c = \frac{2\gamma}{r} \quad \text{and} \quad p = \int_r^\infty \alpha(r)dr \tag{4}$$

where r is the pore size invaded and $\alpha(r)$ is the pore size distribution, this, in turn, will impart a gradient in the percolation probability, p. Thus, in the presence of viscous forces, the process will be also characterized by a gradient, and we expect that it will contain features of one of the two versions of IPG described above.

The displacement pattern, being initially of the IP type, will subsequently evolve along one of the two directions shown in Figure 1. Thus, fully developed drainage will be characterized by one of two possible *global* regimes: A Stabilized Displacement (SD), namely one involving the two local regimes of IP and PL, as indicated along the arrow $A \rightarrow B$ in Figure 1, and a Capillary Viscous Fingering (CVF) regime, namely one involving the local regimes of IP and VF, as indicated along the arrow $C \rightarrow D$ in Figure 1. A schematic of the expected patterns is given in Figure 2, obtained from pore-network simulations. Some of the properties of these regimes were analyzed in Xu et al. (1998). Here, we propose that the various properties of SD and CVF, the delineation of their validity, the stability of SD and the validity of the continuum approach can be inferred by the two versions of IPG referred to above, and by determining the spatial variation of p and the sign of its gradient.

UNCORRELATED HETEROGENEITY

Consider drainage at constant volumetric flow rate Q, in a random porous medium represented as a network of pores (e.g. $L \times N$ in 2-D or $L \times L \times N$ in 3-D, where N is variable).

A non-wetting fluid of viscosity μ_{nw} is displacing a wetting fluid of viscosity μ_w. Assume constant lattice spacing l, and a pore throat size distribution $\alpha(r)$, with mean r_m and standard deviation Σr_m. To illustrate the proposed method, we first consider the problem in the absence of gravity.

a. Absence of Gravity

In the absence of gravity, the properties of the two regimes, SD and CVF, were discussed in Xu et al. (1998). The SD regime is characterized by a transition from an IP pattern at the front to a more compact pattern upstream of the front. The front moves at a constant velocity v, followed by a saturation profile in the form of a spreading wave, as dictated by the classical Buckley-Leverett solution. For an SD (Figure 2a) the front has a pattern of the IP type, of width σ and lateral extent L^{d-1}, where d is the embedding dimension. The frontal region is centered around the mean front position, $X_c(t)$, which travels with velocity v, and, in analogy with IPG, is defined as the place where the transverse average of p is equal to the percolation threshold, $p(X_c) = p_c$. It was shown in Xu et al. (1998) that use of IPSG results into the following equation for the determination of the front width

$$\left(b\sigma^{\frac{\zeta+\nu(D-1)}{\nu}} - M\sigma\right) \sim \frac{2\Sigma}{Ca_F}\sigma^{-\frac{1}{\nu}} \tag{5}$$

where M is the viscosity ratio, $M = \frac{\mu_w}{\mu_{nw}}$, $Ca_F = \frac{v\mu_{nw}}{\gamma}$ is the capillary number at the front and b is a dimensionless constant. Exponents ν, ζ and D correspond to the correlation length, the conductance and the mass fractal dimension of the percolation cluster, respectively (Stauffer and Aharony, 1992). Upstream of the front there is a compact region (Figure 2a), the transition to which can be described by a cross-over function. This function can be used to describe the saturation profile within and upstream of the front, using concepts from IPG (see Xu et al., 1998).

Equation (5) is obtained by applying the self-consistency argument of Gradient Percolation (Gouyet et al., 1988), which states that since σ delineates the extent of the IP cluster, we must also have the condition

$$\Delta p \sim \sigma^{-\frac{1}{\nu}} \tag{6}$$

where Δp ($\equiv -\sigma\frac{dp}{dx}$) is the variation of p in that region, namely

$$\Delta p \sim \frac{Ca_F}{2\Sigma}\left(b\sigma^{\frac{\zeta+\nu(D-1)}{\nu}} - M\sigma\right) \tag{7}$$

In turn, Eq. (7) is obtained by using the relation between P_c and p, refered to in (4), and the following expression for the change in capillary pressure,

$$\Delta P_c \sim \frac{v\mu_{nw}}{r_m}\sigma\left(b\sigma^{\frac{\zeta+\nu(D-2)}{\nu}} - M\right) \tag{8}$$

obtained by estimating the pressure drops in this region (Xu et al., 1988). Essentially, the term in the brackets of (5) or (7) expresses the difference between the pressure drops in the nw and w phases. The power-law reflects the progressively increasing resistance to flow

of the nw phase, which occupies part of a percolation cluster, as its size increases. The non-linearity must be noted.

Now, it is easily shown that (5) admits a unique positive solution for *all* values of M and Ca_F. In particular, at small Ca_F, this solution approaches the power-law asymptote

$$\sigma \sim \left(\frac{Ca_F}{2\Sigma}\right)^{-\frac{\nu}{1+\zeta+\nu(D-1)}} \tag{9}$$

which is independent of M. Comparing (9) to (refipveq1a), one can identify a suitable Bond number, B_{SD}, for this problem

$$B_{SD} \sim \left(\frac{Ca_F}{2\Sigma}\right)^{\frac{1+\zeta+\nu(D-1)}{\nu+1}} \tag{10}$$

Thus, in this case, the Bond number increases with an increase in the capillary number. It is also interesting to note that an increase in the disorder of the pore structure (increasing Σ) has an effect which is equivalent to stronger capillarity (smaller capillary number). This explicit representation of the disorder of the pore network in the description of the displacement is an interesting result.

The fact that a solution for (5) exists for all M and Ca_F also means that a fully developed SD exists (but will not necessarily be reached) for all M and Ca_F. The inference that a SD exits arises from noting that because of the existence of a solution, the LHS of (5) is positive, hence p decreases in the direction of displacement. To establish whether this regime will actually develop, however, we must examine the *initial* phase of the displacement, before a travelling-wave solution develops.

Before we proceed with this analysis, we also briefly mention the CVF regime (Figure 2b). In the context of IPG, this will develop when p *increases* in the direction of displacement, in which case the Bond number is negative and the process will be IPDG. In analogy with (3) we expect that in such a displacement the fingers will be influenced by both viscous and capillary effects. This is in contrast to the standard DLA approach, in which the finger width is equal to the resolution of the discretization. Xu et al. (1998) showed that under certain conditions, this problem becomes a standard IPDG problem with a suitbale Bond number

$$B_{CVF} \sim -\frac{CaM}{2\Sigma} \tag{11}$$

through which the average finger width can be directly obtained by using (3), namely

$$\sigma \sim \left(\frac{CaM}{2\Sigma}\right)^{-\frac{\nu}{\nu+1}} \tag{12}$$

We note that this power law has an exponent identical to Lenormand's (1989) for the scaling of the IP-VF boundary in his phase diagram. However, Lenormand's study did not pertain to the width of a finger, or for that matter to the particular CVF regime of destabilizing IPG discussed here. This result also shows that under the asumption made, the finger width will decrease with an increase in Ca and M, eventually reducing to a thin finger of the size of a single pore (and where a DLA regime will emerge). Further study of the CVF regime is currently in progress.

Phase diagram

Consider, now, the delineation of the validity of these regimes, in which case as explained above one needs to address the *initial* phase of the displacement. During this initial period, the displacement has an extent $\chi(t) \times L^{d-1}$, where χ is increasing with time. Its pattern will be of the IP type as long as $\chi(t) \leq \chi_\epsilon(Ca, M)$, where $\chi_\epsilon(Ca, M)$ is to be determined. When the pattern first departs from percolation (at $\chi = \chi_\epsilon$), the transition towards a fully developed displacement starts. The latter will either become a SD (with a compact region following an IP front) or a CVF regime, depending on whether at χ_ϵ, p decreases or increases in the direction of displacement, respectively. To trace this transition we need, first, to identify χ_ϵ and, second, to determine the sign of the gradient of p at that point.

The analysis is similar to the SD case presented previously. The pressure drops are expressed similarly, but now with χ in place of σ and by taking $Q_{nw} = Q$ (there are no travelling fronts). Note also that here the entire cluster is a self-similar fractal. As previously, the most important quantities are ΔP_c and Δp across a region of extent χ, which here read in absolute value as follows

$$|\Delta P_c| \sim \frac{2\gamma\Sigma}{r_m}|\Delta p| \sim \frac{q\mu_{nw}}{r_m}\left|c\chi^{\frac{\zeta+\nu(D-1)}{\nu}} - M\chi\right| \tag{13}$$

where c is another constant. To define χ_ϵ we follow Lenormand (1989) and request that at χ_ϵ, we must have $\left|\frac{\Delta N_p}{N_p}\right| = \epsilon \ll 1$, where N_p is the fraction of sites of the nw phase occupying an IP cluster. The scaling of the latter can be obtained from a standard application of percolation theory, i.e. $N_p \sim (\text{const})(p - p_c)^\beta$ (see also Stauffer and Aharony, 1992). Proceeding as in Lenormand (1989), substituting $|\Delta p| = |p - p_c|$ from (13), and taking $\chi = \chi_\epsilon$, then gives the following equation for χ_ϵ

$$\frac{Ca}{\Sigma}\chi_\epsilon^{\frac{1+\nu}{\nu}}\left|c\chi_\epsilon^{\frac{\zeta+\nu(D-2)}{\nu}} - M\right| \sim \epsilon \tag{14}$$

This is a key *nonlinear* equation from the analysis of which we will delineate the various regimes. Its solution is discussed below. This equation represents a generalization of two equations in Lenormand (1989) describing the IP-to-PL and IP-to-VF boundaries, respectively (which were determined in Lenormand, 1989, in what amounts to a $\chi_\epsilon \times \chi_\epsilon$ lattice under the assumption that the pressure drop occurs only in one phase).

Before we analyze (14), we note that $c\chi_\epsilon^{\frac{\zeta+\nu(D-2)}{\nu}}$ actually represents the large-χ asymptote of the ratio $\frac{M\Delta P_{nw}}{\Delta P_w}$. Indeed, equation (14) can be rephrased as

$$\frac{CaM}{\Sigma\Delta P_w}\chi_\epsilon^{\frac{1+\nu}{\nu}}|\Delta P_{nw} - \Delta P_w| \sim \epsilon \tag{15}$$

When the lattice has a finite size and χ_ϵ is small, the ratio of the pressure drops is not a power-law, and a more general expression, obtained numerically, must be used. Using 3-D pore network simulations, Yortsos et al. (1997) computed the ratio of the two flow conductances $\frac{G_w}{G_{nw}}$ for unit viscosity ratio, which is equivalent to $\frac{M\Delta P_{nw}}{\Delta P_w}$ in the present problem. Typical results obtained are shown in schematic of Figure 3. We note that at relatively large χ, the function has the expected power-law scaling, although it eventually reaches a plateau,

reflecting finite-size effects. On the other hand, at sufficiently small χ, the curve approaches a constant value M^*, which was found to be realization-dependent.

The solution of (14) (ro more generally of (15)) depends on the sign of $c\chi_\epsilon^{\frac{\zeta+\nu(D-2)}{\nu}} - M$ (or more generally of the difference $\Delta P_{nw} - \Delta P_w$). It is apparent from Figure 3 that we must distinguish two different cases:

(a) If $M < M^*$ (region $\mathcal{A}$ in Figure 3), the term between the brackets in (14) (or (15)) is positive, and the resulting equation is very similar to (5) describing the extent of the stabilized zone in SD. As in that case, it admits a solution for *all* values of Ca, with the same dependence on parameters as σ. Moreover, and for the same reasons as in SD, p will be decreasing with distance for all $\chi(t) \leq \chi_\epsilon$, the problem becoming an IPSG process. This means that when χ_ϵ is reached, the regime that will set in will be an SD. Thus, when $M < M^*$ the displacement is an *unconditionally* stabilized displacement. This conclusion is similar to that of conventional stability analyses (where $M^* = 1$ in Chuoke et al., 1959, and $M^* > 1$ and also dependent on other petrophysical properties in Yortsos and Hickernell, 1989), but is reached here using IPG.

(b) If $M > M^*$, the solution χ_ϵ can lie either in region $\mathcal{B}_d$ or in region $\mathcal{B}_s$ (Figure 3). If in region $\mathcal{B}_d$, the term in the brackets of (14) (or (15)) is negative, which means that p *increases* with distance (note that Δp has the same sign as $c\chi_\epsilon^{\frac{\zeta+\nu(D-2)}{\nu}} - M$). In this case, therefore, the pattern when χ_ϵ is reached will depart from percolation toward the CVF regime. Assuming for simlicity equation (14) from now on, χ_ϵ solves

$$-\chi_\epsilon^{\frac{1+\nu}{\nu}} \left(c\chi_\epsilon^{\frac{\zeta+\nu(D-2)}{\nu}} - M \right) \sim \frac{\Sigma}{Ca}\epsilon \tag{16}$$

However, and contrary to the case (a), a solution of (16) *does not* exist for all M or Ca. Indeed, the LHS of this equation goes through a maximum as a function of χ, which, substituted back in (16) gives the following condition for a solution to exist

$$\frac{Ca}{\Sigma} M^{\frac{\zeta+1+\nu(D-1)}{\zeta+\nu(D-2)}} \geq O(\epsilon) \tag{17}$$

where we grouped all constants into an O(1) parameter in the RHS. This inequality expresses the condition for the existence of the CVF regime. It shows that for M above M^*, the displacement will become CVF provided that Ca or M are sufficiently large. Otherwise, the pattern will remain at percolation as the displacement proceeds throughout region $\mathcal{B}_d$ (since a solution to (16) will *not* exist), as well as *after* $\mathcal{B}_d$ is exited (at χ_0, Figure 3) and region $\mathcal{B}_s$ is entered. In the latter region, the term within the brackets in (14) is positive, the resulting equation having a solution for *all* values of M or Ca. Reasoning as in case (a), we conclude that if (17) is violated, the transition will be toward a SD.

We summarize the above as follows: A stabilized displacement (and a conventional description) is possible either if $M < M^*$ for all Ca, or if $M > M^*$ but for sufficiently small Ca, as dictated by (17). Otherwise, the displacement wil be destabilized. These results can be portrayed in a phase diagram of fully developed drainage as shown in Figure 4. The two regimes SD and CF are separated by a line, which at large M is asymptotically straight with slope $\frac{\zeta+1+\nu(D-1)}{\zeta+\nu(D-2)}$, and as M approaches M^* becomes asymptotically vertical. At large Ca, the boundary delineating SD from CVF is a vertical line independent of Ca. In the absence

of disorder, etc., we can take $M^* = 1$. However, in a real porous medium, the effective mobility ratio st the transition would also depend on the relative permeability characteristics, the trapped saturations, etc., as can be shown by a traditional stability analysis (Chikhliwala et al., 1988). It must also be noted that in actuality, condition (17) needs to be modified near M^*, where χ_ϵ is relatively small and the various power-law scalings of percolation do not apply, as pointed out above. Near M^*, we expect condition (17) to involve $M - M^*$ and a different dependence.

The boundary separating the two global regimes also serves to delineate the *validity* of the conventional continuum description, which only applies to a SD displacement. Hence, the phase diagram of Figure 4 shows the region of applicability of the conventional approach using conventional relative permeabilities and capillary pressures based on percolation theory. The resolution of this important issue has been long-standing.

Before closing we note that continuum predictions to the continuum breakdown can be obtained using the linear stability analysis of SD. In the two different approaches to this problem referred to above, the fastest growing finger was found to have the two different scalings

$$l_{max} \sim \sqrt{\frac{k}{(M-1)Ca}} \quad \text{or} \quad l_{max} \sim \frac{\sqrt{k}}{(M^*-1)Ca} \tag{18}$$

by Chuoke et al. (1959) or Yortsos and Hickernell (1989), respectively. By requesting that this thickness is comparable to the pore size (which scales as $\sim \sqrt{k}$, where k is permeability, e.g. see Katz and Thompson, 1986), the continuum breakdown is predicted to occur when

$$Ca(M^* - 1) \sim O(1) \tag{19}$$

This equation is the continuum counterpart of (17). At large M, both expressions are power laws but with very different exponents (1 for the continuum and 2.78 or 2.20 for the IPG approach, in 2-D or 3-D, respectively).

b. Presence of Gravity

Consider, now, the extension of the problem in the presence of gravity (but in the absence of gravity override). The equations for the pressure drop across any region must be modified to include the effect of gravity. For example, the equation for the pressure drop of the wetting phase over a distance of length l should read

$$\Delta P_w = \frac{\mu_w l q \sigma}{k} - \rho_w l \sigma g_x \tag{20}$$

and likewise for ΔP_{nw}. Proceeding as before it is readily shown that the equation analogous to (14) is

$$\frac{Ca}{\Sigma} \chi_\epsilon^{\frac{1+\nu}{\nu}} \left| c\chi_\epsilon^{\frac{\zeta+\nu(D-2)}{\nu}} - (M - N_g) \right| \sim \epsilon \tag{21}$$

where we have defined the gravity number

$$N_g = \frac{(\rho_w - \rho_{nw}) g_x k}{q \mu_{nw}} \tag{22}$$

Equation (21) shows that the effect of gravity is stabilizing if $N_g > 0$, and destabilizing if $N_g < 0$. Indeed, comparing (21) with (14) shows that we have effectively replaced M in equation (14) by $M - N_g$. Proceeding exactly as above, we then reach the following conclusions:

1. If $M - N_g < M^*$, the process is unconditionally a stabilized displacement (SD). In particular, by taking $M^* = 1$, the condition can be rearranged to read

$$\mu_w - \mu_{nw} < \frac{(\rho_w - \rho_{nw}) g_x k}{q \mu_{nw}} \tag{23}$$

We recognize this as the condition for the long-wave stability of a flat interface in miscible displacement in the absence of dispersion (eg. Hill, 1952). A more complicated expression would result in the immiscible case, where is not necessary that $M^* = 1$.

2. If, on the other hand, $M - N_g > M^*$, the process will become a CVF regime influenced by gravity, provided that the following condition applies

$$\frac{Ca}{\Sigma} (M - N_g)^{\frac{\zeta + 1 + \nu(D-1)}{\zeta + \nu(D-2)}} \geq O(\epsilon) \tag{24}$$

This equation is the generalization of the previous result (17) that includes gravity in the direction of displacement. We conclude that the effect of gravity in this analysis enters through the combination $M - N_g$, which effectively replaces M. Hence, the same phase diagram as Figure 4 would also be applicable here, as well, provided that the appropriate substitutions are made. We must also point out that near the vertical boundary, equation (24) is not applicable, and as in the previous, it must be replaced by a different expression in which the combination $M - M^* - N_g$ must be used. This will not be further considered here, however.

CORRELATED HETEROGENEITY

When the pore network is correlated with (dimensionless) correlation length, λ, the previous approach is not necessarily valid, due to the different scaling of the pressure drop in the displacing phase with distance χ, depending on whether $\chi \gg \lambda$ or $\chi \ll \lambda$, respectively. In the first case, where the correlation length is small, we expect results identical to the previous, provided that

$$\chi_\epsilon \gg \lambda \tag{25}$$

In the second case, the problem is essentially the same with that of displacement in a long-range correlated lattice (for example, of the fBm type). Invasion percolation (IP) in such a lattice was studied by Isichenko (1992) and more recently by Du et al. (1996), and was shown to take the form of compact rather than fractal patterns. In addition, Invasion Percolation in a Gradient (IPG) in an fBm lattice was investigated by Du (1996), who showed that in

the case of an IPSG process, the usual GP scaling (2) applies, except that now the scaling exponent reduces to a classical value, namely that

$$\sigma \sim B^{-1} \tag{26}$$

This result is consistent with the theoretical argument that in an fBm lattice, $\nu = \infty$ (Isichenko, 1992).

Consider, now, drainage in a correlated field. In the presence of viscous forces, we expect that the postulated previous analogy to IPG would still be valid, with the exception that because of the channel-like aspects of this correlated displacement, the pressure drop will not have the power-law scaling of the fractal patterns of the uncorrelated case. Furthermore, two new patterns should arise, one corresponding to SD, to be denoted as HS (Heterogeneity Stable), and another corresponding to CVF, to be denoted as HUS (Heterogeneity UnStable), both of which will occur in a long-range correlated field. Two characteristic patterns are shown in Figure 5. The HS pattern shows channeling behavior, with a compact structure where channeling occurs, while the HUS pattern is much more fingered. The specific properties of these patterns are not fully known and they are currently under study. However, we may still delineate their validity by proceeding as before. In the following, we will first delineate the validity of the previous SD and CVF patterns, and subsequently describe the boundaries of the two new patterns.

For the SD pattern to be valid, condition (25) must apply. Consider, first, the case $M < M^*$. The solution of equation (14) can be greatly simplified if we neglect the effect of M. This can be done without loss to a first approximation. Inserting the resultin solution in (25) gives the following condition

$$\frac{\epsilon\Sigma}{Ca} \gg O(\lambda^{\alpha}) \tag{27}$$

for the validity of the SD pattern, where we have defined for simplicity the exponent $\alpha = \frac{\zeta+1+\nu(D-1)}{\nu}$. This condition delineates the validity of the SD regime for $M < M^*$ in the general case of correlated networks. This condition is represented by a straight line paralllel to the $\log M$ axis in the modified phase diagram shown in Figure 6. We note that as λ increases, the region of validity of the SD regime decreases and becomes restricted to smaller values of Ca. This is consistent with what is expected intuitively. To delineate the boundary of the SD regime on the other side of M^*, we consider the asymptotic solution of (14) at large M. Inserted in (14), this gives the following condition

$$M \gg \lambda^{\alpha-\beta} \tag{28}$$

where we defined the exponent $\beta = \frac{\nu+1}{\nu}$. This condition states that M should be sufficiently large. However, since this has already been assumed in the analysis, we will assume that (28) is implicitly satisfied by the assumption made and we will place our emphasis on the validity of the CVF regime, instead.

For the CVF pattern to be reached, a similar analysis applies. Here, we will restrict the analysis to the large M limit, in which the solution of (16) simplifies considerably. Inserting the results to (25), leads to the following condition for the validity of the CVF regime at large M

$$\frac{\epsilon\Sigma}{CaM} \gg O(\lambda^{\beta})) \tag{29}$$

The resulting boundary in the logCa-log$M$ diagram of Figure 6 is a straight line with slope -1. Given that this slope is less than the slope of the boundary separating the CD and CVF regimes, we reach the conclusion that the CVF regime will always exist, for sufficiently large M. However, the region of its applicability diminishes as the correlation length, λ, increases. This is indicated in Figure 6. We caution again that condition (29) applies only for relatively large values of M. For values in the intermediate range, an explicit condition is not readily available, as the two exponents α and β are not integers and require a numerical solution. Furthermore, for sufficiently small M, the power-law scaling of the conductance ratio is no longer valid (compare with Figure 3) and the boundary deviates from the straight line with slope -1. We expect that the delineating boundary will converge with that of the boundary delineating the SD-CVF transition, as depicted qualitatively in Figure 6. A more detailed analysis of these boundaries is needed at finite values of M.

The boundaries calculated above delineate the validity of the SD and CVF regimes. Following a transition region, the two regimes of HS and HUS eventually emerge. To describe the regions of their applicability we consider the equivalent to (14) expression when $\chi \ll \lambda$. As discussed above, in this case the scaling of the pressure drops will be linear for both phases, thus we can write the equivalent to (14) expression

$$\frac{Ca}{\Sigma}\chi_{\epsilon}|d - M| \sim \epsilon \tag{30}$$

where we introduced the O(1) constant d. The two different limiting regimes HS and HUS will correspond to the two cases $d - M > 0$ and $d - M < 0$, respectively. Note that d may be realization-dependent. Now, the validity of either of these regimes requires the necessary condition

$$\chi_{\epsilon} \ll \lambda \tag{31}$$

Hence, the validity of the HS regime requires the necessary conditions

$$Ca \gg \frac{\Sigma\epsilon}{\lambda(d - M)} \quad \text{and} \quad d > M \tag{32}$$

depicted in Figure 6 for the case $d = M^*$. We note that at small M, the delineating boundary approaches a constant of order $\frac{\Sigma}{\lambda}$. Inversely, the validity of the HUS regime requires the conditions

$$Ca \gg \frac{\Sigma\epsilon}{\lambda(M - d)} \quad \text{and} \quad M > d \tag{33}$$

also depicted in Figure 6 for the case $d = M^*$. We note that at large values of M, the boundary becomes in the log-log plot of the phase diagram a straight line with slope -1, namely it becomes parallel to the boundary delineating the validity of the CVF regime.

CONCLUDING REMARKS

In this paper we used Invasion Percolation in a Gradient, to connect drainage processes at the pore-network scale with the displacement at the macroscale. A phase diagram involving the capillary number, the mobility ratio and the correlation length was constructed to delineate the regions of validity of various regimes. The transition between stabilized displacements and viscous-driven fingering is controlled by the change of the sign of the gradient of the percolation probability. Transition boundaries were described by scaling laws involving the capillary number, the viscosity ratio and the correlation length. Essentially, the approach presented represents a stability analysis at the pore-network scale. When the mobility ratio M is sufficiently small, the displacement is stabilized and can be described by Invasion Percolation in a Stabilizing Gradient, involving two regimes, denoted as SD and HS, depending on whether the displacement is controlled by randomness or correlation, respectively. In the opposite case, the displacement has common features with Invasion Percolation in a Destabilizing Gradient and involves the regimes of CVF and HUS in the cases of correlated and uncorrelated heterogeneity, respectively. The asymptotic properties of the boundaries delineating these regimes were identified.

The limiting regimes identified under the conditions of IPSG, namely SD and HS, are also the regimes where conventional theories (such as the Buckley-Leverett equation) apply. By comparing Figures 4 and 6, it is apparent that the boundary separating SD from CVF in Figure 4, is essentially the boundary that delineates the applicability of the conventional (Buckley-Leverett) description. In these regimes, saturation-dependent relative permeabilities can be defined, subject to the additional two points: 1. Although the HS regime is subject to a conventional Buckley-Leverett analysis, the relative permeabilities and capillary pressure functions to be used there should be stochastic functions, since the distribution of phases will also depend on the particular realization of the heterogeneity field (for example, see Du et al., 1996, and Paterson et al., 1997). 2. The relative permeabilities in the SD regime may additionally depend on the capillary number of the displacement through the dependence of the trapped saturation of the displaced phase on Ca. Indeed, when the displacement process is IPSG, the trapped saturation will *decrease* as the Bond number of the displacement increases. Given that in the SD case, the Bond number can be identified as being proportional to the capillary number to a power (compare with (10)), it is apparent that an increase in Ca will lead to an increase in B_{SD}, hence to a decrease in the trapped saturation. The precise dependence, however, needs to be evaluated numerically. Additional work is also needed in the study of the properties of the limiting heterogeneity regimes as well as the properties of the delineating boundaries at values of M near the critical.

REFERENCES

1. J. Bear, Dynamics of Fluids in Porous Media, Elsevier (1972).

2. M.J. Blunt, *SPEJ* **2**, 70 (1997).

3. M.J. Blunt and P. King, *Transport Porous Media* **6**, 407 (1991).

4. R. Chandler, J. Koplik, K. Lerman and J.F. Willemsen, *J. Fluid Mech.* **119**, 244 (1982).

5. M. Chaouche, N. Rakotomalala, D. Salin, B. Xu and Y.C.Yortsos, SPE 26658 (1993).

6. M. Chaouche, N. Rakotomalala, D. Salin, B. Xu and Y.C.Yortsos, *Phys. Rev. E* **49** , 4133 (1994).

7. E.D. Chikhliwala, A.B. Huang and Y.C. Yortsos, *Transport Porous Media* **3**, 257 (1988).

8. R.L. Chuoke, P. van Meurs and L.B. van der Poel, *Trans. AIME* **216**, 188 (1959).

9. R.E. Collins, Flow of Fluids Trough Porous Materials, Reinhold (1961).

10. C. Du, PhD Dissertation, University of Southern California (1996).

11. C. Du, C. Satik and Y.C. Yortsos, *AIChEJ* **42**, 2392 (1996).

12. F.A.L. Dullien, Porous Media, Fluid Transport and Pore Structure, Academic Press (1992).

13. V. Frette, J. Feder, T. Jossang and P. Meakin *Phys. Rev. Lett.* **68**, 3164 (1992).

14. J.F. Gouyet, B. Sapoval and M. Rosso, *Phys. Rev. B* **37**, 1832 (1988).

15. A.A. Heiba, M. Sahimi, L.E. Scriven and H.T. Davis, SPE 11015 (1982).

16. S. Hill, *Chem. Eng. Sci.* **1**, 247.

17. J.-P. Hulin, E. Clement, C. Baudet, J.F. Gouyet and M. Rosso, *Phys. Rev. Lett.* **61**, 333 (1988).

18. M.B. Isichenko, *Rev. Mod. Phys.* **64**, 961 (1992).

19. A.J. Katz and A.H. Thompson, *Phys. Rev. B* **34**, 8179 (1986).

20. L.W. Lake, *Enhanced Oil Recovery*, Prentice Hall (1989).

21. R. Lenormand, E. Touboul and C. Zarcone, *J. Fluid Mech.* **189**, 165 (1988).

22. R. Lenormand, *Proc. Roy. Soc. Lond.* **A423**, 159 (1989).

23. R. Lenormand, *J. Phys. C.: Condens. Matter* **2**, SA79 (1990).

24. C.M. Marle, Multiphase Flow in Porous Media, Gulf (1981).

25. P. Meakin, J. Feder, V. Frette and T. Jossang, *Phys. Rev. A* **46**, 3357 (1992).

26. P.E. Oren, S. Bakke and O.J. Arntzen, SPE 3880 (1997).

27. L. Paterson, J.-Y. Lee and W.V. Pinczewski, SPE 38882 (1997).

28. D. Stauffer and A. Aharony, *Introduction to Percolation Theory* Francis-Taylor (1992).

29. D. Wilkinson, *Phys. Rev. A* **30**, 520 (1984).

30. D. Wilkinson, Phys. Rev. A, **34**, 1380 (1986).

31. B. Xu, J. Kamath, Y.C. Yortsos and S.H. Lee, SPE 38879 (1997).

32. B. Xu, Y.C. Yortsos and D. Salin, *Phys. Rev. E* **57**, 739 (1998).

33. Y.C. Yortsos and F.J. Hickernell, *SIAM J. Appl. Math.* **49**, 730 (1989).

34. Y.C. Yortsos, C. Satik, J.-C. Bacri and D. Salin, *Transport Porous Media* **10** , 171 (1993).

35. Y.C. Yortsos, B. Xu and D. Salin, *Phys. Rev. Lett.* **79**, 4581 (1997).

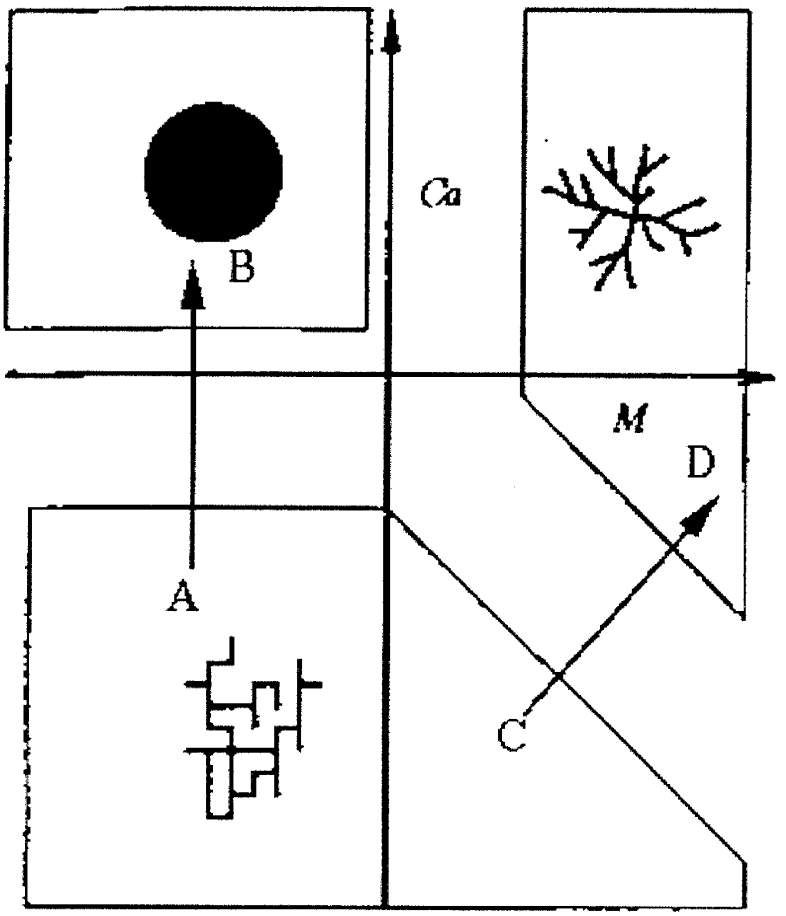

Figure 1: Phase diagram for drainage (adopted from Lenormand, 1989). Arrows indicate the transition from percolation- to viscous- dominated regimes, expected in fully-developed displacements.

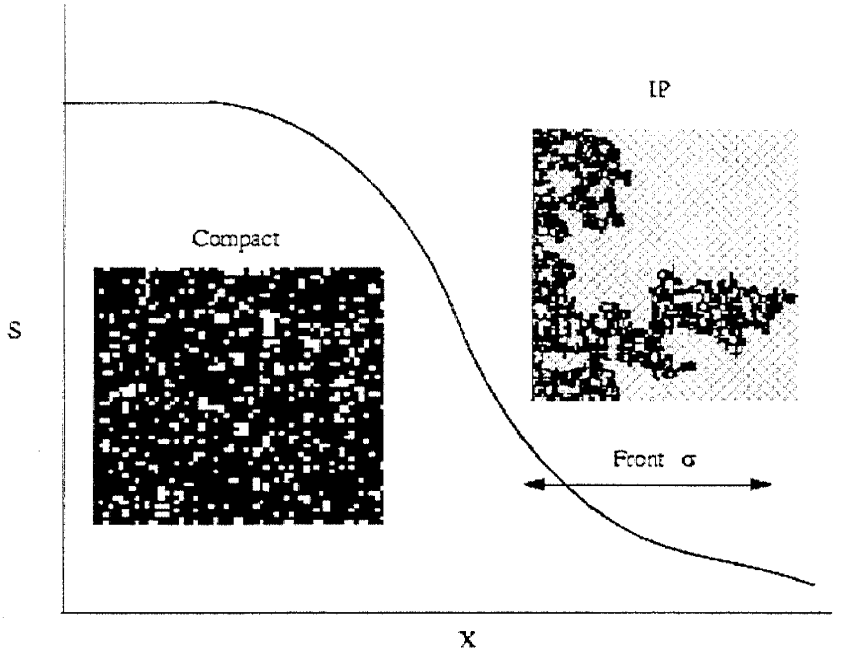

(a)

CVF

(b)

Figure 2: Schematics of fully-developed drainage: (a) Stabilized Displacement (S denotes the volumetric fraction of the invading phase), (b) Capillary-Viscous Fingering.

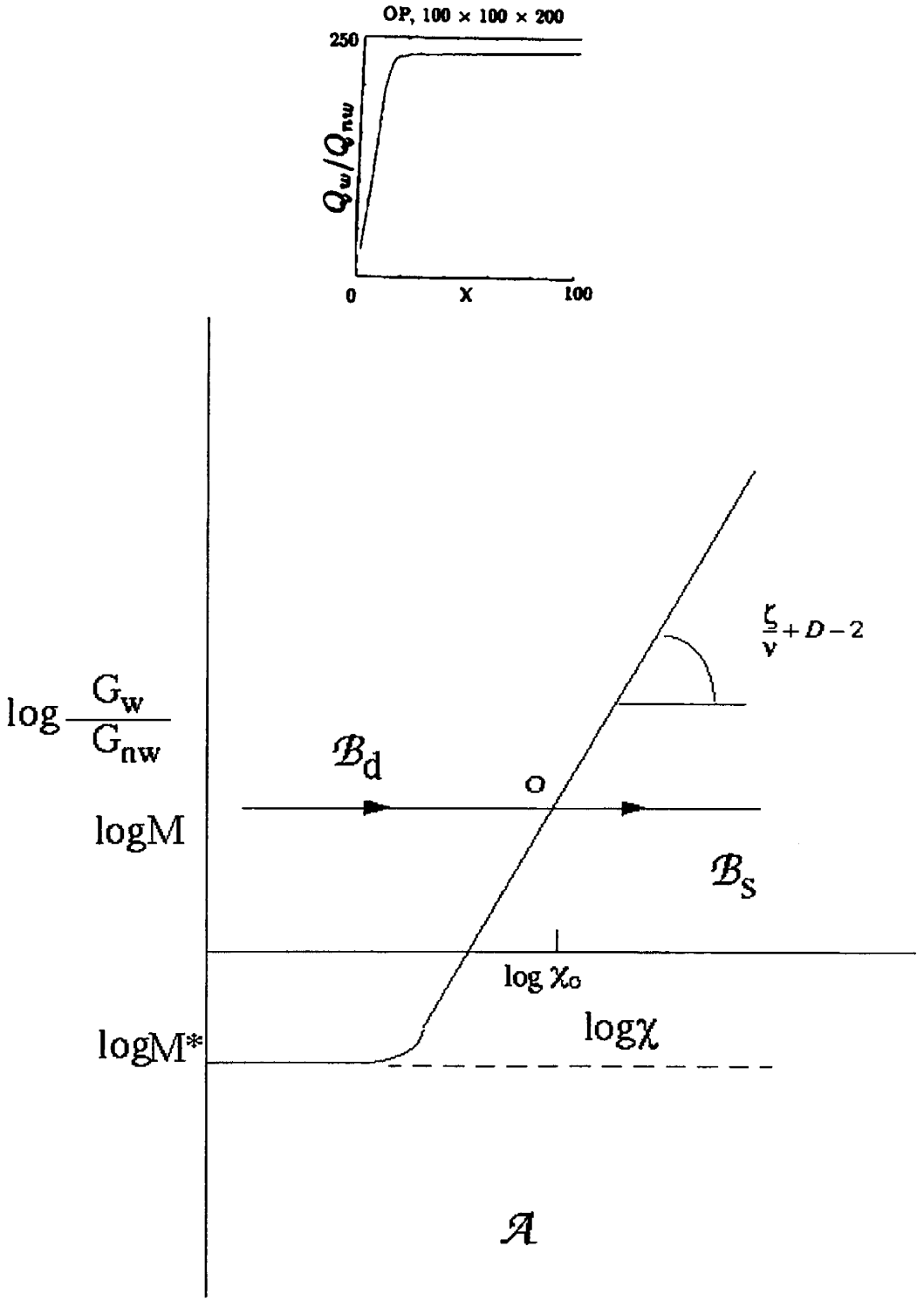

Figure 3: The ratio $\frac{M\Delta P_{nw}}{\Delta P_w}$ (first term between brackets in (14)) vs. the extent χ_ϵ. In the inset are results from simulations in a $100 \times 100 \times 200$ pore-network.

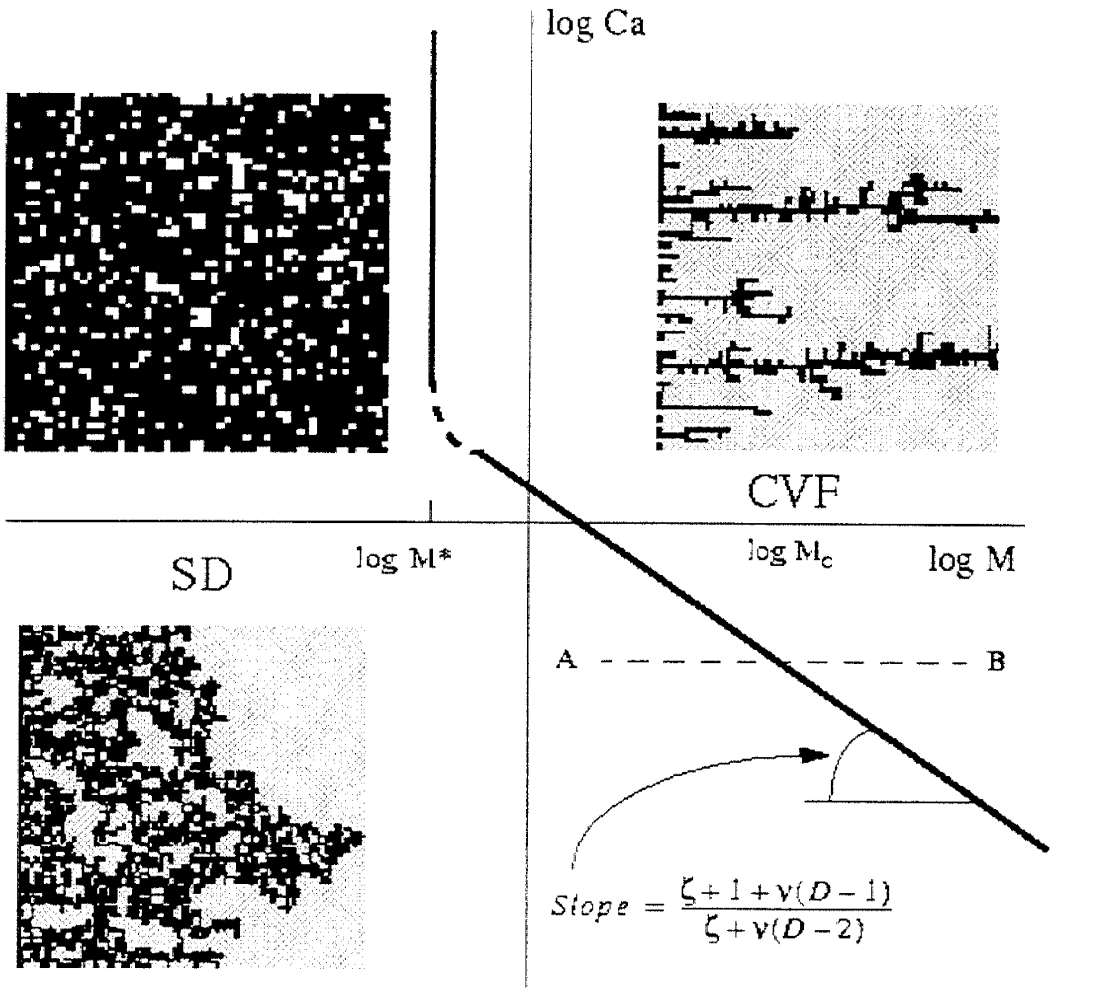

Figure 4: Phase diagram of fully developed displacement in drainage for uncorrelated pore networks.

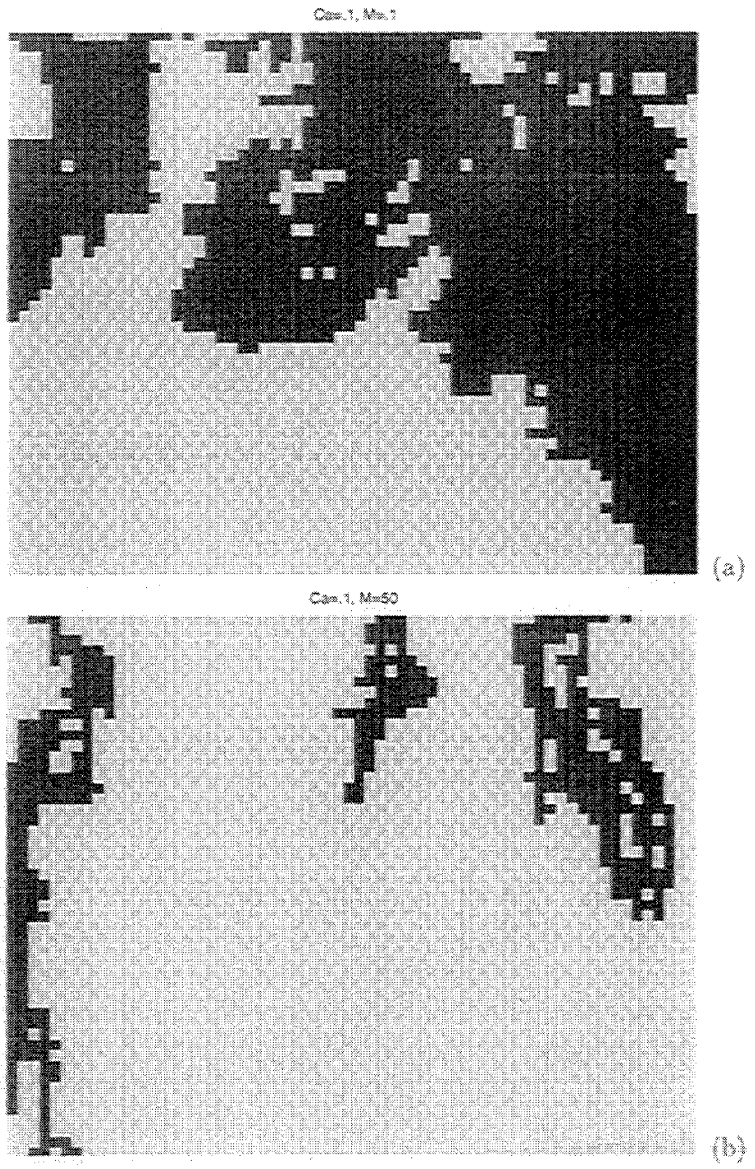

Figure 5: Characteristic patterns corresponding to the two regimes HS and HUS, obtained from 2-D pore-network simulations in an fBm lattice with Hurst exponent $H = 0.8$: (a) The correlation structure. (b) Displacement pattern for $Ca = 0.1$, $M = 0.1$. (c) Displacement pattern for $Ca = 0.1$, $M = 50$.

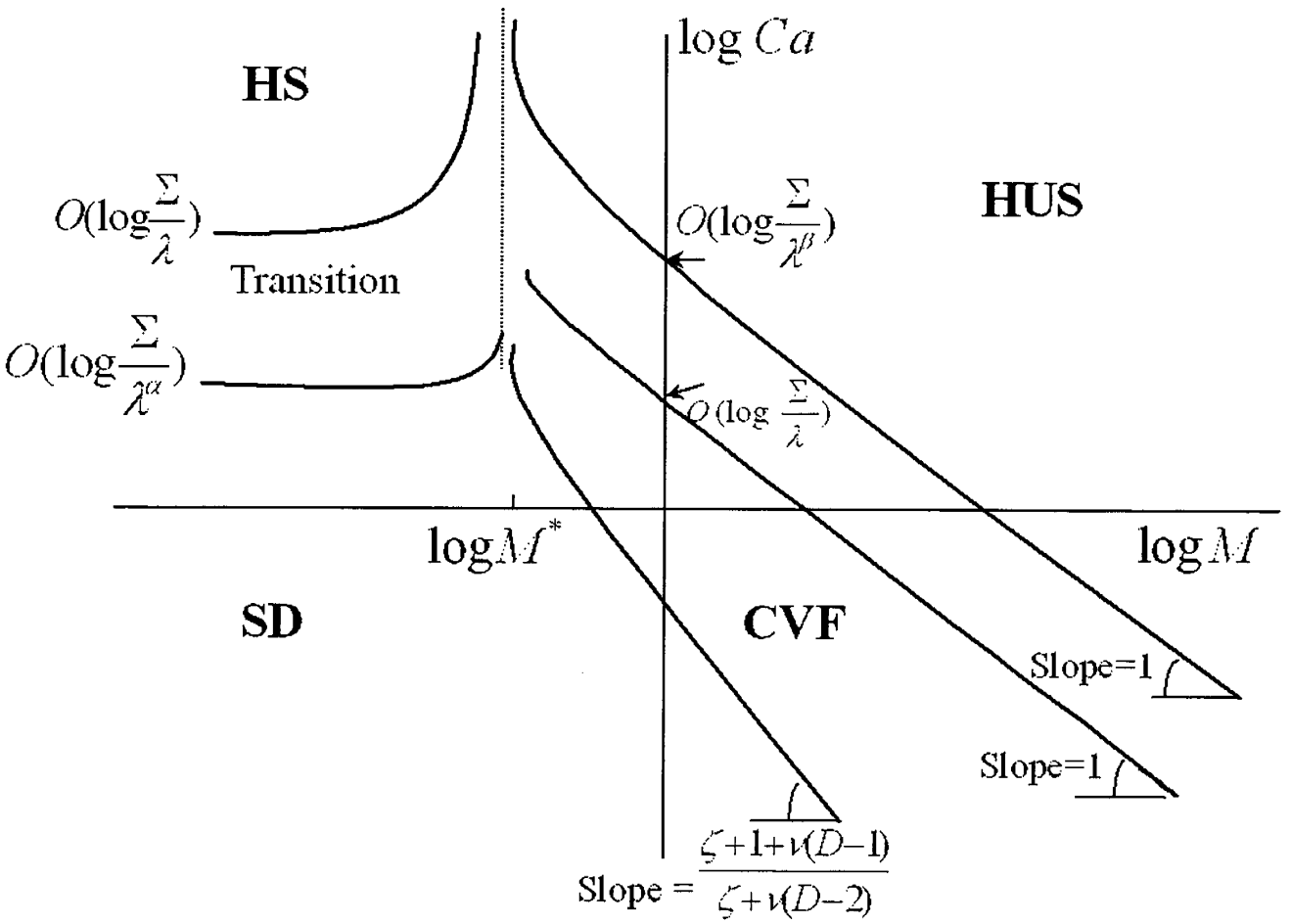

Figure 6: Phase diagram of fully developed displacement in drainage for correlated pore networks.

5. INVASION PERCOLATION WITH MEMORY

H. Kharabaf and Y. C. Yortsos

ABSTRACT

Motivated by the problem of finding the minimum threshold path (MTP) in a lattice of elements with random thresholds, τ_i, we propose a new class of invasion processes, in which the front advances by minimizing or maximizing the measure $S_n = \sum_i \tau_i^n$ for real n. This rule assigns long-time memory to the invasion process. If the rule minimizes S_n (case of minimum penalty), the fronts are stable and connected to Invasion Percolation in a Gradient [1] but in a correlated lattice, with Invasion Percolation [2] recovered in the limit $|n| = \infty$. For small n, the MTP is shown to be related to the optimal path of the Directed Polymer in Random Media (DPRM) problem [3]. In the large n limit, however, it reduces to the backbone of a mixed site-bond percolation cluster. The algorithm allows for various properties of the MTP and the DPRM to be studied. In the unstable case (case of maximum gain), the front is a Self-Avoiding Random Walk (SAW).

INTRODUCTION

Many processes of practical interest involve disordered media or lattices of elements with randomly distributed thresholds, $\tau_i > 0$. The typical problem consists of the application of an overall difference in potential (or in pressure in the case of fluid flow in porous media), $\Delta\Phi$, across opposite ends of a lattice (or of the pore-network representing the porous medium). A lattice element remains closed to transport if the local potential difference is smaller than its threshold, $\Delta\phi_i < \tau_i$, but becomes open in the opposite case, $\Delta\phi_i > \tau_i$. In these problems, a quantity of significant interest is the minimum overall threshold, $\Delta\Phi_{min}$, or, equivalently, the minimum gradient

$$|\nabla\Phi|_{min}(L) \equiv \frac{\sum_i \tau_i}{L} \tag{1}$$

at which a path of open elements first forms. In the above, the sum is over the Minimum Threshold Path (MTP), which is unknown and must also be determined. The problem typically arises in networks of diodes [4], in the flow of Bingham plastics in porous media [5], and in the mobilization of foams in porous media [6]. In a more general context, where each threshold is viewed as a penalty [6], it is a problem of determining the minimum overall penalty (a problem in global optimization).

Roux et al. [4] studied aspects of this problem in the context of a network of diodes, by considering two different cases, one in which the path is directed (no backtracking allowed) and one in which it is not. They suggested that $|\nabla\Phi|_{min}$ is akin to a percolation threshold and studied its dependence on the lattice size L. Their findings showed finite-size scaling similar to Directed Percolation (DP) or Ordinary Percolation (OP), respectively, from which they concluded that the onset of connectivity in this problem is of the same universality class as percolation. Using numerical simulations in 2-D lattices of thresholds uniformly distributed in (0,1), they further estimated $|\nabla\Phi|_{min}(\infty) = 0.231$ and $|\nabla\Phi|_{min}(\infty) = 0.227$ for the directed and non-directed cases, respectively. They also made the very interesting

observation that the two problems of the onset of conduction in a lattice of thresholds and percolation, ought to be connected, as their respective thresholds are special cases of the more general expression

$$\mathcal{L}_n = \min\left(\frac{\sum_i \tau_i^n}{L}\right)^{1/n} \tag{2}$$

with $n = 1$ corresponding to the threshold-lattice problem and $|n| = \infty$ to OP. Additional information on the MTP or on its connection to percolation, was not provided, however.

Sahimi [5] provided estimates of $|\nabla\Phi|_{min}(\infty)$ and conjectured that the MTP has the same scaling properties as the well-studied [6] minimum path, l_{min}, of a percolation cluster. The latter (also known as the chemical distance) denotes the path on the percolation cluster with the minimum total length (or tortuosity). It is known to be a self-similar fractal [7], scaling as $l \sim L^{D_{min}}$, where D_{min} is equal to 1.13 in 2-D and 1.34 in 3-D. Rossen and Mamun [6] proceeded along similar lines and proposed a percolation approach for the MTP, consisting of occupying lattice elements with progressively higher thresholds. Although commenting that such a process is actually only an approximation, they also identified the MTP with the minimum path, l_{min}, of the percolation cluster thus obtained.

Closely related to the above is the problem of a Directed Polymer in Random Media (DPRM) (see [3] and references therein). Here, a well-studied version involves a a directed (stretched) polymer in a square lattice with one end anchored at the origin ($x = 0$, $y = 0$), which is allowed to move in discrete steps along the two directions, x and y, subject to the constraint $|y(x+1) - y(x)| = 0$ or 1, and that the polymer cannot turn back in the x direction (overhangs not allowed). An energy cost, ϵ, randomly distributed, is associated with every step. The objective is to find the configuration that minimizes the total energy. This problem was mapped to the celebrated KPZ equation (see [8]), which is known to give rise to self-affine fractals, and is also connected to the more general problem of interface growth and surface roughening (for example, wetting in porous media, burning of paper, etc.) which also lead to self-affine fractals. As the MTP and DPRM problems both involve the minimization of a global quantity, we expect that they also would be closely related.

At present, a firm connection of the lattice-threshold problem to percolation appears to be lacking. In particular, the relation of the MTP to the minimum path of percolation, if it indeed exists, is not self-evident. The latter pertains to the minimum sum of equal length segments on the OP cluster, while the former is the minimum sum of distributed thresholds in a regular lattice. Understanding this connection forms the main objective of this paper. We present a new algorithm for the construction of the MTP, based on which its properties can be studied. The novelty of the algorithm is that it requires the simulation of an invasion process, similar to Invasion Percolation (IP), except that here the rules for the front advance depend on the front history, as explained below. In implementing this algorithm, and in conjuction with the remark in Ref. [3], however, we realized that the MTP problem can benefit from the study of more general invasion processes, in which the front advances by minimizing (or maximizing) the general measure

$$S_n = \sum_i \tau_i^n \tag{3}$$

for n real, and where the sum is over any path connecting any site at the front to the

inlet boundary. As these involve the entire history of the process, we will refer to them as Invasion Percolation with Memory (IPM). Both the non-directed and the directed problems are considered.

In the non-directed case, the properties of invasion and of the generalized MTP, over which S_n is minimal, are studied. It is shown that the process of minimizing S_n is related to Invasion Percolation in a Gradient (IPG) [1], but in a correlated lattice, from which it is inferred that the invasion fronts are rough, but not self-similar at all scales. A connection of the MTP to the backbone of a mixed site-bond percolation cluster (obtained in the limit $|n| = \infty$) is, next, established. In the directed case, the IPM algorithm allows for a generalization of the DPRM problem to arbitrary values of n and shows that the optimal path of the latter approaches the backbone of the mixed site-bond Directed Percolation cluster. We note in advance that an important difference between our approach and the conventional one is that here we identify the optimum configuration between any two curves (namely the polymer can originate from any point on a given curve, and not from the origin only). For $n = 1$, the optimum path in the DPRM problem and the MTP are found to be very similar, although not identical, based on which we conjecture that the MTP in the small n limit is also self-affine. The identification (opening) of paths of higher energy, as the applied potential difference exceeds the minimum value, is briefly studied. Finally, for the sake of generalization, we also consider the case of maximizing S_n (maximum gain), where, in the presence of a trapping rule, the front is shown to be a Self-Avoiding Random Walk (SAW).

Before we proceed, we note that the consideration of the various moments of τ is equivalent to considering distributions of new thresholds $\eta = \tau^n$, with pdf, arithmetic mean and standard deviation equal to

$$f(\eta) = \frac{1}{|n|}\eta^{\frac{1}{n}-1}\ , \qquad <\eta>= \frac{1}{n+1}\ , \qquad \sigma_\eta = \frac{n}{(1+n)\sqrt{1+2n}} \tag{4}$$

respectively. For the more general problem of finding the MTP of arbitrary threshold distributions, we expect a rough analogy between patterns with the same ratio of standard deviation to arithmetic mean, $m \equiv \frac{\sigma_\eta}{<\eta>}$, which for the present case reads $m = \frac{n}{\sqrt{1+2n}}$. Thus, we anticipate that the results for large or small n would be analogous to those for processes with arbitrary threshold distributions and large or small m, respectively. From (4), it is apparent that for the existence of the arithmetic mean we must have $n > -1$, while for that of the variance, $n > -\frac{1}{2}$. Therefore, for finite first and second moments of general threshold distributions, we must restrict (3) to $n > -\frac{1}{2}$. However, some results for smaller n (which formally correspond to Levy flights [9]) will also be presented (see Kharabaf [10] for more details). We note that the DPRM problem with the pdf of (4) and n in the range $(-1/2, 0)$ was singled out as a special case by Marconi and Zhang [9] who found that, in that range, the meandering growth exponent varies with n.

The paper is organized as follows: First, the basic rules of the algorithm and the construction of the MTP are presented. The process is generalized to arbitrary n and it is shown that it reduces to IP in the two limits $n \to \pm\infty$. Then we discuss the application of the same algorithm to the solution of a simple version of the DPRM problem. IPM is subsequently shown to be related to IPG in a correlated lattice, where an appropriate *Bond* number is defined. Based on this analogy, the properties of the invasion fronts are elucidated.

From these two relations to DPRM and IPG, it is suggested that the invasion fronts and the corresponding MTPs of IPM are generally rough, reducing to self-similar fractals only in the limit $|n| = \infty$. Various properties of the fronts and the MTP are studied. Then, the properties of higher-energy paths as the applied potential difference increases above its minimum value, are briefly discussed. Finally, we present an extension of the IPM process to the destabilizing case, where S_n is maximized and where the front is shown to reduce to a SAW.

IPM PROCESSES

Invasion Algorithm

Consider an invasion process from right to left in a lattice of sites and bonds. Invader and defender reside on the sites of the lattice. The bonds have thresholds, τ_i, randomly assigned from a uniform distribution in (0, 1). The invading front advances one-site-at-a-time following rules to be described below. Because both sites and bonds are involved, this problem is actually a mixed site-bond problem, which is prototypical of fluid displacements in porous media [11]. The rule for the front advance is as follows: Denote by F an arbitrary site currently on the front, by F' one of its (nearest-neighbor) perimeter sites in the defender region (Fig. 1a, where a 2-D square lattice is used), by F_G the site from which invasion will actually proceed next, and by F'_G the perimeter site to which the front advances during the next step (Fig. 1b). A value $V_n(F)$ is recursively assigned to every site F on the front (hence, to all sites that have been invaded), through the following algorithm.

Let $\tau_{FF'}$ denote the threshold connecting site F with one of its perimeter sites F', and form the sum

$$S_{n,FF'} = V_n(F) + \tau^n_{FF'} \tag{5}$$

Then, the threshold to be invaded next will connect the two sites, a "growth" site F_G and the site to be occupied next, F'_G, for which $S_{n,FF'}$ is minimum. We point out that in our terminology, the term growth site has a different meaning from that of Roux and Guyon [12]. Having made this determination, site F_G is identified, the front advances to F'_G, the assignment

$$V_n(F'_G) = V_n(F_G) + \tau^n_{F_G F'_G} \tag{6}$$

is subsequently made and the process is repeated. In this way, and by using the initial condition $V_1(R) = 0$ for all sites R on the initial interface (which here is the right boundary, but could be any other curve) (Fig. 1), all invaded sites are assigned a unique value V_n. In contrast to IP, where the front advances by the local rule of selecting the smallest (or largest) available threshold, here the advance depends on the past history, thus imparting to the process a long-time memory. Through this algorithm, it is straightforward to show that the value $V_n(A)$, assigned to every invaded site A, actually represents the minimum sum of thresholds among all paths that connect A to the right boundary (see Appendix A). The corresponding minimum path from A to the injection (initial) side can be easily identified, as discussed below.

Typical snapshots of the occupied sites and of the corresponding MTP for $n = 1$ in a 2-D square lattice are shown in Fig. 2 at different stages of invasion (Fig. 2a-2c). Both the front and the MTP have the appearance of rough but not self-similar curves. The MTP across the lattice can be directly identified when the front first reaches the LHS boundary (at "breakthrough", site L^*, Fig. 2c). It can be traced recursively, by starting from L^*, proceeding in the direction of decreasing V_n and identifying the next site P that belongs to the path, and neighbors a site P' already on this path (Fig. 2d), by requiring that the condition $V_n(P') = V_n(P) + \tau^n_{PP'}$ be identically satisfied. A similar procedure is used to find the minimum paths (from the current front location to the right boudary) during the different stages of invasion (Fig. 2a-2b), as well as the MTP originating from any invaded site A. These paths are not necessarily subsets of the MTP.

In the simulations shown in Fig. 2, a trapping rule similar to Invasion Percolation with Trapping (IPT) [13] was applied, such that a trapped site cannot be invaded. Thus, in the invaded region, there exist closed regions, the sites of which have not been visited (Fig. 2). However, this does not affect the values of V_n or the minimum path, as any paths that traverse trapped regions cannot, by construction, be minimum paths. In the cases shown in Fig. 2, the number density of the trapped regions is high, although their size is small. We must point out, however, that by relaxing the trapping rule, and by continuing the invasion process following breakthrough, all sites of the lattice can be invaded.

Because the function V_1 is taken to be single-valued, a site cannot be invaded more than once, hence a non-invaded bond between two adjacent sites at the front, such as F and F_G in Fig. 1, cannot become open in any subsequent step (it is trapped). This has the following consequences: (i) Between any invaded site A and the right boundary there is one and only one self-avoiding path occupied by invaded sites. By construction (see Appendix A), this path is the MTP from A to the boundary. (ii) Because of this absence of reconnections, all invaded sites belong to distinct dendritic branches which originate from the right boundary, but, otherwise, do not intersect one another (see also below). (iii) Depending on the coordination number Z of the lattice, an occupied site can be the growth site for two or more branches, but cannot be the termination point of two branches.

The IPM algorithm bears some relation with the "burning trees" algorithm of Herrmann et al. [14] for obtaining information on the backbone and other properties of the percolation cluster, and to the matrix transfer algorithm used in the DPRM problem. In the former, a process mimicking invasion in a percolation cluster is considered and invaded sites are labelled sequentially using consecutively increasing integers. However, the IPM algorithm is more general. The "burning trees" algorithm results as a special case of the IPM problem if the invasion is restricted to a percolation cluster only, all thresholds take the same value, and a standard invasion percolation rule is taken for the invading front. The matrix transfer algorithm can also be obtained as a special case of IPM if the invasion is initiated from a single point only. We also mention an alternative but rather cumbersome algorithm, also employed in MTP, which involves solving the Laplace equation in the original lattice, using an applied potential difference sufficiently large for all elements to be open to conduction and incrementally reducing the potential until flow ceases, at which point the minimum pressure gradient is identified [5].

Patterns

Typical patterns of the invasion fronts at breakthrough, along with the corresponding generalized MTP, are shown in Fig. 3 for various values of n. In these and subsequent simulations, lattice sizes ranged from 50×50 to 500×500 in 2-D, and from $10 \times 10 \times 10$ to $40 \times 40 \times 40$ in 3-D.

At small values of $|n|$, the fronts appear to be self-affine, with front widths and trapped fraction of sites decreasing with decreasing $|n|$. For $n = 0$ (Fig. 3a), the displacement is compact, the front width is equal to the pixel size, there are no trapped sites, and the MTP is a straight line, as the minimum measure S_0 is simply the smallest Euclidean distance from the front to the right boundary. At a slightly larger n (Fig. 3b) the MTP appears to have the structure of a multi-faceted curve. As n increases further (Fig. 3c-3e), front width and trapped fractions increase, and the MTP is more tortuous. In the limit $n \to \infty$, the patterns are shown to approach IP (Fig. 3f), where the front advances by selecting the perimeter site with the minimum size. The corresponding IP pattern (Fig. 3f) suggests that this is indeed the case. The same also holds for the case $n \to -\infty$ (compare Fig. 3h and Fig. 3i), where it can be shown that the pattern approaches that of IP, where the front advances by invading the bond with the maximum size [10].

To prove the reduction to the IP problem in the limit $n \to \infty$, we proceed as follows: Consider any two pairs of neighboring sites (F_1, F_1') and (F_2, F_2') such that the threshold of the bond F_1F_1' is smaller than that of bond F_2F_2'

$$\tau_{F_1F_1'} < \tau_{F_2F_2'} \tag{7}$$

We will show that in the large n limit the following inequality holds

$$V_n(F_1) + \tau^n_{F_1F_1'} < V_n(F_2) + \tau^n_{F_2F_2'} \tag{8}$$

If valid, this implies that site F_1' is invaded before site F_2', which is the desired IP rule. For the proof, we rearrange (8) to read

$$V_n(F_1) < V_n(F_2) + \tau^n_{F_2F_2'}\left[1 - \left(\frac{\tau_{F_1F_1'}}{\tau_{F_2F_2'}}\right)^n\right] \tag{9}$$

and take the large n limit. In view of (7), the inequality in this limit further reduces to

$$V_n(F_1) < V_n(F_2) + \tau^n_{F_2F_2'} \tag{10}$$

However, the latter is always valid, as its reverse implies $V_n(F_2') < V_n(F_1)$, namely that site F_2' has been occupied before site F_1, in contradiction with our implied assumption that site F_2' is a perimeter site. It follows that in this limit, it is the bond with the smallest threshold that is invaded next. This is identical to the IP rule (which in this particular example has a rough physical analogue in imbibition, namely the displacement of a wetting by a non-wetting fluid in porous media [11]). An identical argument applies for the limit $n \to -\infty$, except that now it is the bond with the largest threshold that is occupied next [10]. Either problem involves site-occupancy, bond-percolation with bond trapping. The existence of bond trapping is important for the properties of the limiting percolation problems. Patterns

in the range $(-1/2, 0)$ were also investigated, in view of the special attention paid to this range in the corresponding DPRM problem. The patterns were found to be similar to the case of small and positive n, however.

The IPM algorithm can readily simulate IPM in a radial geometry, in which invasion originates from a single point. In essence, this is a modification of the conventional DPRM problem to invasion which is not directed. An invasion pattern and the corresponding MTP for $n = 1$ is shown in Fig. 4. The pattern reveals a rather compact displacement with a rough front, quite analogous to the rectilinear invasion case. Similar results were found for the same process in 3-D lattices [10]. Finally, we note that processes with other measures can also be defined: For example, we may consider a *stage* process, where each element (stage) has efficiency τ_i, with $0 < \tau_i < 1$, and where the maximization of the overall efficiency, $\prod_i \tau_i$, is sought. Through the transformation $\eta = -\log\tau$, the problem can be mapped into the case $n = 1$, considered previously, except that now the measure to be minimized is $H = -\sum_i \log\tau_i$, namely the thresholds are distributed in the different interval $(0, \infty)$. Likewise, we may define the information (entropy) measure $I = -\sum_i \tau_i \log\tau_i$. The minimization of either H or I also leads to fronts similar to the $n = 1$ case (see [10]).

Directed Invasion

The IPM algorithm was next modified to simulate a directed invasion percolation process. In this version, the front is not allowed to invade bonds in a direction opposite to the main invasion direction (which in the illustrations of Fig. 1-3 is from- right-to-left). As a result, the corresponding MTP is also directed. To show this, we recall that the tracing of the MTP involves the successive connection of pairs of sites, which at some stage of the process were a front growth site and its perimeter site to be occupied next, respectively. As a result, this renders the MTP directed. Using arguments identical to Appendix A for the non-directed case we can show that the directed version leads to the identification of paths that are directed and also minimize the sum of thresholds. In particular, the MTP at breakthrough corresponds to the optimal path of the simplest version of the DPRM problem which shares the same origin as the MTP. The IPM algorithm can be used in the study of more general DPRM problems, and we hope to report on these in the future.

Snapshots of the resulting patterns are shown in Fig. 5 for various values of n. In the case $n = 1$, the optimal path of the DPRM problem is known to be a self-affine curve with a zero transverse average, but with an increasing variance

$$< |y(x)| > \sim x^{\nu_{DP}} \tag{11}$$

where the meandering exponent ν_{DP} has the exact value $\nu_{DP} = 2/3$ [15]. As pointed out, this problem can be mapped to the KPZ equation [8], which is a generic model for surface roughening and surface growth. The self-affine behavior is apparent in Fig. 5b. As in the non-directed case, the path appears to be multi-faceted for sufficiently small n (Fig. 5a), while fronts and minimum paths become more tortuous as n increases (Fig. 5c-5d). In the limit $|n| \to \infty$ the problem becomes a directed, site-occupancy bond IP with bond trapping, and the optimal path becomes its backbone (see Fig. 5e and Fig. 5f). The approach to this limit can also be proved theoretically using arguments similar to those for the non-directed case.

The significant variation of the path properties as n varies has not been reported previously, to our knowledge, most investigations having focused on either $n = 1$ or $-1/2 < n < 0$. In fact, the apparent effect of disorder in varying the patterns from multi-faceted (at small n) to self-similar (at $n \to \infty$) is analogous to the behavior reported in [16], in a different context, and deserves further attention, as it may contradict the apparent universality associated with the DPRM problem.

Comparison with the non-directed case (Fig. 3) shows that for small values of n the two processes are identical (for example compare the patterns for $n = 1$ or smaller, and also note the very close similarity even for $n = 3$). In fact, the two patterns for $n = 1$ in Fig. 3 and 5 are identical, although this happens to be a coincidence of the particular realization. Different realizations show that the MTP for $n = 1$ contains occasional overhangs, the probability of which is briefly discussed below. As n increases to larger values the difference between directed and non-directed invasion increases, both with respect to the invasion patterns and the resulting MTP. The close relation between non-directed and directed IPM processes at small n suggests that the MTP for $n = 1$ has properties similar to the optimal path of the DPRM. On the other hand, the divergence of patterns and paths at larger n shows that this connection does not extend to arbitrary threshold distributions, and specifically those involving relatively large n (large threshold variance or large m). We infer that the MTP coincides with the optimal path of the DPRM at small n, but it differs from it at larger n.

CONNECTION TO GRADIENT PERCOLATION

In essence, the IPM algorithm simulates an Invasion Percolation process, in which the front advances by penetrating perimeter sites with the smallest value of V_n. The front dynamics reflect the distribution of this field, and to understand better the IPM process, it is necessary to consider the distribution of V_n. For future use, we need to point out that the value of V_n at a site can be likened to the energy of the minimum path from that site to the boundary, just as in the DPRM problem, the statistics of which have been well elucidated.

Fig. 6 shows various properties of the distribution of V_1 for a fixed spatial location x (namely over all sites on a column transverse to the main invasion direction). The pdfs at a fixed x appear to be close to a Gaussian (Fig, 6a), but with spatially varying arithmetic mean, $\bar{V}_1$, and standard deviation, σ_{V_1}, and to have the general dependence

$$f(V, x) = \frac{g(\zeta)}{\sigma_{V_1}(x)} \tag{12}$$

Here g is the distribution function, the precise form of which is not important to this paper, and we have defined the normalized variable $\zeta = \frac{V - \overline{V}(x)}{\sigma_{V_1}(x)}$. The functional form (12) is consistent with the corresponding results for the DPRM problem [17]. The variation of $\overline{V}_1$ with x is shown in Fig. 6b. After a short transient, the mean is found to increase linearly with distance, with a constant slope C_1, which is closely related to $\mathcal{L}_1$. The latter also varies with distance, to reflect the finite-size scaling anticipated from [4]. Analogous results are expected for the general n case, where we have $d\overline{V}_n/dx \to C_n$. However, we expect that the approach to the limit is much slower at large n, and in fact that at $n \to \infty$ the transient

lasts until breakthrough. The variation of the mean with distance is consistent with the corresponding result in the DPRM problem, where [17]

$$\frac{d < E >}{dx} = D_1 + D_2 x^{-\frac{2}{3}} \tag{13}$$

The variation of the standard deviation, σ_{V_1}, is shown in Fig. 6c. It is apparent that the variance increases (at least for a substantial fraction of the lattice length), although its rate of increase diminishes at larger x, suggesting a power-law variation with an exponent smaller than unity. We recall [17] that the corresponding DPRM problem has the scaling

$$\sigma_E \sim L^{\frac{1}{2}} f\left(\frac{x}{L^{\frac{3}{2}}}\right) \tag{14}$$

where L is the lattice size and the function f has the asymptotic behavior, $f \sim x^{\frac{1}{3}}$ for $x \ll 1$ and $f \sim$ const. for $x \gg 1$. By analogy, therefore, we expect a similar scaling for the general n MTP problem

$$\sigma_{V_n} \sim L^{\chi_n} f_n\left(\frac{x}{L^{z_n}}\right) \tag{15}$$

where the exponents χ_n and z_n may depend on n and need to be determined. This is not attempted here. In this paper, we will proceed only with the assumption that $0 < \chi_n < 1$, as suggested in the simulations. In passing, we note that previously reported DPRM simulations pertain to $n = 1$, and it is possible that the exponents of (13) and (14) may also vary as a function of n. This problem also deserves further attention.

From the above it is apparent that V_n consists of a transverse average linearly increasing with x and of a perturbation, ψ, namely

$$V_n = C_n x + \psi \tag{16}$$

with $\overline{\psi} = 0$ and with σ_ψ scaling as in (15). In view of the previous, the ratio of the standard deviation to the mean must decrease as x increases. The two facts that the transverse average of V_n increases with x and that the rule for the front advance is to seek the minimum V_n, suggests that IPM is closely related to Invasion Percolation in a Gradient (IPG). We recall that IPG is invasion percolation in an externally applied gradient (e.g. due to a body force, such as gravity, or to a gradient in the bond size [18]), giving rise to a percolation probability gradient measured by the *Bond* number, B. The invasion pattern has the fractal properties of an IP cluster near the front over a scale equal to the front width, σ_F, but it occupies a compact region away from it. The front width scales with B as [1]

$$\sigma_F \sim B^{-\frac{\nu}{\nu+1}} \tag{17}$$

where ν is the *OP* correlation length exponent.

To investigate the connection to IPG, the properties of the perturbation ψ are needed. Fig. 7 shows a grayscale plot of ψ obtained from simulations in a 200× 200 lattice. Also shown, for comparison, is a map of white noise on the same lattice (Fig. 7b). It is clear that the noise generated by the IPM is not an uncorrelated white noise (as in standard IPG) but it is *correlated* in space. For a more quantitative measure of the correlation we constructed the

variograms of ψ in the two different directions [10]. Both variograms displayed correlations growing as a power-law in space, similar to fractional Brownian motion (fBm), with a positive Hurst exponent (H) [19]. For the case $n = 1$, we found $H = 0.32 < 0.5$ and $H = 0.41 < 0.5$ in the respective directions. The Hurst exponent was found to steadily decrease with n (for example, $H = 0.13$ and $H = 0.19$ in the respective directions for $n = 5$, see [10]).

The development of strong large-scale correlations at relatively small n is expected from the definition of the invasion rules. After the front has reached a steady-state mean velocity, the perturbations of two adjacent sites A and B would satisfy $\psi_B = \psi_A + \tau^n_{AB}$, if sites A and B are along the y-direction, or $\psi_C = \psi_A + \tau^n_{AC} - \mathcal{L}^n_n$, if along the x-direction (and where we assumed that the pairs of sites are the growth site and its next to be occupied site, respectively). Then, it is evident that the perturbations of adjacent sites are strongly correlated, and that this correlation diminishes with increasing n. However, this argument also shows that the correlation should be isotropic. We suspect that the anisotropy found in [10] is due to the early transient.

Using the above information we can establish a connection between IPM and IPG. The connection to IPG is demonstrated in Appendix B, where we show that after the early transient, IPM is an IPG with a *Bond* number given by

$$B_n = D_c \left[\frac{\frac{d\bar{V}}{dx}}{\sigma_{Vn}(x_F)} \right] \tag{18}$$

where the constant D_c solves an algebraic equation depending on the form of the scaling function g. The two keys to this relationship is the assumed scaling of V_n, equation (12), and the decay of the derivative of σ_{Vn} with distance, equation (15) (although for a 2-D square lattice and a symmetric g the latter condition is not necessary, see Appendix B). Contrary to conventional IPG, however, the above *Bond* number is not constant but varies with x, as a result of the variation of σ_{Vn}. Equation (18) can be further approximated as

$$B_n \sim \frac{\mathcal{L}^n_n}{\sigma_{Vn}(x_F)} \tag{19}$$

since C_n eventually approaches $\mathcal{L}^n_n$ (see below).

The identification of IPM with IPG allows us to express the scaling of the front width, σ_F, with the above-defined *Bond* number. Now, however, we must consider IPG in a correlated lattice with growing correlations, as suggested in Fig. 7. Despite this, the same arguments used for the conventional IPG scaling (17) apply here as well (see also [20]), except that ν should be the correlation length exponent corresponding to percolation in such a lattice. Percolation in long-range correlated lattices of the fBm type has been studied by Isichenko [21] who showed that for $H > 0$ the correlation length exponent diverges, $\nu \to \infty$. For IPG in such lattices, therefore, substitution in (17) leads to the scaling

$$\sigma_F \sim B_n^{-1} \tag{20}$$

The theoretical prediction (20) is tested in Fig. 8, which shows a plot of the front width, computed as in [1], vs. the above-defined *Bond* number. The data at relatively large B_n are fitted very well with a straight line of slope -1, as indeed predicted from (20). At smaller

B_n (larger n), the slope decreases and eventually becomes zero, as the lateral lattice size interferes with the process (as in IPG) and the front width saturates.

Equation (20) also allows us to relate the standard deviation of V_n to that of the front. Substitution of (18) in (20) yields

$$\sigma_F \sim \sigma_{Vn}(x_F) \tag{21}$$

which suggests that the ratio of the front width to the standard deviation of V_n is constant. A plot of this ratio for a particular realization of IPM with $n = 1$ is shown in Fig. 9. It is clear that after some early transients, the ratio fluctuates around a constant value, as predicted from equation (21). This behavior was also confirmed for other values of n, although the transient period increases with n. Equation (21) indicates that the variation of the front width with distance follows the same scaling as the standard deviation of V_n, which was conjectured in (15) to have a self-affine scaling. This leads to the result

$$\sigma_F \sim L^{\xi_n} f_n\left(\frac{x}{L^{z_n}}\right) \tag{22}$$

where the function f has the same asymptotic scaling.

In summary, in this section we established a connection of IPM with IPG, with two important twists: that in IPM the probability gradient is generated dynamically during the process instead of being externally specified; and, at least for finite n, the process is one of Gradient Percolation in a *correlated* field. We note that identical findings also apply for the directed problem, hence a connection must exist between the DPRM problem and IPG in a correlated field. This connection is worth exploring further.

GENERAL RESULTS

Using the previous algorithm, various quantities of interest can be calculated. In particular, we consider the MTP, the minimum gradient and the MTP tortuosity. A study of the distribution of thresholds can be found in [10]. All these results are for the non-directed case. Results for the directed problem will be reported in a future study.

Minimum Threshold Path

The MTP for $n = 1$ is shown in Fig. 10 for invasion in a cubic lattice. Generalized MTPs for variable n were shown in Fig. 3. These vary from a straight line for $n = 0$ to self-similar fractals for $n = |\infty|$. The increase in tortuosity as $|n|$ increases is due to the change of the invasion front from compact to self-affine to self-similar, as discussed above. For a finite n, therefore, and specifically for $n = 1$, we expect that the MTP is a self-affine curve (in the more general definition of Feder [19], which also encompasses gradient percolation fronts) with a width that decreases as $|n|$ decreases. In particular for sufficiently small $|n|$, the MTP coincides with the optimal path of DPRM. As $|n| \to \infty$, the MTP approaches a specific limiting curve. To understand its properties we first recall that for any n, the invading phase resides on self-avoiding dendritic branches emanating from the right boundary. These branches have the property that any two invaded sites on the same branch can be joined

by only one self-avoiding path consisting of invaded sites, while invaded sites belonging to different branches cannot be joined by any such path (except by a path that passes from the origin). The MTP is part of the backbone of these branches, after dendritic fractions are suppressed. Figure 11 shows the backbones of the various branches at the breakthrough point for $n = 1$ and $n = \infty$. In the first case (and also when $|n|$ is not large), many parallel-like branches co-exist, and the MTP is the part of the particular branch that has reached the opposite side. However, in the percolation limit, $|n| = \infty$, a dominant branch develops. By definition, this branch, which is also the MTP at the $|n| = \infty$ limit, is the backbone of the cluster of a site occupancy-bond IP with bond trapping, obtained in the large $|n|$ limit. Therefore, in the general n case, the MTP is unrelated to a property of the percolation cluster. In particular, the MTP for $n = 1$ is not a self-similar fractal, but instead it is a member of a general family of self-afine curves that includes as a limit (large $|n|$) the backbone of a site-bond percolation cluster. Because, contrary to regular site- or bond-percolation, this percolation process involves a *looples* percolation cluster, the MTP in that limit is also a *loopless* fractal. It can be shown that the latter is a subset of the backbone of the invasion cluster in conventional bond percolation, but it does not coincide with the conventional chemical distance of percolation [10].

In a recent paper, pointed to us by one of the reviewers, Cieplak et al. [25] proposed a loopless IP similar to IPM for $n = \infty$. They reported that the backbone is a self-similar fractal with fractal dimension $D = 1.22$ in 2-D and $D = 1.42$ in 3-D. In agreement with our observations, they also found that the geometry of this backbone is not the same with that of the chemical distance on the percolation cluster.

Similar results are obtained for the optimal path of the DPRM problem in the large $|n|$ limit, which can be shown to be the loopless backbone of the corresponding directed IP cluster. The significance of the variation of the optimal path of the DPRM problem with n was commented in section II.

Minimum Gradient

Another quantity of significant interest is the generalized percolation threshold, $\mathcal{L}_n$, which in the case $n = 1$ reduces to the minimum gradient, $|\nabla\Phi|_{min} \equiv \mathcal{L}_1$. It was found that after some transients, $\mathcal{L}_1$ stabilizes to a mean value approximately equal to 0.305 ± 0.01. The corresponding value for 3-D cubic lattices was found to be 0.196 ± 0.005. These compare well with the respective values of 0.29 and 0.17, reported by Sahimi [5]. The value of 0.22 found by Roux and Herrmann [4] in a square lattice tilted at 45° is also consistent with the above, if we make the obvious transformation $0.305/\sqrt{2} \approx 0.22$, to reflect the difference in the definition of length L in the two problems. The latter results were also verified in [10] by additional simulations in a tilted 200×200 lattice, which gave the value of 0.2232.

The variation of the more general measure $\mathcal{L}_n$ with n is shown in Fig. 12 (including $n < 0$). For positive n, this measure is a monotonically increasing function of n and approaches the limit $\mathcal{L}_\infty \to p_c = 0.5$, as anticipated by Roux et al. [4]. Indeed, from definition, we have

$$\sum_i \tau_i^n = \tau_{max} \left[1 + \sum_{i \neq max} \epsilon_i^n \right] \to \tau_{max}^n \tag{23}$$

where the notation is self-evident and we have taken $\epsilon_i = \tau_i/\tau_{max}$. It follows that

$$\mathcal{L}_\infty = \min \lim_{n\to\infty} \frac{\tau_{max}}{L^{1/n}} = \min \tau_{max} \left(\frac{1}{L}\right)^0 = \min \tau_{max} = p_c \tag{24}$$

where p_c is the threshold to a percolation process in which the front advances by invading the minimum threshold. A similar analysis holds for the opposite limit $n \to -\infty$, where the limit $\mathcal{L}_{-\infty} \to 1 - p_c$ was also verified. In view of the relation between the moments for general n and general pdfs, these results provide a qualitative picture of the dependence of the minimum sum of thresholds distributed from general pdfs, on the ratio of the standard deviation to the arithmetic mean.

We also note that $\mathcal{L}_n^n$ is related to the slope C_n of the spatial variation of the mean for the following reasons: The arithmetic mean $\overline{V}_n$ approaches the mean of V_1 sampled over all front sites. However, the latter also approaches $\mathcal{L}_n^n$, because by construction, the maximum difference between any two values of V_n at the front is bounded by $\max\tau^n = 1$. Hence, for a sufficiently large lattice or a sufficiently small n, all values at the front (including the minimum sum $\mathcal{L}_n^n$) eventually must grow at the same rate. This does not necessarily imply that the width of the front approaches a constant, however. Thus, we also expect the asymptotic relationship

$$\frac{d\overline{V}_n}{dx} \approx \mathcal{L}_n^n \tag{25}$$

for all n.

Tortuosity of the MTP

A final quantity of interest is the tortuosity of the MTP. We expect the tortuosity to be constant for a self-affine curve and size-dependent for a self-similar fractal. The variation of the tortuosity, t_1, of the MTP with $n = 1$ with lattice size was studied in [10], where it was found that although fluctuating at smaller sizes, it approaches a constant value at large sizes, the width of the fluctuations decreasing to zero. This adds support to our observation on the self-affinity of the MTP. From our simulations we found $t_1 = 1.31 \pm 0.01$ and 1.55 ± 0.02, for 2-D square and 3-D cubic lattices, respectively. These tortuosity data are new. The tortuosity of the generalized MTP was found to increase with n, however, reflecting the increased variance of the threshold distribution (see [10]).

Since the tortuosity is not a universal property, it will be affected by the particular shape of the threshold distribution. A simple, local, model for an arbitrary distribution of thresholds can be obtained as follows: We recall that the tortuosity of the MTP reflects the advantage incurred to the path in occasionally taking transverse steps that minimize the energy cost. Fig. 13 shows schematically some of the infinitely many possibilities, for the advancement of the path in one increment in the direction, x. Denote by P_k the probability of the MTP taking a total of k steps in order to advance by a single increment in x,

$$P_k = \Pr[\tau_2 + \tau_3 + \cdots + \tau_{k+1} < \tau_1] \quad ; \quad \mathrm{k} = 2, 3, \cdots \tag{26}$$

where the values of τ are random thresholds from a given pdf. Then, the total path length l is equal to

$$l = L(1 + \sum_{i=2,\infty} w_i(i-1)P_i) \tag{27}$$

where w_i is the number of different configurations corresponding to a given number of steps (for example, $w_5 = 2$ in Fig. 13). Given a pdf, the various probabilities above can be computed. In particular, for the case of a uniform pdf in (0, 1), which is also the previous $n = 1$ case, we can compute the probabilities of (26) to find [10]

$$P_k = \frac{1}{(k+1)!} \tag{28}$$

For the tortuosity of the path requires that the weights w_i be computed. For the square lattice configuration of Fig. 13, $w_2 = w_3 = w_4 = 1$, but $w_5 = 2$, etc.. Configurations of a larger number of steps have larger w_i, but substantially smaller probability. If, as an approximation, we take $w_i = 1$ for all i, we obtain the result $t_1 \approx 4-e = 1.282$, which is reasonably close to the numerical value given above. The discrepancy is due to the assumption made. Inclusion of path multiplicity, which increases with k, will lead to an improved agreement. This simple model can be used to investigate the effect on the MTP tortuosity of more general pdfs [10], or to estimate the probability of an overhang in a path (such as depicted in Fig. 13e, for example).

HIGHER-COST PATHS

In many applications, such as the flow of Bingham plastics and foams in porous media [5], [6], [22], the behavior following the onset of flow or displacement is of significant interest. In this context, the identification of paths of higher cost (energy) than the MTP is necessary. This problem also arises in the DPRM case, where patterns reminiscent of river deltas were found [3]. In this section, we use the IPM algorithm to identify these paths as the applied potential difference across the lattice increases. We note, again, that contrary to the DPRM problem, where all paths originate from a single point, here the paths can originate from many different points on the injection face.

When the applied potential gradient exceeds the minimum $|\nabla\Phi| > |\nabla\Phi|_{min}$, additional bonds, not belonging to the MTP, can become open. The new paths that are formed are identified by the condition that the overall sum of thresholds on them exceeds the minimum potential difference but is smaller than or equal to the applied. We proceed by identifying the sequence of paths with progressively higher energy. Only the threshold across a bond is considered to contribute to the cost across an open bond (namely there is no flow-induced potential drop, as would be for example the case in the flow of a Bingham plastic). The new paths can be completely new paths, unrelated to the MTP or other open paths, or they may share with them some of their bonds. In the latter case, an open path could act as a bridge between two already open paths, it may form a loop with one path, or it may connect one end of the lattice to a point of an already open path. The algorithm to find such paths must simultaneously identify the path and also determine its cost (the necessary potential

gradient to make it open). It is described in the following. For simplicity, the discussion will be restricted to the $n = 1$ case, the generalization to other values of n being straightforward.

We recall that at the conclusion of IPM, a value V (where the subscript n was ommitted) is assigned to every invaded site, that denotes the minimum overall threshold from the site to the RHS boundary of the lattice. Consider, next, another IPM process, now from the left side, through which another function, W, is assigned to each site, that denotes the minimum overall threshold from the site to the LHS boundary of the lattice. The minimum potential Φ_{ij} needed to open a bond between two adjacent lattice sites i and j (see Fig. 14) must be the minimum of the cost of the two alternative pathways, namely

$$\Phi_{ij} = \min\left(V_i + \tau_{ij} + W_j, V_j + \tau_{ij} + W_i\right) \tag{29}$$

Hence, from a knowledge of the functions V and W at every site, the minimum potential to open a given bond, Φ_{ij}, can be computed.

Having assigned Φ, the algorithm proceeds sequentially from low to high energies by identifying the candidate bonds belonging to the next open path. Fig. 15 shows the opening of the various paths as the potential difference increases. As expected, the first such path is the MTP. The successive opening of new paths is apparent in the model. These form correlated pathway regions (valleys), which are different than the paths of OP. The successive opening of pathways leads to "flooded" regions of increasing width analogous to the "river deltas" of the DPRM problem. Based on these results, the fraction of bonds belonging to open paths vs. the applied potential gradient can be computed. Fig. 16 shows the results obtained. After the minimum gradient, the fraction of open bonds increases following an S-shape curve. The curve has percolation-like characteristics, in that there is a threshold $\mathcal{L}_1$, but it is not actually related to percolation, except in the limit of large n. In fact, the scaling of the curve (for $n = 1$) near the threshold, was shown by Roux et al. [4] to be a power-law with exponent equal to 2. The results of Fig. 16 were used in [22] to model the fraction of flowing foam in porous media.

UNSTABLE PROCESSES

In the above, we studied stable IPM. We can extend the study to "unstable" invasion processes, where the thresholds are viewed as gains, rather than penalties, and where instead of minimizing the cumulative threshold (penalty) we maximize the cumulative gain. Thus, the rule for the advance of the front would maximize, instead of minimizing, the measure S_n. The corresponding algorithm is trivially implemented. A typical snapshot of such processes from simulations in a 2-D lattice is shown in Fig. 17, where a trapping rule was implemented. In the case of trapping, the invading phase consists of a singly-connected self-similar thread of sites. Contrary to the previous case, the front is a self-similar fractal and was found to be identical for all n.

In the case of trapping, we can show that this path of maximum gain is a Self-Avoiding Random Walk (SAW) constrained to take place to the right of the invasion boundary. Indeed, by construction, the growth site is always the tip of the front, the site to be invaded next being the one of $Z-1$ neighbors (where Z is the coordination number of the lattice) with the largest value of $\tau^n_{F,F'}$. This process can be equivalently simulated by randomly advancing the tip to

one of its neighboring unoccupied sites. The resulting path has the SAW properties. Because of the trapping rule, however, the path obtained is not the global maximum, which would obviously consist here of a path that covers the entire lattice (of dimension 2). Properties of SAW have been extensively discussed in previous references [23].

The difference in the invasion fronts as we switch from minimizing the penalty to maximizing the gain is similar to the change from IPG in a stabilizing gradient to IPG in a destabilizing gradient in percolation processes [24]. The rule of minimizing the cumulative penalty stabilizes the propagation of the front, in contrast to the rule of maximizing the cumulative gain, which creates a great degree of instability. A similarity can also be drawn between anti-DLA compact fronts and DLA fractal fronts [11], which characterize viscous stable and viscous unstable, respectively, displacements in porous media.

CONCLUSIONS

Motivated by the problem of finding the path that minimizes the sum of thresholds in a lattice of elements with thresholds τ_i, randomly distributed in $(0,1)$, we developed a class of invasion processes, in which the front advances by minimizing or maximizing the measure $S_n = \sum_i \tau_i^n$, where n is a real number. Because this rule assigns long-time memory to the invasion front, these processes belong to a new class of Invasion Percolation with Memory (IPM). Depending on whether the rule minimizes or maximizes S_n, the invasion fronts are either stable and self-affine (case of minimum penalty) or unstable and fractal (case of maximum gain). The stable case was connected to Invasion Percolation in a Gradient [1], but in a correlated lattice with self-affine correlations of the fBm type (positive Hurst exponent [19]), with Invasion Percolation [2] recovered in the limit $|n| = \infty$. In the unstable case, the IPM process was found to be a Self-Avoiding Random Walk (SAW), for any n. These processes also include as a special case the (simplest) problem of Directed Polymer in Random Media (DPRM) [3], by restricting the invasion to one direction. An important difference is that the IPM algorithm leads to optimal paths that can originate from any point along a curve.

The algorithm is well suited for the identification of minimum threshold paths (MTP) that minimize the sum of τ_i^n across any two curves (as well as from any site to a given curve). For the corresponding DPRM problem, the MTP becomes the optimal path of DPRM, which for the case $n = 1$, is known to be self-affine. In general, the MTP was shown to range from a straight-line in the case of $n = 0$ to a multi-faceted curve at small n to a self-similar fractal in the large $|n|$ limit. The latter is the backbone of a mixed site-bond percolation cluster, and differs from the standard backbone of OP in that it does not contain reconnections (it is loopless). Its properties were recently studied in [25]. The MTP for $n = 1$, corresponding to the classical problem, is not a self-similar fractal and does not coincide with the minimum path of OP. Instead, it is very closely related to the optimal path of DPRM and appears to be self-affine. The dependence of the MTP on n raises questions about the universality of the corresponding optimal path of the DPRM problem, when distributions with a large variance are considered. Various results on the MTP, the minimum gradient and the path tortuosity were obtained. In particular, the algorithm allows the identification of paths of higher energy (cost), which generalize the "river deltas" of the DPRM problem.

References

[1] B. Sapoval, M. Rosso, and J. F. Gouyet, J. Phys. (Paris) Lett. **46**, L149 (1985); J. F. Gouyet, M. Rosso, and B. Sapoval, Phys. Rev. B **37**, 1832 (1988); J. P. Hulin, E. Clement, C. Baudet, J. F. Gouyet, and M. Rosso, Phys. Rev. Lett. **61**, 333 (1988).

[2] D.Wilkinson and J. F. Willemsen, J. Phys. A **16**, 3365 (1983).

[3] T. Halpin-Healy, anf Y.-C. Zhang, Phys. Reports **254**, 215 (1995); A.-L. Barabasi and H. E. Stanley, *Fractal Concepts in Surface Growth* (Cambridge University Press, 1995).

[4] S. Roux, A. Hansen and E. Guyon, J. Physique **48**, 2125 (1987); S. Roux and H.J. Hermann, Europhys. Lett. **4**, 1227 (1987).

[5] M. Sahimi, AIChE J. **39**, 369 (1993); C.B. Shah, H. Kharabaf and Y.C. Yortsos, Proc. 6th UNITAR Conference, Houston, TX (Feb. 12-16, 1995).

[6] W. R. Rossen and C. K. Mamun, Phys. Rev. B **47**, 11815 (1993).

[7] B. Stauffer and A. Aharony, *Introduction to Percolation Theory* (Francis-Taylor, 2nd. Edition, 1992).

[8] M. Kardar, G. Parisi, and Y.-C. Zhang, Phys. Rev. Lett. **56**, 889 (1986).

[9] U. M. B. Marconi, and Y.-C. Zhang, J. Stat. Phys. **61**, 885 (1990).

[10] H. Kharabaf, Ph.D. Dissertation, University of Southern California (1996).

[11] R. Lenormand, J. Phys. Condens. Matter **2**, SA79 (1990); M. Blunt, M. J. King and H. Scher, Phys. Rev. A **46**, 7680 (1992).

[12] S. Roux and E. Guyon, J. Phys. A: Math Gen. **22** 3693 (1989); P. Meakin, J. Feder, V. Frette, and T. Jossang, J. Phys. Rev. A **46** 3357, (1992); P. Meakin, A. Birovljev, V. Frette, J. Feder, and T. Jossang, *Phycica A* **191** 227 (1992).

[13] M. M. Dias and D. J. Wilkinson, J. Phys. A, **19**, 3131- 3146 (1986); see also Y. C. Yortsos and M. Sharma, AICHEJ **32**, 46 (1986).

[14] Herrmann, H. J., Hong, D. C., Stanley, H. E., J. Phys. A: Math. Gen. **17** L261-L266 (1984).

[15] M. Kardar, and Y.-C. Zhang, Phys. Rev. Lett. **58**, 2087 (1987).

[16] C. S. Nolle, B. Koiller, N. Martys, and M. O. Robbins, Phys. Rev. Lett. **71**, 2074 (1993); C. S. Nolle, B. Koiller, N. Martys, and M. O. Robbins, Physica A, **205**, 342 (1994).

[17] J. M. Kim, A. J. Bray, and M. A. Moore, Phys. Rev. A **44**, 2345 (1991).

[18] M. Chaouche, N. Rakotomalala, D. Salin, B. Xu and Y. C. Yortsos, Phys. Rev. E **49**, 4133 (1994).

[19] J. Feder, *Fractals* (Plenum, New York, 1988).

[20] L. A. N. Amaral, A.-L. Barabasi, S. V. Buldyrev, S. T. Harrington, S. Havlin, R. Sadr-Lahijany, and H. E. Stanley, Phys. Rev. E **51**, 4655 (1995).

[21] M.B. Isichenko, Rev. Mod. Phys **64**, 961 (1992).

[22] H. Kharabaf, and Y.C. Yortsos, paper SPE 36663, presented at the 1996 SPE Annual Technical Conference and Exhibition, Denver, Co, Oct. 7-9 (1996).

[23] B. Nienhuis, Phs. Rev. Lett. **49**, 1062 (1982); P. Grassberger, J. Phys. A: Math. Gen. **26**, 1023 (1993).

[24] V. Frette, J. Feder, T. Jossang, and P. Meakin, Phys. Rev. Lett. **68**, 3164 (1992).

[25] M. Cieplak, A. Maritan and J.R. Banavar, Phys. Rev. Lett. **76**, 3754 (1996).

APPENDIX A

Proving that $V_n(A)$ represents the minimum sum of thresholds from site A to the injection boundary, is equivalent to proving that the minimum threshold path from A to the injection boundary is the MTP determined algorithmically using the IPM process (path $\mathcal{L}$ in Fig. 18). First, we recall that through the IPM algorithm, *all* sites in the lattice can be invaded, and thus be assigned a unique value V_n. This can be accomplished by continuing the invasion process following breakthrough, and by also removing the trapping rule.

To prove our assertion, we use a *reduction in absurdio* argument: Assume that there exists another alternative path, denoted as $\mathcal{L}^*$ in Fig. 18, and consider the first site B on path $\mathcal{L}$ at which the two paths first diverge. Without loss in generality, we can take this site to be site A. (In the opposite case, we can apply the argument for site B. If the minimum threshold path from B is the MTP determined from the IPM algorithm, then, by extension, path $\mathcal{L}$ from A will also be the MTP). For future use, we consider the invasion stage when site A becomes invaded for the first time. In the notation of the text, at that time site A will be denoted as site G'. By construction, the value $V_n(A)$ assigned to it corresponds to the minimum value of $S_{n,FF'} = V_n(F) + \tau^n_{FF'}$, for every site F on the invasion front at that time. By the same token, $V_n(A)$ must also be larger than the value $V_n(I)$ assigned to all invaded sites I (including the front sites) prior to this time, since in the opposite case, site A would have been invaded at an earlier time. Hence, we have the inequalities

$$V_n(F) < V_n(A) \leq V_n(F) + \tau^n_{FF'} \tag{30}$$

for all sites at the front. Furthermore, the second inequality also implies

$$V_n(A) < V_n(I') \tag{31}$$

for all sites I' invaded following the invasion of site A. The corresponding MTP (path $\mathcal{L}$ in Fig. 18) connecting A to the RHS boundary is traced with the use of the IPM algorithm as

discussed in the text. In particular, this path contains the bond AG, where G is the growth site for A.

Assume, now, that path $\mathcal{L}^*$ is the MTP. This implies that the sum of thresholds along this path is equal to a new value, $V_n^*(A)$, where

$$V_n^*(A) < V_n(A) \tag{32}$$

and that site G^* on $\mathcal{L}^*$ adjacent to A has also assigned to it a value $V_n^*(G^*)$ such that

$$V_n^*(A) = V_n^*(F_{G^*}) + \tau^n_{F_{G^*}F'_G} \tag{33}$$

where

$$V_n^*(F_{G^*}) < V_n(F_{G^*}) \tag{34}$$

Inequality (34) follows from the fact that in the reverse case, we would have $V_n^*(A) > V_n(A)$, due to (30) and (33), in case site G^* was a front site at the time site A was invaded, or due to (31), in case G^* was invaded after site A. By comparing (32) and (34) it follows that to prove the existence of a path at A alternative to the MTP determined from the IPM algorithm, requires to prove the same for site G^*. By induction, therefore, the problem is reduced to proving the validity of inequality (32) for the first ever site A invaded. But this is not possible, since for such a site, $V_n(A)$ represents by construction the minimum threshold adjacent to the injection face. It follows that inequalities (34) and (32) are not valid, thus, the MTP determined from the IPM algorithm is the path that minimizes the sum of thresholds, as claimed.

APPENDIX B

Consider bond Invasion Percolation in a field of V values (where we have omitted subscript n for simplicity), with the following pdf

$$f(V,x) = \frac{g(\theta)}{\sigma_V(x)} \tag{35}$$

where g is a function of the normalized vairable $\theta = \frac{V-\overline{V}(x)}{\sigma_V(x)}$. Conventionally, in IP the front advances by penetrating the perimeter bond with the smallest value of V. Let the mean front position at a given stage of the process be x_F, and assume that the bond to be invaded next has the value V_M. Then, we can assign to any position x, a percolation probability fraction p

$$p(x) = \int_0^{V_M} f(V,x)dV \tag{36}$$

which, in view of (35) can be simplified to

$$p(x) \approx G\left(\frac{V_M - \overline{V}(x)}{\sigma_V(x)}\right) \tag{37}$$

Here we defined

$$G(\theta) = \int_{-\infty}^{\theta} g(\eta) d\eta \tag{38}$$

and also assumed that x is sufficiently large for $\overline{V}(x)/\sigma_V(x) \gg 1$ (since at large x, σ_V grows slower than $\overline{V}(x)$). Now, (37) also applies at the mean front position, where as is well known from the theory of Gradient Percolation [1], p is equal to the percolation threshold, p_c. Hence,

$$p_c = G\left(\frac{V_M - \overline{V}(x_F)}{\sigma_V(x_F)}\right) \tag{39}$$

This is an algebraic equation with respect to the argument, the solution of which leads to an expression for V_M. By denoting its root by θ_c, we find

$$V_M = \sigma_V(x_F)\theta_c + \overline{V}(x_F) \tag{40}$$

As an example, we may take a Gaussian distribution, for which the expressions corresponding to (38) and (39) read $G(\theta) = \frac{1}{2}(1 + \mathrm{erf}\theta)$ and $p_c = \frac{1}{2}\left(1 + \mathrm{erf}\left(\frac{V_M - \overline{V}(x_F)}{\sigma_V(x_F)}\right)\right)$, respectively, and where θ_c is the root of

$$\frac{1}{2}(1 + \mathrm{erf}\theta_c) = p_c \tag{41}$$

In the latter case, we also have, $\theta_c = 0$, or $\theta_c = -0.48$ for a 2-D square or a 3-D cubic lattice, respectively. We note that the result $\theta_c = 0$ is also valid for all 2-D square lattices with even g.

Now, we can substitute (40) in (37) and expand in a Taylor series around the mean front position x_F to obtain around the front

$$p = p_c - B(x - x_c) + O((x - x_c)^2) \tag{42}$$

where the *Bond* number B is equal to

$$B = G'(\theta_c)\left[\frac{\frac{d\overline{V}}{dx}}{\sigma_V(x_F)} + \theta_c \left.\frac{\frac{d\sigma_V}{dx}}{\sigma_V}\right|_F\right] \tag{43}$$

which for a Gaussian, also reads

$$B = \frac{\exp(-\theta_c^2)}{\sqrt{\pi}}\left[\frac{\frac{d\overline{V}}{dx}}{\sigma_V(x_F)} + \theta_c \left.\frac{\frac{d\sigma_V}{dx}}{\sigma_V}\right|_F\right] \tag{44}$$

Thus, if we further assume that $\frac{d\ln\sigma_V}{dx}$ decreases with x to zero, as is the case with V_n, the second term in the RHS inside the brackets becomes negligible at large x, hence

$$B \approx D_c\left[\frac{\frac{d\overline{V}}{dx}}{\sigma_V(x_F)}\right] \tag{45}$$

where $D_c = G'(\theta_c)$. This relationship is exact for $\theta_c = 0.5$, for example for even pdf's in a square lattice.

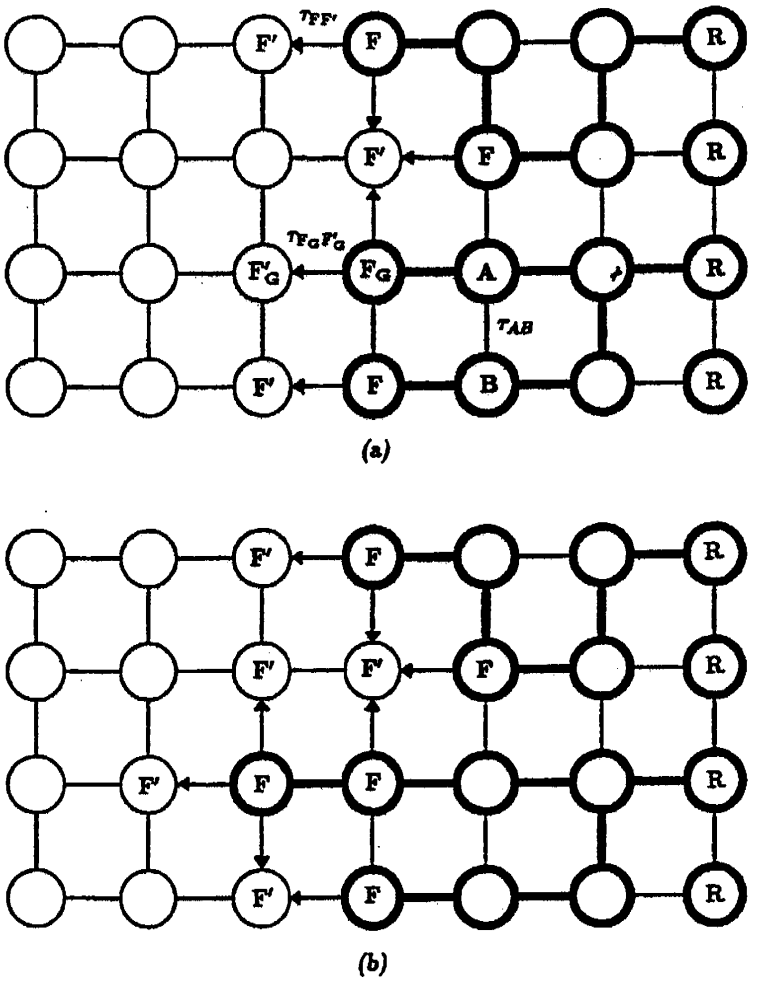

Figure 1: Description of the invasion rules, before (a) and after (b) a growth step. Invasion occurs from right to left. F denotes a front site, F' a perimeter site, F_G is a growth site and F'_G is the site occupied next. The process is site-occupancy bond-invasion percolation.

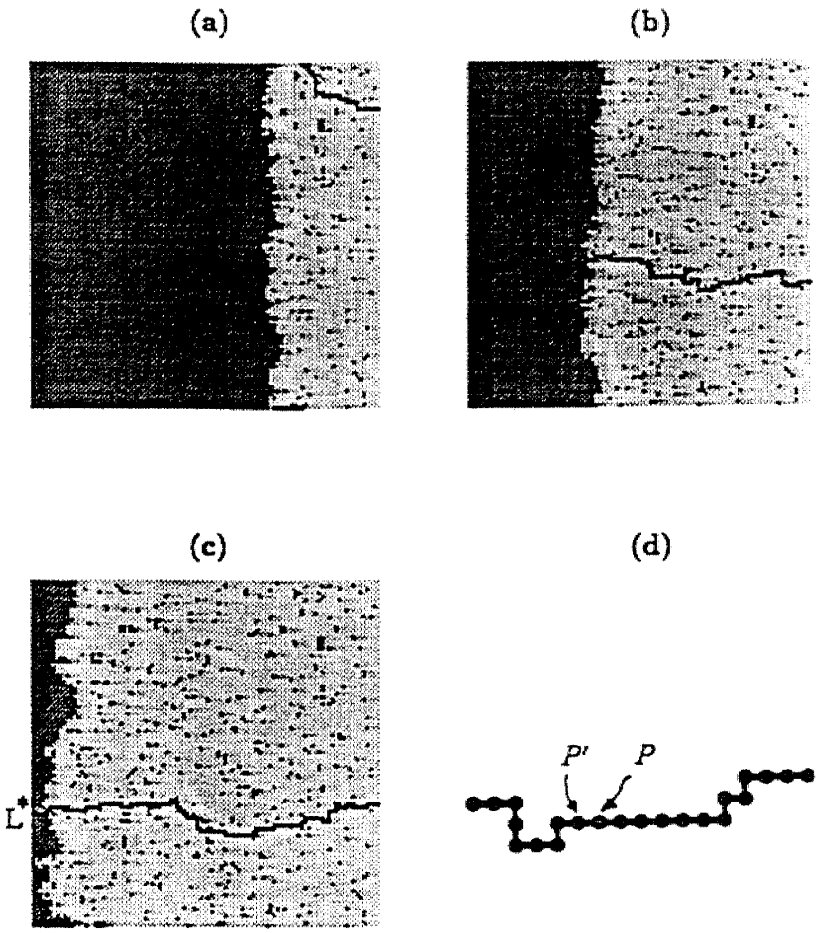

Figure 2: Snapshots of the invasion process (occupied sites in grey) and of the MTP at different stages of invasion (a)-(c) for $n = 1$ in a 100×100 square lattice. Periodic boundary conditions were used. L^* denotes the site at "front breakthrough" on the left boundary. Fig. 2d shows the terminology used to identify the MTP. Note that the MTP at different stages is not necessarily a subset of the final MTP.

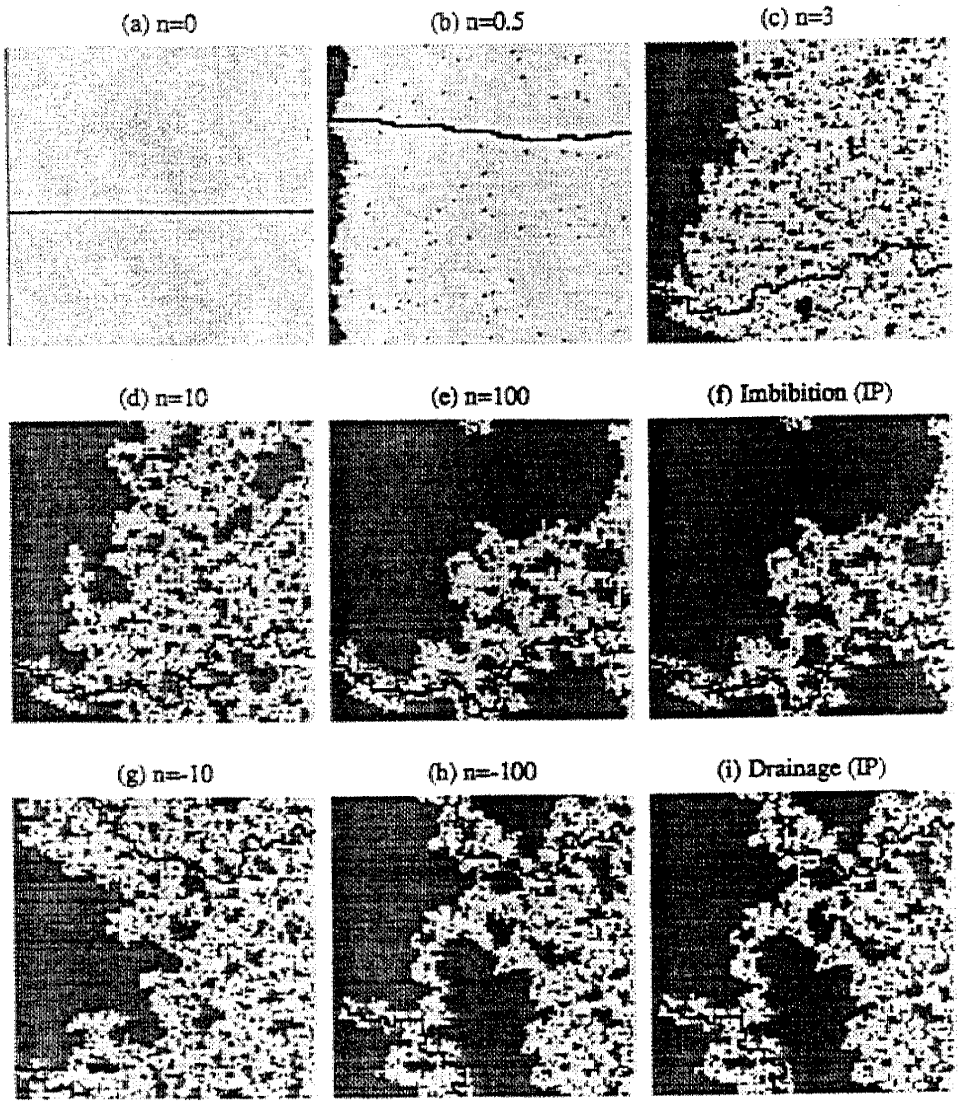

Figure 3: Invasion fronts at "breakthrough" and corresponding MTPs in a 100×100 lattice, for $n = 0$ (a), $n = 0.5$ (b), $n = 3$ (c), $n = 10$ (d), $n = 100$ (e). Pattern (f) is Invasion Percolation, where the front advances by penetrating the bond with the smallest threshold. Pattern (g) is for $n = -10$, pattern (h) for $n = -100$ and pattern (i) corresponds to Invasion Percolation, where the front advances by penetrating the bond with the largest threshold. Note the similarity of (e) with (f) and of (h) with (i). Fronts become more self-similar, and the fraction of trapped sites increases (MTPs are more tortuous) as n increases.

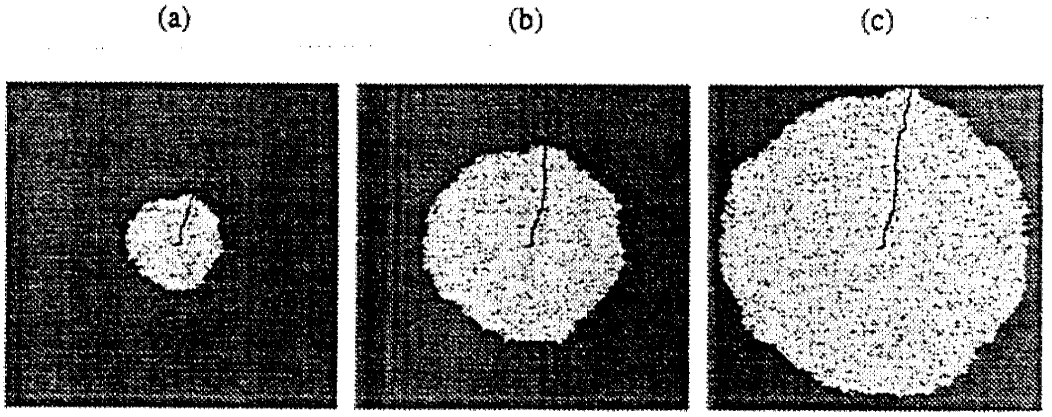

Figure 4: Invasion pattern and the corresponding MTP for $n = 1$ for IPM in radial geometry (originating from a single point of a 300×300 square lattice).

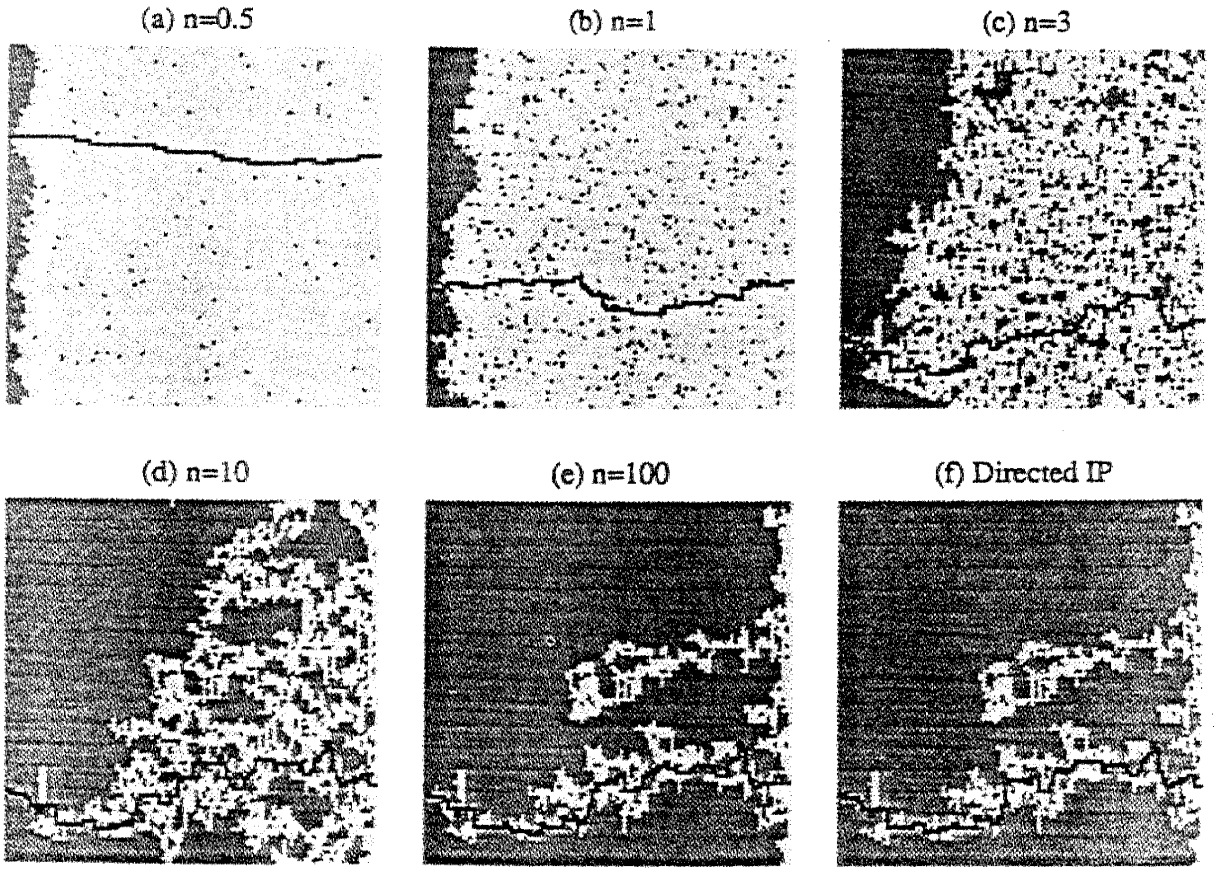

Figure 5: Invasion fronts at "breakthrough" and corresponding MTPs for directed invasion and for $n = 0.5$ (a), $n = 1$ (b), $n = 3$ (c), $n = 10$ (d), $n = 100$ (e), and Directed IP (f). The optimal path of this DPRM at large n is the backbone of a directed percolation cluster.

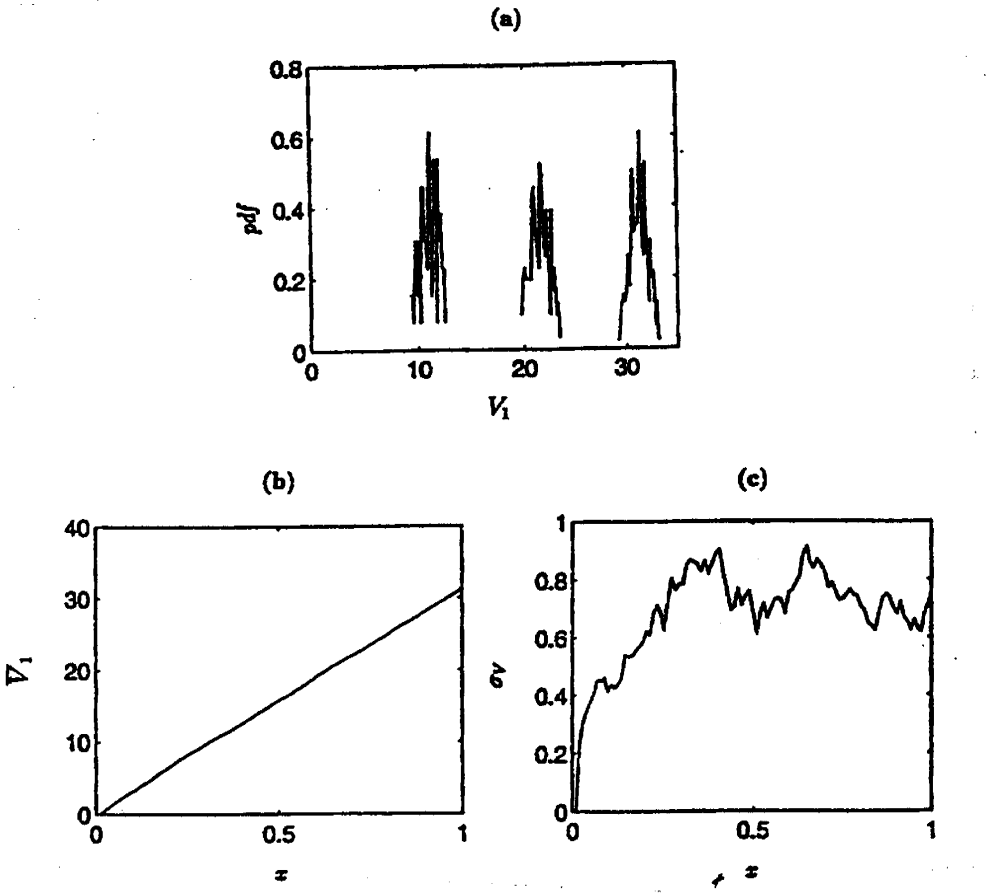

Figure 6: Statistics of the energy (cost) distribution V_1 from simulations in a 100×100 lattice: (a) The pdf at three different values of x (equal to 0.25, 0.50 and 0.75), (b) the variation of the arithmetic mean $\overline{V}_1$ with x, and (c) the variation of the standard deviation, σ_{V_1} with x.

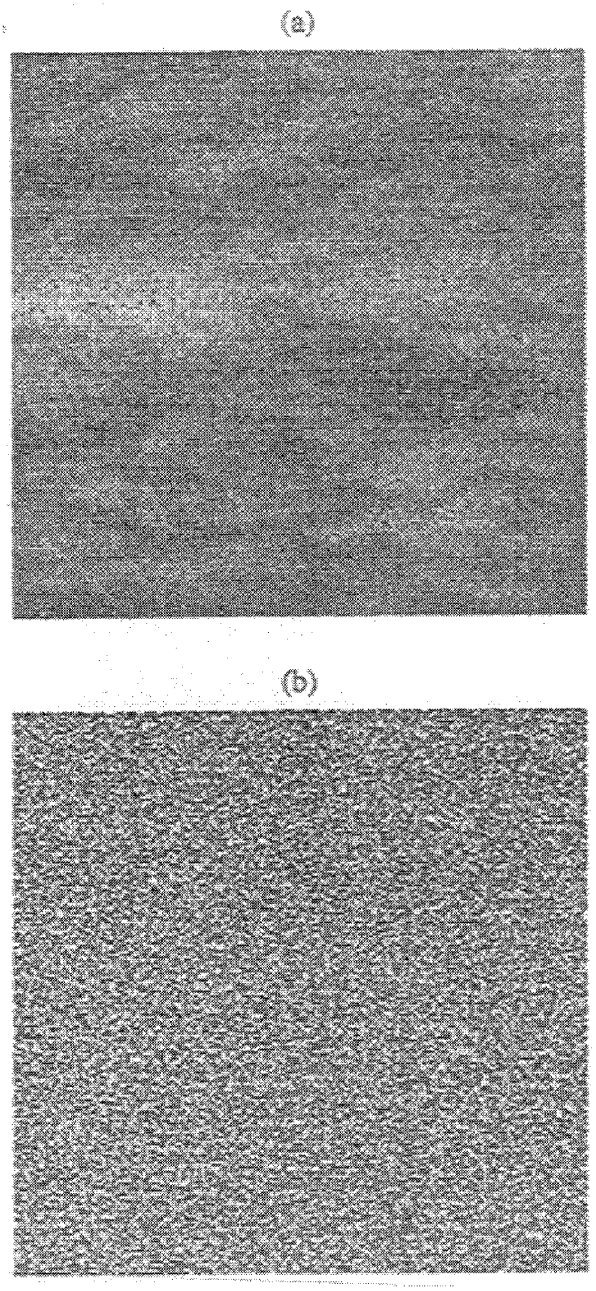

Figure 7: Grayscale plot of the perturbation ψ for $n = 1$ from simulations in a 200×200 lattice (a). Figure (b) shows a Gaussian noise for the same lattice. Darker colors correspond to smaller values.

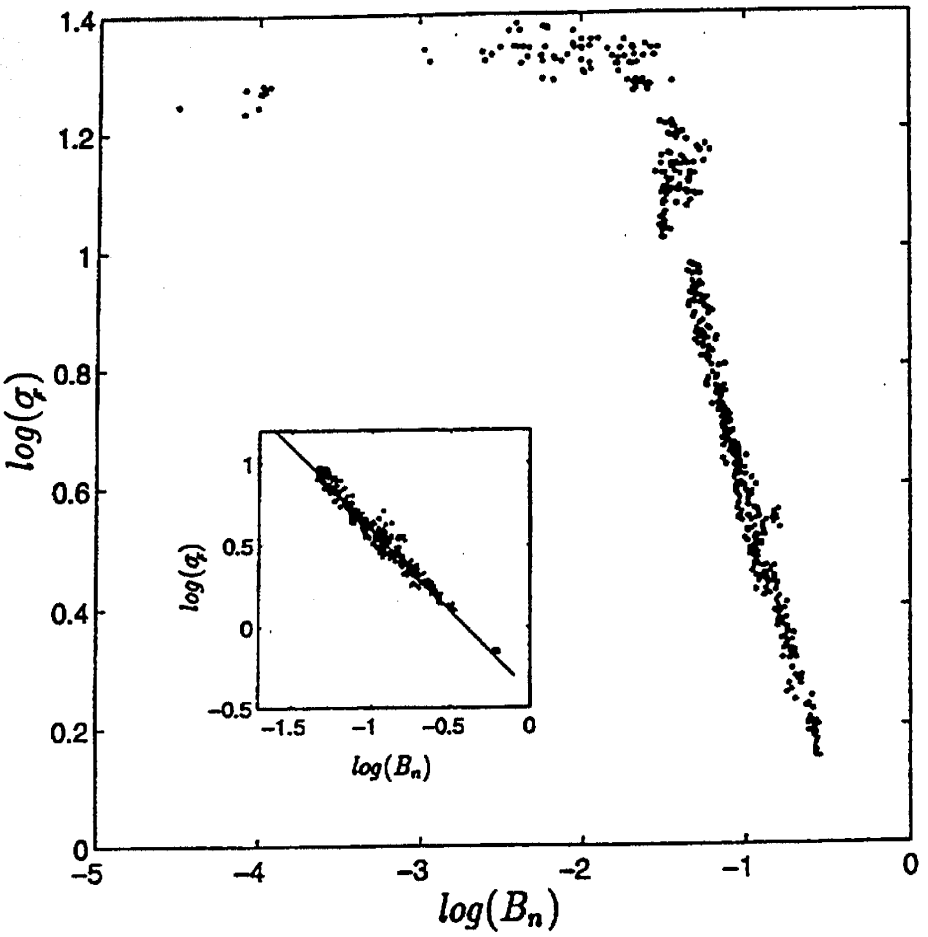

Figure 8: Log-log plot of the front width σ_F vs. B_n for different lattice sizes and for n in the range $(0, 3)$. The straight line in the inset has a slope of -1. Comparison with the theoretical slope $-\frac{\nu}{\nu+1}$, suggests that IPM is an IPG in a long-range correlated field ($\nu = \infty$).

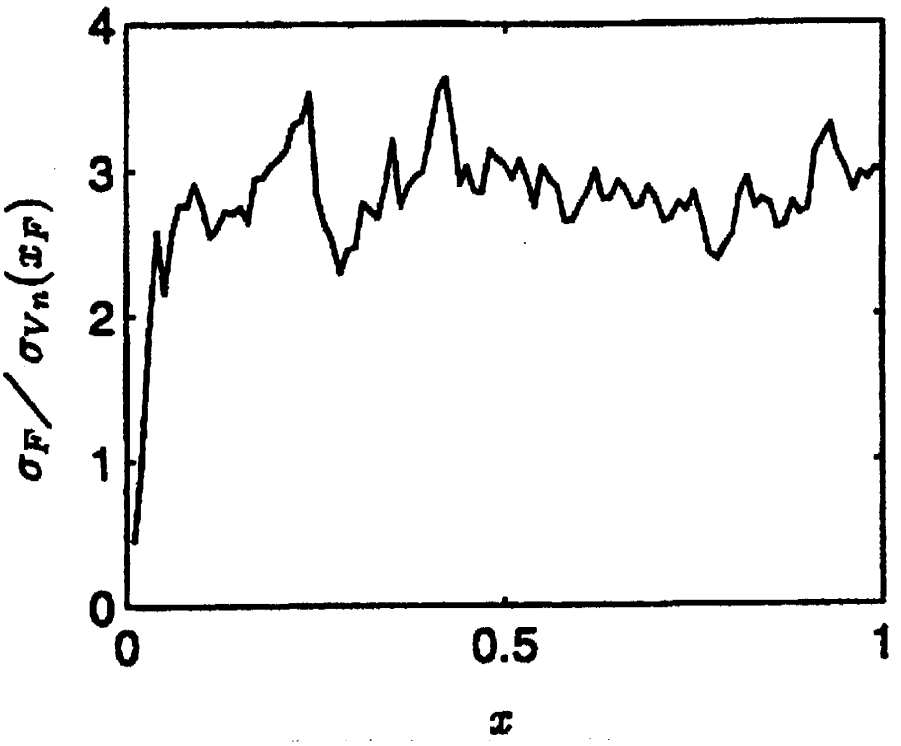

Figure 9: Spatial Variation of the ratio of the front width vs. the standard deviation of V_1. The ratio stabilizes to a constant value after an early transient, consistent with the prediction of (21).

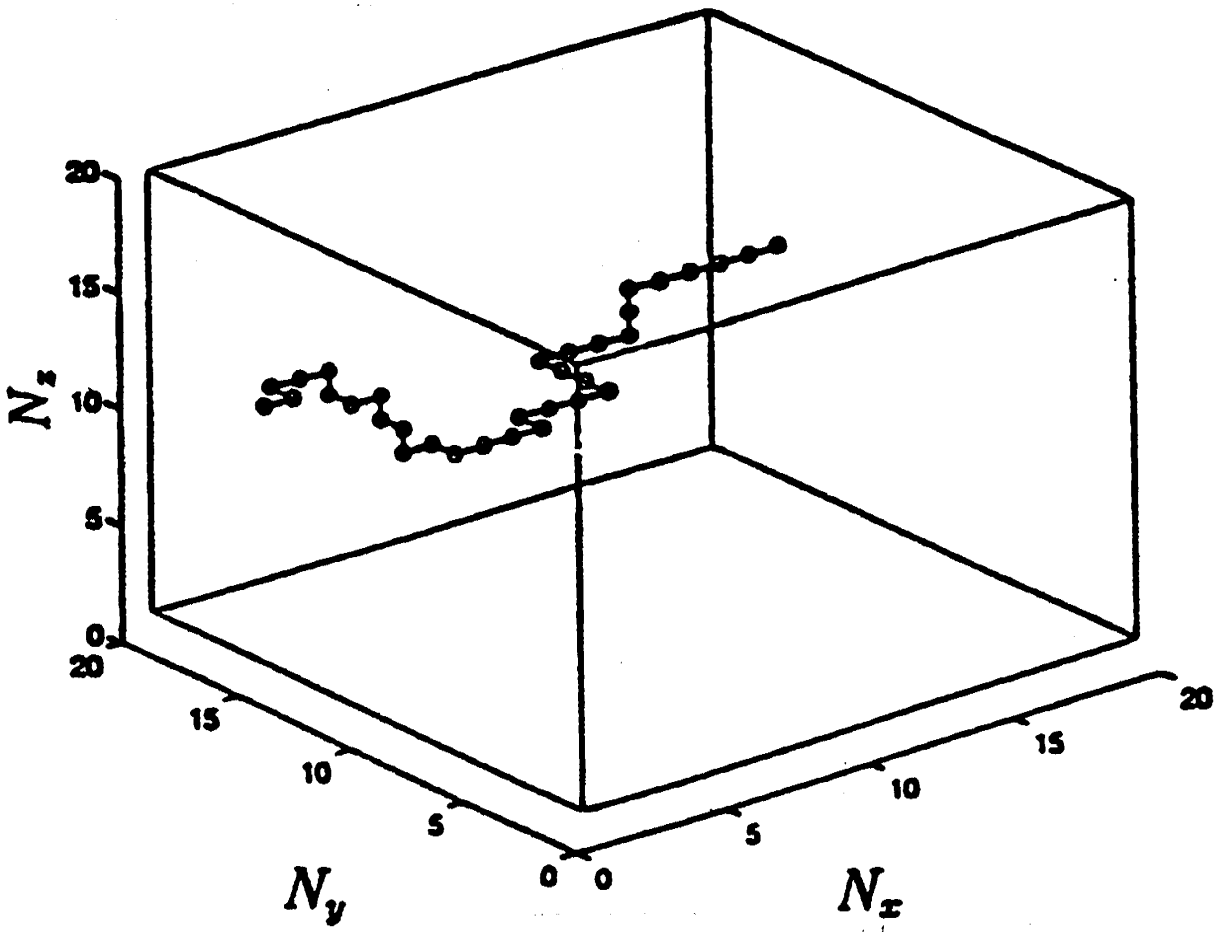

Figure 10: The MTP for $n = 1$ for a 3-D cubic lattice $20 \times 20 \times 20$.

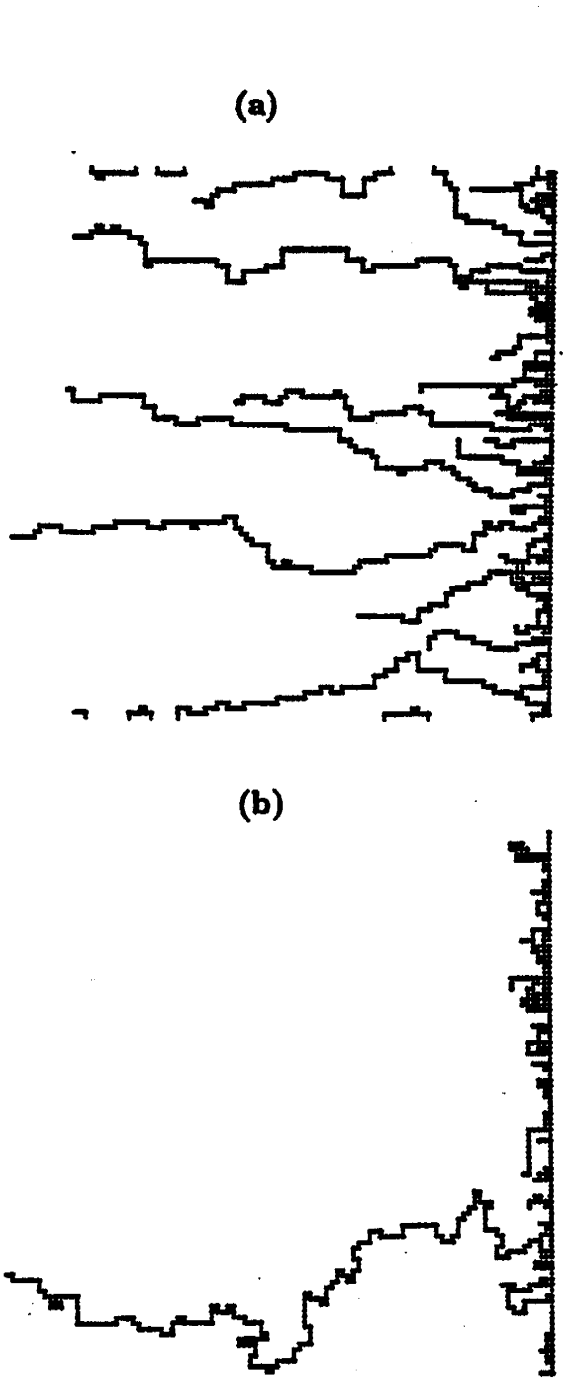

Figure 11: The backbones of the dendritic branches, on which all invaded sites reside, originating from the right boundary for IPM with (a) $n = 1$ and (b) $n = \infty$ (site-occupancy, bond-invasion percolation with bond trapping), from simulations in a 100×100 lattice. For $n = 1$ the backbones appear self-affine and "parallel" to each other. Note the single dominant branch for $n = \infty$. The MTP for $n = \infty$ corresponds to the backbone of the loopless IP and it is a self-similar fractal. Periodic boundary conditions were used in the simulation.

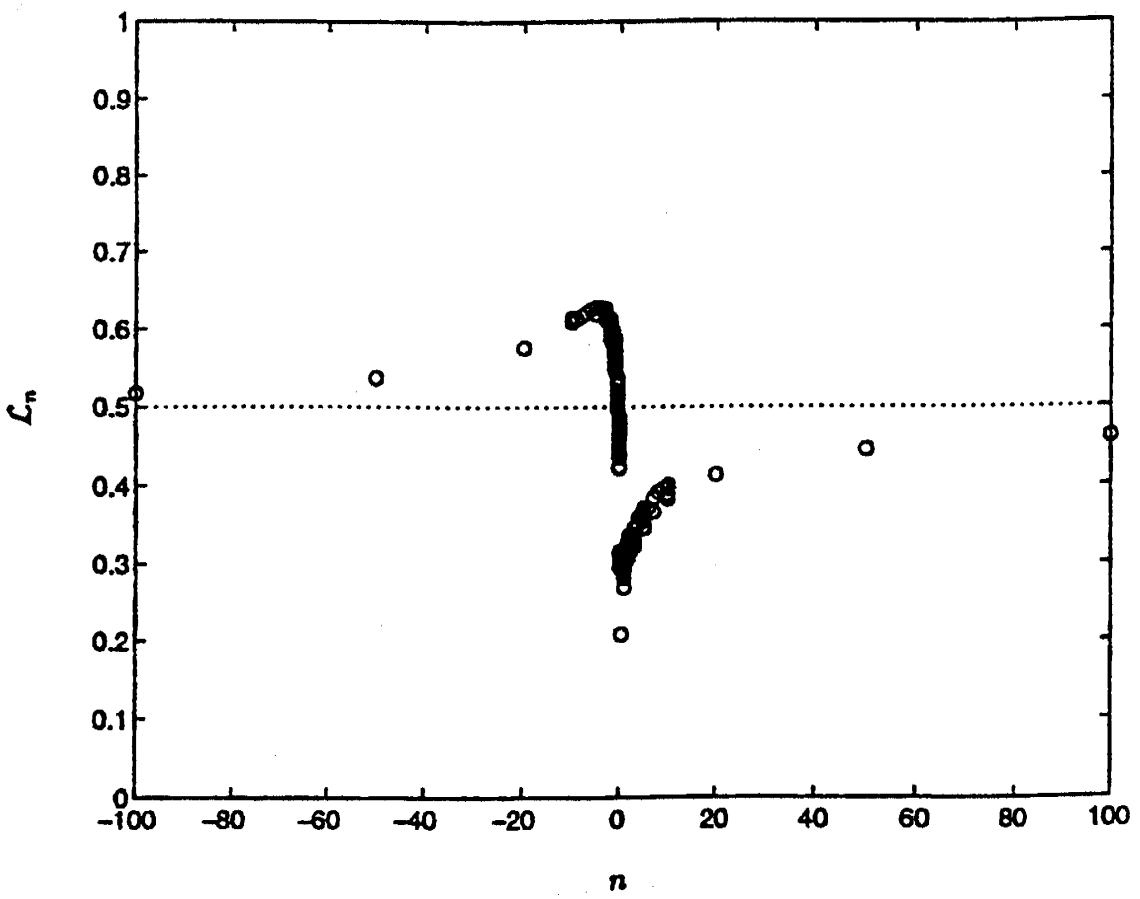

Figure 12: The variation of the generalized minimum gradient $\mathcal{L}_n$ with n. Note the asymptotic approach to p_c and $1 - p_c$ as n approaches ∞ and $-\infty$, respectively.

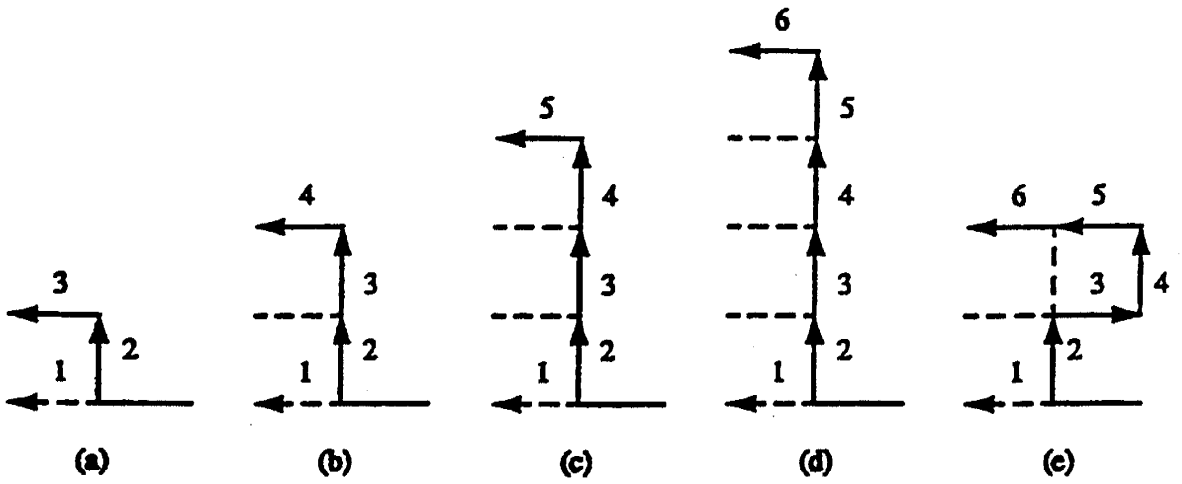

Figure 13: Alternative pathways that can be taken by the MTP to advance by one step in the x direction (here from right-to-left). The possibilities of two steps (a), three steps (b), four steps (c), and five steps (d) and (e), are indicated. Note the backtracking ("overhang") in Figure (e).

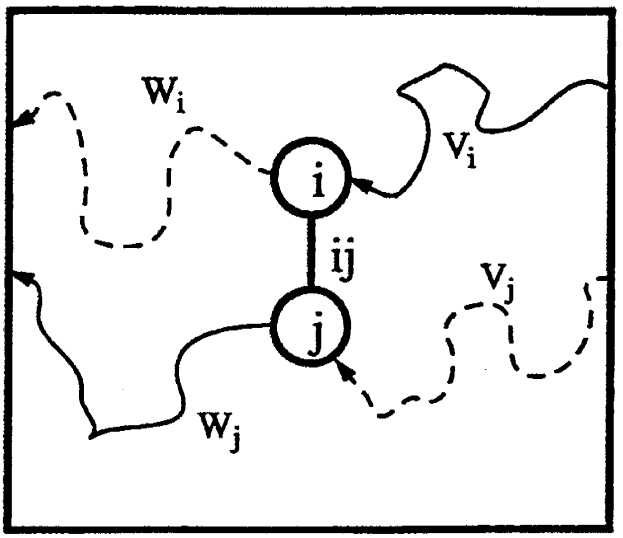

Figure 14: The two alternative pathways (solid and dashed lines, respectively) that can lead to the opening of bond ij connecting adjacent sites i and j.

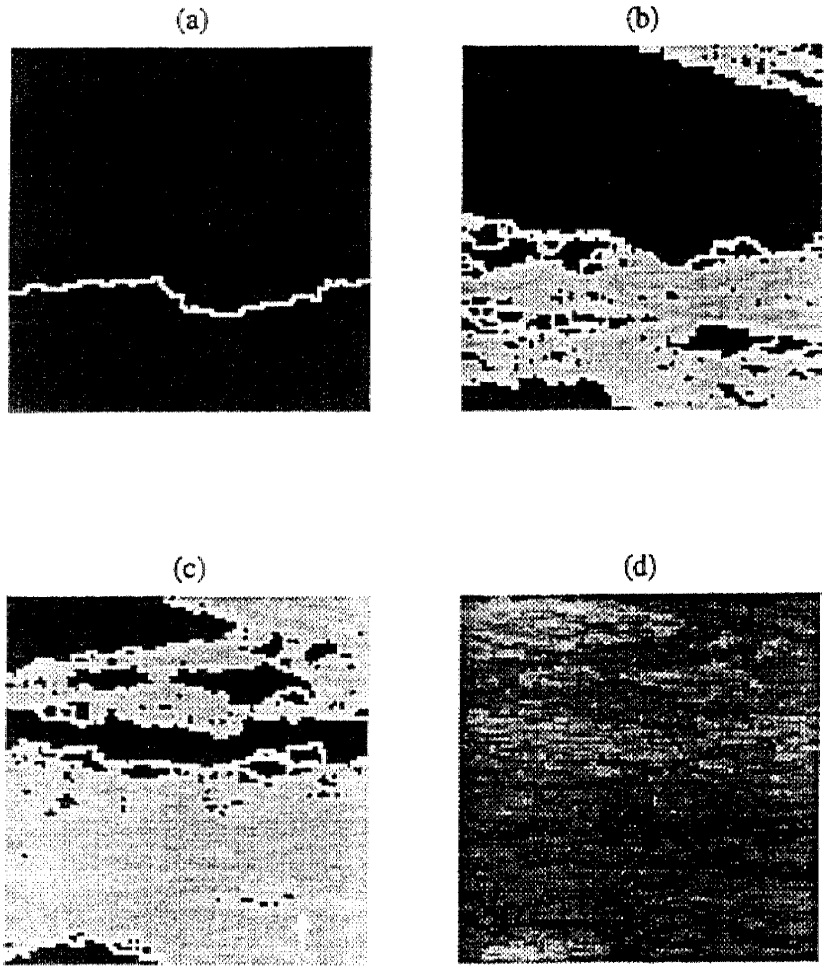

Figure 15: Representation of the open paths as the applied potential increases at different stages: (a) MTP, (b) one-third, (c) two-thirds, and (d) three-thirds of all possible open paths, for a 100×100 lattice.

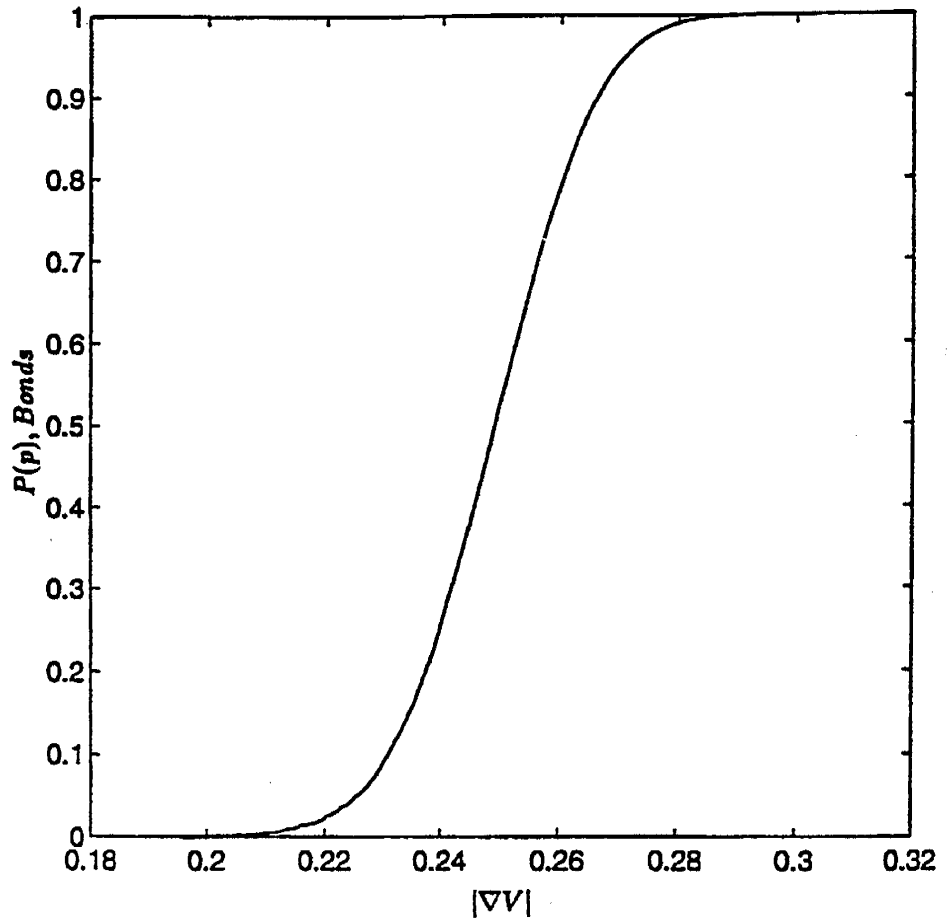

Figure 16: The fraction of open bonds as a function of the applied gradient for $n = 1$ from simulations in a $40 \times 40 \times 40$ lattice.

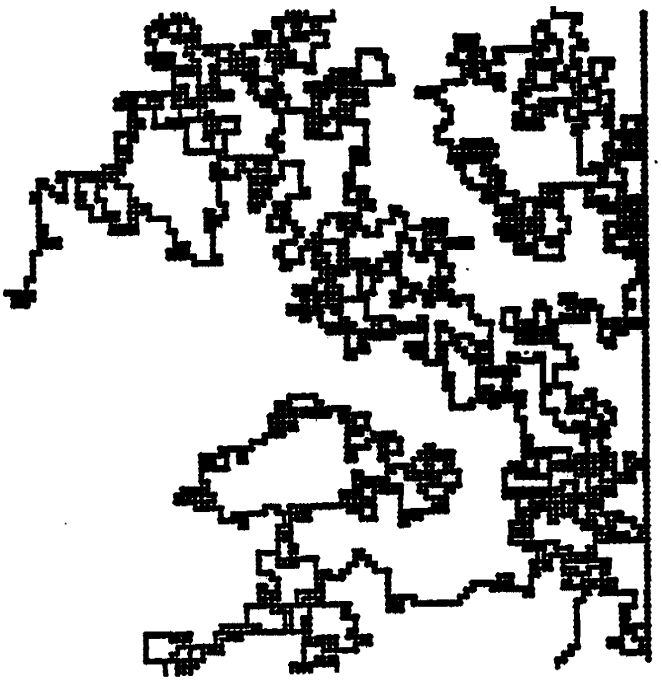

Figure 17: Snapshot of unstable IPM with trapping, from simulations in a 100×100 lattice. The pattern is a SAW constrained to occur on the LHS of the rightmost boundary.

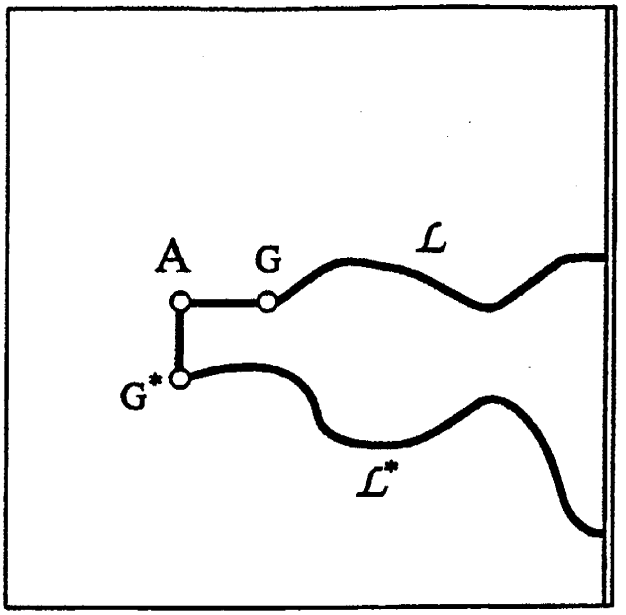

Figure 18: Schematic of the various alternative minimum threshold paths from site A to the RHS boundary. Path $\mathcal{L}$ is the MTP of IPM, while $\mathcal{L}^*$ is the hypothetical alternative.

6. OPTIMIZATION OF FLUID FRONT DYNAMICS IN POROUS MEDIA USING RATE CONTROL: EQUAL MOBILITY FLUIDS

B. Sudaryanto and Y. C. Yortsos

ABSTRACT

In applications involving the injection of a fluid in a porous medium to displace another fluid, a main objective is the maximization of the displacement efficiency. For a fixed arrangement of injection and production points (sources and sinks), such optimization is possible by controling the injection rate policy. Despite its practical relevance, however, this aspect has received scant attention in the literature. In this paper, we provide a fundamental approach based on optimal control theory, for the case when the fluids are miscible, of equal viscosity and in the absence of dispersion and gravity effects. Both homogeneous and heterogeneous porous media are considered. From a fluid dynamics viewpoint, this a problem in the deformation of material lines in porous media, as a function of time-varying injection rates. It is shown that the optimal injection policy that maximizes the displacement efficiency, at the time of arrival of the injected fluid, is of the "bang-bang" type, in which the rates take their extreme values in the range allowed. This result applies to both homogeneous and heterogeneous media. Examples in simple geometries and for various constraints are shown, illustrating the efficiency improvement over the conventional approach of constant rate injection. In the heterogeneous case, the effect of the permeability heterogeneity, particularly its spatial correlation structure, on diverting the flow paths, is analysed. It is shown that "bang-bang" injection remains the optimal approach, compared to constant rate, particularly if they were both designed under the assumption that the medium was homogeneous. Experiments in a homogeneous Hele-Shaw cell are reported to test the theory.

INTRODUCTION

The injection of a fluid in a porous medium to displace another fluid (miscible or immiscible) initially in place is common to applications involving the recovery of subsurface fluids (for example, in oil recovery or in environmental soil remediation). Injected fluids are typically water, solvents, steam, etc., the initial fluid being oil or organic contaminants, in the two applications mentioned. The displacement occurs by injection from various injection wells (sources) and by production from a number of production wells (sinks). A variety of patterns have been analyzed in classical works (e.g. Muskat[1], Bear [2]), several decades ago. A typical example of relevance to our work, is shown in Figure 1 and involves two injection wells and a production well in a bounded "reservoir". In practice, the location of injection and production wells is generally determined semi-empirically, based on a variety of geologic, economic, and practical considerations.

In many applications, the main objective is the maximization of some measure of the displacement efficiency (the recovery efficiency). Aspects of the optimization of displacement processes in porous media have been studied before, notably by Ramirez and his co-workers[3–7], in the context of maximizing the profitability over a fixed time interval of various Enhanced Oil Recovery (EOR) processes. In these, the important variable is the volume of a (costly) component (e.g. surfactant, polymer) injected along with the fluid,

which improves the microscopic (pore-level) displacement efficiency. There, the emphasis is mostly on the physicochemical action of the injected fluid (for instance, on the reduction of the interfacial tension) rather than on the dynamics of the flow itself. Typically, in those studies, a pair of injection and production wells in a symmetric, homogeneous pattern were considered.

However, in problems where the injected fluid composition is fixed and it is not a control parameter (for example in water displacing oil), the only available control of the displacement is the allocation of the injected fluid to the injection wells (and of the produced fluid to the production wells). In general, this can be accomplished by varying the injection rates and/or the injection (or production) intervals in individual wells. In the particular case of a 2-D geometry of interest here, the wells can be considered as point sources and sinks, thus the maximization of the displacement efficiency should be sought by optimizing well injection rates. This fundamental problem has not been systematically addressed before (although various attempts have been made, e.g. see Asheim[8] and Virnovsky[9]). The conventional approach has been to design symmetric well patterns, and allocate injection rates equally to all wells. This practice relies on the premise that the permeability field is homogeneous, an assumption which is rarely true. Indeed, in heterogeneous porous media, the flow streamlines do not necessarily have the symmetry of the well pattern, even at constant injection rates. Furthermore, injection at constant and equally partitioned rates, which is a common practice, has not been shown to be the optimal policy, certainly not in the absence of well symmetry, even for a homogeneous porous medium.

To make progress, we elected to study in this paper a "first-order" problem, namely equal-viscosity, first-contact miscible displacement, in two dimensions and in the absence of dispersion or gravity. In the case of a homogeneous permeability field, this, then, becomes a problem of control of fluid fronts under conditions of potential flow. As will be shown below, this problem is amenable to a non-linear dynamics description. For heterogeneous permeability fields, a similar although computationally more complex, description applies. Accounting for the presence of dispersion, of immiscible fluids and of unequal viscosities, which are all neglected here, introduces additional complexities. For example, when the fluids are immisicible, issues of relative permeabilities arise. While in the case of a less viscous fluid displacing a more viscous one, viscous fingering instabilities will occur[10–13], requiring a generally cumbersome numerical approach, isntead of the simpler potential flow description used here. Some of these more general problems are discussed in a companion paper[14], which relies, however, on the present approach for their solution.

From a fluid dynamics point of view, the problem under consideration is the evolution of displacement fronts in porous media, as a function of time-varying injection rates at point sources. In essense, this is a study of the deformation (map) of initial material lines subject to a time-varying flow field (for example, as described in Ottino[15]). Given that 2-D steady-state potential flow is integrable[15], it is the time dependence of the injection rates at discrete points (sources and sinks) that potentially introduces interesting aspects. The general problem of the deformation of arbitrary fluid volumes in various porous media flow fields is discussed elsewhere[16] and will form the subject of a future article. In this paper, the focus is on how to control the displacement fronts to optimize a certain measure of the displacement. For the latter, we select the displacement efficiency at the time when the injected fluid first arrives ("breaks through") at the production well. Delaying as much as possible the arrival of the

injected fluid at the production well is a desirable objective in many recovery processes. We note that interesting work on the arrival time statistics in heterogeneous porous media has been recently carried out[17].

Thus, we consider the equal-mobility, miscible displacement of incompressible fluids in a 2-D geometry in the absence of dispersion and gravity. For the sake of presentation, we will refer to the injected fluid as "water" and to the displaced fluid as "oil", without any particular physicochemical meaning attached to this designation, however. The paper is organized in two sections, as follows: First, we formulate the control problem in a homogeneous permeability field, involving multiple injectors and one producer. We apply an optimal control methodology and show that the optimal control policy is of the "bang-bang" type, namely, the control parameter, which here is the injection rate at individual point sources, takes only its extreme values (maximum or minimum) in the range in which they are constrained. Numerical experiments are subsequently conducted to illustrate the applicability of the methodology and to carry out a sensitivity study. Then, we report on physical flow experiments conducted in a Hele-Shaw cell to test the theoretical predictions. In the second section of the paper, we present a generalization of the approach to heterogeneous reservoirs, always under conditions of equal mobility, and conduct a sensitivity study of the effect of heterogeneity on the optimal injection policy.

HOMOGENEOUS POROUS MEDIA

1. Formulation

Under the previous assumptions of equal mobility, incompressible miscible fluids, and in the absence of dispersion and gravity effects, the displacement in homogeneous porous media is governed by potential flow

$$\nabla^2 \Phi = 0 \tag{1}$$

where Φ is a normalized flow potential. The solution of (1) for a multiple-well, multiple-rate problem in 2-D reads, in appropriate dimensionless notation, as

$$\Phi(x,y) \sim -\sum_{l=1}^{N_T} q_l(t) \ln\left[(x-x_{wl})^2 + (y-y_{wl})^2\right] \tag{2}$$

where N_T is the total number of wells, q_l is the flow rate of well l ($q_l \geq 0$ for injection and $q_l \leq 0$ for production), and the pair (x_{wl}, y_{wl}) denotes the coordinates of well l. Throughout the paper, sources are not allowed to become sinks, and vice versa. We add that in the case of bounded symmetric reservoirs, N_T also includes the image wells present as a result of the method of superposition.

From equation (2) and the use of Darcy's law, the flow velocities read, in appropriate dimensionless notation

$$v_x = \sum_{l=1}^{N_T} q_l(t) \left[\frac{x - x_{wl}}{(x-x_{wl})^2 + (y-y_{wl})^2}\right] \tag{3}$$

and

$$v_y = \sum_{l=1}^{N_T} q_l(t) \left[\frac{y - y_{wl}}{(x - x_{wl})^2 + (y - y_{wl})^2} \right] \tag{4}$$

Equations (3)-(4) can also be used to define fluid fronts by tracking front particles emanating from the various sources. With this description, the optimization problem can be formulated as an optimal control problem of a non-linear dynamical system. Define as state variables the coordinates (x_k, y_k) of the (theoretically infinite) particles at the fronts. Then, the state equations are

$$\dot{x}_k = \sum_{l=1}^{N_T} q_l(t) \left[\frac{x_k(t) - x_{wl}}{(x_k(t) - x_{wl})^2 + (y_k(t) - y_{wl})^2} \right] \tag{5}$$

and

$$\dot{y}_k = \sum_{l=1}^{N_T} q_l(t) \left[\frac{y_k(t) - y_{wl}}{(x_k(t) - x_{wl})^2 + (y_k(t) - y_{wl})^2} \right] \tag{6}$$

where dots denote differentiation with respect to time, subject to the initial conditions $x_k(0) = x_k^0$ and $y_k(0) = y_k^0$. The latter are determined by specifying the particular source and the particular streamline angle from which the particle emanated (recall the locally radial flow near a source or a sink).

In this dynamical system, the control variables are the time-varying injection rates $q_l(t)$. These are subject to various constraints. For example, consider the case in which there is a single sink, denoted by subscript 1, and $N_W - 1$ sources. A plausible constraint is to assume that the overall injection rate is constant, and equal to 1, in the dimensionless notation, in which case we have the conditions

$$q_1(t) = -1 \quad , \quad \sum_{l=2}^{N_W} q_l(t) = 1 \quad , \quad 0 \le q_l(t) \le 1 \quad , \quad l = 2, \cdots N_W \tag{7}$$

Other constraints are also possible, for example on the maximum possible rates in individual wells (see below and Ref. [16]). Now, for the case of incompressible fluids at a constant-overall injection rate, maximizing the efficiency at breakthrough is equivalent to maximizing the breakthrough (arrival) time, t_f. In this case, therefore, the performance index $\mathcal{J}$ to be maximized is

$$\mathcal{J} = t_f \tag{8}$$

The arrival time is determined from the solution of the state equations. In the numerical approximation to be used below, the front will be approximated by a finite number N_S, of particles. Because of the singularity of flow near the sink, the following terminal condition will be imposed

$$\psi(t_f) \equiv \prod_{k=1}^{N_S} \left([x_k(t_f) - x_w 1]^2 + [y_k(t_f) - y_w 1]^2 - \epsilon^2 \right) = 0 \tag{9}$$

where $\epsilon \ll 1$ is a normalized source "radius". Thus, breakthrough is defined when condition (9) is satisfied for the first time, which occurs when the fastest particle, under the particular injection rate policy, first arrives at the sink.

In summary, the optimal control problem to be solved can be stated as follows: Find the admissible control parameters $q_l(t)$, $l = 2, \cdots, N_W$, satisfying the constraints given by (7) which maximize the performance index (8), subject to the state equations (5)-(6) and the stopping criterion (9). This problem can be addressed by using a standard control methodology[18].

For this, we introduce the Hamiltonian,

$$\mathcal{H} = \sum_{k=1}^{N_S} \lambda_{xk}(t) \left[\sum_{l=1}^{N_T} q_l(t) \left[\frac{x_k(t) - x_{wl}}{(x_k(t) - x_{wl})^2 + (y_k(t) - y_{wl})^2} \right] \right] + \sum_{k=1}^{N_S} \lambda_{yk}(t) \left[\sum_{l=1}^{N_T} q_l(t) \left[\frac{y_k(t) - y_{wl}}{(x_k(t) - x_{wl})^2 + (y_k(t) - y_{wl})^2} \right] \right] \tag{10}$$

and adjoin the state equations (5)-(6) and the terminal condition (9) to the objective function (8), using the vector Lagrange multipliers $\lambda_{xk}(t)$ and $\lambda_{yk}(t)$ and the scalar Lagrange multiplier ξ. This leads to the augmented objective function

$$\mathcal{J}_A = t_f + \xi\psi + \int_0^{t_f} \left[\mathcal{H} - \sum_{k=1}^{N_S} (\lambda_{xk}(t)\dot{x}_k + \lambda_{yk}(t)\dot{y}_k) \right] dt \tag{11}$$

from which the Lagrange multipliers are determined

$$\dot{\lambda}_{xk} = -\frac{\partial \mathcal{H}}{\partial x_k} \quad \dot{\lambda}_{yk} = -\frac{\partial \mathcal{H}}{\partial y_k} \quad \text{and} \quad \xi^{-1} = -\left[\sum_{k=1}^{N_S} \left(\frac{\partial \psi}{\partial x_k}\dot{x}_k + \frac{\partial \psi}{\partial y_k}\dot{y}_k \right) \right]_{t_f} \tag{12}$$

subject to the boundary conditions

$$\lambda_{xk}(t_f) = \xi \left(\frac{\partial \psi}{\partial x_k} \right)_{t_f} \quad \text{and} \quad \lambda_{yk}(t_f) = \xi \left(\frac{\partial \psi}{\partial y_k} \right)_{t_f} \tag{13}$$

A computational procedure for the maximization of (11) will be described shortly. Before we proceed, however, we make a key observation: We note that the state equations (5)-(6) are *linear* with respect to the control parameters $q_l(t)$. Under these conditions, we can apply Pontryagin's Maximum Principle (PMP), which states that the optimal variable q_l^* is determined from the value of the switch function $\frac{\partial \mathcal{H}}{\partial q_l}$ as follows (e.g. see Bryson and Ho[18]): $q_l^* = q_{min}(= 0)$ if $\frac{\partial \mathcal{H}}{\partial q_l} < 0$; $q_l^* = q_{max}(= 1)$ if $\frac{\partial \mathcal{H}}{\partial q_l} > 0$; while q_l^* is undetermined if $\frac{\partial \mathcal{H}}{\partial q_l} = 0$. Therefore, if the values of the switch functions are non-zero, except possibly at a finite number of points, the optimal (non-singular) control is of the "bang-bang" type, and the control variables take their extreme values only (which in the present case are 0 and 1).

2. Computational Procedure

Because of the bang-bang control nature of the problem, therefore, we only need to specify the switch times and the control value of the first bang arc. The problem reduces into finding the optimum location of the switch times. Various algorithms[19–22] have been proposed for this purpose. In this study, we will use the STO (switching time optimization) algorithm, developed by Meier and Bryson[22], which is based on a first-order gradient method and consists of the following steps:

1. Obtain the initial switch time and the control value of the first-bang arc (see further below).

2. Using the initial control policy from step (1), integrate the state equations (5) and (6) forward in time until the stopping criterion (9) is satisfied. Record all state variables $x_k(t)$ and $y_k(t)$ $(k = 1, \cdots N_S)$ and the value of the objective function.

3. Calculate the Lagrange multipliers $\lambda_{xk}(t)$, $\lambda_{yk}(t)$ $(k = 1, \cdots N_S)$ and ξ from the co-state equations (12) by integrating backward in time, starting from the terminal time t_f and using the boundary condition (13).

4. Calculate the improvement in the switch time, dt_{lm}, by using the expression

$$dt_{lm} = \frac{w_{ll}}{\Delta q_l} \left(\frac{\partial \mathcal{H}}{\partial q_l} \right)_{t_{lm}} \tag{14}$$

where t_{lm} is the m-th switch time of the control variable q_l, w_{ll} is the diagonal element of a positive definite weight matrix W (see Ref. [16] for more details), and $\Delta q_l \equiv q_l(t_{ml}) - q_l(t_{ml} + dt_{ml})$ is here equal to $\Delta q_l = \pm 1$.

4. Repeat steps (2)-(4) using the new switch times obtained from step (4) until the change in the objective function is less than a prescribed small positive number.

To get started, the STO algorithm requires an initial guess of switch times (step (1)), which can be obtained by solving a modified non-bang-bang problem that approximates the original bang-bang problem[22]. In the modified problem, a term that approximates the control bounds must be added to the performance index. This term penalizes the deviation of the controls away from the bounds. Using the above gradient procedure (see ref. [16] for more details), the control parameters of the modified problem are driven toward their bounds to maximize the performance index J. Results are presented below.

3. Numerical Results

All numerical results to be shown in this subsection correspond to a three-well system (two injectors and one producer) in a rectangular, bounded reservoir (Fig. 1). In the solution of the problem, we used the method of images by superposing image wells to satisfy the no-flow conditions at the boundaries (for example, see Refs. [1]-[2]). A total of seventy-two image wells was found to be numerically sufficient for this purpose. We note that a similar approach can also be implemented for arbitrary reservoir geometries[16]. The numerical experiments were typically conducted by fixing the positions of wells A and C, and of the angle $\alpha = A\hat{C}B$ and placing well B at variable positions. Of course, various other geometrical configurations are also possible. The following general results were found: In all cases under the constraint of constant-overall injection rate, only one injector (source) is active at any given time.

(However, this is not necessarily the case for different constraints, as will be shown later.) The optimal injection policy is bang-bang with one switch time only: it consists of injecting first from the source well located "farther" away from the sink (well A in Fig. 1), up to the optimal switch time, at which injection switches to the injector located "nearest" to the producer (well B in Fig. 1). Furthermore, the optimal switch time was found to be such that the fronts from both injectors arrive simultaneously at the producer.

Snapshots of the displacement fronts under the optimal injection policy are shown in Fig. 1. Before the switch time, only injection from the point source A takes place (Fig. 1b). Following the switch, injection terminates at source A and commences at source B. The particles originating from source A are now subject to the flow field created by the source at point B, and they are displaced in the direction of the sink C (Fig. 1c). During this process, part of the front emanating from source A recedes, although the total volume it encloses remains constant, due to incompressibility. In the present problem, where there is no hysteresis in the flow properties, the receding of the front is not an issue of concern. However, it is likely to be so in the case of immiscible displacements, where flow properties, for example relative permeabilities and capillary pressure, are indeed hysteretic[23]. Upon breakthrough (Fig. 1d) both fronts arrive simultaneously at the sink.

To illustrate the advantage of the bang-bang control, we compared its displacement efficiency to the conventional case, where injection rates are constant. In particular, we considered the case, where the partition of the (constant) rates between the well is such that it maximizes the displacement efficiency. For most geometries, these rates are such that breakthrough in well C occurs simultaneously from both fronts (however, this not always true, as shown below). We will refer to this optimal case as constant-rate injection. Fig. 2 shows the fronts at breakthrough for the two different policies. The two displacements have different features. The swept area due to injection from well B in the constant rate case is much smaller than that for the bang-bang case. Because of its proximity to the sink, well B cannot accept a high injection rate, which will lead to early breakthrough. This is not so for the bang-bang case, where well B is put into action after some time has elapsed, thus it can accomodate a high (in fact, the highest) injection rate without the risk of a premature breakthrough. In the constant rate case, each source establishes its own "drainage" area, the shape of which is determined from the strength of the sources and the competition with other sources. The streamlines of the particles emanating from a given source, are thus restricted to this particular area, due to the flow fields from the other sources. In the bang-bang case, the fronts are not subject to this confinement. As shown previously, some of the streamlines emanating from the first well A will bend backwards, when injection from well B commences, and will eventually be diverted towards the sink C. This allows for a better displacement from well B and leads overall to a better displacement efficiency.

To assess quantitatively the effectiveness of the bang-bang policy, we compared the efficiency at breakthrough with that from the constant-rate injection. Fig. 3 shows a plot of the normalized breakthrough time as a function of the ratio of the distances between the two wells (always for a constant angle $A\hat{C}B = 45^{o}$). For all values of the latter, bang-bang injection gives a better displacement efficiency at breakthrough than the constant-rate case. The efficiency improvement depends on the distance ratio, with a maximum that in Fig. 3 can reach 13.7%, when the distance ratio is about 0.6. This improvement, although not very dramatic, is non trivial, given that it is accomplished only by flow rate control. Fig. 3

shows that the efficiency depends on the geometric arrangement of the wells, which essentially dictates the streamline lengths. We note that in heterogeneous fields, the efficiency would additionally depend on the permeability structure, as possible spatial correlations will lead to channels and affect the streamlines (see Section II below). The switch time was found to decrease monotonically, from a value of 1 to a value of 0.342, as the distance ratio increased. It is worth noting, that for the constant-rate injection, optimal efficiency is not always associated with simultaneous injection from both wells. Thus, for a geometry with a distance ratio below approximately 0.6, injection from the closest injector (well B) does not improve the efficiency at breakthrough. Rather, the efficiency is maximized by injecting only from the farthest injector (well A, Fig. 3). Similar results were also found for other well arrangements and reservoir geometries[16].

The bang-bang condition of the simultaneous arrival at the sink for optimal displacement efficiency can be interpreted readily. Indeed, consider a bang-bang policy, $\mathcal{S}$, in which when the front from well B first arrives in well C, the front from well A is at some finite distance away and duringa finite time before breakthrough, injection occurs only from well B. We will show that $\mathcal{S}$ is not the optimal injection policy. Indeed, given that the flow always remains potential, breakthrough of the front from well B will occur from particles moving along the diagonal BC, which is the fastest trajectory, when injection occurs only from well B, as assumed in this policy. Now, let us consider a time at a small time interval δt, before breakthrough, suitably chosen, and apply the different policy $\mathcal{S}'$, consisting of interrupting injection from well B and recommencing injection from well A in that time interval. It is clear that in this period of time, there will be no breakthrough of either front: Particles emanating from well B will now travel along curved, rather than straight streamlines, hence will not reach well C in time δt, while particles emanating from well A will not be sufficiently close to well C, under suitably small δt, in order to break through. Therefore, neither of these particles will reach breakthrough in this time interval, and policy $\mathcal{S}'$ will lead to a higher displacement efficiency, contrary to our initial assertion. It follows that policy $\mathcal{S}$ is not optimal. A similar argument holds if we were to reverse the roles of A and B, thus leading to the simultaneous arrival as a condition for an optimal bang-bang displacement.

From the above it can also be shown that the displacement efficiency of the bang-bang policy exceeds that of the two limiting cases, where only of one of the two wells is active. Indeed, the bang-bang efficiency will be greater than that due to well B only, since by construction the bang-bang policy includes, as a subset, injection until breakthrough from well B (this constitutes the second part of the policy, for example see Fig. 1). Proving that it is also greater than that from injection from well A only, follows by applying argument in the previous paragraph, in which the roles of wells Aand B are reversed. In this sense, the efficiency of the bang-bang policy satisfies a "triangle inequality".

4. Constraint on Injectivity

In the above, the overall rate was constrained to be constant. In certain practical cases, however, it is possible that the individual injection rates may not exceed a maximum value, which depends on the local conditions of the individual well. For example, we may have the constraint

$$0 \leq q_l(t) \leq q_{l,max} \quad ; \quad l = 2, \cdots, N_W \tag{15}$$

where $q_{l,max}$ may not necessarily be the same for every l. Under this constraint, the optimal control formalism remains the same as before, except for the performance index, which now becomes

$$\mathcal{J} = \int_0^{t_f} \left(\sum_{l=2}^{N_W} q_l(t) \right) dt \tag{16}$$

Despite the different constraints, the linearity to the injection rates still remains, and the optimal injection policy is again predicted to be of the bang-bang type. The computational method for the solution of this problem is similar to the previous and details can be found in Sudaryanto[16].

A number of numerical experiments were conducted for various constraints of the type (15) and for geometries similar to Fig. 1. In all cases, the optimal injection policy was found to have one switch time, as before. However, now there is the possibility that more than one injection wells are active simultaneously. Indeed, the optimal injection policy was found to consist of the following: (a) constant injection from the farthest injector and at its maximum rate throughout the process until breakthrough; and (b) no injection from the nearest injector until the switch time, after which injection commences at the maximum injection rate for that well, until breakthrough. Here, the farthest injector was defined as the one which gives longer breakthrough times when injection is from that well only and at its maximum rate. Snapshots illustrating front movements for bang-bang injection under the injectivity constraints $0 \leq q_A \leq 0.5$ and $0 \leq q_B \leq 1$, are shown in Fig. 4. Commencement of injection at well B, after a certain time has elapsed (Fig. 4c), causes the streamlines from well A to bend towards well C, as in the case of Fig. 1. A comparison between the displacement efficiency at breakthrough between bang-bang and constant-rate injection policies is shown in Fig. 5. Here, because the overall rates are not constant, there is no equivalence between breakthrough times and displacement efficiency, however. The results show that bang-bang injection leads to both a better efficiency *and* a shorter breakthrough time, compared to constant-rate injection. Namely, here there is the additional benefit of faster recovery, associated with the bang-bang injection. The improvement in efficiency is similar to that for the constant overall rate constraint (Fig. 3). However, the reduction in breakthrough time can be significant and approaches 25%, in the best case, for the conditions of Fig. 5. This example shows that the injectivity constraints can play important and unexpected roles in the maximization of the displacement efficiency.

5. Experimental Results

To test the theoretical predictions, flow experiments in a Hele-Shaw cell were conducted. Although lacking the pore microstructure of actual porous media, Hele-Shaw cells are excellent experimental devices for the visualization of 2-D potential flows, under single-phase conditions. The Hele-Shaw cell consisted of two parallel 3/8 inch-thick glass plates of dimensions 24 inches x 18 inches separated by 1 inch-wide flat rubber strips placed along the edges

of the cell that serve as a spacer (to maintain the gap thickness) and as a gasket (to seal the edges). The rubber strips have a thickness of 0.08 cm. Experiments were also conducted for a modified geometry, in which a large-scale flow barrier was added to the cell (see section II below). Three holes with a diameter of 1 cm were drilled in the bottom glass plate, two of which served as injection wells and the third as the production well. The injection wells were connected to two peristaltic (Masterflex) pumps, while the production well was connected to the ambient environment. The pumps were variable-flow computerized with easy-load pump heads, and were connected to a PC,through which the variable flow rates were programmed and controlled according to the desired injection policy. In the experiments, dyed (methylene blue) water was injected to displace water originally in place, at a constant overall rate of 20 cc/min. A video camera mounted vertically above the cell captured the front movement. Injection policies corresponding to the optimal control policy as obtained above, as well as to constant rate injection were used. The schematic of the experimental set-up is shown in Fig. 6.

Snapshots of the displacement fronts under the optimal bang-bang policy are shown in Fig. 7. As discussed above, injection starts first from the more distant well, then switches at an optimal time to injection from the well nearest to the producer. Following the switch, the fluid originating from the more distant well is shown to be driven towards the production well, as expected theoretically. During this process, part of the front actually recedes, as predicted. The two fronts break through almost (but not exactly) at the same time. We believe that the reason for the slight discrepancy in front arrival is dispersion, which was not included in the theory. To estimate the effect of dispersion we used the standard Taylor-Aris expression for the dispersion coefficient

$$D = D_m + \frac{8u^2h^2}{945D_m} \tag{17}$$

where $2h = 0.08$ cm is the gap between the plates and $D_m \approx 10^{-5}$ cm^2/sec is the molecular diffusivity. In rectilinear flows, the Peclet number is maximized at a specific value of the injection rate. Thus, operating at the smallest possible dispersion is possible by optimizing the overall injection rate. In our experiments, however, the displacement is not rectilinear, certainly not everywhere, and the Peclet number is spatially variable. To minimize dispersion, the experimental injection rate was chosen to be as close as possible to an optimal rate, subject, however, to the resolution constraints of the pumps, which did not allow for too small velocities. To provide a rough estimate of D the velocity was estimated as $u = 0.12$ cm/sec, away from the wells. This value will lead to the estimate $D \approx 0.02$ cm^2/sec, which shows that dispersion cannot really be neglected (as it leads to spreading of the order of 1 inch for an experiment lasting for 300 seconds).

Fig. 8 shows snapshots of the displacement fronts at breakthrough from two different flow experiments, one under the optimal bang-bang policy and another under constant-rate injection. For comparison, the results of the corresponding analytical approach, which is free of dispersion, are also shown. The two results are similar, but not identical. The area swept by the injected fluid at breakthrough in the physical experiments is slightly smaller and less compact compared to the corresponding area from the numerical experiments. We attribute this difference to the dispersion in the Hele-Shaw cell. Nonetheless, the efficiency was found to be higher under the optimal bang-bang policy than for the constant rate case. For the

particular geometrical arrangement of Fig. 7, the ratio of the breakthrough time under bang-bang injection to that under constant-rate injection is predicted from the calculation to be 1.03. In fact, the result from the physical experiment is estimated to be slightly larger, 1.04, indicating that even in the presence of dispersion, the bang-bang policy is better than constant rate injection. (The relatively small improvement is here due to the particular geometrical arrangement considered. As shown in Fig. 3, the improvement in efficiency can reach larger values, depending on the geometry.) Additional experiments are discussed below in Section II.

HETEROGENEOUS POROUS MEDIA

Consider, next, the optimization problem in a heterogeneous medium. It is well known that geological porous media exhibit a great degree of heterogeneity in permeability[24], the consideration of which is paramount for realistic predictions. Typically, the permeability is expressed in terms of a stochastic function in space, with various assumed forms of spatial correlation. A popular description is in terms of self-affine noise of the fBm type[25–28] (fractional Brownian motion), where correlations grow with distance and the correlation length is unbounded. In such cases, the texture of the permeability field is characterized by its Hurst exponent H, $0 < H < 1$, larger values of H corresponding to a smoother field[26]. For example, $H = 0.5$ corresponds to the classical Brownian motion. Examples of random and correlated permeability fields of this type are shown in Fig. 9. Layered reservoirs are also common. As in many applications involving geologic media, however, full knowledge of the heterogeneity structure is not available in the typical case. As a result, one has to rely on a statistical description, in which a number of different permeability realizations are conducted, and from which results on average behavior can be extracted.

In this section, we will consider the optimal control problem for heterogeneous reservoirs in a miscible displacement with equal mobilities and in the absence of dispersion, as above. For simplicity, only the case with a constant overall injection rate constraint will be considered, other constraints being readily implemented. Now, as in the case of a homogeneous reservoir at unit mobility ratio, the state equations are linear with respect to the injection rates. Since the performance index to be maximized is also linear, then the non-singular optimal control is again of the bang-bang type.

However, in the heterogeneous case, we cannot take advantage of the potential flow formalism. Nonetheless, and because of the unit mobility ratio assumption, the displacement can still be expressed as a superposition of the response of individual wells. This facilitates considerably the problem description and its computation, as shown below. Unlike potential flow, where the well responses can be obtained analytically, however, displacements in heterogeneous reservoirs require a numerical solution.

1. Formulation

For simplicity, we will consider again a problem consisting of $N_W - 1$ injection wells of varying injection rates, and of one production well. Now, the flow field is obtained by solving the flow equations in a heterogeneous medium, namely we can write

$$\nabla \cdot k(\mathbf{x}) \nabla p = 0 \tag{18}$$

and

$$\mathbf{v}(\mathbf{x}, t) = -k(\mathbf{x}) \nabla p \tag{19}$$

with appropriate boundary conditions. Because the time dependence enters only through the boundary conditions, however, the velocity field can be also expressed in terms of the superposition of $N_W - 1$ two-well responses, namely

$$\mathbf{v}(\mathbf{x}, t) = \sum_{l=2}^{N_W} q_l(t) \mathbf{v}^{l,1}(\mathbf{x}) \tag{20}$$

where $\mathbf{v}^{l,1}(\mathbf{x})$ is the velocity field induced only by a two-well system, involving injection at unit strenght in well l and production in well 1. Equation (20) shows that the variation in time is the superposition of the responses of individual well pairs, the spatial variation of which is independent of time and needs to be computed only once. This facilitates greatly the computation of the optimal control problem, which involves repeated iterations. Thus, the non-linear dynamical description derived for the homogeneous system remains valid, except that now the spatial dependence must be computed numerically, in general.

To proceed, we follow the same approach as in Section I, subject to the following changes. In equations, such as (3) for example, the sum must be rearranged to read

$$v_x = \sum_{l=2}^{N_W} q_l(t) \left[\frac{x - x_{wl}}{(x - x_{wl})^2 + (y - y_{wl})^2} - \frac{x - x_{w1}}{(x - x_{w1})^2 + (y - y_{w1})^2} \right] \tag{21}$$

Thus, the approach to be followed is identical, if the substitution is made

$$v_x^{l,1} \longleftrightarrow \sum_{l=2}^{N_W} q_l(t) \left[\frac{x - x_{wl}}{(x - x_{wl})^2 + (y - y_{wl})^2} - \frac{x - x_{w1}}{(x - x_{w1})^2 + (y - y_{w1})^2} \right] \tag{22}$$

In this way, the optimal control formalism becomes identical for the two problems. Calculation details can be found in Sudaryanto[16]. Here, we will briefly note the following: In the numerical solution, we used a block-centered finite-differences grid, the solution being computed at the center of each grid block. Harmonic averaging was used for the spatially varying permeabilities. The resulting matrix for the pressure was solved with an LSOR method. In tracking the front, expressions for the velocity coefficients in points other than the grid-block centers are often needed. These were obtained using multilinear interpolation from the values known at the four corner points of the square, within which the front resides at any given time. Likewise, the evolution of the Lagrange multipliers was obtained by solving numerically the corresponding equations, which now also involve evaluating numerically the spatial derivatives of $v_x^{l,1}$ and $v_y^{l,1}$ $(l = 2, \cdots N_W)$. These were computed using three-point finite-differences. In some cases, streamtube simulation was also used. The optimal control computation was similar to Section I.

2. Numerical Results

Various forms of heterogeity were used in the numerical experiments, including a large-scale flow barrier, a layered medium, and random and spatially correlated permeabilities of the fBm type.

In the first example, we considered a large-scale flow barrier intended to model the presence of an impermeable fault. The numerical results show that, in all cases, the optimal injection policy is bang-bang with one switch time. As before, the optimal switch time corresponds to the simultaneous arrival of the displacement fronts from the two injectors at the producer. Fig. 10 shows snapshots of the front movement under the optimal bang-bang injection policy. The particle tracking method used gives the expected results. The flow barrier impedes the flow towards the sink, while following the switch in injection, the front from well A is re-directed towards the sink. These results agree well with the results of flow experiments in the Hele-Shaw cell to be discussed below. Fig. 11 shows a comparison of the displacement efficiency at breakthrough under bang-bang and constant-rate injection policy. As expected, bang-bang injection outperforms constant-rate injection, with a maximum efficiency improvement of 13.8% in the particular geometry considered.

In the second example, we considered displacement in a layered reservoir, consisting of two regions with constant but different permeability values, k_1 and k_2 (e.g. see Fig. 12a, where $k_1 = 0.25k_2$). The numerical results show that, in most cases, the optimal injection policy has one switch time. However, for some geometries, two switch times are also possible. In all cases, the optimal policy involves steering the displacement fronts towards the low permeability region, first, to delay breakthrough as much as possible. Fig. 12 shows snapshots of the front movement under such a bang-bang policy, where two switch times are involved, corresponding right after the snapshots in Fig. 12b and 12c, respectively. The response of the streamlines after the switch in injection is apparent in the figure. As before, bang-bang injection gives better displacement efficiency at breakthrough than constant-rate injection for all distance ratio values tested[16].

The last example of reservoir heterogeneity corresponds to random and spatially correlated fields. A log-normal permeability distribution with a modest permeability contrast of four ($k_{max} = 4k_{min}$) was studied. The uncorrelated field was generated by randomly assigning values from a log-normal distribution. The spatially correlated fields were constructed using the successive random addition algorithm[26,29]. In the numerical experiments, values of the Hurst exponent equal to 0.2, 0.5, and 0.8 were used. For each case, a total of 100 different realizations were generated. The results showed that the optimal injection policy is always bang-bang with one switch time. Snapshots of the front movement under the optimal bang-bang policy are shown in Fig. 13 for a particular realization of the uncorrelated case. An example of the correlated case is given in Fig. 14, where displacement fronts at breakthrough under bang-bang and constant-rate injection policy, and for a particular realization of the permeability field, are shown. The results show that bang-bang injection policy gives better displacement efficiency at breakthrough than constant-rate injection policy. Figures similar to Fig. 3 can be constructed for all these cases, but are not shown here for the sake of brevity. For example, for the particular realization of Fig. 13, the maximum efficiency improvement is in the range of 16%.

We must point out, that in addition to its dependence on well geometry, the improvement

in efficiency depends on the particular realization of permeability field and the exponent H, however. Fig. 15 shows the efficiency improvement for a particular well geometry (a three-well system with distance ratio = 0.707 and angle α= 45°), for different realizations of the permeability field and different H exponents. The range of efficiency improvement is essentially the same for each model of spatial correlation, almost independent of the value of the Hurst exponent. However, the efficiency improvement varies significantly from one realization to another, reflecting the different spatial arrangement of the flow paths. Another illustration of this effect is the variation of the (normalized) switch time of the bang-bang policy (Fig. 16). This time is shown to vary in a relatively narrow range (from about 0.85 to 1.05) for the case of uncorrelated permeability fields. As the spatial correlation increases, however, the range of variation increases significantly (from about 0.7 to 1.3) and it has a weak increasing dependence on H.

3. A Sensitivity Study

To complete the study of heterogeneity, we considered a sensitivity study, in which we posed the question what would be the reduction in efficiency, if the heterogeneity of the medium were ignored in the designing of the displacement process. To address this question, we compared the displacement efficiency at breakthrough from the application of a bang-bang injection policy, which is optimal for the assumed homogeneous problem, to that from constant-rate injection policy which is also optimal for the same assumed homogeneous reservoir. Answering this question will essentially dictate whether the advantage of bang-bang over constant rate optimal injection carries over to heterogeneous systems, even though they were both designed on the assumption that the reservoir is homogeneous. Numerical experiments were conducted for one particular well geometry, namely a three- well system with distance ratio = 0.707 and an angle of 45°. The permeability of the homogeneous medium was taken equal to the mean value of the heterogeneous field. For the heterogeneous problem we considered the previous (modestly heterogeneous) models.

The results are shown in Fig. 17. In almost all cases (the two exceptions in the random case are probably due to numerical error), bang-bang injection gives a better displacement efficiency at breakthrough than constant-rate, even though it was designed on the assumption of a homogeneous reservoir. On average, the improvement and its variance increase as the spatial correlation of the permeability becomes stronger. Thus, the benefits of bang-bang injection carry over (even more accentuated) to the heterogeneous case. In assessing these results one should also note that the permeability contrast was taken to be relatively narrow (only a factor of 4). In many realistic situations, permeability contrasts of much larger magnitude, reaching several orders of magnitude, are not uncommon. Under such conditions, we expect that optimal bang-bang policies will offer additional quantitative improvement.

4. Experiments

Experiments corresponding to the geometry of the first example in the previous subsection were also carried out. We used the previous Hele-Shaw cell with a large-scale flow barrier (Fig. 18), put in place using a 4 inch x 1 inch rubber strip between the glass plates. Shown

in Fig. 18 are snapshots of the front movement under the optimal bang-bang injection policy computed as described above. The corresponding numerical results were given in Fig. 10 and show very similar features. By appropriately switching the injection rates, both fronts are steered towards the production well, in which they arrive at almost the same time as predicted (the slight discrepancy due again to dispersion). The difference with the constant injection rate case (where the rates were chosen to optimize the displacement efficiency) is shown in Fig. 19. The final configurations are different, with more displacement due to injection from the nearest well, in the bang-bang case. The improvement in the efficiency ratio between bang-bang and constant rate policies was estimated to be 1.06 in the physical flow experiments, compared to a predicted value of 1.05. As with the previous case, this slight difference is probably due to the presence of dispersion in the physical experiment.

CONCLUSIONS

In this paper, the problem of the control of flows, and more specifically of displacement fronts, in porous media by controlling the injection rates at various point sources, was addressed. We presented an approach based on optimal control theory to maximize the displacement efficiency at breakthrough in 2-D miscible displacements, when the mobilities of the two fluids are the same, and effects of gravity and dispersion are negligible. The approach relies on formulating the problem as a non-linear dynamics problem for the particles that define the front. In the case of homogeneous media, this formulation is analytic. In the case of heterogeneous media, we used a superposition approach to separate time and spatial dependences, which substantially reduces the computational requirements.

It was found that the non-singular optimal control policy is of the bang-bang type, namely a policy in which any given well operates at any time at the extreme limits of its injection rate. Then, the problem becomes one of determining the optimal switch times for each well. Depending on the problem, multiple switch times are possible, although most examples shown correspond to one switch time only. Numerical results showed that this policy leads to an improved displacement efficiency at breakthrough, compared to the case of constant rate injection. The improvement is based on the underlying assumption that miscible flows are not direction-dependent, hence displacement fronts emanating from a given source, can recede and change direction reversibly, upon the activation of another source. This assumption may not hold for immiscible flows where flow properties are hysteretic. Sensitivity studies in heterogeneous media showed that the results depend sensitively on the particular realization of the permeability field, as well as on the presence or absence of spatial correlation. In particular, it was shown that on average, the advantages of the bang-bang control remain, and in fact become greater, compared to constant-rate injection, even if one were to design the optimal control process in the absence of information on the permeability heterogeneity. Experimental results in a Hele-Shaw cell supported to a certain extent, the theoretical findings.

The above theory can be extended to address problems of variable mobility and of immiscible displacements[14]. Objctive functions other than the displacement efficiency at breakthrough of the injected fluid, considered here, are amenable to a similar analysis. Likewise, extensions to more complex problems, particularly in 3-D with partially active sources, etc.,

are feasible. These problems capture important temporal and spatial dynamical features of flows in porous media as a result of the time dependence of injection rates at various point sources. In particular, they are related to the more general problem of the dynamics of deformation of material lines in porous media flows, which is a subject of further research[16].

ACKNOWLEDGEMENTS

This research was also partly supported by PERTAMINA, the contributions of which is gratefully acknowledged.

REFERENCES

[1]M. Muskat, *The Flow of Homogeneous Fluids through Porous Media*, McGraw-Hill, New York (1937).
[2]J. Bear, *Dynamics of Fluids in Porous Media*, Dover, New York (1988).
[3]W.F. Ramirez, Z. Fathi, and J.L. Cagnol, "Optimal injection policies for enhanced oil recovery : Part 1- Theory and computational strategies," SPE Journal, 328 (1984).
[4]Z. Fathi and W.F. Ramirez, "Optimal injection policies for enhanced oil recovery : Part 2- Surfactant flooding," SPE Journal, 333 (1984).
[5]Z. Fathi and W.F. Ramirez, "Use of optimal control theory for computing optimal injection policies for enhanced oil recovery," Automatica **22** (1), 333 (1986).
[6]Z. Fathi and W.F. Ramirez, "Optimization of an enhanced oil recovery process with boundary controls: a large-scale non-linear maximization," Automatica **23** (3), 301 (1987).
[7]W.F. Ramirez, *Application of Optimal Control Theory to Enhanced Oil Recovery*, Elsevier, Amsterdam (1987).
[8]H. Asheim, "Maximization of water sweep efficiency by controlling production and injection rates," paper SPE 18365 presented at the SPE European Petroleum Conference, London, UK, Oct. 16-19, 1988.
[9]G.A. Virnovsky, "Waterflooding strategy design using optimal control theory," paper presented at the 6th European IOR Symposium, Stavanger, Norway, May 21-23, 1991.
[10]S.B. Gorell and G.M. Homsy, "A theory of the optimal policy of oil recovery by secondary displacement processes," SIAM J. Appl. Math. **43**, 79 (1983).
[11]G.M. Homsy, "Viscous fingering in porous media," Annu. Rev. Fluid Mech. **19**, 271 (1987).
[12]Y.C. Yortsos, "Instabilities in displacement processes in porous media," J. Phys.: Condens. Matter **2**, SA 443 (1990).
[13]P. Petitjeans, C.-Y. Chen, E. Meiburg and T. Maxworthy, "Miscible quarter five-spot displacements in a Hele-Shaw cell and the role of flow-induced dispersion," Phys. Fluids **11**, 1705 (1999).
[14]B. Sudaryanto and Y.C. Yortsos, "Optimization of Fluid Front Dynamics in Porous Media Using Rate Control: II. Variable Mobility Fluids," to be submitted.
[15]J.M. Ottino, *The Kinematics of Mixing: Stretching, Chaos and Transport*, Cambridge University Press, Cambridge (1989).

[16]B. Sudaryanto, "Optimization of displacement efficiency of oil recovery in porous media using optimal control theory," Ph.D. Dissertation, University of Southern California (1998).
[17]N.V. Dokholyan, Y. Lee, S. Buldyrev, S. Havlin, P.R. King and H.E. Stanley, "Scaling of the distribution of shortest paths in percolation," J. Stat. Phys. **93**, 603 (1998).
[18]A.E. Bryson, Jr. and Y.C. Ho, *Applied Optimal Control: Optimization, Estimation, and Control*, Hemisphere, Washington, DC. (1975).
[19]K. Glashoff and E. Sachs, "On theoretical and numerical aspects of the bang-bang principle," Numer. Math. **29**, 93 (1977).
[20]R.R. Mohler, *Nonlinear Systems, Volume II: Applications to Bilinear Control*, Prentice Hall, Englewood Cliffs, NJ (1991).
[21]C.Y. Kaya and J.L. Noakes, "Computations and time-optimal controls," Optimal Control Appl. Meth. **17**, 171 (1996).
[22]E.B. Meier and A.E. Bryson, Jr., "Efficient algorithm for time-optimal control of a two-link manipulator", J. Guid. Control Dyn. **13**, 85 (1990).
[23]F.A.L. Dullien, *Porous Media: Fluid Transport and Pore Structure*, Academic Press, New York (1992).
[24]G. Dagan, *Flow and Transport in Porous Formations*, Springer-Verlag, Berlin (1989).
[25]T.A. Hewett, "Fractal distributions of reservoir heterogeneity and their influence on fluid transport", paper SPE 15386 presented at 61st Annual Technical Conference and Exhibition of SPE, New Orleans, LA Oct. 5-8, 1986.
[26]J. Feder, *Fractals*, Plenum Press, New York (1988).
[27]A.-L. Barabasi and H.E. Stanley, *Fractal Concepts in Surface Growth*, Cambridge University Press, Cambridge (1995).
[28]C. Du, C. Satik and Y.C. Yortsos, "Percolation in a fractional Brownian motion lattice," AICHEJ **42**, 2392 (1996).
[29]H.O. Peitgen and D. Saupe, *The Science of Fractal Images*, Springer-Verlag, New York (1988).

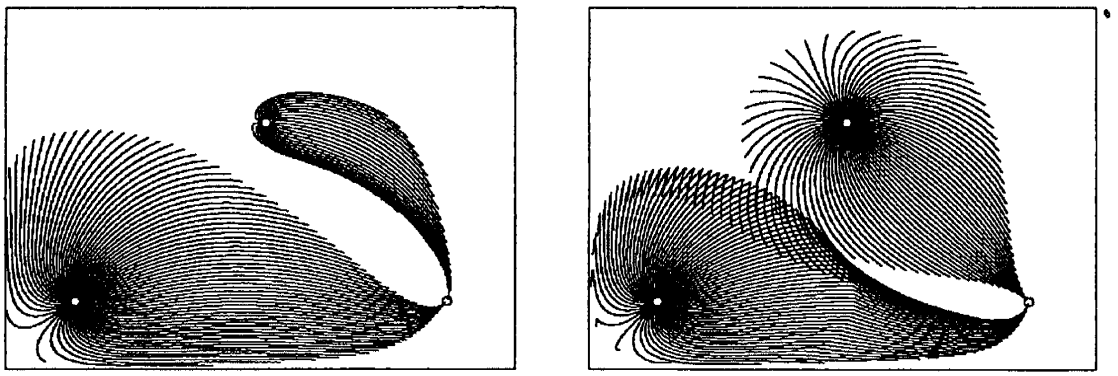

(a) Constant-rate injection policy **(b) Bang-bang injection policy**

Figure 1: Snapshots of front movement under bang-bang injection policy. (a) At initial time, (b) at time just before the injection switches from well A to well B, (c) at time when injection is only through well B. [Note the bending of the trajectories following the switch of injection from well-A to well-B], and (d) at breakthrough. (Potential flow, rectangular reservoir, distance ratio equal to 0.7, angle equal to 45°.)

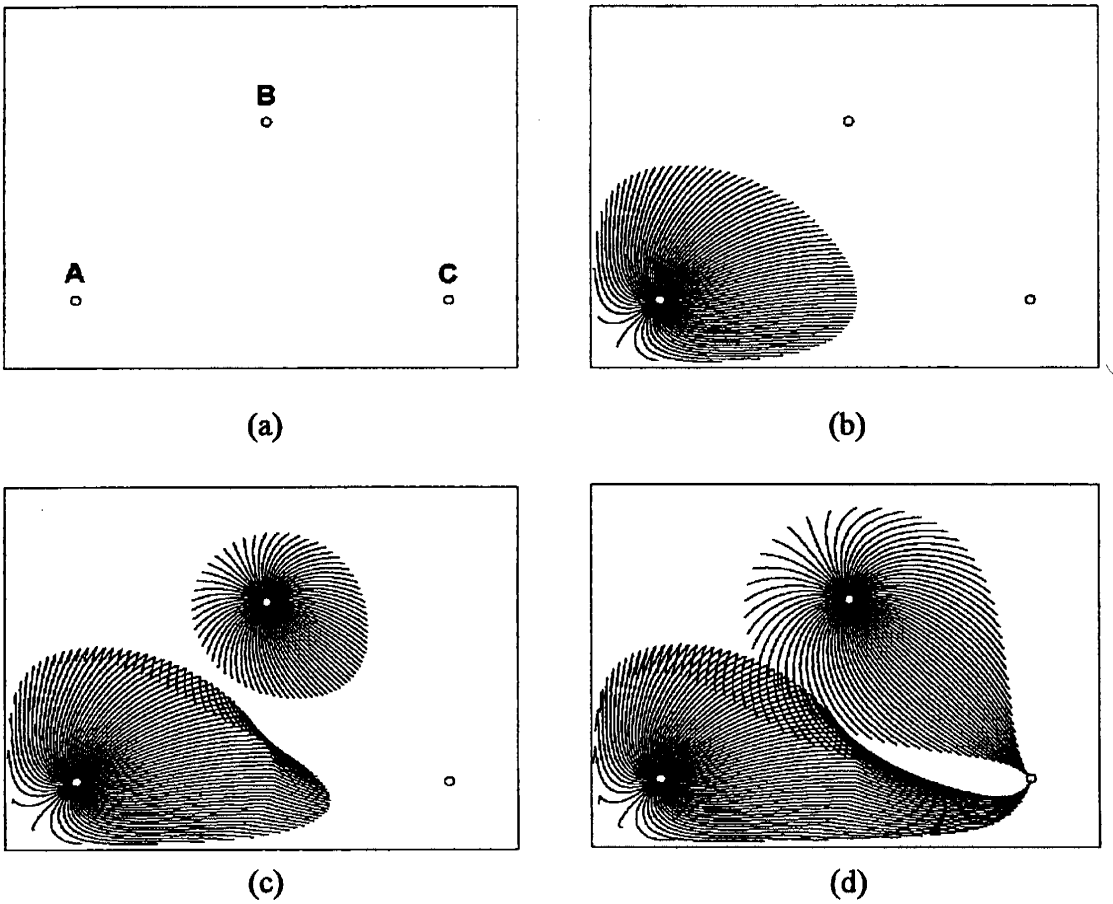

Figure 2: Displacement fronts at breakthrough under constant-rate and bang-bang injection policies. (Potential flow, rectangular reservoir, distance ratio equal to 0.7, angle equal to 45°.)

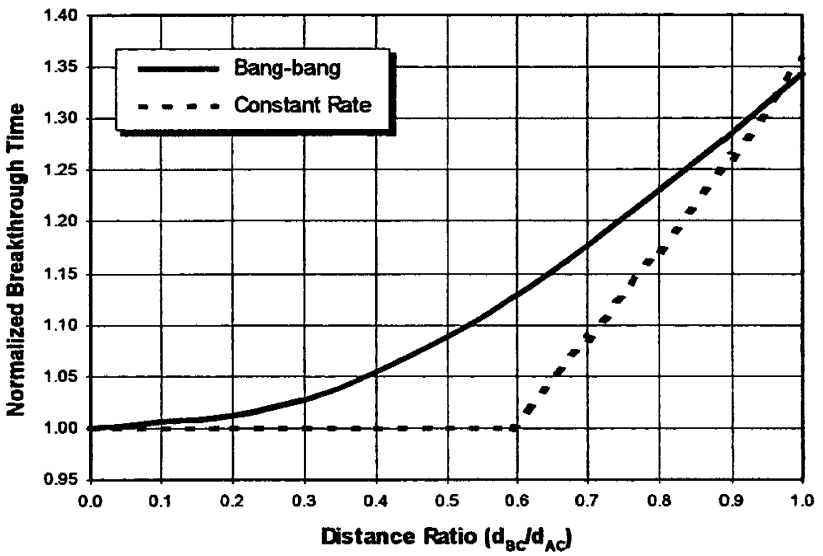

Figure 3: Normalized breakthrough time under constant-rate and bang-bang injection policies as a function of the distance ratio. (Potential flow, rectangular reservoir, distance ratio equal to 0.7, angle equal to 45°.)

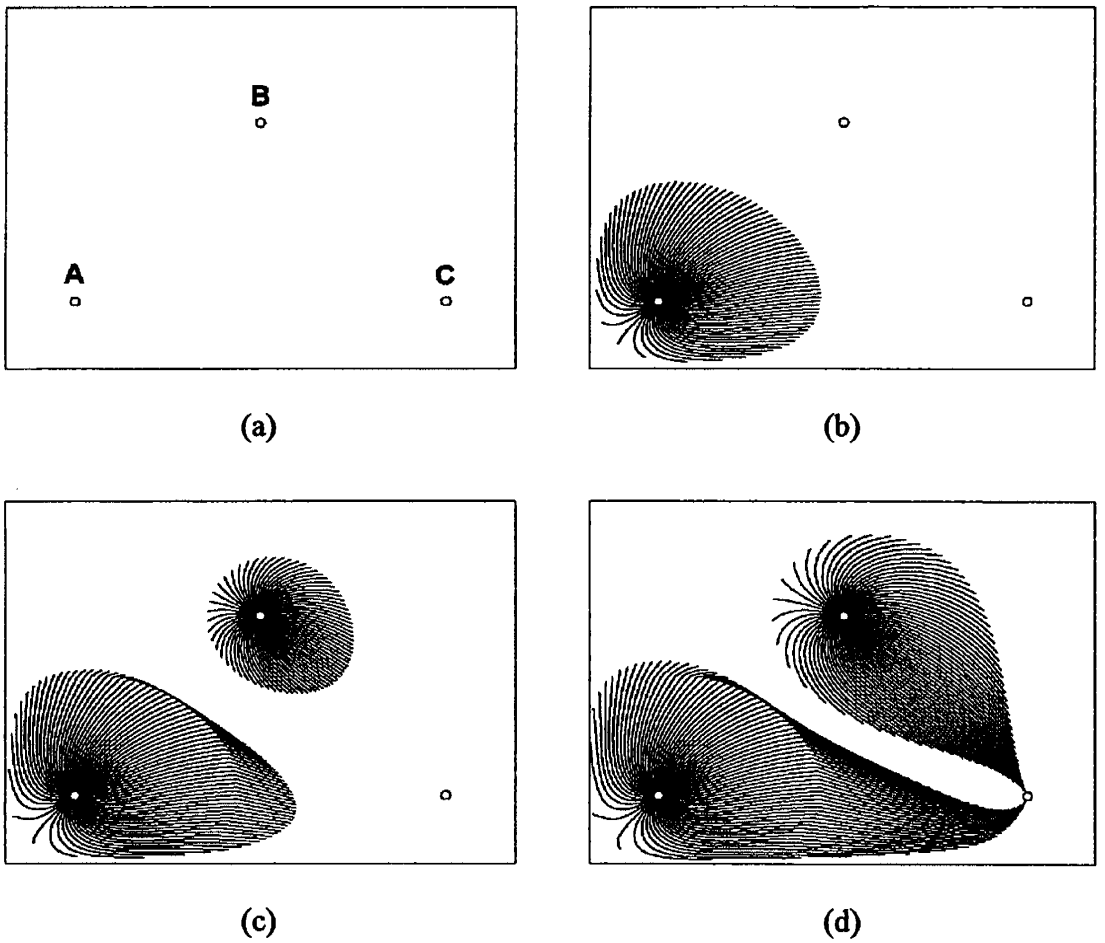

Figure 4: Snapshots of front movement under bang-bang injection policy. (a) At initial time, (b) at time just before injection from well B started, (c) at time when both injectors A and B are active, and (d) at breakthrough. (Potential flow, rectangular reservoir, distance ratio equal to 0.7, angle equal to 45°, well injectivity constraint.)

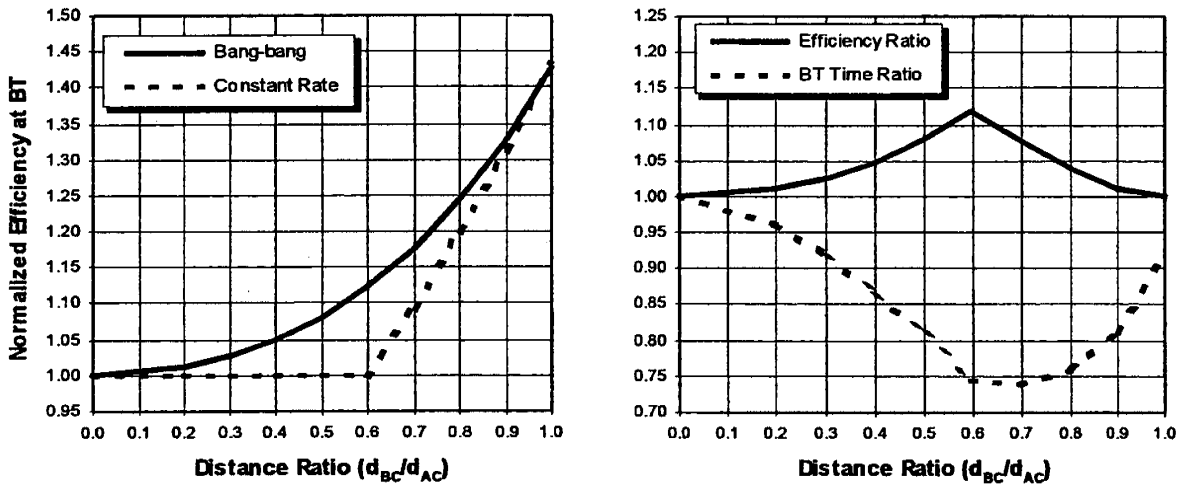

Figure 5: Efficiency at breakthrough (left), efficiency ratio and breakthrough time ratio (right) as a function of the distance ratio. (Potential flow, rectangular reservoir, angle equal to 45°, well injectivity constraint.)

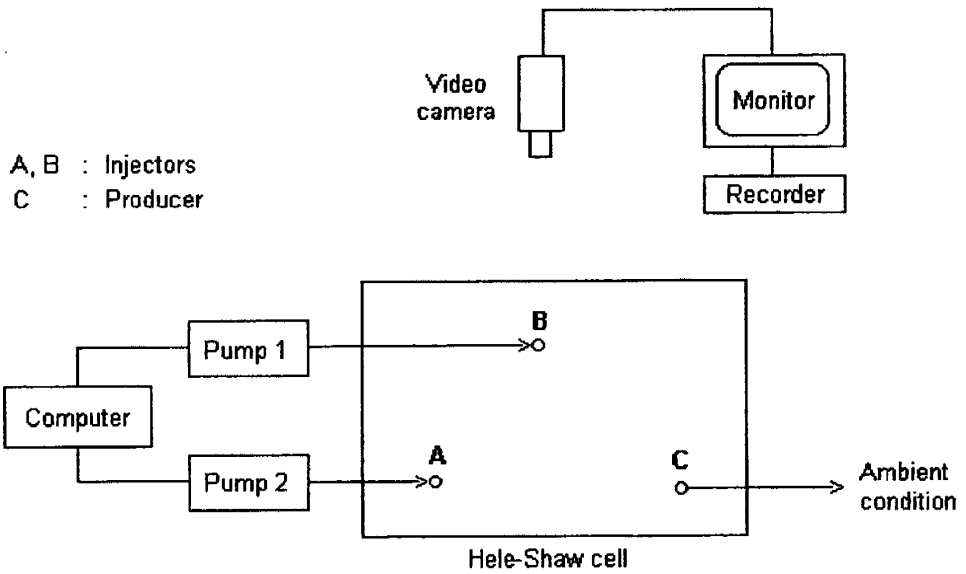

Figure 6: Schematic of the experimental set-up.

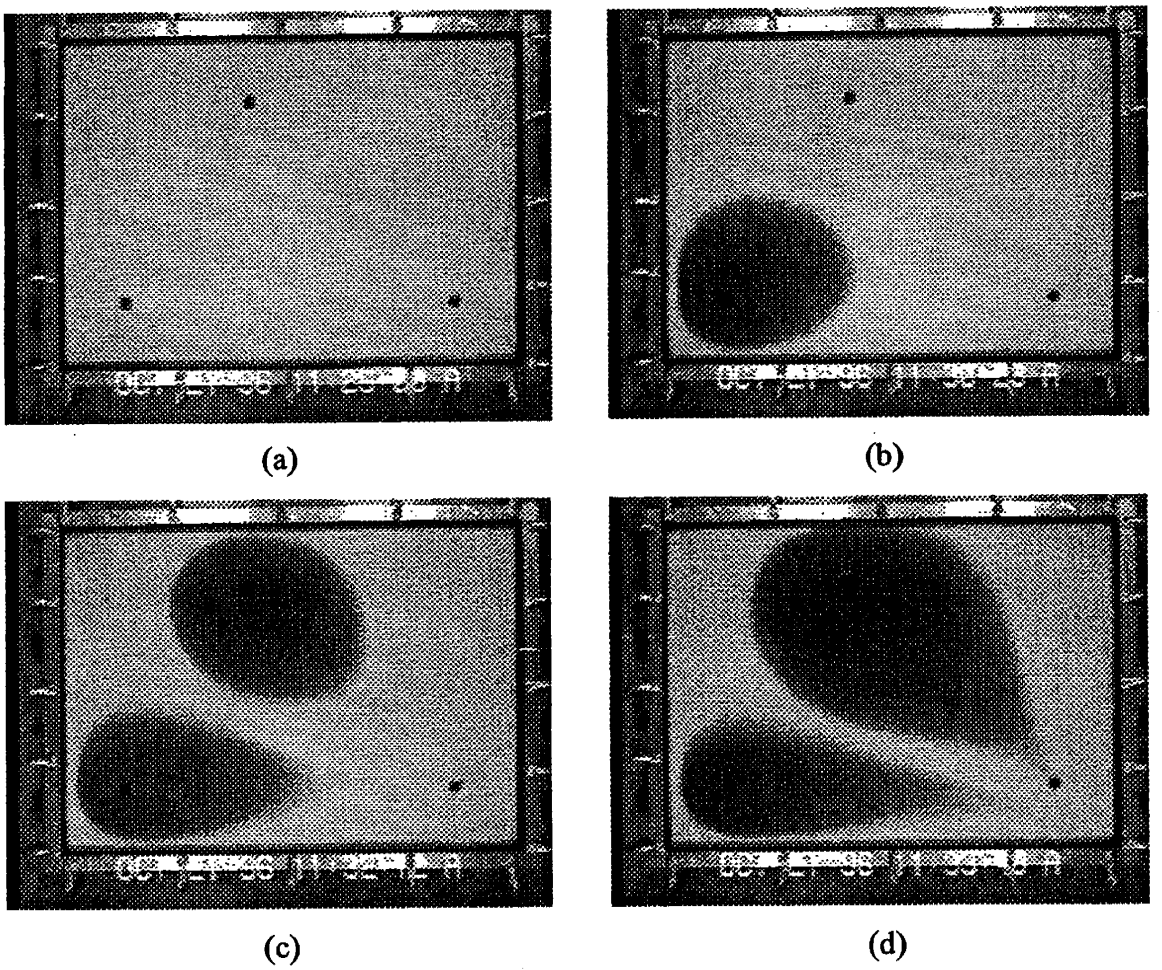

Figure 7: Experimental snapshots of front movement under bang-bang injection policy. (a) At initial time, (b) at time just before the injection switches from well A to well B, (c) at time when injection is only through well B, and (d) at breakthrough. (Tracer displacement in a rectangular Hele-Shaw cell, distance ratio equal to 0.884, angle equal to 45^o.)

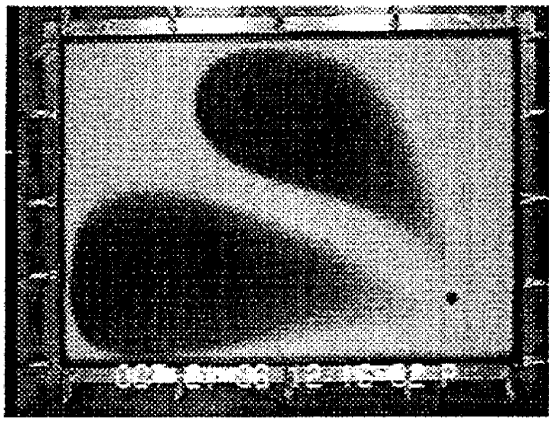

(a) Constant-rate injection policy

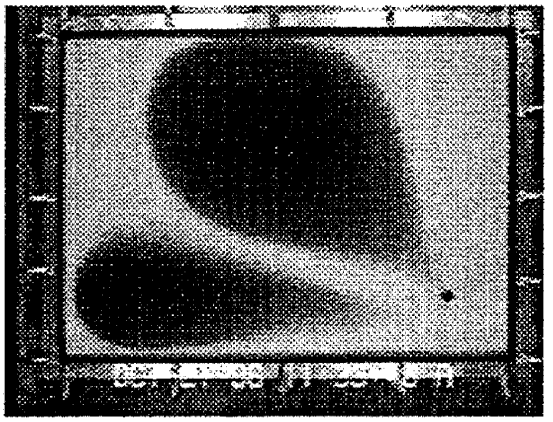

(b) Bang-bang injection policy

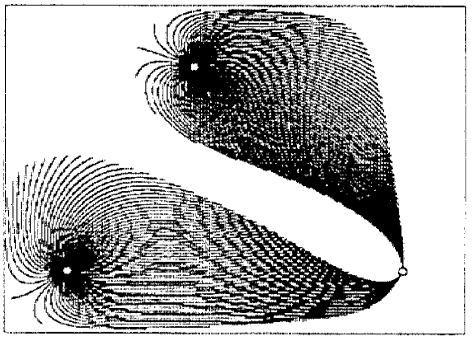

(a) Constant-rate injection policy

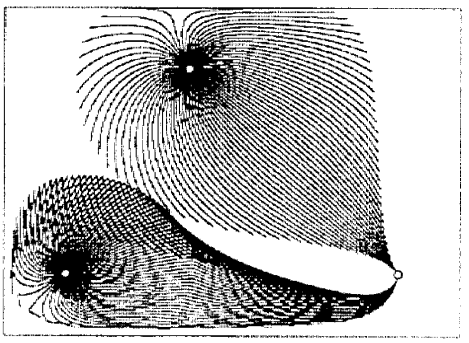

(b) Bang-bang injection policy

Figure 8: Comparison between experimental (top) and numerical results (bottom) for the displacement patterns at breakthrough under constant-rate (left) and bang-bang (right) injection.

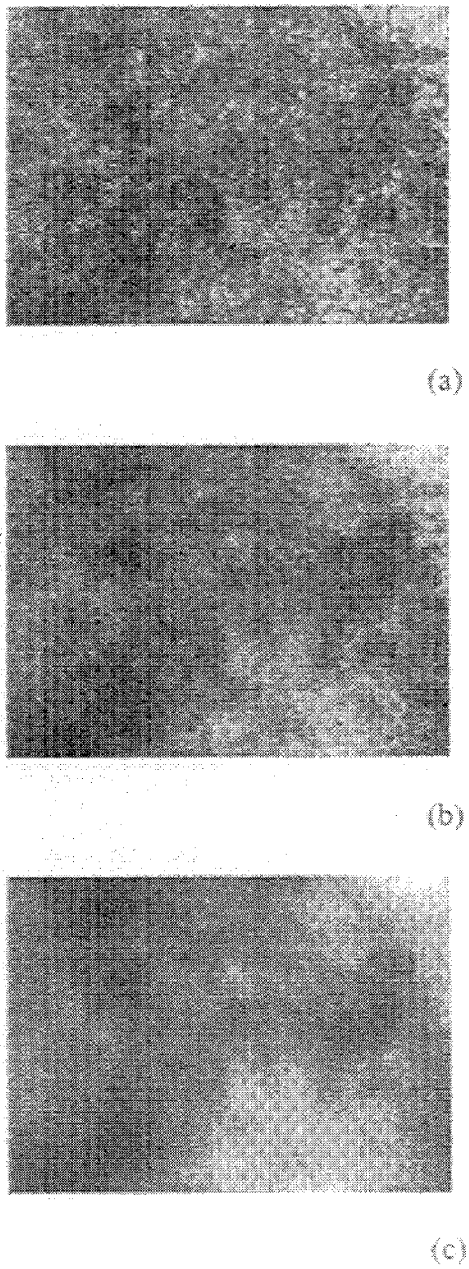

Figure 9: Realizations of correlated permeability fields of the fBm type with Hurst exponents $H = 0.2$, 0.5 and 0.8.

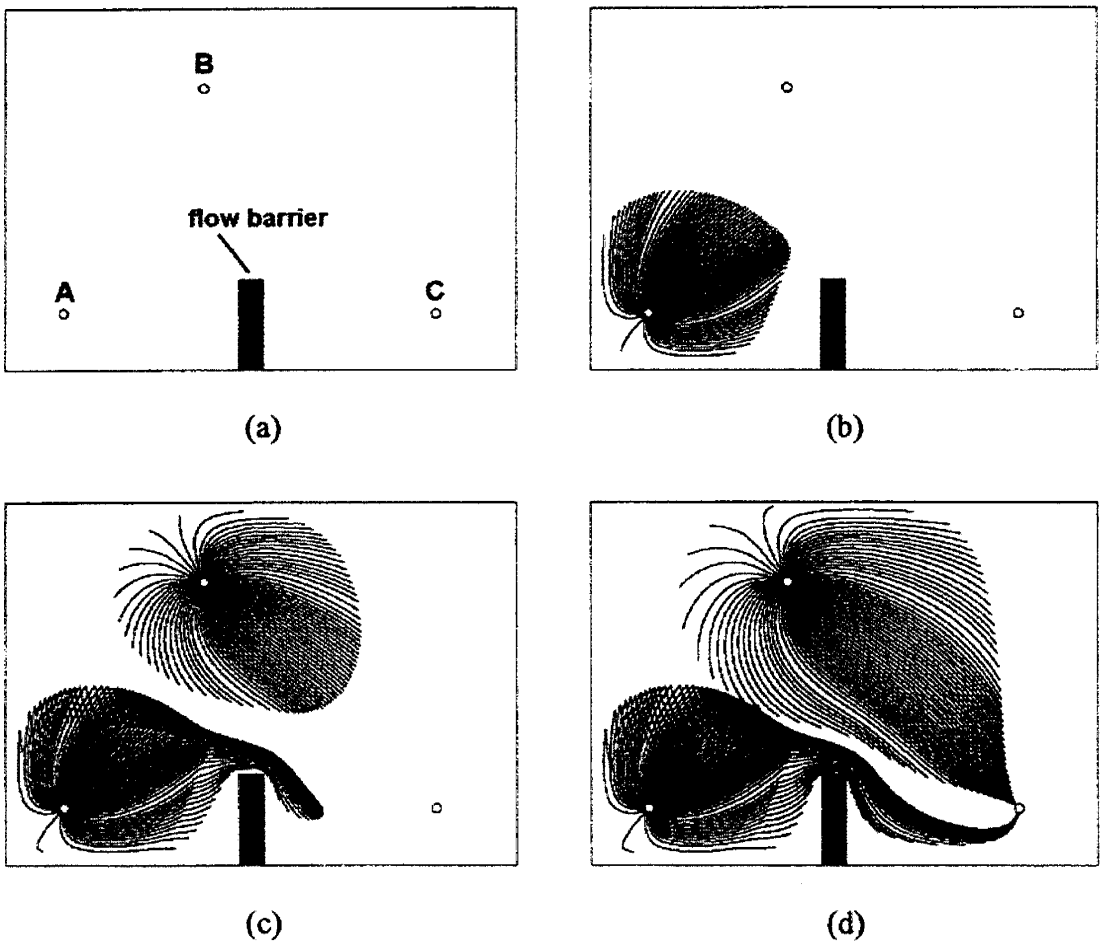

Figure 10: Snapshots of front movement under bang-bang injection policy. (a) At initial time, (b) at time just before injection switches to well B, (c) at time when injection is only through well B, and (d) at breakthrough. (Potential flow, rectangular reservoir with a flow barrier, distance ratio equal to 0.884, angle equal to 45°.)

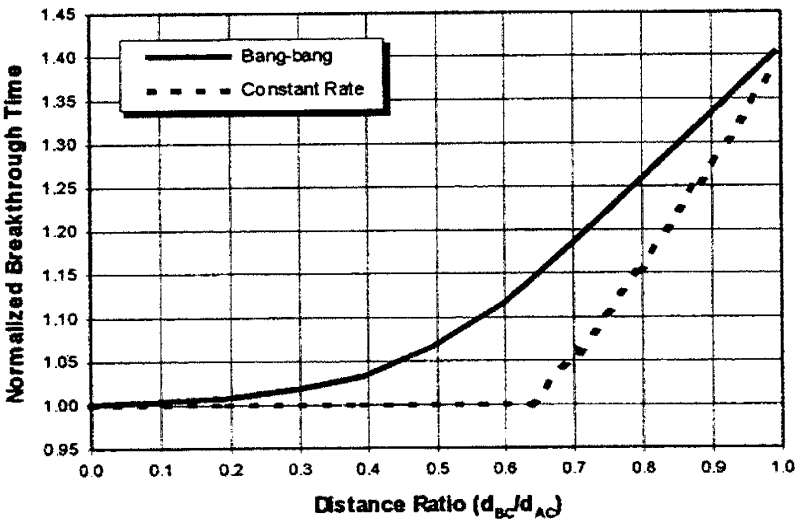

Figure 11: Normalized breakthrough time under constant-rate and bang-bang injection policy as a function of the distance ratio. (Potential flow, rectangular reservoir with a flow barrier, distance ratio equal to 0.884, angle equal to 45°.)

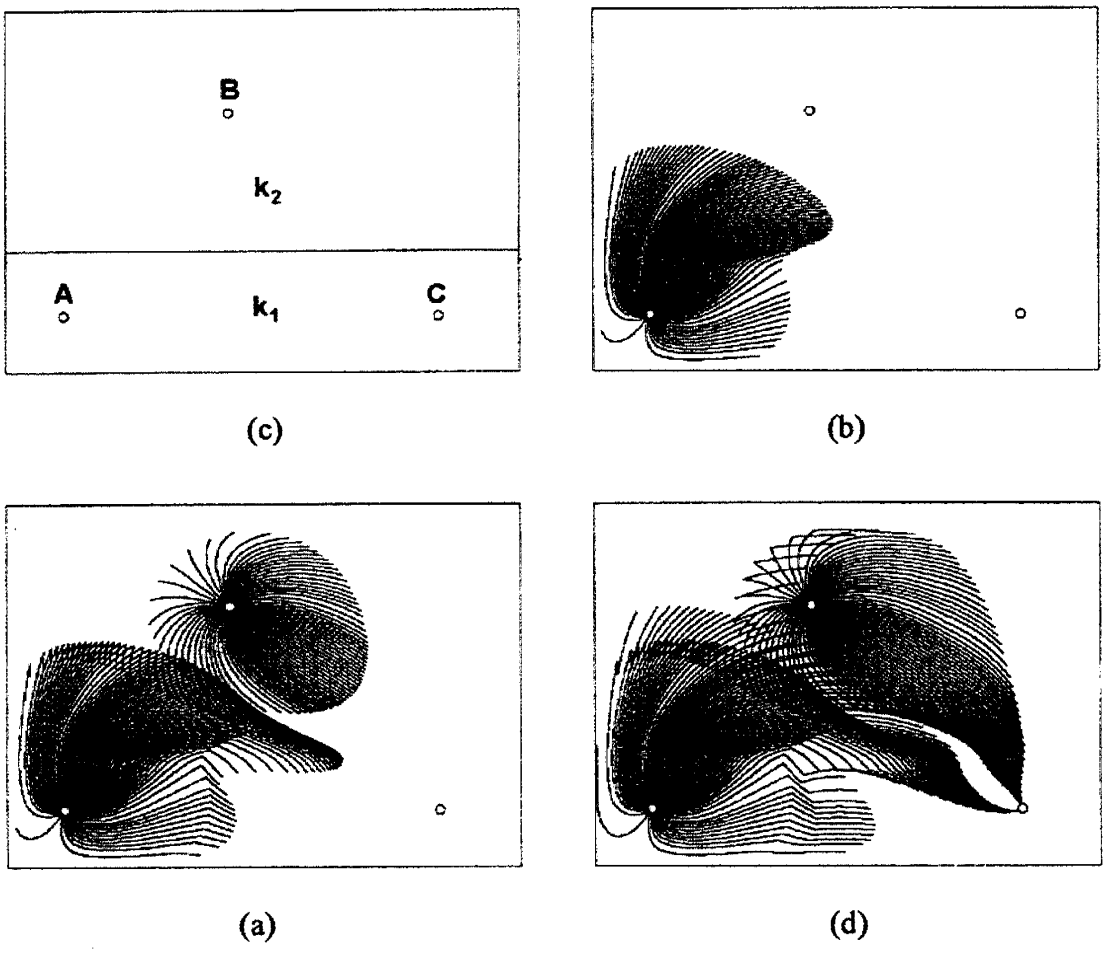

Figure 12: Snapshots of front movement under bang-bang injection policy. Two switch times are involved: (a) At initial time, (b) at time just before injection switches to well B, (c) at time just before injection switches back from well B to well A, and (d) at breakthrough. (Layered reservoir, $k_1 = 0.25k_2$, distance ratio equal to 0.795, angle equal to 45°.)

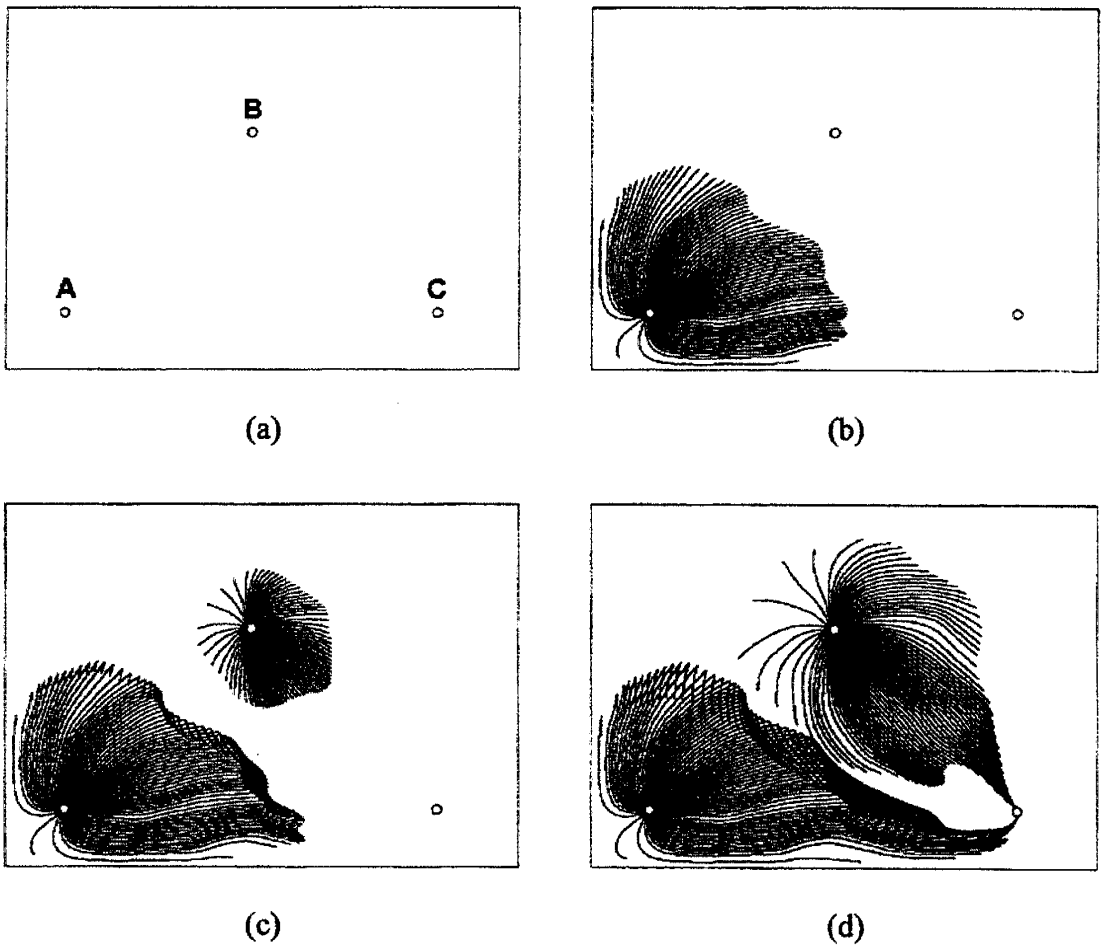

Figure 13: Snapshots of front movement under bang-bang injection policy. Two switch times are involved: (a) At initial time, (b) at time just before injection switches to well B, (c) at time when injection is only through well B, and (d) at breakthrough. (Random permeability field, distance ratio equal to 0.707, angle equal to 45°.)

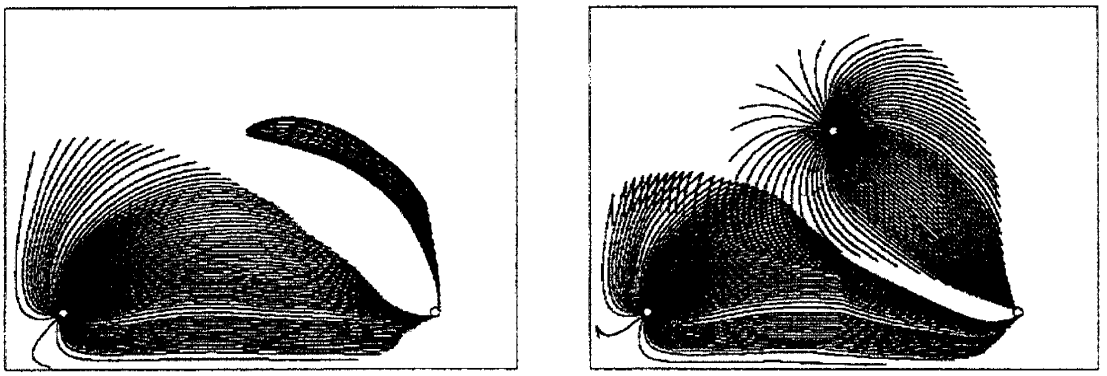

(a) Constant-rate injection policy

(b) Bang-bang injection policy

Figure 14: Displacement fronts at breakthrough under constant-rate and bang-bang injection policies. (Correlated (fBm) permeability field with $H = 0.8$, distance ratio equal to 0.707, angle equal to 45°.)

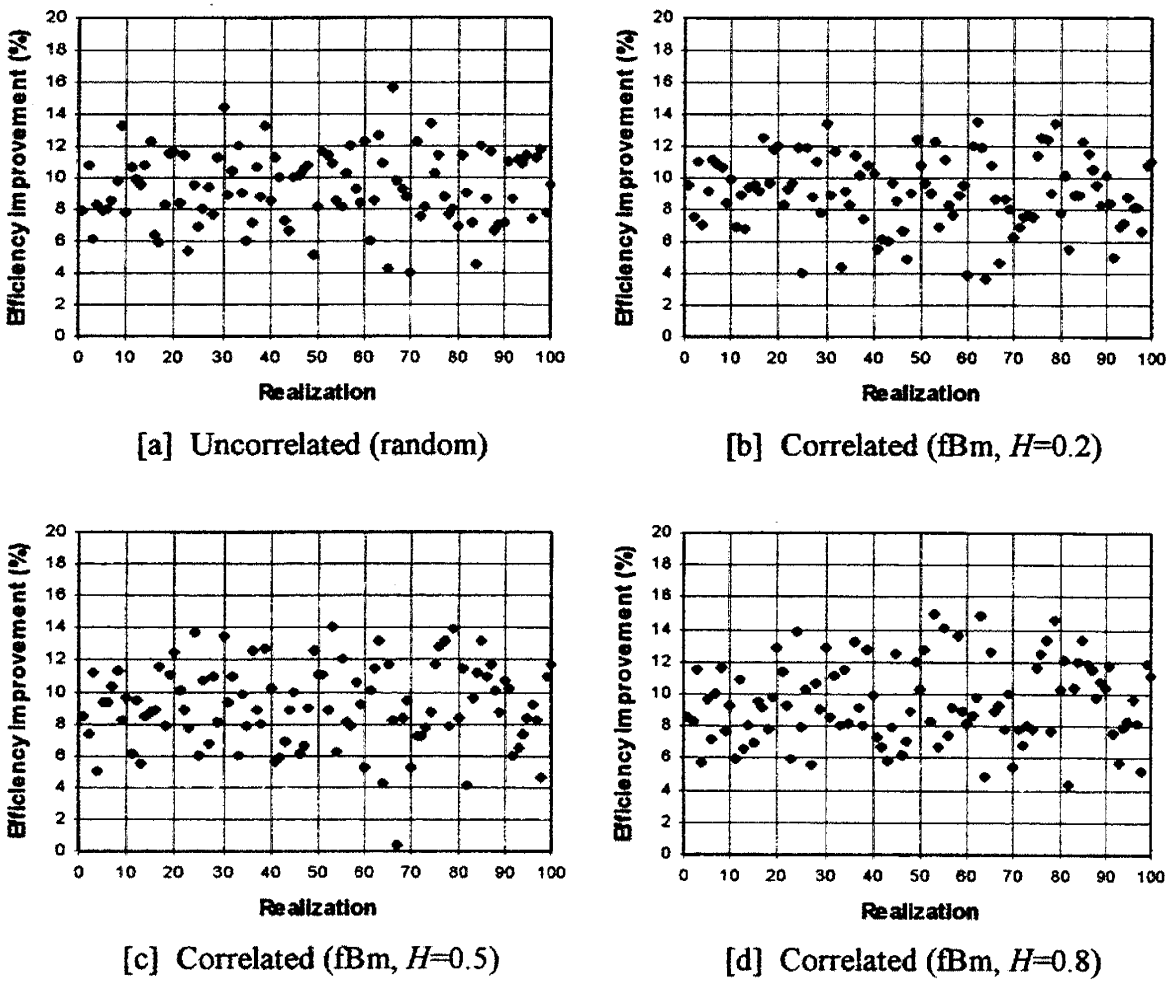

Figure 15: Efficiency improvement of bang-bang over constant-rate injection policy for different realizations of uncorrelated and correlated permeability fields.

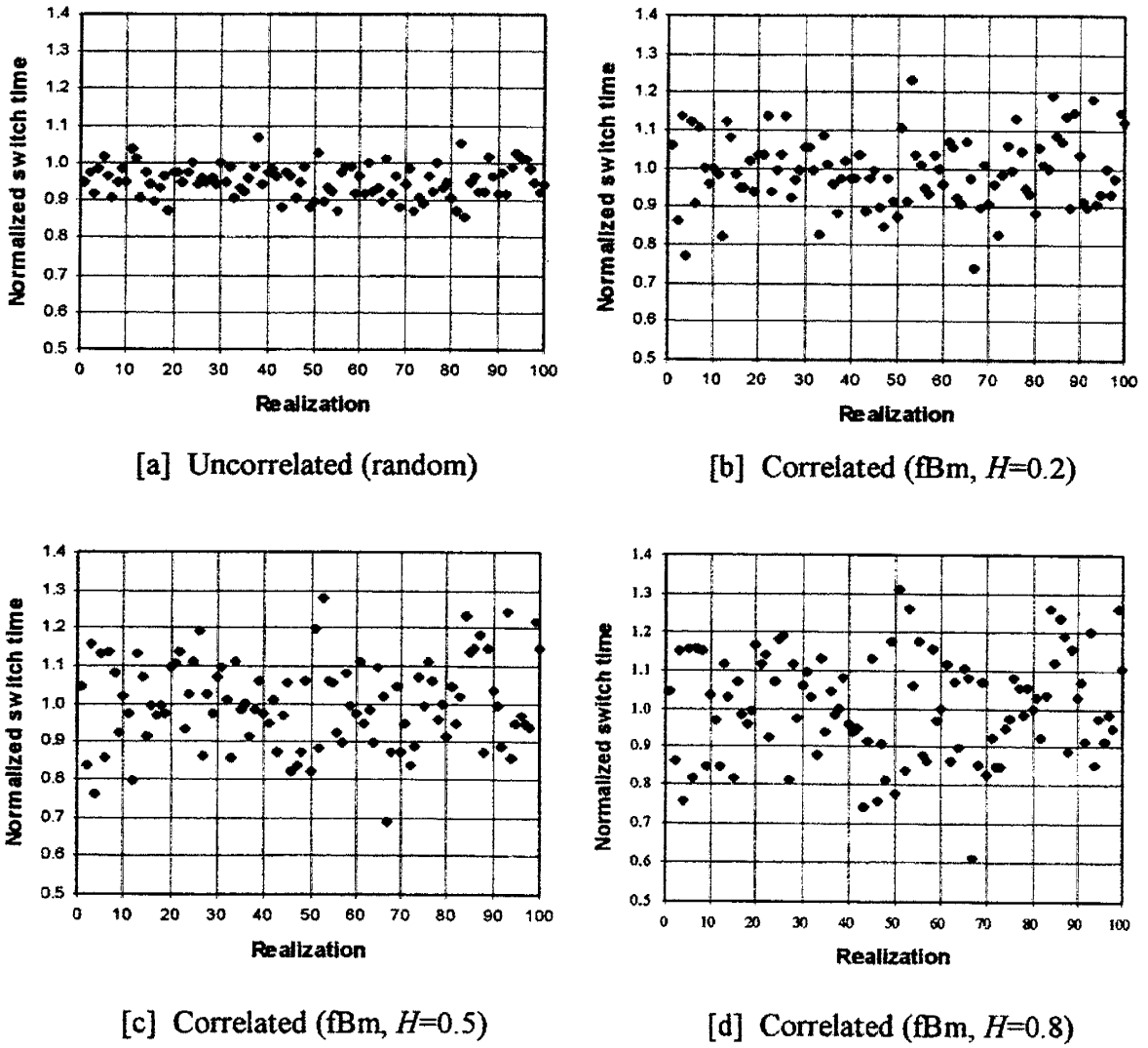

Figure 16: Normalized optimal switch time for different realizations of uncorrelated and correlated permeability fields.

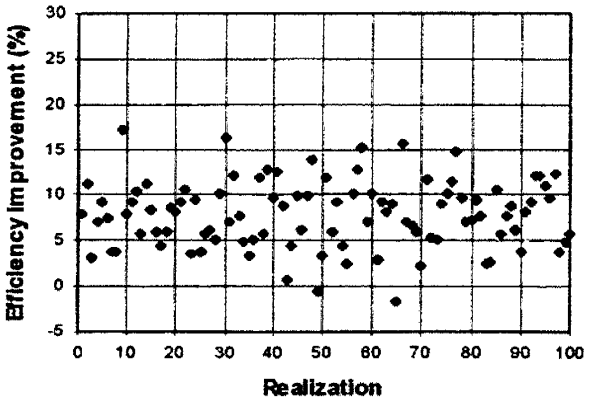

[a] Uncorrelated (random)

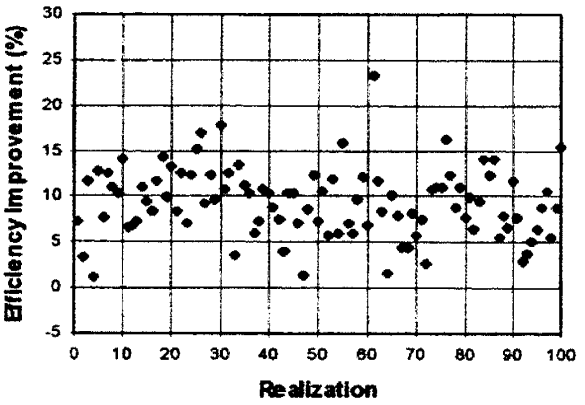

[b] Correlated (fBm, H=0.2)

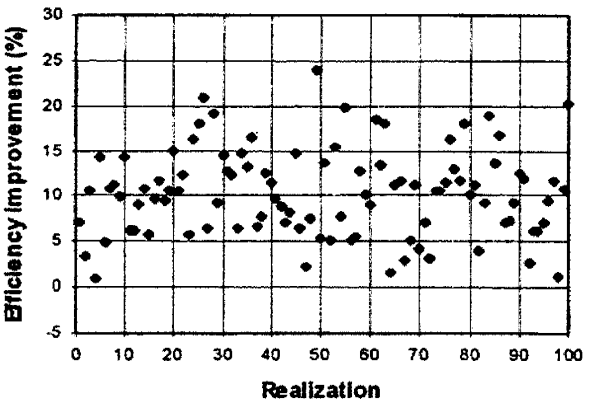

[c] Correlated (fBm, H=0.5)

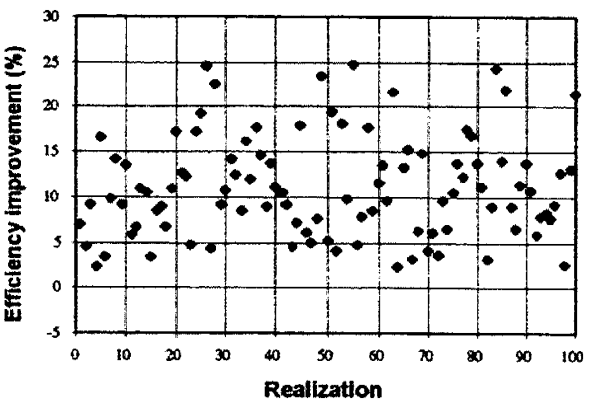

[d] Correlated (fBm, H=0.8)

Figure 17: Efficiency improvement of bang-bang over constant-rate injection policy (both injection policies are optimal for a homogeneous system) for different realizations of uncorrelated and correlated permeability fields.

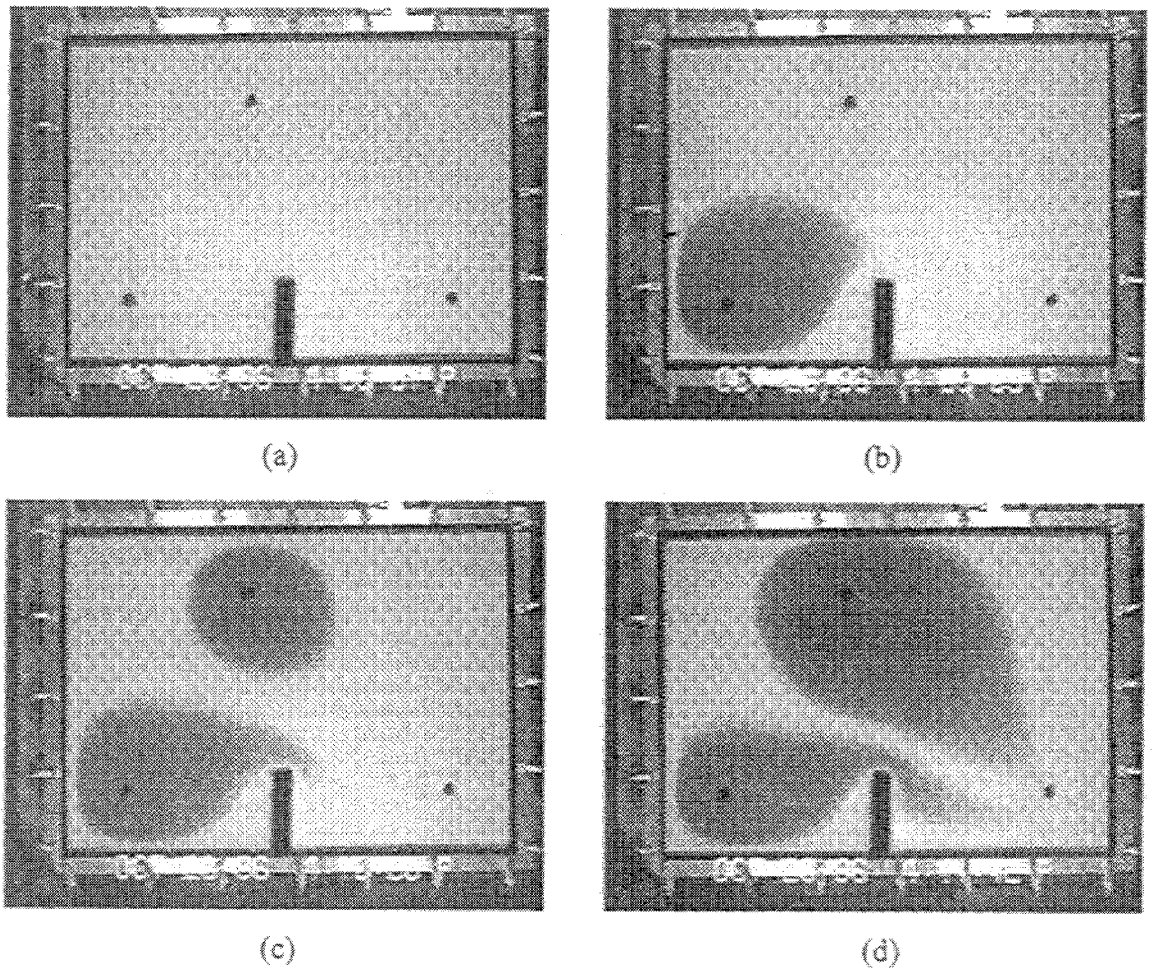

Figure 18: Experimental snapshots of front movement under bang-bang injection policy. (a) At initial time, (b) at time just before the injection switches from well A to well B, (c) at time when injection is only through well B, and (d) at breakthrough. (Tracer displacement in a rectangular Hele-Shaw cell with a flow barrier, distance ratio equal to 0.884, angle equal to 45°.)

7. IDENTIFICATION OF THE PERMEABILITY FIELD OF A POROUS MEDIUM FROM THE INJECTION OF A PASSIVE TRACER

L. Zhan and Y.C. Yortsos

ABSTRACT

We propose a method for the direct inversion of the permeability field of a porous medium from the analysis of the displacement of a passive tracer. By monitoring the displacement front at successive time intervals (for example, using a tomographic method), the permeability can be directly obtained from the solution of a non-linear boundary-value problem. Well-posedness requires knowledge of the pressure profile or the permeability at the boundaries of the system. The method is tested using synthetic data in 2-D (and some 3-D) geometries for a variety of heterogeneous fields and found to work well when the permeability contrast is not too large. However, it is sensitive to sharp variations in permeability. In the latter case, a modified approach based on the successive injection in both directions and the use of an optimization technique leads to improved estimates. An important feature of the direct method is that it also applies to anisotropic porous media. When the principal axes of anisotropy are known, a suitable procedure is proposed and demonstrated using synthetic data.

INTRODUCTION

Permeability heterogeneity is a most important feature of natural porous media, as it affects significantly flow and fluid displacement properties. These dictate flow paths, and the migration and dispersion of in-situ or injected fluids in porous media, with applications ranging from the recovery of in-situ fluids to the fate of environmental contaminants in the subsurface [1]. Heterogeneity is manifested at various scales, from the laboratory (core) to the megascopic (field) scale. Its ubiquitous and multi-scale nature has attracted the interest of many investigators, and a variety of studies have been devoted to its characterization and identification [2].

The classical approach for identifying permeability heterogeneity is based on the inversion of pressure data, under single-phase flow conditions [3]. Given that the transient flow of slightly compressible fluids obeys the diffusion equation, a variety of field tests (well tests) have been devised to infer permeability features by matching pressure data at well locations to the solution of the diffusion equation. While significant advances can be made with this approach, the sparsity of data restricts the detail as well as the uniqueness of the characterization. Pressure transient methods have also been applied to characterize the heterogeneity of laboratory cores, using mini-permeameters [4]. These devices conduct mini-well tests on the surface of a laboratory core (by injecting a small pulse of air and monitoring the resulting pressure transient) and essentially provide a map of the permeability heterogeneity at the external surface of the sample.

An alternative approach to permeability identification is based on the analysis of the arrival times during the injection of passive tracers (namely of tracers which do not affect the fluid viscosity and density). Various efforts have been made at the field scale to relate the arrival times to the permeability, and to match assumed permeability fields to such data

[5]. These techniques are usually indirect, based on optimizing arbitrary (or constrained) initial guesses to match data at various, usually sparse, locations. As a result, they suffer from non-uniqueness. Nonetheless, useful information can be extracted, which can be used to constrain images of the subsurface permeability field.

When knowledge of the displacement front at successive time intervals is available, for example through visual or tomographic techniques, arrival time methods should in principle be able to provide direct maps of the permeability heterogeneity. Brock and Orr [6] reported one such attempt, using qualitative arguments, based on the visualization of displacements in a 2-D heterogeneous bead pack. Withjack et al. [7] considered the application of X-ray Computerized Tomography (CT). They proposed a model to infer the permeability heterogeneity from the analysis of CT-derived concentration contours. Their model is based on a number of simplifying assumptions, the main of which is that each streamtube has constant (but unknown) permeability and porosity, and is, thus, tantamount to an assumption of a layered structure. Although restrictive, the work of Withjack et al. [7] was the first to point out the potential of CT in identifying the permeability heterogeneity of porous media. CT techniques are now routinely applied to monitor displacement fronts in porous media at the laboratory scale. Advances in field scale tomography, for example by seismic methods or cross-hole tomography, are also likely to lead to analogous results at the field scale [8]. Yet, well-defined methods to invert such information to determine the permeability heterogeneity are currently lacking.

In this paper, we propose a new method which focuses on this question, namely on how to invert data on arrival times at various (and numerous) points in the porous medium to map the permeability field. The method, elements of which were briefly described in [9], is based on a direct inversion of the data, as will be described below, rather than on the optimization of initial random (or partly constrained) guesses of the permeability field, to match the available data, as typically done in the analogous problem of pressure transients. The direct inversion is based on two conditions, that Darcy's law for single-phase flow in porous media is valid, and that the dispersion of the concentration of the injected tracer is negligible. While the former is a well-accepted premise, the latter depends on injection and field conditions, and may not necessarily apply in all cases. Based on these conditions, we formulate a non-linear boundary value problem, the coefficients of which depend on the experimental arrival time data. Because of the hyperbolic nature of the problem, uniqueness requires that either the permeability or the pressure at the bounding surface of the porous medium be available. This information is then combined to obtain a solution of the boundary-value problem from which the permeability field can be directly calculated. An important feature of the method is that it can be applied to determine the heterogeneity of anisotropic media, where the permeability field is a tensor, as is often the case in many natural porous media. For this, displacements in two (for 2-D) or three (for 3-D) different directions must be conducted, as will be described below.

In our approach, the experimental information on arrival times enters in the form of spatial derivatives. As a result, the solution method is sensitive to errors in the estimation of these derivatives, which are expected to increase when the variations in the permeability are sharp and large. The errors are magnified around certain limiting streamlines, the width of which increases in the downstream direction, and may lead to poor estimates of the permeability in some regions. To circumvent this problem, we have modified the inversion

method in such cases, by considering a *forth-and-back* hybrid approach, in which arrival times are recorded a second time by repeating the tracer displacement in the reverse direction. This approach is then combined with an optimization technique to improve the resulting estimates.

The paper is organized as follows: In section II we describe the inversion method for isotropic media. Section III shows numerical examples which test the applicability of the method for various forms of permeability heterogeneity and its sensitivity to permeability variation and spatial correlation. Section IV describes the hybrid approach for inverting permeability fields with sharp and large contrasts. The extension of the method to anisotropic media of known and fixed principal axes is presented in section V. We close with a related discussion and concluding remarks.

DIRECT INVERSION ALGORITHM: ISOTROPIC MEDIA

We consider the injection in a heterogeneous and isotropic porous medium of a passive tracer. In the absence of dispersion, the concentration $C(\mathbf{x},t)$ satisfies the equation

$$\phi(\mathbf{x})\frac{\partial C}{\partial t} + \mathbf{v}\cdot\nabla C = 0 \tag{1}$$

where $\phi(\mathbf{x})$ is the porosity of the medium and $\mathbf{v}$ is the superficial fluid velocity. Under slow, viscous flow conditions, the latter satisfies Darcy's law

$$\mathbf{v} = -\mathbf{K}\cdot\nabla\Phi \tag{2}$$

where $\mathbf{K}(\mathbf{x})$ is the symmetric permeability tensor and Φ is a flow potential, $\nabla\Phi = \frac{1}{\mu}(\nabla p - \rho\mathbf{g})$, where μ is viscosity, here taken as a constant, p is pressure, ρ is density, also assumed constant, and $\mathbf{g}$ is the acceleration of gravity. In this section, permeability is assumed to be a scalar, $\mathbf{K}(\mathbf{x}) = k(\mathbf{x})\mathbf{I}$, where $\mathbf{I}$ is the identity tensor. The anisotropic case is discussed in Section V. Assuming incompressible fluids, the continuity equation reads

$$\nabla\cdot\mathbf{v} = 0 \tag{3}$$

In the absence of dispersion, we define the front location by the equation

$$\mathcal{F}(\mathbf{x},t) \equiv t - f(\mathbf{x}) = 0 \tag{4}$$

where, assuming constant or monotonic injection rates, the function $f(\mathbf{x})$ is single-valued, thus a single arrival time is associated with a given point $\mathbf{x}$. Then, the concentration is given by

$$C(\mathbf{x},t) = C_i(t)H(t - f(\mathbf{x})) \tag{5}$$

where $C_i(t)$ is the injection concentration, and H is the Heaviside step function.

The direct algorithm is based on the following two steps: First, we equate the two expressions for the normal velocity at the front, given by the kinematics and by Darcy's law, respectively. Noting that the normal at the front is given by

$$\mathbf{n} = \frac{\nabla \mathcal{F}}{|\nabla \mathcal{F}|} = -\frac{\nabla f}{|\nabla f|} \tag{6}$$

we use (5) and (6) in (1) to obtain a kinematic expression for the normal velocity there, namely

$$v_n = -\frac{\phi(\mathbf{x})}{|\nabla f|} \tag{7}$$

Darcy's law (equations (2) and (6)) gives another expression for the same quantity

$$v_n = \frac{k(\mathbf{x}) \nabla \Phi \cdot \nabla f}{|\nabla f|} \tag{8}$$

Thus, (7) and (8) lead to the following result for the permeability

$$k(\mathbf{x}) = -\frac{\phi(\mathbf{x})}{\nabla \Phi \cdot \nabla f} \tag{9}$$

which, in principle, can be evaluated in terms of Φ and f. The second step consists of substituting the above expression in Darcy's law and making use of the continuity equation (3) to obtain a non-linear equation for Φ,

$$\nabla \cdot \left[\frac{\phi(\mathbf{x}) \nabla \Phi}{\nabla \Phi \cdot \nabla f} \right] = 0 \tag{10}$$

Equations (9) and (10) constitute the keys of the direct inversion method. Equation (10) is a partial differential equation which determines Φ given appropriate boundary conditions and information on the porosity, $\phi(\mathbf{x})$, and the arrival time function, $f(\mathbf{x})$. From its solution, the permeability field can be directly calculated using (9).

The following remarks are in order:

1. For the solution of (10), the porosity must be a known function of the spatial coordinates. For applications using CT, this can be readily available.

2. Although at first glance equation (10) appears to be an elliptic (Laplace type) equation, it is in fact a system of first-order hyperbolic equations. This can be readily shown, e.g. in 2-D, by defining

$$u \equiv \frac{\frac{\partial \Phi}{\partial y}}{\frac{\partial \Phi}{\partial x}} \tag{11}$$

in which case (10) becomes

$$\frac{\partial}{\partial x} \left[\frac{\phi(\mathbf{x})}{f_x + u f_y} \right] + \frac{\partial}{\partial y} \left[\frac{\phi(\mathbf{x}) u}{f_x + u f_y} \right] = 0 \tag{12}$$

where subscripts indicate partial derivatives (and similarly for 3-D). These two equations (11) and (12) form a pair of first-order hyperbolic equations. For their solution, and thus for the solution of (10), information on the potential Φ at the (no-flow) boundaries is necessary. Equivalently, this information can be furnished from a knowledge of the permeability at

the boundaries (which, for instance, can be obtained by a mini-permeameter, as previously noted). At no-flow boundaries (where in the normal direction $\frac{\partial \Phi}{\partial n} = 0$), equation (9) becomes a partial differential equation for the variation of Φ along the two tangential directions (for the 3-D case), which can be integrated, given k and f at the boundary, to yield the required profile. We must point out, however, that in all applications to be shown below, we solved (10) assuming known pressure profiles at all boundaries. In this way, the numerical method utilizes information from all boundaries, essentially solving an elliptic-like, rather than a hyperbolic system.

3. A notable feature of (9) and (10) is that they depend on the gradient of the front arrival time rather than the arrival time itself. On the positive side, this reflects a desirable sensitivity of the method to heterogeneity. However, this dependence also introduces numerical instability which can lead to problems when the permeability contrast is sharp and large. A technique to circumvent these problems is described later in Section IV.

In summary, supplied with boundary conditions on the potential, equations (9) and (10) can be solved directly to yield the permeability field in a heterogeneous porous medium based on information on arrival times and the porosity heterogeneity. The resolution of the inverted permeability field depends, among others, on the resolution of the arrival time contours.

A Streamfunction Approach for 2-D Geometries

Before proceeding, it is worthwhile to note that in 2-D geometries, an alternative inversion method is possible, based on the use of the streamfunction Ψ, where $\frac{\partial \Psi}{\partial y} = v_x$ and $\frac{\partial \Psi}{\partial x} = -v_y$. Indeed, rearrangement of (7) leads to

$$\frac{\partial f}{\partial y}\frac{\partial \Psi}{\partial x} - \frac{\partial f}{\partial x}\frac{\partial \Psi}{\partial y} = -\phi(\mathbf{x}) \tag{13}$$

which is a first-order, hyperbolic differential equation for Ψ. The characteristics of the latter are curves of constant f, namely of constant arrival time, which are available experimentally. Therefore, the streamfunction can be computed by integrating along these contours, for example

$$\Psi = \Psi_0 + \int_{y_0}^{y} \frac{\phi}{f_x} dy \tag{14}$$

where, in the case of a rectilinear sample with a no-flow boundary at $y_0 = 0$, we can take $\Psi_0 = 0$ without loss. To compute the potential we make use of the fact that in the isotropic case, equipotentials are orthogonal to the streamlines, hence

$$\frac{\partial \Psi}{\partial x}\frac{\partial \Phi}{\partial x} + \frac{\partial \Psi}{\partial y}\frac{\partial \Phi}{\partial y} = 0 \tag{15}$$

This hyperbolic equation can also be integrated subject to appropriate boundary conditions. Then, the permeability can be estimated from (9), or from the alternative expression $k = \frac{\partial \Psi}{\partial y} / \frac{\partial \Phi}{\partial x}$. Illustrative examples using this approach are discussed below.

APPLICATIONS USING SIMULATED DATA

The direct inversion method was subsequently tested based on simulated data. We used a high-resolution finite-difference simulator (the main features of which are described in [10]) or a streamline-based method to simulate tracer displacement and provide data on arrival times and the pressure profile at the boundaries. The displacement corresponds to constant-rate injection in the absence of gravity. The boundary value problem (10) was solved using a standard SOR finite-difference formalism, which was iterated until convergence. For example, for the 2-D geometry we used the five-point scheme

$$\Theta^m_{i+1/2,j}\Phi^{m+1}_{i+1,j} + \Theta^m_{i-1/2,j}\Phi^{m+1}_{i-1,j} + \Theta^m_{i,j+1/2}\Phi^{m+1}_{i,j+1} + \Theta^m_{i,j-1/2}\Phi^{m+1}_{i,j-1} - (\Theta^m_{i+1/2,j} + \Theta^m_{i-1/2,j} + \Theta^m_{i,j+1/2} + \Theta^m_{i,j-1/2})\Phi^{m+1}_{i,j} = 0 \tag{16}$$

where $\Theta^m_{i,j}$ is the conductivity coefficient at block (i,j) at iteration level m. All other coefficients were evaluated using the harmonic average between $\Theta^m_{i,j}$ and its nearest neighbor. An interpolation routine was used to interpolate the arrival times, when necessary. The spatial derivatives of f were calculated using three-point differences. Equation (16) was solved using the prescribed pressure profiles on both no-flow boundaries. Parenthetically, we note that the forward problem belongs to the general class of problems recently discussed by Sethian [11], and can benefit from the application of a Fast Marching Technique. Such was not implemented here, however.

Figs. 1-3 show results of the application of the inversion method in three 2-D heterogeneity fields of a moderate permeability contrast, corresponding to a layered medium, a medium with a smoothly varying heterogeneity and a permeability distribution following fBm (fractional Brownian motion) statistics. Each figure shows true and directly inverted permeability fields, along with true and directly inverted and potential profiles. In all these examples, the direct inversion is found to give very good results.

Fig. 1 shows that the method handles well permeability contrasts transversely to the direction of displacement, with some expected dispersion around the discontinuity. Potential profiles are also reproduced well, again with some differences noted around the discontinuity. We must emphasize that in this example, the success of the method rests on the availability of the potential profile at the boundary, which removes the non-uniqueness of the problem. (Indeed for a 1-D displacement with piecewise constant permeability at constant injection rate, equation (10) becomes indeterminate). Likewise, good results were found when the permeability contrast was in the direction parallel to the displacement. The ability of the method to invert the permeability field in the presence of an arbitrary closed region of sharp permeability contrast is discussed in a later section.

The permeability field of Fig. 2 is smoothly varying and contains two peaks and one valley, with a permeability contrast of about 2. It was generated in a $64\times$ 64 grid using Franke's test function from MATLAB [12]. This function often serves as a test for the interpolation of scattered data. It is noted that the arrival times are much more sensitive to the heterogeneity, than the pressure profiles, which are essentially parallel to the transverse direction. This feature was noted in other cases as well, where the permeability variation is relatively smooth. Fig. 2 shows that the comparison between actual and inverted fields

(in permeability and potential profiles) is very good. This example is characteristic of the success of the method in smoothly varying permeability fields.

A more stringent test is shown in Fig. 3 with a similar permeability contrast. The permeability field is of the fBm type with a Hurst exponent $H = 0.8$, and it is a typical example of a self-affine field, containing large-scale correlations [13]. We remark that fBm statistics with a Hurst exponent larger than 0.5 are often assumed to describe the heterogeneity in the horizontal permeability of natural rocks [14]. Fig. 3 shows that the match between actual and inverted data is also quite good. Potential profiles are closely matched. The inverted permeability reproduces well the main features of this field, namely the regions where the permeability is respectively high, medium or low. However, discrepancies can also be detected in the point-by-point variation of the permeability, where the inverted field is somewhat smoother than the actual. The ability to capture long-wavelength, as opposed to high-frequency, variations is typical of the technique and was noted in other examples, as well. Fig. 4 shows a statistical analysis of the actual and inverted permeabilities. Histograms and the correlation structure (the semi-variograms) match quite well, and the scatter plot is satisfactory. The dispersion around the 45° line indicates a small degree of point-by-point mismatch, as also evidenced in Fig. 3.

The direct inversion technique is equally well applied to 3-D geometries. Before we proceed, however, it is instructive to compare inversion results using the 2-D streamfunction method. Figs. 5 and 6 show the resulting permeability estimates, along with the associated streamfunctions, corresponding to Figs. 2 and 3, respectively. Although the streamlines are well reproduced, it is evident that the inverted permeability fields, although maintaining the large correlation features, miss significant details. There are also notable defects extending along slice-shaped regions, which arise from the integration along the arrival time contours. A statistical analysis, not shown here for lack of space, shows that the inverted permeability reproduces reasonably well the semi-variograms. However, the histograms, and to a greater degree, the scatter plot, have large errors in several places. The streamfunction method is prone to relatively large numerical errors, because it involves a threefold interpolation for spatial derivative estimation and the integration of hyperbolic equations (for determining the streamfunction). These weaknesses make the method unfavorable compared to the direct solution of (9) and (10) (as seen in the comparison of Figs. 2 to 5 and 3 to 6). Advantages of the method, on the other hand, are that the permeability is inverted fast, compared to the previous, while one also readily obtains the streamfunction profile, which may be useful in other applications.

To demonstrate the applicability of the direct inversion method to three dimensions, we considered the 3-D permeability field shown in Fig. 7a, consisting of a log-normal distribution generated by Sequential Gaussian Simulation, with a natural logarithmic mean of 2.0, a standard deviation of 0.2 and a dimensionless correlation length (with respect to the sample size) of 0.5. The permeability variation is somewhat larger than before. Characteristic arrival time contours from the simulation of the forward problem in a $16\times16\times16$ lattice are shown in Fig. 7b. The direct inversion algorithm was applied by using a 3-D version of (16) along with boundary conditions supplied from the forward problem. The results of the permeability inversion in Fig. 8 appear to be in relatively good agreement with the actual (Fig. 7a). A more quantitative comparison is shown in the statistics of Fig. 9, which is calculated by GSLIB [15]. In general, the comparison is good. The inverted field shows a

smaller range of variation than the actual, as reflected in both the semi-variogram and the histogram. Notably, the spatial correlation structure of the former is well captured in the inverted data. The scatter plot indicates somewhat larger dispersion, compared to the fBm field of Figs. 3-4, which is expected, given the larger permeability contrast in this example.

In the above examples, where the permeability contrast is not too large, or where the permeability has relatively large spatial correlations, the direct inversion method gives good results. When the contrast increases and variations in permeability are sharper, however, the method is subject to increased errors. These primarily arise from the approximation of the spatial gradients of the arrival time in regions where the latter varies sharply. For example, Fig. 10 shows arrival time contours, calculated analytically (see Appendix), for flow around an embedded sphere of lower permeability. Even though the permeability contrast is relatively modest (0.6:1), there exist two layers, extending downstream of the sphere, where the arrival times have sharp spatial variations. These layers are centered around the two limiting streamlines tangent to the sphere. In these regions, the evaluation of the coefficients of (10) is likely to introduce errors, and accordingly poor estimates for the permeability in some places. These limiting streamlines also exist in any other field containing regions of sharp permeability contrast. Because these zones extend downstream of the region of the sharp contrast, however, the associated errors in permeability estimates are different depending on the direction of displacement. We have conjectured, therefore, that the estimates of the direct method could be improved substantially, if we were to combine information from two different displacements, one in the forward and the other in the reverse direction.

A HYBRID ALGORITHM

To circumvent the problems posed by high permeability contrasts we propose the following hybrid procedure:

1. Carry out a tracer displacement in the forward direction and directly invert to obtain one permeability estimate, $k_f(\mathbf{x})$.

2. Carry out a tracer displacement in the reverse direction and directly invert to obtain a second permeability estimate, $k_b(\mathbf{x})$.

3. Retain the estimates in places, where they differ in absolute value by no more than a prescribed value and discard in all others. Assign estimates in these regions by an interpolation algorithm (known in the geostatistics literature as kriging).

4. Use an optimization algorithm (to be briefly described below) to fine-tune the so obtained composite permeability estimates.

The optimization algorithm is based on standard gradient methods [16] and will not be discussed here in any detail. We briefly note that we use the objective function

$$\mathcal{J} = \frac{1}{2}\left\{\sum_{i=1}^{N} W_{1i}[f_i(\mathbf{k}) - f_i^m]^2 + \sum_{i=1}^{M} W_{2i}[k_i - k_i^p]^2 + \sum_{i=1}^{L} W_{3i}[\Phi_{bi} - \Phi_{bi}^m]^2\right\} \tag{17}$$

where, the first term in the RHS is the weighted sum of the squares of the differences between the front arrival times obtained from the simulator response, f_i, and the data, f_i^m, and the third is the analogous term for the differences between the potential at the no-flow boundaries obtained from the simulator, Φ_{bi}, and the data, Φ_{bi}^m. The second term represents

the mismatch between the current permeability estimate and its prior. It is a regularization term, as required by Tikhonov's theory [17], and restricts the parameters being optimized to not deviate greatly from the prior information. Numerical experience has demonstrated the necessity of this term for stable and convergent solutions. Nonetheless, the accuracy of the initial guess plays a pivotal role in the convergence to the true solution. It is in this context, that the hybrid algorithm offers an important advantage. Here, the prior information is supplied using the direct inversion method, outlined in steps 1-3 above, which is generally close to the true permeability field. As a result, in many of the cases tried, the optimization method converges close to the true values. By contrast, in many related inverse problems, the prior permeability is typically generated by a geostatistical algorithm constrained to (usually) sparse measurements, and its convergence to the true solution is generally uncertain (e.g. see [26]). At the same time, we must stress that we have also encountered many problems involving sharp permeability contrasts, which cannot be successfully handled even with the hybrid algorithm. Such an example will be shown below.

Applications of the hybrid algorithm using simulated data are illustrated in Figs. 11-14 for three different examples. The medium in Fig. 11 contains two blocks of low permeability with a 1:5 contrast. This particular configuration corresponds to the experimental Hele-Shaw cell used in [19], and was discretized by a 22×10 lattice. The top of Fig. 11 (panels a,b) shows the prior estimate fed to the optimization algorithm, following the steps 1-3. Due to the sharp permeability contrast between low and high permeable regions, the spatial derivatives of the arrival times have significant numerical errors in certain regions, and lead to a mismatch between true and inverted values in various places after steps 1 and 2. Through step 3 (where estimates were discarded when they differed by more than 30%), these errors have been minimized and the directly inverted field (Fig. 11, a,b) has the main trends of the true field, although it is obvious that the contrast is not as sharp as the actual, and is in need of fine-tuning. The results of the application of the optimization algorithm of step 4, using 40 iterations, and based on the initial guess after kriging (top of Fig. 11), is shown in the middle of Fig. 11 (panels c,d). The results are much improved and, with a few exceptions, they are very close to the actual. Although not shown, potential and arrival time profiles are also matched very well. By contrast, if an uniform initial guess, instead of the one after the direct method on the top of Fig. 11, was used in the optimization algorithm, the resulting estimate of the permeability field (after the same number of iterations) is poor in many places, as shown in the bottom of Fig. 11 (panels e,f). This, despite the fact that arrival times and potential profiles were found to match very well. We conclude that, at least for this example, the application of the hybrid method gives a substantial improvement.

Fig. 12 shows the application of the algorithm to a correlated log-normal distribution with a logarithmic mean of 2.0, a standard deviation of 0.5 and a dimensionless correlation length of 0.25. In this example, the block-to-block permeability variation is much larger than in the fBm field of Fig. 3 or the 3-D field of Fig. 7, the largest contrast being of an order of magnitude. The application of the direct inversion method followed by kriging leads to the results shown in the middle of Fig. 12 (panels c,d). Although capturing the general features of the true field, the estimates are generally coarser and smoother than the actual values. Comparison of arrival time and potential profiles based on the inverted field (not shown for lack of space) indicates a mismatch with the actual in some places. To fine-tune the results and recover some of the high-frequency variations, we applied the optimization algorithm of

step 4. Results after 40 iterations are shown on the right of Fig. 12 (panels e,f). Although the algorithm does not reproduce exactly the actual field, and some errors around large variations of permeability are detectable, it is obvious that a significant improvement has been achieved. Fig. 13 shows the corresponding statistical comparison. The mean and the variance from the hybrid algorithm agree very well with the actual. (By contrast, in results that are not shown, the variance from kriging is underestimated by about 20%, although the mean is the same.) The two histograms are roughly equal, while the semi-variograms have the same correlation structure. The scatter plot shows that good agreement exists over a good range of lower permeabilities, although an increasing scatter can be seen at larger permeabilities. In this example, these are typically associated with large contrasts. We need to reiterate that the success of the hybrid algorithm depends to a large extent on the accuracy of the initial guess, which is here provided by the direct method and positions the optimization scheme close to the true solution. By contrast, the estimates resulting from the application of the same optimization algorithm after bypassing steps 1-3 and utilizing a uniform initial guess were quite poor, even though arrival times and potential matched nearly perfectly with the true values.

At the same time, we must point out that we have also encountered several cases where the hybrid algorithm was not as successful as desired. Fig. 14 (panels a,b) is an example of a "checkerboard"-pattern heterogeneous field, with a permeability contrast of 1:4. A pattern similar to this was used in some tracer displacement experiments [20]. The results of the algorithm at the end of the kriging step are shown in the middle of Fig. 14 (panels c,d). The mismatch with the true data is quite apparent. The 2-D projection in the middle of Fig. 14 reproduces roughly the places of maximum permeability variation, but the picture is clearly "out of focus". The results of the application of the optimization method are shown in the right of Fig. 14 (panels e,f). We note a clear improvement, compared to the previous step, and a better focused image. Yet, there is also clear evidence of mismatches in various places, including the smoothing of the sharp contrast around the edges of discontinuity and of other defects, which altogether preclude an exact matching. Thus, although overall the hybrid algorithm appears to be a promising alternative in cases involving large contrasts, we caution that this is not uniformly true and that many counter-examples can readily be constructed where the algorithm will not be as successful.

DIRECT INVERSION ALGORITHM: ANISOTROPIC MEDIA

On the other hand, a strong attribute of the technique proposed is that it can be readily applied to anisotropic porous media. In this section, we consider for simplicity 2-D geometries, where the principal directions of the permeability tensor are constant and coincide with the rectangular coordinates x and y, namely we will assume that

$$\mathbf{K} = \begin{vmatrix} k_x(\mathbf{x}) & 0 \\ 0 & k_y(\mathbf{x}) \end{vmatrix} \tag{18}$$

An extension to the more general case is under consideration and will be presented elsewhere. Under these conditions, the equations analogous to (9) and (10) read as follows

$$(\mathbf{K}\cdot\nabla\Phi)\cdot\nabla f = -\phi(\mathbf{x}) \tag{19}$$

and

$$\nabla(\cdot\mathbf{K}\cdot\nabla\Phi) = 0 \tag{20}$$

Using scalar notation, and substituting from (18), we further have

$$k_x \frac{\partial\Phi}{\partial x}\frac{\partial f}{\partial x} + k_y \frac{\partial\Phi}{\partial y}\frac{\partial f}{\partial y} = -\phi \tag{21}$$

and

$$\frac{\partial}{\partial x}\left[k_x \frac{\partial\Phi}{\partial x}\right] + \frac{\partial}{\partial y}\left[k_y \frac{\partial\Phi}{\partial y}\right] = 0 \tag{22}$$

Equations (21) and (22) constitute a pair of two equations in three unknowns (k_x, k_y and Φ) and require additional information for their solution. One possible approach to furnish this information is by conducting two tracer displacements, one in the x-direction with no-flow boundaries perpendicular to the y-axis, and another in the y-direction with no-flow boundaries perpendicular to the x-axis. If we denote the arrival time functions and the potentials of the two displacements by f_I and f_{II}, and Φ_I and Φ_{II}, respectively, Eq. (21) becomes

$$k_x \frac{\partial\Phi_I}{\partial x}\frac{\partial f_I}{\partial x} + k_y \frac{\partial\Phi_I}{\partial y}\frac{\partial f_I}{\partial y} = -\phi, \tag{23}$$

$$k_x \frac{\partial\Phi_{II}}{\partial x}\frac{\partial f_{II}}{\partial x} + k_y \frac{\partial\Phi_{II}}{\partial y}\frac{\partial f_{II}}{\partial y} = -\phi \tag{24}$$

for the respective displacements. Thus, the permeability components can be determined

$$k_x = -\frac{\phi}{A}\left[\frac{\partial\Phi_{II}}{\partial y}\frac{\partial f_{II}}{\partial y} - \frac{\partial\Phi_I}{\partial y}\frac{\partial f_I}{\partial y}\right] \tag{25}$$

and

$$k_y = -\frac{\phi}{A}\left[\frac{\partial\Phi_I}{\partial x}\frac{\partial f_I}{\partial x} - \frac{\partial\Phi_{II}}{\partial x}\frac{\partial f_{II}}{\partial x}\right] \tag{26}$$

where

$$A = \frac{\partial\Phi_I}{\partial x}\frac{\partial f_I}{\partial x}\frac{\partial\Phi_{II}}{\partial y}\frac{\partial f_{II}}{\partial y} - \frac{\partial\Phi_{II}}{\partial x}\frac{\partial f_{II}}{\partial x}\frac{\partial\Phi_I}{\partial y}\frac{\partial f_I}{\partial y} \tag{27}$$

in terms of the given data f_I and f_{II}, and the calculated potentials Φ_I and Φ_{II}. The latter can be obtained by solving equation (22), with k_x and k_y given by (25)-(27), and with the appropriate boundary conditions corresponding to the two different displacements. To solve the resulting coupled system, we implemented the following iterative algorithm:

1. Based on the ν-level estimates for the potentials Φ_I^ν and Φ_{II}^ν, use Eqs. (25) and (26) to estimate the ν-level iterates k_x^ν and k_y^ν. At the initial iteration ($\nu = 0$), an initial guess, typically in the form of a linear variation, is supplied for the potentials.

2. Based on explicit (ν-level) estimates for k_x^ν and k_y^ν, integrate (22) twice, using SOR finite differences to calculate the potentials at the next iteration level, $\Phi_I^{\nu+1}$ and $\Phi_{II}^{\nu+1}$.

This algorithm was found to work well for the various cases tested so far.

The method was subsequently applied to the anisotropic permeability field shown in the left of Figs. 15-16 (panels a,b). Its statistics are similar to Fig. 7, and involve a log-normal spatially correlated distribution with the same mean and standard deviation. By simulating tracer displacements in the two directions, x and y, respectively, we obtained the respective arrival time functions and potentials at the no-flow boundaries, which were used for the inversion according to the above scheme. The directly inverted fields are shown in the right of the two Figs. 15-16 (panels c,d). Considering the coupled nature of the problem, the reconstruction of the two permeability components is generally good. The method reproduces relatively well the regions of high and low permeability. Compared to the isotropic case under the same permeability contrast, however, the reconstruction is not as sharp, and the projections of the inverted images appear slightly "out of focus" in certain places. This mismatch reflects an underlying slight mismatch in the arrival times and the potential profiles, which is not shown here. Further work is under way to improve the algorithm and fine-tune the direct inversion method, including the implementation of a hybrid algorithm as in the isotropic case.

CONCLUDING REMARKS

In this paper we presented a method for the direct inversion of the permeability of porous media, based on arrival time contours and information on the pressure profiles at the boundaries. The former can be obtained in real systems using techniques of visualization, computerized tomography or cross-hole tomography. The method utilizes Darcy's law for flow in porous media in combination with the kinematics of flow, as expressed in the arrival times, to derive a boundary-value problem, the solution of which leads to a direct reconstruction of the permeability field. An important feature of the technique is that the information from the pressure at the boundaries is used to formulate and solve an elliptic-like formulation, rather than the two hyperbolic equations, which formally describe the problem. The algorithm developed is a rigorous tool for the analysis of arrival time contours.

Using simulated data, the method was found to work well for cases, where the permeability contrast is not very large, and the field is spatially correlated. In general, the technique captures well variations corresponding to larger wavelengths, but not as well the fine-scale details. For sharper contrasts, a hybrid version of the algorithm was developed, in which the direct method is used to generate the initial guess in an optimization algorithm. The hybrid version minimizes the sensitivity of the method to errors in spatial derivatives, which are augmented in the presence of sharp contrasts. Examples in two and three dimensions using simulated data demonstrated that the hybrid algorithm works well and that it is superior to the more conventional case, where the initial input is a uniform distribution. However, other examples can also be constructed, involving sharp contrasts, where the inversion technique is not as satisfactory and requires further improvement. A second advantage of the direct inversion technique is its potential to invert the permeability tensor in anisotropic porous media. Preliminary results for the case where the principal axes of anisotropy are fixed and

known were presented and found to be promising. Further work is currently under way to fine-tune the method and to also extend it to the more general case, where the permeability tensor is full.

The applicability of the technique to real systems relies on several conditions: the availability of pressure profiles at the system boundaries, the absence, or the minimization, of dispersion during the tracer displacement and the availability of an adequate resolution in arrival time contours. The first requirement appears to be the most difficult to meet, in practice, in view of the demand for adequate spatial resolution, which presently available tools may not possess, and the need to enforce Darcy's law near no-flow boundaries. Alternatively, this profile can be obtained by locally probing the surfaces with a mini-permeameter to construct a surface permeability map, from which the pressure profile can be computed. A certain amount of dispersion is also unavoidable, in real porous media, where the dispersion coefficient is proportional to the velocity, thus leading to a constant Peclet number and a finite amount of dispersion. However, for relatively small dispersivities, dispersion effects could be minimized. Sufficient spatial resolution on arrival times would allow to capture fine-scale variations, at the expense of increased computational time in the optimization routine of the hybrid algorithm, and possible instabilities as the degree of resolution increases. However, it must also be remarked that in our experience, so far, a coarse-grid reconstruction can adequately capture the large-scale features of the permeability field, both in the isotropic and the anisotropic cases. The process of validation of the method with actual experimental data is currently under way.

APPENDIX:
Arrival Times For Circular Permeability Heterogeneity

In this appendix, we provide analytical solutions for a simple 2-D problem involving tracer displacement in an infinite domain of constant permeability 1, in which a circular inclusion of radius $r = 1$ and permeability κ is embedded. Thus, the permeability is the step function

$$k = (1 - \kappa)H(r - 1) + \kappa \tag{A-1}$$

Subtracting the homogeneous solution $(-x)$ from the potential, we next consider the solution of

$$\nabla \cdot [k\nabla(x + \psi)] = 0 \tag{A-2}$$

where $\psi = -\Phi + x$. Thus,

$$\nabla \cdot (k\nabla\psi) = -(\kappa + 1)\delta(r - 1)\frac{x}{r} \tag{A-3}$$

where δ denotes the Dirac delta function. To solve (A-3) we use polar coordinates (r, θ) and the following interface conditions at the permeability discontinuity

$$\psi|_{r=1_+} = \psi|_{r=1_-} \tag{A-4}$$

and

$$\kappa \frac{\partial \psi}{\partial r}|_{1-} - \frac{\partial \psi}{\partial r}|_{1+} = (1-\kappa)\cos\theta. \tag{A-5}$$

The solution is obtained in straightforward fashion

$$\psi = \left(\frac{1-\kappa}{1+\kappa}\right) r\cos\theta \quad ; \quad r \leq 1 \tag{A-6}$$

$$\psi = \left(\frac{1-\kappa}{1+\kappa}\right) \frac{1}{r}\cos\theta \quad ; \quad r > 1 \tag{A-7}$$

from which the velocity components can be calculated. We find,

$$\begin{aligned} v_x &= \frac{2\kappa}{1+\kappa} \quad ; \quad r \leq 1 \\ v_x &= 1 + \left(\frac{1-\kappa}{1+\kappa}\right) \frac{y^2 - x^2}{(x^2+y^2)^2} \quad ; \quad r > 1 \end{aligned}$$

and

$$\begin{aligned} v_y &= 0 \quad ; \quad r \leq 1 \\ v_y &= -\left(\frac{\kappa(1-\kappa)}{1+\kappa}\right) \frac{2xy}{(x^2+y^2)^2} \quad ; \quad r > 1 \end{aligned}$$

Finally, the streamlines are the solution of

$$\begin{aligned} \frac{dy}{dx} &= 0 \quad ; \quad r \leq 1 \\ \frac{dy}{dx} &= -\frac{2(1-\kappa)xy}{(1+\kappa)(x^2+y^2)^2 + (1-\kappa)(y^2-x^2)} \quad ; \quad r > 1 \end{aligned}$$

from which the arrival times are obtained by integrating along the streamlines

$$t - t_0 = \int_{x_0}^{x} \frac{\phi}{u_x(x', y)} dx' \tag{A-8}$$

where ϕ is the porosity. These results were used to compute the streamlines and the arrival time contours of Fig. 10 in the text.

REFERENCES

[1] L. W. Lake, *Enhanced Oil Recovery*, (Prentice Hall, Englewood Cliffs, NJ, 1989); L. W. Gelhar, *Stochastic Subsurface Hydrology*, (Prentice-Hall, Englewood Cliffs, NJ, 1993).

[2] W. G. Yeh, Water Resources Res., **22**(2), 95 (1986); N. Z. Sun, *Inverse Problems in Groundwater Modeling*, (Kluwer Academic Publishers, Netherlands, 1994); D. McLaughlin and L. R. Townley, Water Resource Res., **32**(5), 1131 (1996).

[3] C. S. Matthews and D. G. Russell, *Pressure Buildup and Flow Tests in Wells*, (SPE Monograph Vol. 1, Dallas, 1967); R. C. Earlougher, *Advances in Well Test Analysis*, (SPE

Monograph Vol. 5, Dallas, 1977); R. N. Horne, *Modern Well Test Analysis*, (Petroway, Palo Alto, CA, 1995).
[4] S. C. Jones, in Soc. Petrol. Eng. 67th Annual Meeting Proceedings, SPE paper 24757 (1992); S. Ganapathy, D. Wreath, G. Pope and K. Sepehrnoori, Soc. Petrol. Eng. Formation Evaluation, **9**, 273 (1993).
[5] C. F. Harvey and S. M. Gorelick, Water Resources Res., **31**(7), 1615 (1995); B. J. Wagner, J. Hydrology, **135**, 275 (1992); A. Datta-Gupta, S. Yoon, I. Barman and D. W. Vasco, J. Petrol. Tech., **50** (12), 72, (1998).
[6] D. C. Brock and F. M. Orr, in Soc. Petrol. Eng. 66th Annual Meeting Proceedings, SPE paper 22614 (1991).
[7] E. M. Withjack, S. M. Graham, and C. T. Yang, Soc. Petrol. Eng. Formation Evaluation, **7**, 447 (1991).
[8] D. E. Lumley and R. A. Behrens, Soc. Petrol. Eng. Reservoir Evaluation and Engineering, **1**, 528 (1998).
[9] L. Zhan and Y. C. Yortsos, 10th European Symposium on Oil Recovery Proceedings, Brighton, UK (1999).
[10] Z-M. Yang and Y. C. Yortsos, Phys. Fluids, **9**(2), 286 (1997).
[11] J. A. Sethian, *Level Set Methods and Fast Marching Methods*, Cambridge University Press, New York (1999).
[12] *Spline Toolbox User's Guide*, The Mathworks, Inc. (1999).
[13] R. F. Voss, in *The Science of Fractal Images*, (Springer-Verlag, New York, 1988); J. Feder *Fractals*, (Plenum Press, New York, 1988).
[14] T. A. Hewett, in *Reservoir Characterization 2*, (Society of Petroleum Engineers, Houston, TX, 1989).
[15] C. V. Deutch and A. C. Journel, *GSLIB: Geostatistical Software Library and User's Guide*, (Oxford University Press, Oxford, UK, 1992).
[16] A. Tarantola, *Inverse Problem Theory, Methods for Data Fitting and Model Parameter Estimation*, (Elsevier Science Publishers, Amsterdam, 1987).
[17] A. N. Tikhonov and V. Y. Arsenin, *Solutions of Ill-posed Problems*, (Halsted Press, New York, 1977).
[18] P. R. Ballin, A. G. Journel and K. Aziz, J. Can. Petrol. Tech., **31**(4), 52 (1992).
[19] P. Berest, N. Rakotomalala, J.P. Hulin and D. Salin, Eur. Phys. J. A.P **6**, 309 (1999).
[20] R. Lenormand, Transport in Porous Media, **18**, 245 (1995).

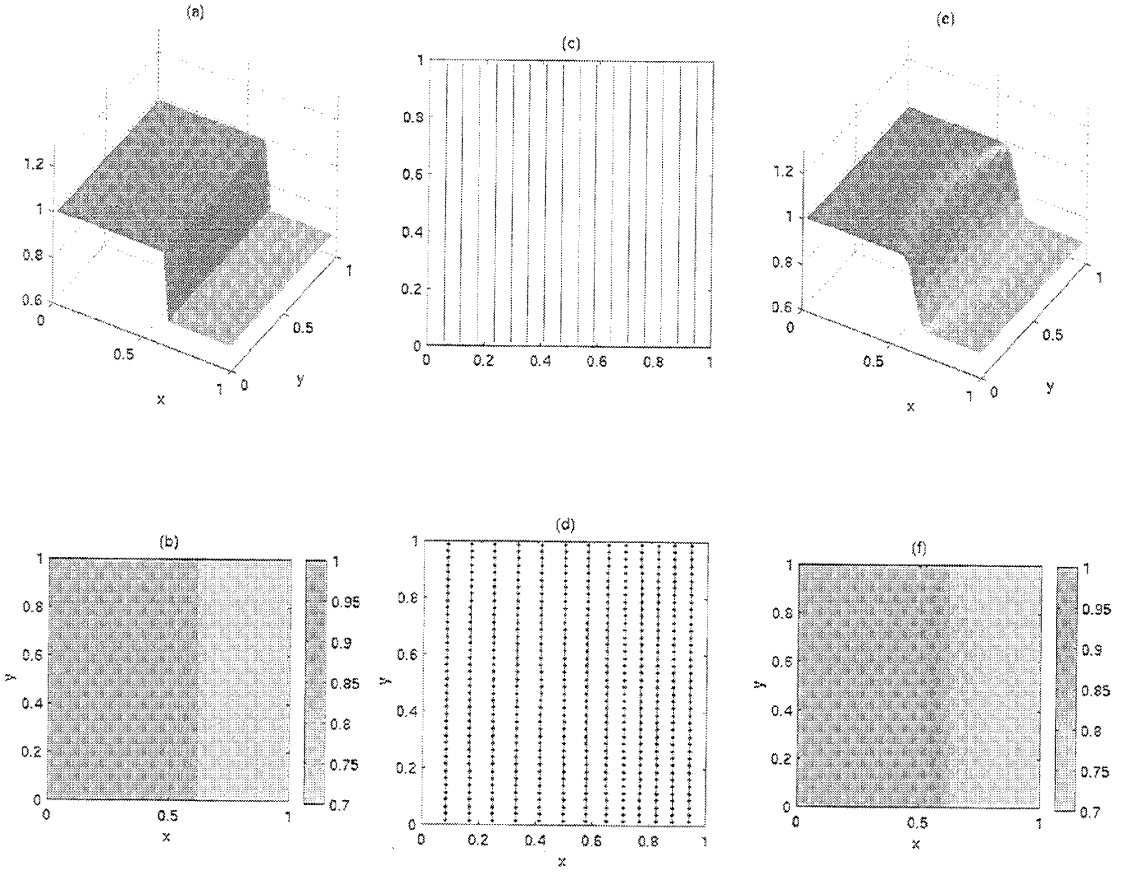

Figure 1: Application of the direct inverse method to a layered system shown in the left side: (a)-(b) actual permeability plots; (c) actual arrival times; (d) actual (solid lines) and inverted (dotted lines) potential profiles; (e)-(f) inverted permeability plots.

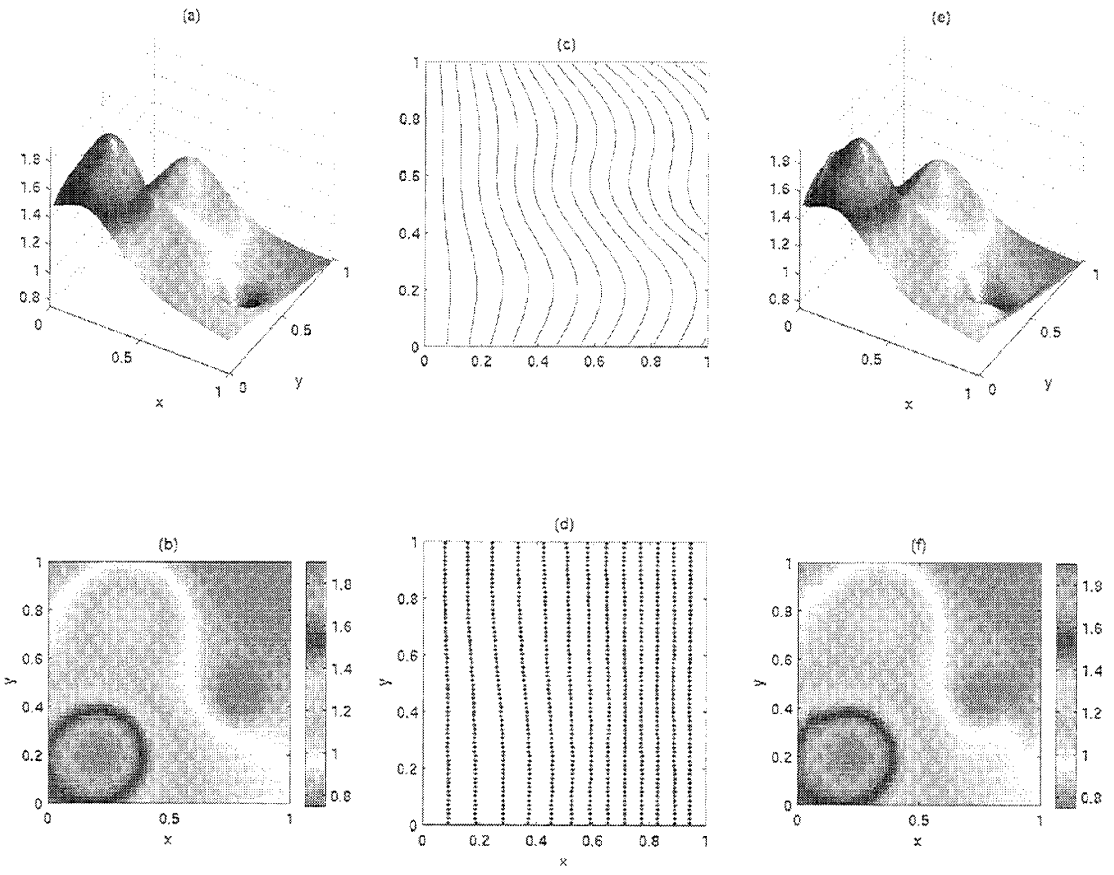

Figure 2: Application of the direct inverse method to a smoothly varying field shown in the left side: (a)-(b) actual permeability plots; (c) actual arrival times; (d) actual (solid lines) and inverted (dotted lines) potential profiles; (e)-(f) inverted permeability plots.

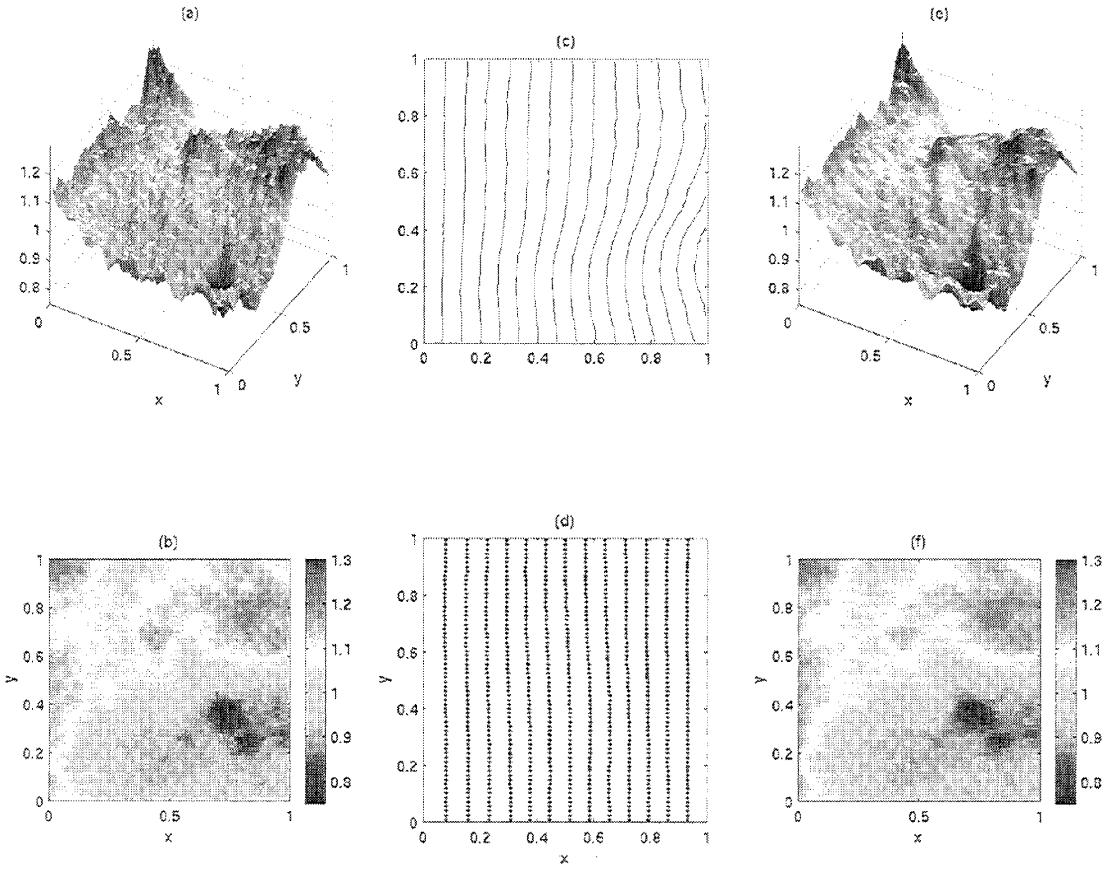

Figure 3: Application of the direct inverse method to an fBm field with $H = 0.8$ shown in the left side: (a)-(b) actual permeability plots; (c) actual arrival times; (d) actual (solid lines) and inverted (dotted lines) potential profiles; (e)-(f) inverted permeability plots.

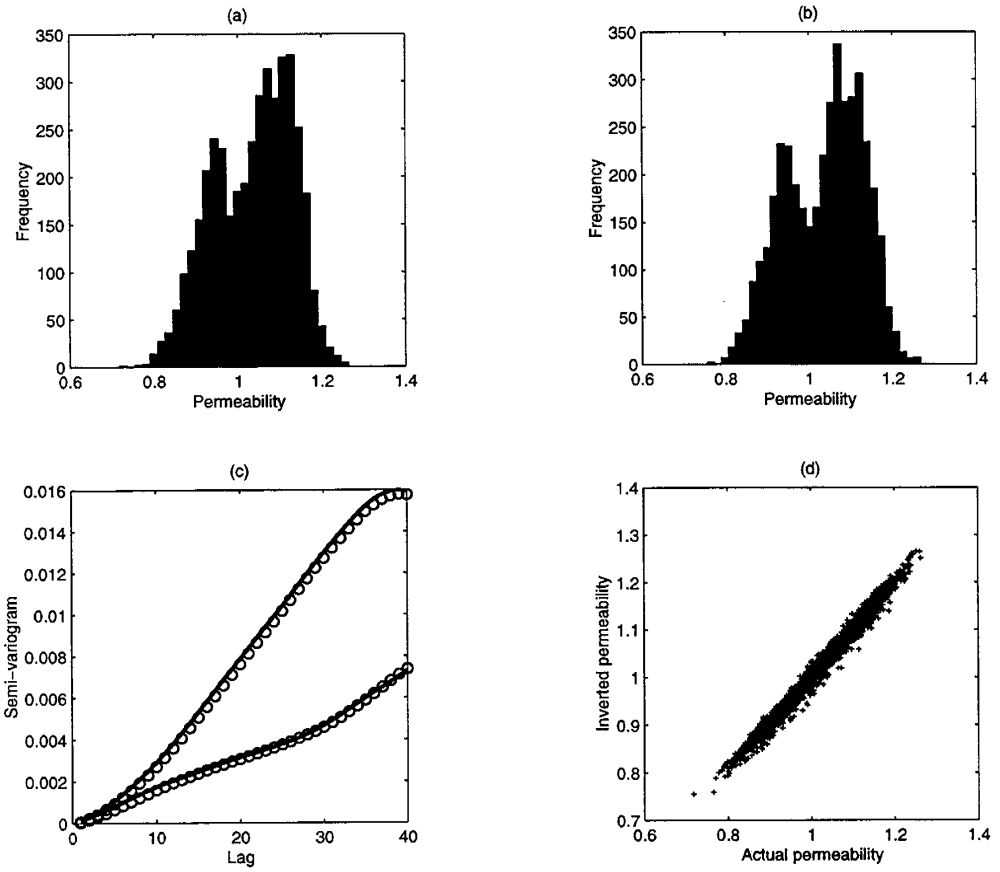

Figure 4: Statistical comparison between actual and inverted permeabilities of Fig. 3: (a) histogram of actual permeability; (b) histogram of inverted permeability; (c) semivariogram in two different directions of the actual (solid lines) and inverted (circles) data; (d) scatter plot of actual and inverted data.

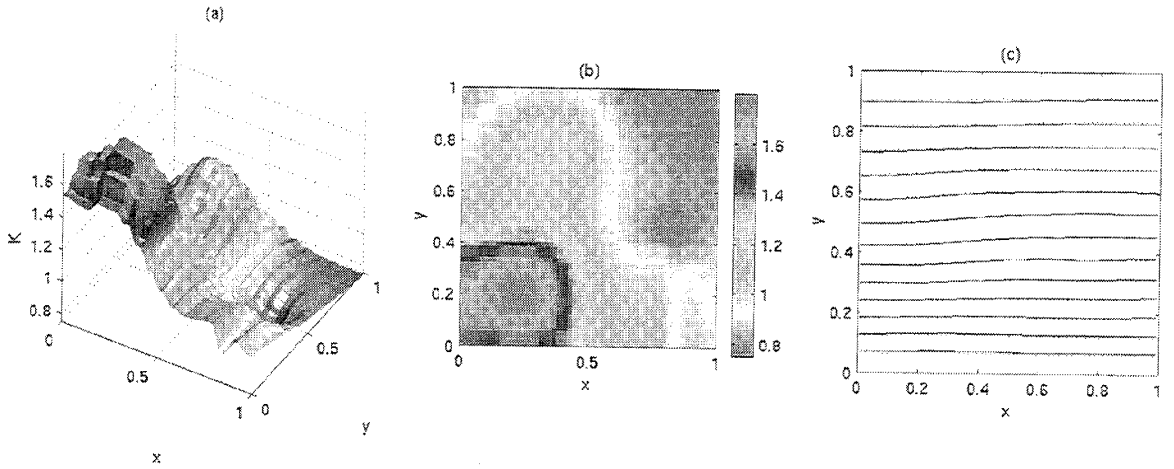

Figure 5: Application of the streamfunction approach to the medium of Fig. 2: (a)-(b) inverted permeability plots; (c) actual (solid lines) and inverted (dotted lines) streamlines.

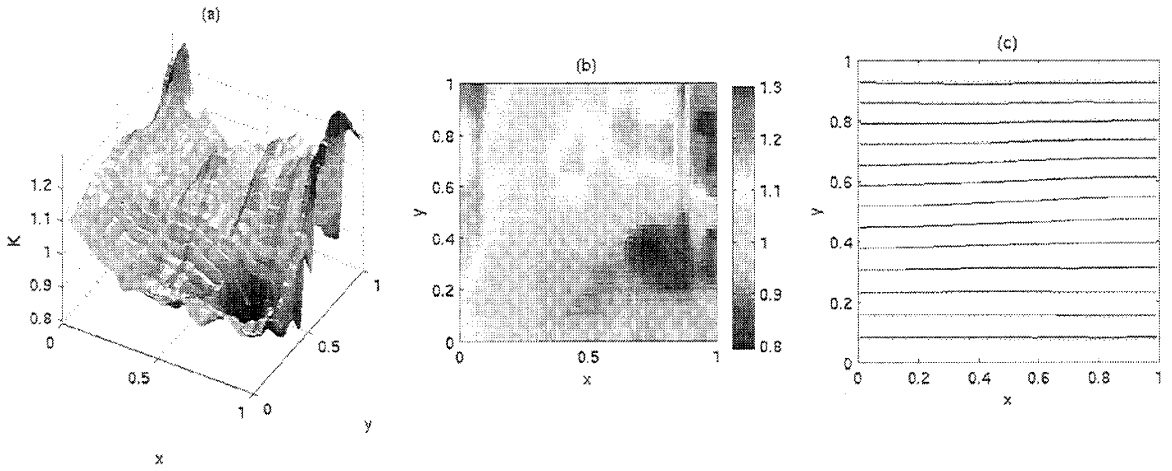

Figure 6: Application of the streamfunction approach to the medium of Fig. 3: (a)-(b) inverted permeability plots; (c) actual (solid lines) and inverted (dotted lines) streamlines.

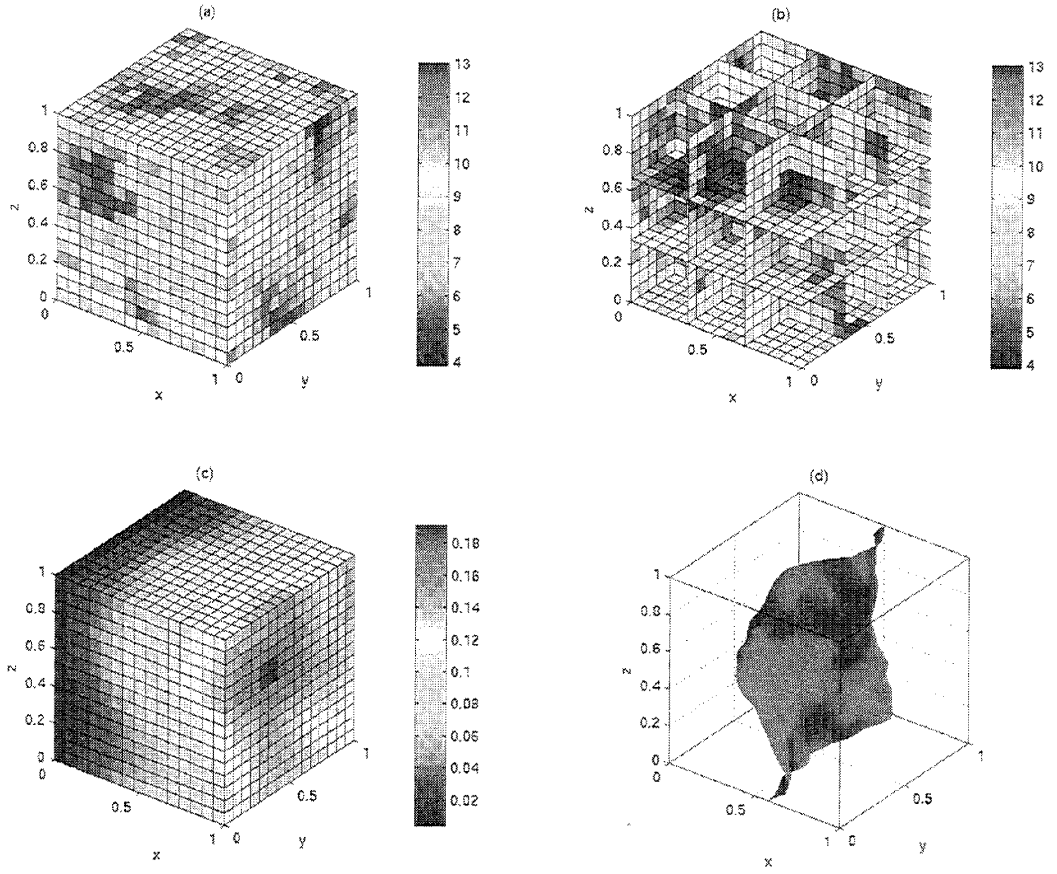

Figure 7: A 3-D permeability field and corresponding arrival times: (a)-(b) the actual permeability field in different cross-sections; (c) the arrival time distribution; (d) arrival time isosurface at $t = 0.07$.

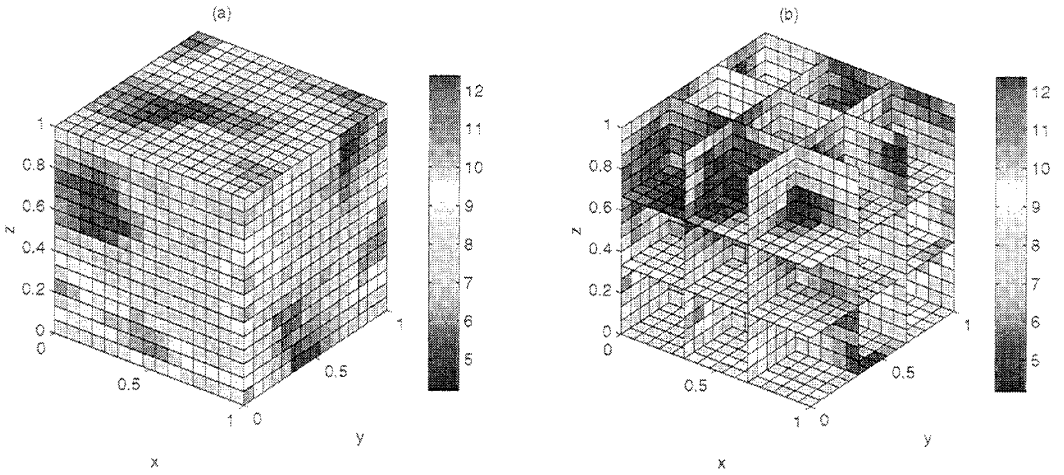

Figure 8: Application of the direct inverse method to the 3-D field of Fig. 7: (a)-(b) representation of the inverted data in different cross-sections.

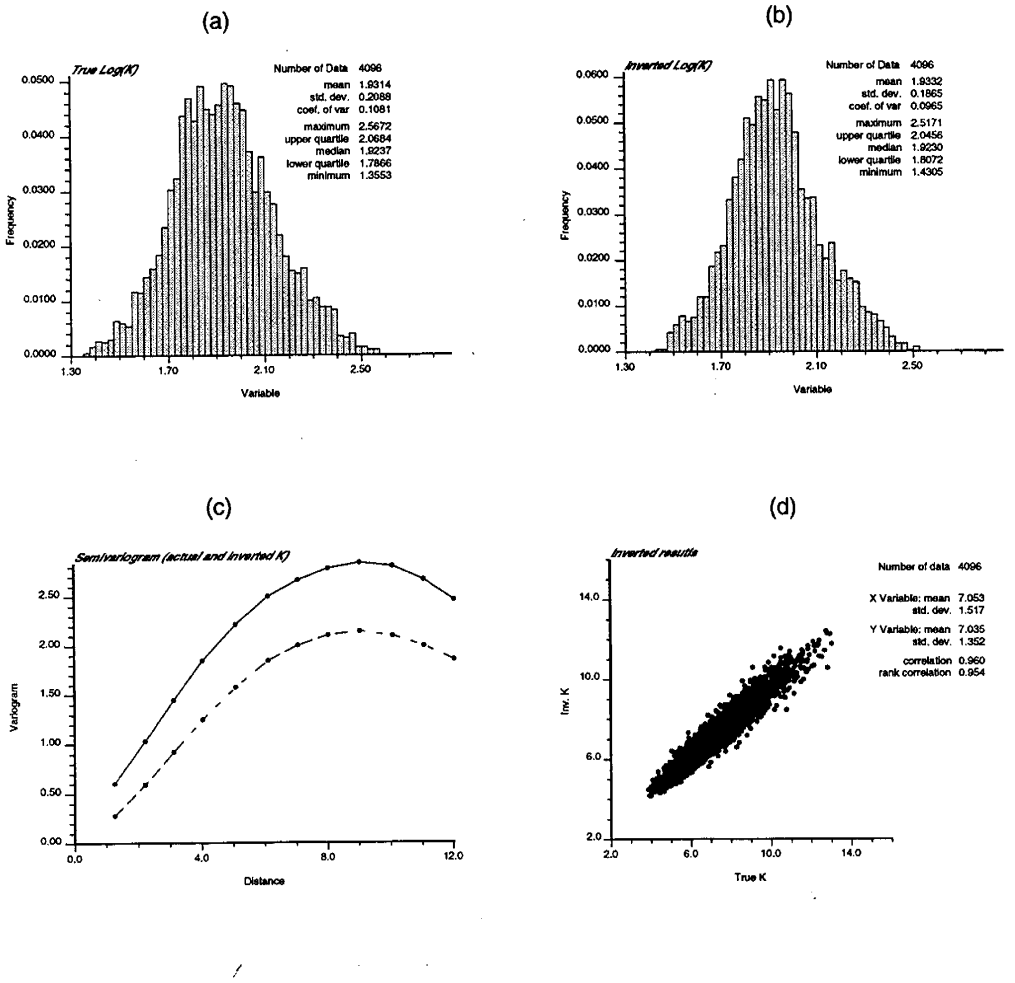

Figure 9: Statistical comparison between actual and inverted permeabilities of Fig. 8: (a) histogram of actual permeability; (b) histogram of inverted permeability; (c) omni-direction semivariogram of the actual (solid lines) and inverted (dash lines) data; (d) scatter plot of actual and inverted data.

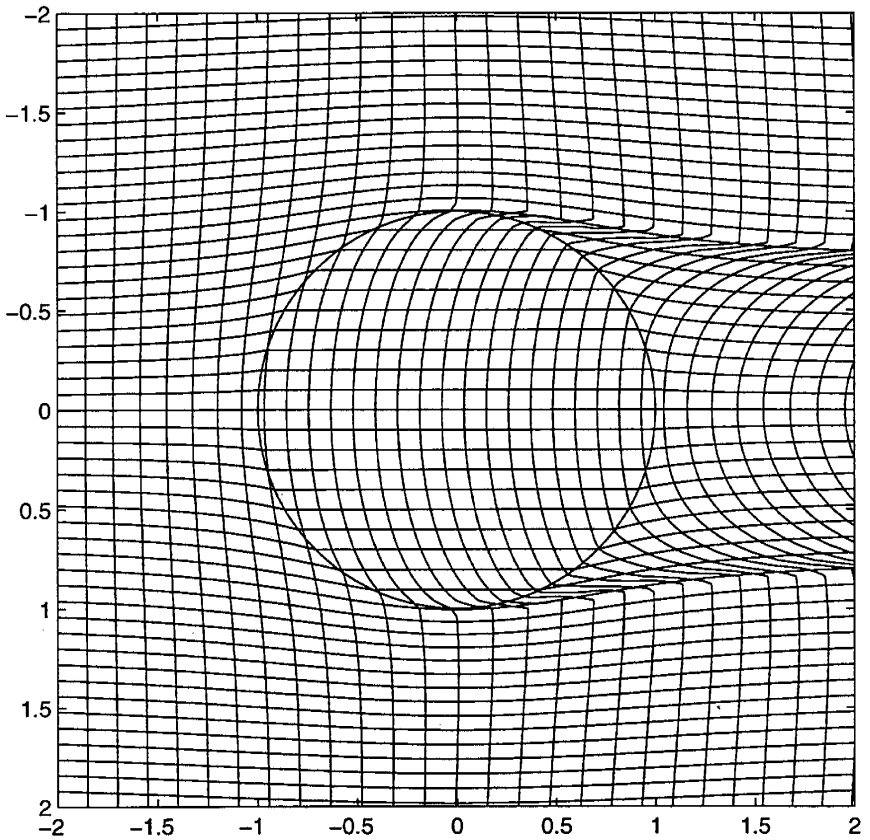

Figure 10: Streamlines and arrival time contours corresponding to a medium of uniform permeability in which a circular inclusion of lower permeability is embedded (permeability contrast is 0.6:1). The contours are calculated analytically (see Appendix). Displacement is from left to right.

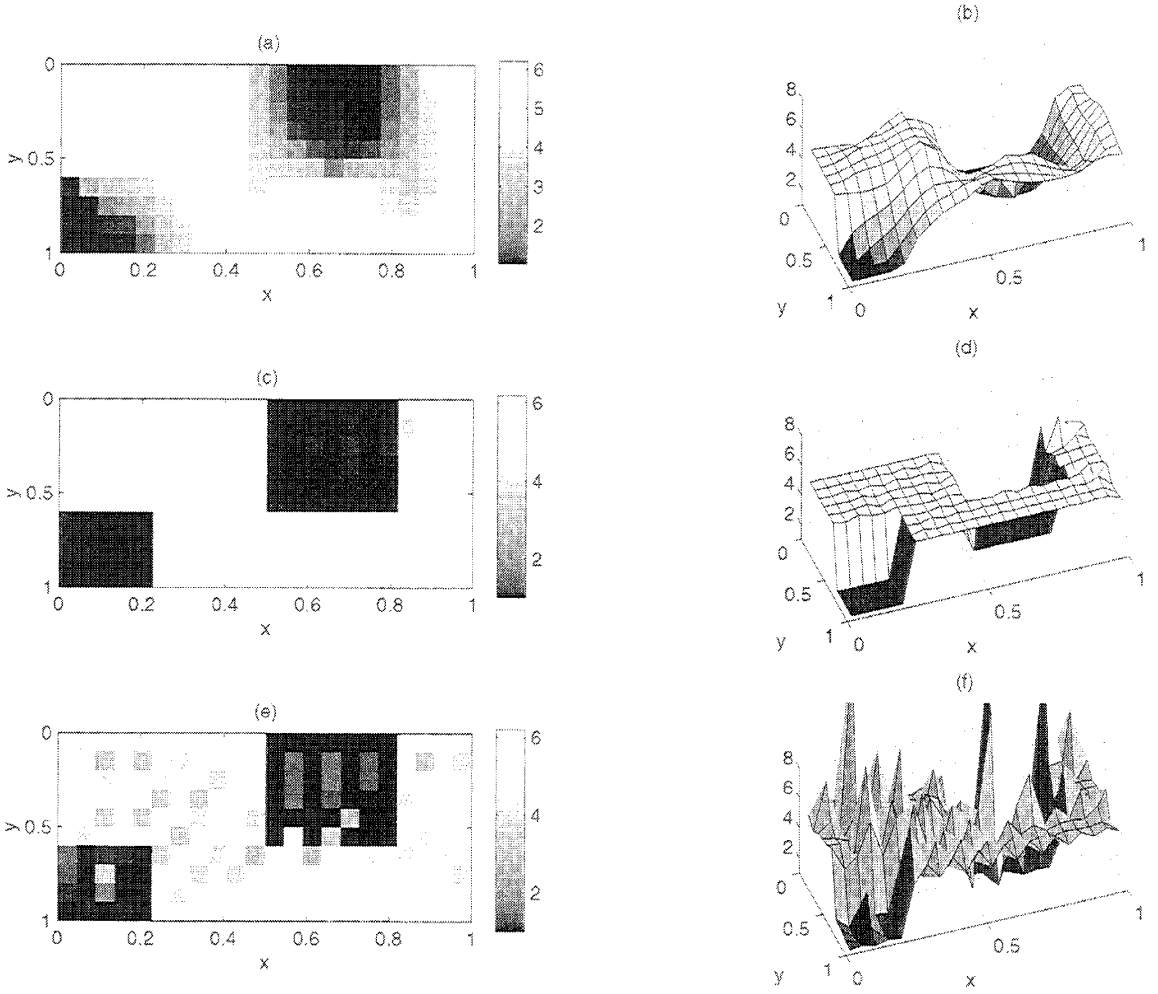

Figure 11: Application of the hybrid algorithm to a system with block discontinuities in permeability (permeability contrast is 1:5): Top two plots (a)-(b) show permeability estimates after steps 1-3 (Kriging). Middle two plots (c)-(d) show permeability estimates after step 4 (optimization). Note the closeness to the actual data. Bottom two plots (e)-(f) show permeability estimates using the optimization method but with a uniform permeability initial guess.

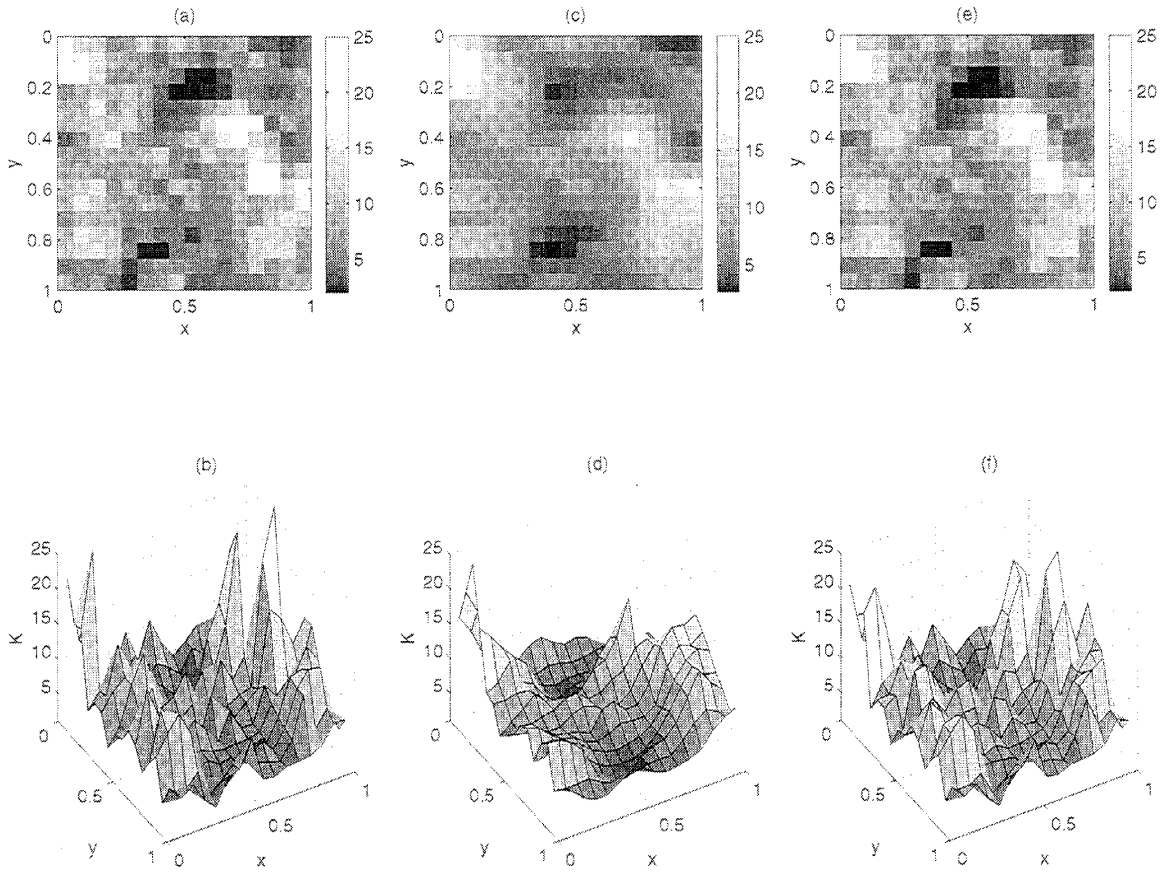

Figure 12: Application of the hybrid algorithm to a field with log-normal distribution with maximum contrast of about 10: (a)-(b) actual permeability plots; (c)-(d) plots of permeability estimates after steps 1-3 (Kriging); (e)-(f) plots of permeability estimates after step 4 (optimization). Note that the cut-off value of the colorbars in the image plots is set at 25.

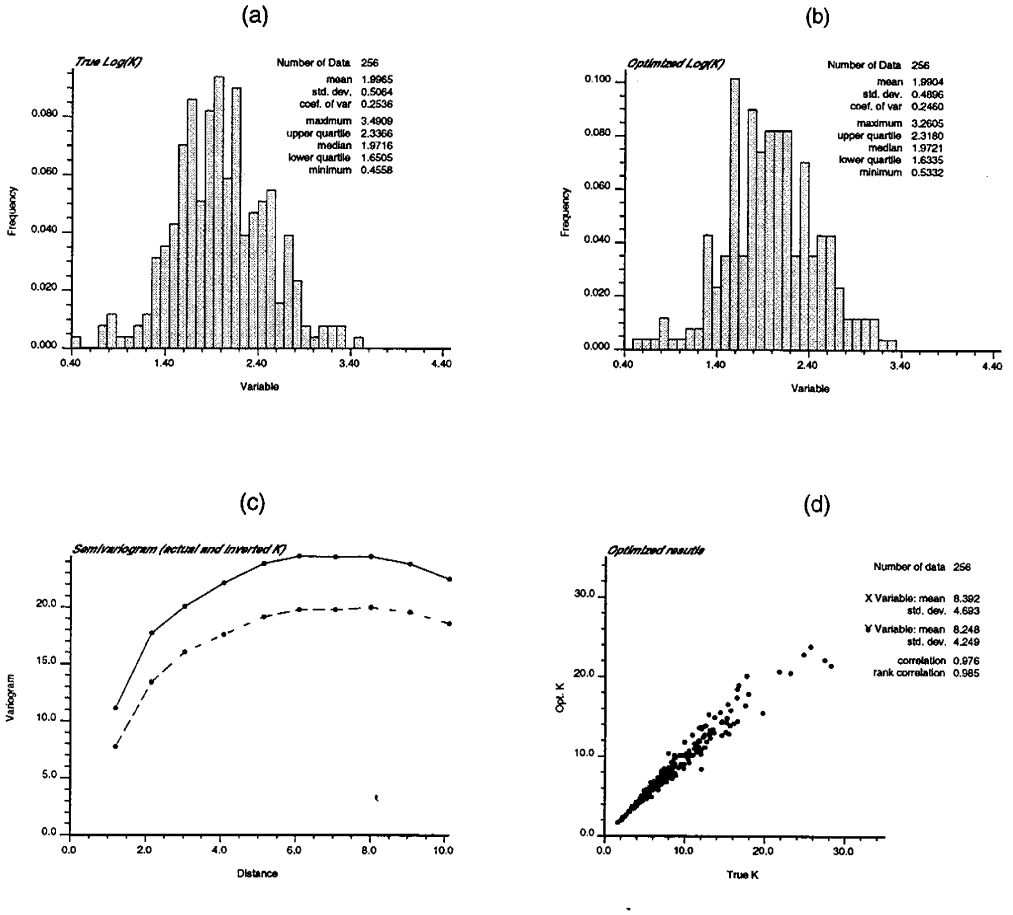

Figure 13: Statistical comparison between actual and inverted permeabilities of Fig. 12: (a) histogram of actual permeability; (b) histogram of inverted permeability; (c) omni-direction semivariogram of the actual (solid lines) and inverted (dash lines) data; (d) scatter plot of actual and inverted data.

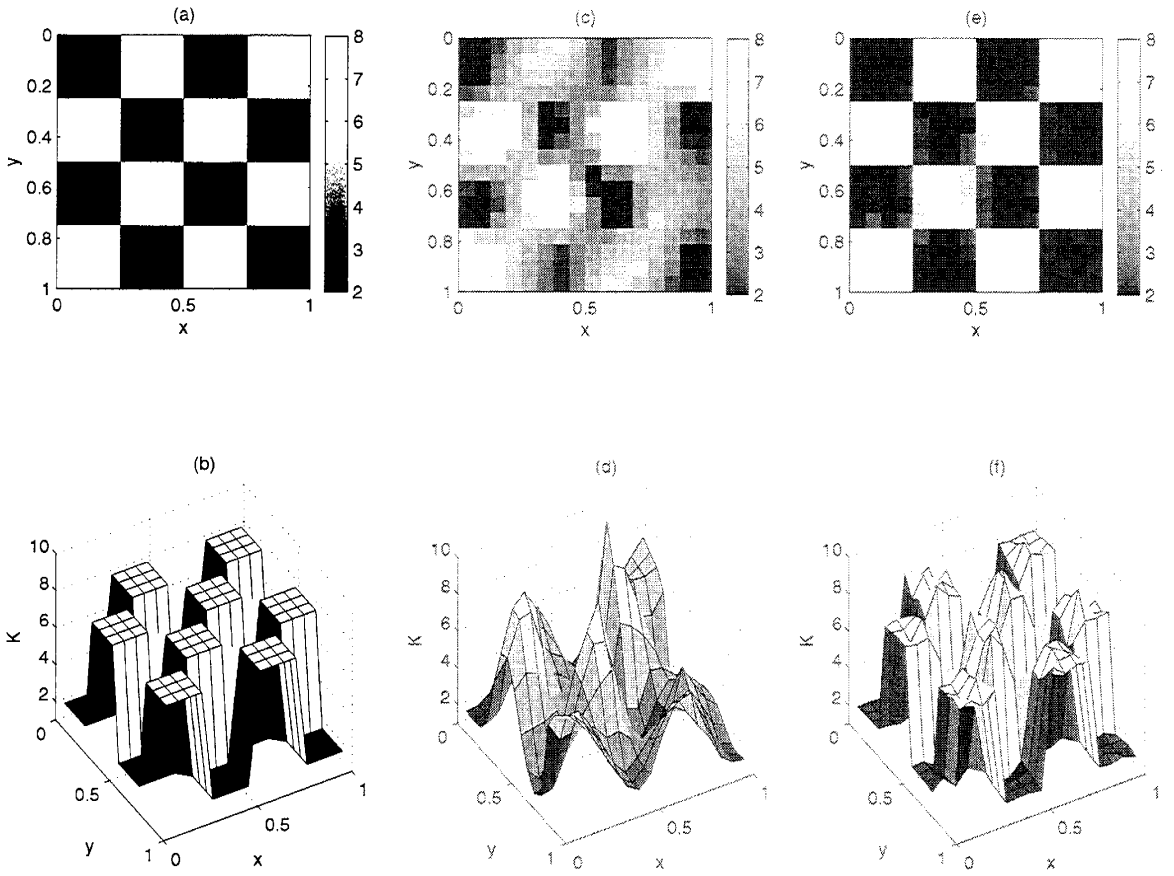

Figure 14: Application of the hybrid algorithm to a checkerboard permeability pattern (contrast is 2:8): (a)-(b) actual permeability plots; (c)-(d) plots of permeability estimates after steps 1-3 (Kriging); (e)-(f) plots of permeability estimates after step 4 (optimization). Note that the cut-off value of the colorbars in the image plots is set at 8.

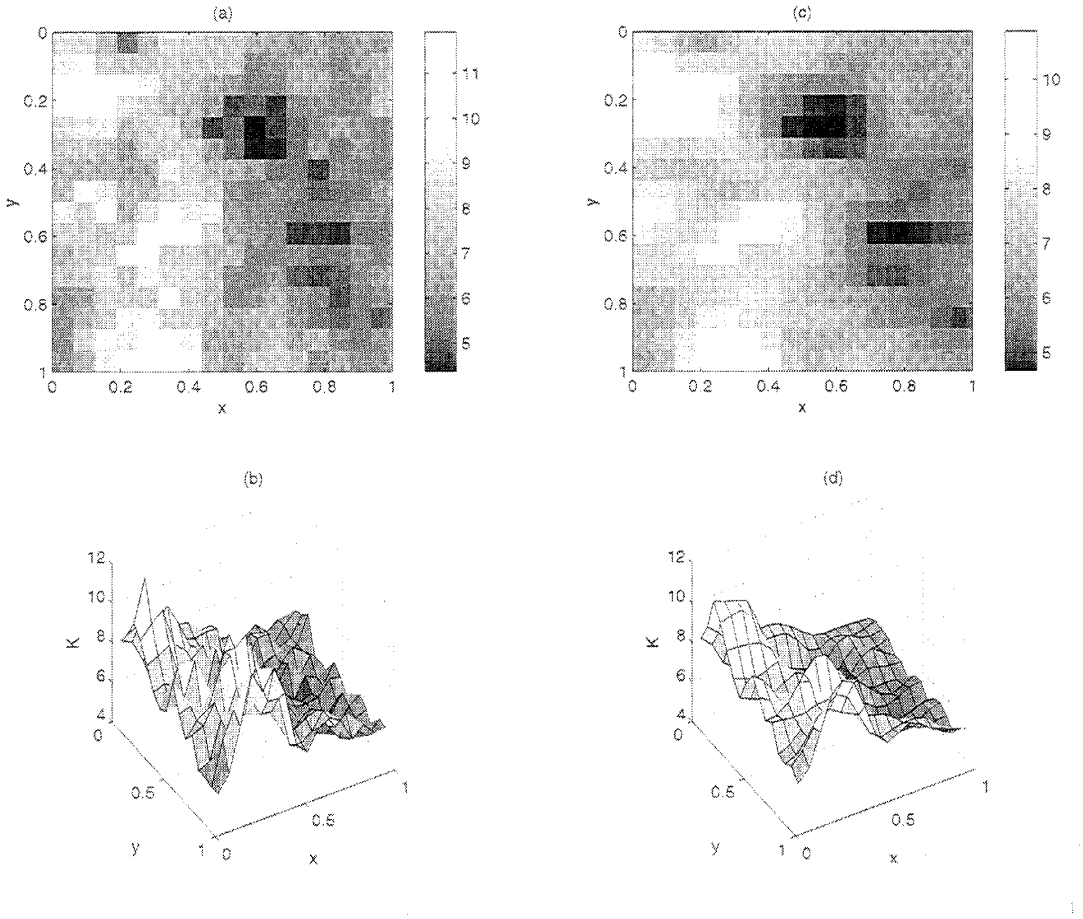

Figure 15: Application of the direct inverse method to an anisotropic field with known and fixed principal axes of anisotropy. Results for k_x: (a)-(b) plots of the actual permeability component values; (c)-(d) plots of the inverted permeability component values.

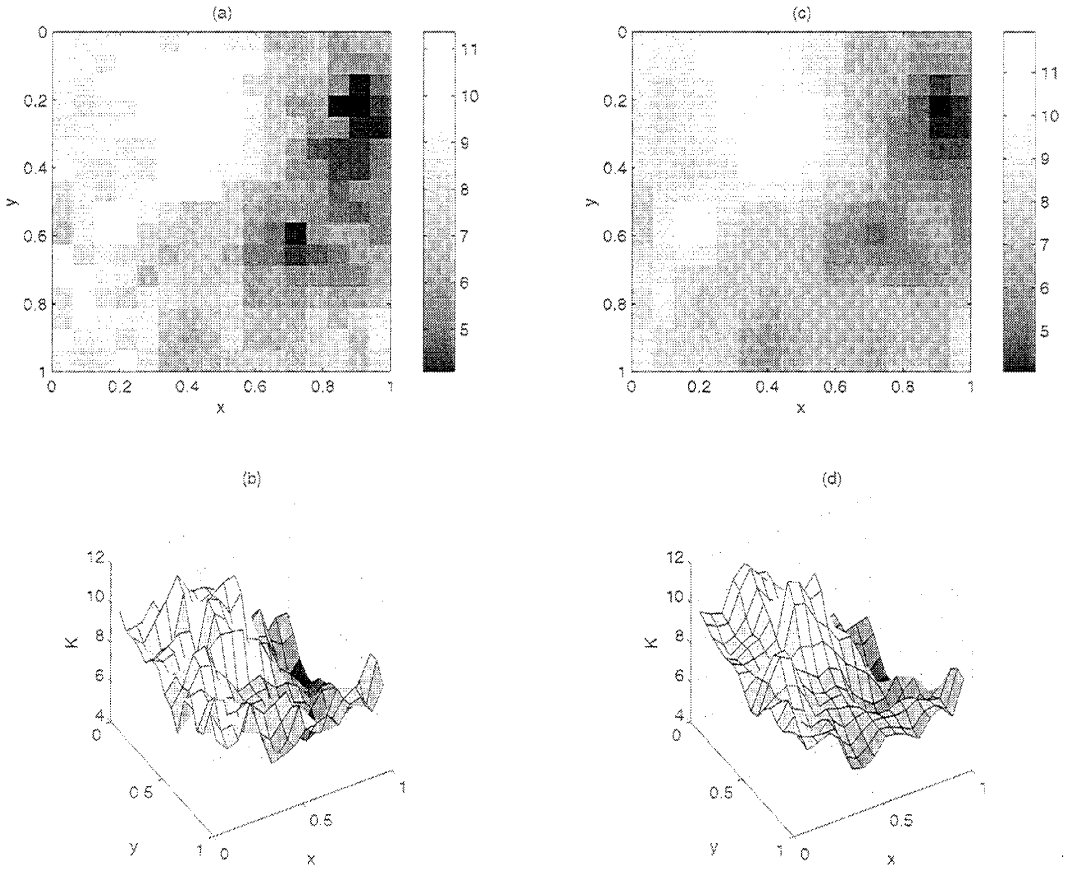

Figure 16: Application of the direct inverse method to an anisotropic field with known and fixed principal axes of anisotropy. Results for k_y: (a)-(b) plots of the actual permeability component values; (c)-(d) plots of the inverted permeability component values.